A Study of Interferometric Distance Measurement Systems on a Prototype Rapid Tunnel Reference Surveyor and the Effects of Reference Network Errors at the International Linear Collider

John Dale
Wolfson College, Oxford

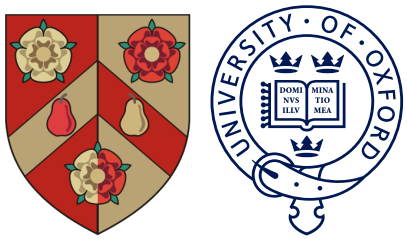

Thesis submitted in partial fulfilment of the requirements for the degree of Doctor of Philosophy at the University of Oxford

Michaelmas Term, 2009

Abstract

The International Linear Collider (ILC) aims to collide electrons and positrons with a centre of mass energy of 500GeV and a luminosity of 2×10^{34} $cm^{-2}s^{-1}$. To achieve this luminosity, the nominal final emittance of the electron and positron beams have to be below 10μm.rad horizontally and 0.04μm.rad vertically. To prevent the emittance from becoming too large, the main linacs will require alignment at an unprecedented level. The ILC main linacs will be aligned with respect to a reference network which runs along the entire length of the tunnel. The Linear Collider Alignment and Survey (LiCAS) Rapid Tunnel Reference Surveyor (RTRS) is the prototype of a device proposed to survey the ILC reference network. The LiCAS RTRS has several measurement systems; its Frequency Scanning Interferometry (FSI) measurement system is studied in this thesis. The FSI system has three distinct sub-systems: the reference interferometers, the external FSI measurement system and the internal FSI measurement system. The errors on the length of the reference interferometers are shown to be of the order of 1.1μm (0.3ppm). The external FSI measurement system is shown to measure distances close to 0.42m with errors of $\pm1.9\mu$m stat $\pm0.16\mu$m syst and the internal FSI measurement system is shown to measure distances close to 4.2m with errors of $\pm0.24\mu$m stat $\pm1.6\mu$m syst.

A survey of the ILC reference network using laser trackers is simulated without taking account of systematic measurement errors from refraction in the tunnel air. The simulated networks are used to misalign the simulated accelerators in Dispersion Matched Steering (DMS) simulations. The DMS simulations show that only 30% of the simulated accelerators produce an acceptable final corrected vertical emittance. It is further shown that the introduction of long range distance measurements between primary reference markers (PRMs) using GPS, reduces the long range error growth in the network, and that 95% of simulated accelerators give acceptable performance. A simplified network simulation model, which is capable of simulating reference networks surveyed by conventional and novel devices, is produced and compares favorably to full simulations.

To my family.

Acknowledgements

I would like to acknowledge all of the people who have helped and supported me during the four years of my DPhil. I should begin by thanking the members of the LiCAS and MONALISA groups and first of all my fellow DPhil students Greg Moss and Matthew Warden. I thank them for keeping the office an enjoyable place to work, and especially to Greg for his help during the long shifts in the DESY tunnel; I wish them both all the best with the completion of their DPhils. Many thanks to Patrick Brockill for his help with understanding non-linear least squares, to Paul Coe and David Urner for all their help and advice, and of course, to my supervisor Armin Reichold for all his supervision, help and guidance over the past four years.

I would like to thank all of the members of the Oxford Physics design office, central electronics and mechanical workshops; without their help and support the LiCAS RTRS would never have become a reality. From central electronics I would especially like to thank Mark Jones and Roy Wastie who developed the electronics and firmware for the FSI. From the mechanical workshops I would like to thank Mike Tacon, Tony Handford and Richard Swift for putting up with my constant questions about the mechanical components and for their help with the construction of the RTRS.

I would like to thank all the people at DESY Hamburg who helped me during my LTA, especially Markus Schlösser for his help with understanding surveying and the PANDA software and Freddy Poirier for his help with understanding Merlin.

Finally to my family, without all their love and support, this would never have been possible.

To you all, thank you

The author gratefully acknowledges financial support for his work from STFC under the auspices of studentship PPA/S/B/2005/04260.

This thesis was written using the LaTeX2$_\epsilon$ typesetting package. All graphs were produced using JHPlot, Corel Draw, Corel Photo Paint and DIA unless otherwise stated. This thesis and the research it describes are original work carried out solely by the named author.

Published at the University of Oxford, United Kingdom

Contents

List of Figures

List of Tables

Chapter 1

Introduction

Over the past century particle physics has grown into a mature field with large international collaborations and multi-billion dollar experiments. To date, the crowning achievement of particle physics has been the development of the standard model of particle physics (SM). The SM can predict phenomena seen in particle physics experiments and in the past has been used to predict the existence of new particles which have later been discovered. The SM is at best a low energy approximation to a more powerful theory. For example, the SM does not explain why particles come in three generations and why there is a mass hierarchy across the generations. There are many possible extensions to the standard model and to determine which one regime is realised in nature, particle physics experiments need to move into the TeV energy scale.

1.1 Physics at the TeV energy scale

There are many motivations for the study of particle physics beyond at TeV energies; for example, the discovery of the Higgs boson and the discovery of Supersymmetry.

1.1.1 The Higgs mechanism

The unified electroweak theory of the standard model is locally gauge invariant[1]. This local gauge invariance leads to a symmetry which requires all gauge bosons to be massless and have integer spin. This is a problem, as from experiments it is known that two of the gauge bosons of electroweak interactions, the $W^{\pm}$ and Z have a large mass. To solve this problem the SM Higgs mechanism is introduced which spontaneously breaks the electroweak symmetry [2][1]. The Higgs mechanism postulates that there is an all-pervading field, the Higgs field, an excitation of which is the Higgs boson.

The Higgs boson's properties, except for its mass, can be predicted by the SM. The predicted properties include the coupling of the Higgs boson to the other particles. The Higgs boson couples strongly to heavy particles, such as the $W^{\pm}$ and Z, and weakly to light particles such as neutrinos, electrons and muons. As the light Higgs has already been excluded by the LEP2 experiment, this leads to one of the first obstacles when trying to detect the Higgs boson; we need to produce heavy particles. The production of heavy particles requires large centre of mass energy collisions. The mass of the Higgs boson is not predicted by the SM, but experiments have put limits on it. The lower limit of the mass of the Higgs has been determined by the LEP2 experiment to be 114.4 GeV. The upper limit to the Higgs boson mass at the 95% confidence level, through a fit of all current experimental electroweak precision data is 200 GeV[1]; however the region 160GeV to 170GeV has been ruled out at the 95% confidence level by the DØ and CDF calaborations [3].

There are extensions to the SM, such as the minimal supersymmetric (MSSM) extension, which extend the Higgs model and increase the number of Higgs bosons. The discovery of the Higgs boson or bosons and the understanding of how their interactions affect matter,

are strong motivations for exploring physics at the TeV energy scale.

1.1.2 Supersymmetry (SUSY)

There are several theories which extend the SM to energies beyond those of current experiments, one of which is supersymmetry (SUSY). In SUSY, every particle which exists in the standard model has a supersymmetric partner referred to as a sparticle. A sparticle has the same quantum numbers as the corresponding particle, except for its spin and mass; the mass difference is generated through symmetry breaking mechanisms. Particles with spin 1/2 (fermions) partner with a sparticle with spin 0, and particles with spin 1 (bosons) partner with a sparticle with spin 1/2.

SUSY is an appealing theory as it solves some problems with the SM. SUSY extensions of the SM allow the strong, electromagnetic and weak forces to be unified at approximately 1×10^{16}GeV in a Grand Unified Theory (GUT)[2]; this is not possible in the current formulation of the SM alone. SUSY also offers a solution to the naturalness problem. The naturalness problem is that the Higgs mass has contributions from radiative corrections involving gauge bosons and fermion loops [2]. These corrections lead to divergences in the Higgs mass under re-normalisation. By introducing sparticles, which have the same couplings as their corresponding particles, the radiative corrections to the Higgs mass are approximately cancelled[1] and will lead to a well defined Higgs mass.

The SM currently does not have any candidates for cold dark matter, which, from cosmological data, makes up about 25% of the energy density of the universe [4]. SUSY predicts the existence of massive, electrically neutral, weakly interacting particles or WIMPs which could be candidates for cold dark matter.

One shortcoming of SUSY is that to date no sparticles have been detected. If SUSY was an exact symmetry the sparticles would have the same mass as their corresponding particles, which is not the case. This implies that SUSY must be broken in some way. There

[1]Only approximately as sparticles do not have the same mass as their partnered particles

are several SUSY models which break the symmetry using different mechanisms, for example the MSSM[2][1] model; these mechanisms will not be discussed further. The determination of the correct SUSY model and the detection of the particles it predicts should be possible at TeV energy colliders.

1.2 TeV energy particle accelerators

There are several possible ways to study physics beyond the SM, one of which is to collide particle beams with greater energies than those available at current particle accelerators. The Large Hadron Collider (LHC) will collide proton beams with a centre of mass energy of 14TeV [5] and is likely to discover new physics. The LHC will have difficulty making precise measurements on new physics it discovers because it is designed for the discovery of new particles, and therefore collides proton beams. The collisions of the proton beams create a low signal to noise environment. An LHC proton bunch will consist of approximately 1.1×10^{11} protons and a proton consists of partons each carrying a fraction of the energy of the proton. When the LHC brings two proton beams into collision, multiple protons from a pair of crossing bunches will interact with each other in the same bunch crossing. The constituent partons strongly interact, which, due to confinement will lead to showers of particles in the detectors which cause a large background.

There is an international consensus that precise measurements are required on the discoveries made at the LHC. Precise measurements are required in order to fully identify which of the many possible SM extensions have been realised in nature. For precision measurements to be made, a much cleaner environment is needed, with the current best solution being an e^+e^- collider. e^+e^- colliders have a much cleaner environment because the collisions are all close to the centre of mass energy. Also electrons and positrons interact via the electroweak forces, leading to a lot less hadronic events and a smaller background. A future e^+e^- machine will have to be a linear collider to reach centre of mass energies of greater than 500GeV. This is because synchrotron radiation limits the beam energy available in

circular e^+e^- colliders. Synchrotron radiation is emitted when the trajectory of a charged particle is bent. This implies that in a circular machine, the beam would require constant re-acceleration and so limits the maximum centre of mass energy. The energy loss per turn (U_0) through synchrotron radiation can be shown to be [6]:

$$U_0 \propto \frac{E^4}{\rho}. \tag{1.1}$$

Where E is its energy of the beam and ρ is the radius of the accelerator. If we take the LEP II collider, which had a radius of 4.7km, a centre of mass energy of 180GeV and $U_0 = 1.5$GeV, and scale it to 500GeV, to keep the energy loss per per unit length constant, a machine with a radius of 36km would be required. This would be prohibitively expensive to build and rules out the construction of a circular machine at centre of mass energies of 500GeV for e^+e^- colliders.

For an e^+e^- linear collider to study physics beyond the SM, not only does it have to produce high energy beams, but the collisions require high luminosity, $\mathcal{L}$, because the cross sections for the processes of interest are very small. The luminosity is the number of interactions per unit time per beam cross section and is given by [6]:

$$\mathcal{L} = \frac{nN^2\mathcal{H}_\mathcal{D}f}{4\pi\sigma_x\sigma_y}. \tag{1.2}$$

Where n is the number of bunches per train, N is the number of particles in a bunch, f is the machine repetition rate, $\mathcal{H}_\mathcal{D}$ is the disruption parameter and σ_x and σ_y are the RMS horizontal and vertical beam dimensions at the IP.

The dominating problem when achieving high luminosity in the next generation of high energy e^+e^- colliders, will be the generation of small beam sizes. To generate small beam sizes the horizontal and vertical emittances (ϵ_x and ϵ_y respectively) of the beam have to be minimised. The emittance is a measure of the area occupied by the beam in space, x, and its divergence angle, x' [6]. If x is plotted against x' for all the particles in a particle beam,

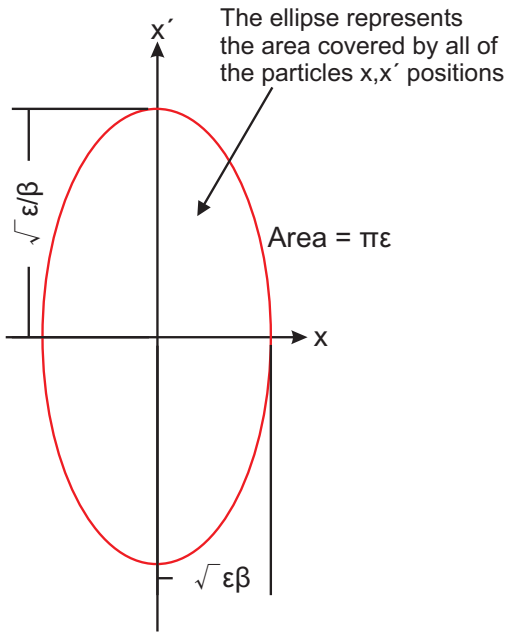

Figure 1.1: The idealised transverse phase space plot for a large number of particles in a beam. β is the transverse amplitude of the focusing lattice [7].

as shown in figure 1.1, they will form an ellipse[2] [7]. Where β, in figure 1.1, is transverse amplitude of the focusing lattice in the horizontal (x) or vertical (y) planes, which is a property of the accelerator.

As a particle beam is accelerated, it is more convenient to talk about the normalised emittance. The normalised emittance is an expression of the emittance in canonical phase space (q,p) and this is invariant under acceleration [6]; normalised emittance is given by:

$$\epsilon_n = \gamma\beta_{rel}\epsilon. \tag{1.3}$$

where γ is the Lorentz factor and β_{rel} is the relativistic beta ($\beta_{rel} = v/c \approx 1$ for high energy electron beams). From this point forward the term emittance will refer to the normalised emittance. It is possible to define the normalised beam emittance in terms of beam sizes:

$$\epsilon_x = \frac{\gamma\pi\sigma_x^2}{\beta_x}, \tag{1.4}$$

$$\epsilon_y = \frac{\gamma\pi\sigma_y^2}{\beta_y}. \tag{1.5}$$

[2]this is the ideal case more complex shapes are usually formed

If the emittance of the particle beam can be reduced then the luminosity of the machine will be increased and therefore its performance improved. Note that the units for emittance is m rad, however the rad is dropped by convention.

1.3 The International Linear Collider (ILC)

One of the proposed future e^+e^- colliders is the International Linear Collider (ILC). The ILC aims to collide beams with a centre of mass energy of 500GeV (upgradeable to 1TeV) and a peak luminosity of 2×10^{34} cm^{-2}s^{-1}. The design of the accelerator is described in detail in [8] and [9]. The collider is based on superconducting (SC) RF technology, with the ILC SC RF cavities operating at 1.3GHz (L-band). A brief description of the ILC design follows.

1.3.1 The ILC accelerator subsystems

A schematic of the ILC is shown in figure 1.2. The ILC accelerator baseline design is broken down into several sections. This description follows the electron side of the machine, the positron side follows a similar set-up, except the source is different and will be described at the end of this section. The first stage is the generation of the electrons at the electron source (section 1.3.3). In the electron source the electrons are accelerated to 5GeV and then injected into the electron damping ring (section 1.3.5). The electron damping ring reduces the beam emittance to 8.0μm horizontally, 20nm vertically and then injects the beam into the electron ring to main linac (RTML) section (section 1.3.6). The electron RTML transports the beam from the damping ring to the entry point of the electron main linac (section 1.3.7); near its end the RTML compresses the electron bunches from 9mm to 0.3mm. During bunch compression the beam is accelerated to 15GeV. The electron ML accelerates the beam from 15GeV to 250GeV while keeping the emittance below 9.4μm horizontally and 34nm vertically. After the ML the beam enters the beam delivery system (BDS) (section 1.3.8); the BDS focuses the e^- and e^+beams and brings them into collision and finally transports the spent beams to the dumps

The positrons are produced using the electron beam taken from the electron ML (section 1.3.4). After the positrons are generated they follow a similar system to the electrons, but from the other side of the interaction point. The electron and positron damping rings are positioned on top of each other.

1.3.2 Beam parameters

To achieve a centre of mass energy (E_{cms}) of 500GeV with a luminosity of $2{\times}10^{34}\text{cm}^{-2}\text{s}^{-1}$, the ILC design parameters, given in table 1.1, have been chosen along with the beam parameters at the interaction point (IP), given in table 1.2. In table 1.2 a range of beam parameters are given, this is because the machine is designed to have a range of parameters that will give the same luminosity and E_{cms}. For example, if the bunch population is low ($1{\times}10^{10}$), then to achieve the same luminosity the number of bunches needs to be increased to 5340, and the emittance of the beam decreased to 30nm. The beam is not a continuous chain of bunches but it is broken down into pulses as shown in table 1.1.

Parameter	Unit	Value
Center-of-mass energy range	GeV	200 - 500
Peak Luminosity[a]	$\text{cm}^{-2}\text{s}^{-1}$	$2{\times}10^{34}$
Average beam current in pulse	mA	9.0
Pulse rate	Hz	5.0
Pulse Length (beam)	ms	1
Number of bunches per pulse		1000 - 5400
Charge per bunch	nC	1.6 - 3.2
Accelerating gradient[a]	MV/m	31.5
RF pulse length	ms	1.6
Beam power (per beam)[a]	MW	10.8
Typical beam size at IP[a] ($h \times v$)	nm	640×5.7
Total AC power consumption[a]	MW	230

Table 1.1: The basic design parameters for the ILC [8].([a] values for E_{cms} of 500GeV)

1.3.3 Electron source

The electron source has the following primary functions [8]:

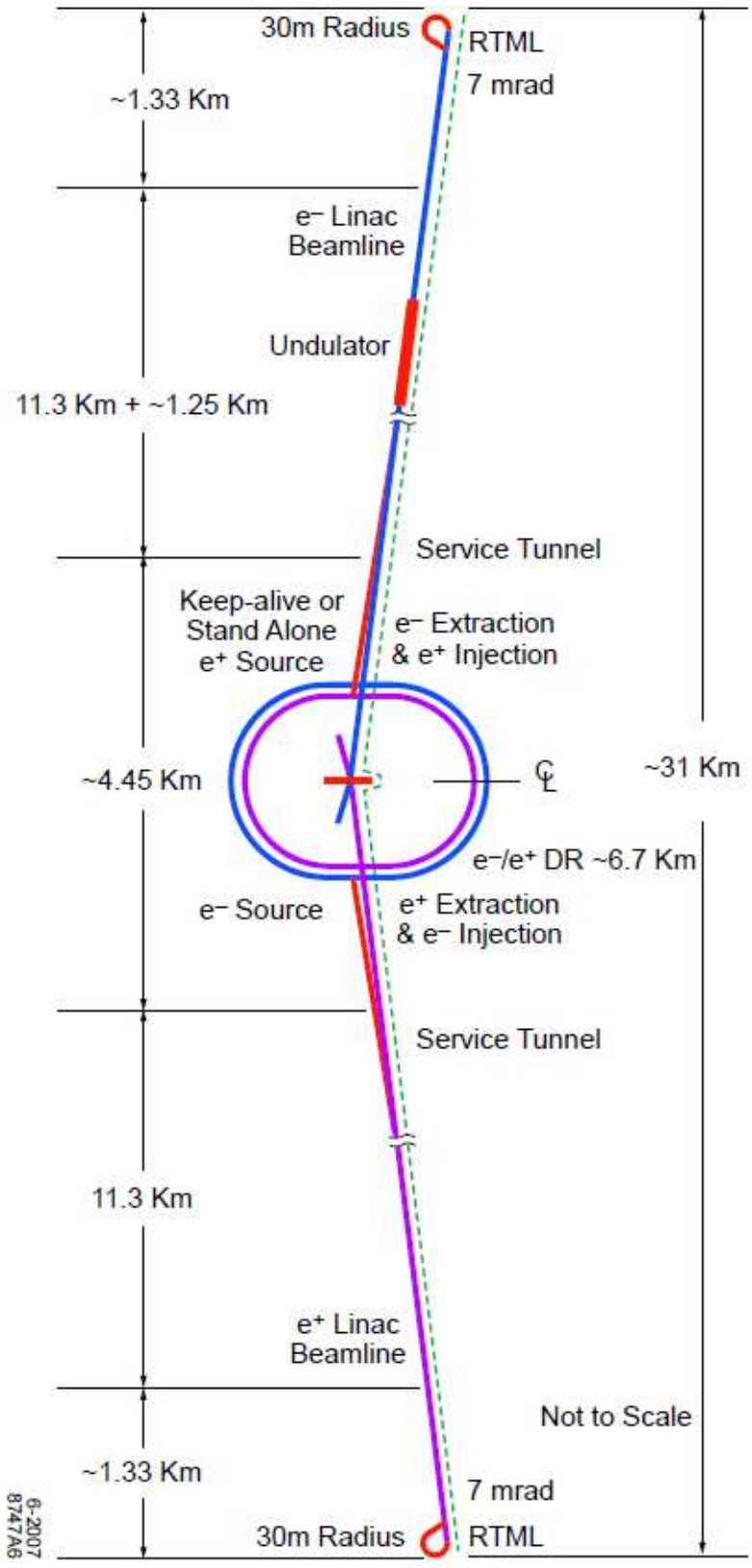

Figure 1.2: Schematic of the ILC for 500 GeV Centre of Mass [8].

Parameter	min	nominal	max	unit
Bunch population	1	2	2	$\times 10^{10}$
Number of Bunches	1260	2625	5340	
Linac bunch interval	180	369	500	ns
RMS bunch length	200	300	500	μm
Normalised horizontal emittance at IP	10	10	12	μm
Normalised vertical emittance at IP	0.03	0.04	0.08	μm
Horizontal beta function at IP	10	20	20	mm
vertical beta function at IP	0.2	0.4	0.6	mm
RMS horizontal beam size at IP	474	640	640	nm
RMS vertical beam size at IP	3.5	5.7	9.9	nm
Vertical disruption parameter	14	19.4	26.1	
Fractional RMS energy loss to beamstrahlung	1.7	2.4	5.5	%

Table 1.2: The range of beam parameters at the IP. The min. and max. columns do not represent consistent sets of parameters, but only indicate the design range for each parameter. [9]

- Generate a bunch train of polarized electrons with >80% polarisation.
- Perform energy collimation to remove low energy and large transverse momentum electrons.
- Accelerate the electron bunches from 76MeV to 5GeV.
- Perform energy compression and spin rotation into the vertical plane.
- Inject the beam into the electron damping ring.

Figure 1.3 shows a schematic of the electron source for the ILC. The electron beam is generated by illuminating a photocathode in a DC gun with a laser. There are two independent laser and gun systems to provide redundancy. The electrons are bunched and accelerated to 76MeV using normal conducting (NC) accelerating structures. The electron beam then passes through an energy collimator to remove low energy and large transverse momentum electrons. The beam is then accelerated to 5GeV in an SC linac. SC solenoids are used to rotate the electrons spin vector into the vertical plane before a SC RF structure is used for energy compression. After energy compression the beam is injected into the electron damping ring (section 1.3.5). Table 1.3 shows key parameters of the beam before it is injected into the electron damping ring.

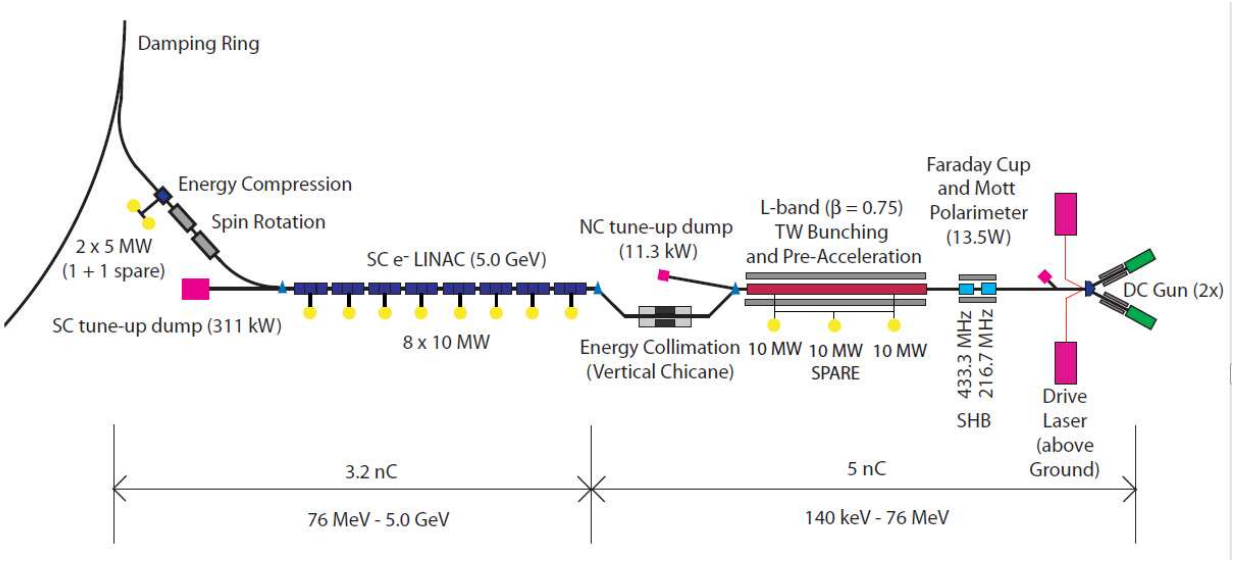

Figure 1.3: Schematic of the electron source [8].

Parameter	value
Electrons per Bunch	2×10^{10}
Bunches per Pulse	2625
Bunch Repetition Rate	3 MHz
Train Repetition Rate	5Hz
Electron Energy	5GeV
Electron Polarisation	>80%

Table 1.3: Key electron beam parameters before injection into the electron damping ring

1.3.4 Positron source

There will be two positron sources for the ILC: the primary source and the "keep-alive" source. The primary source uses electrons from the ML to generate the positron beam, and the keep alive source allows for commissioning and tuning of the positron systems when the high energy electron beam is not available. The ILC positron sources have the following primary functions [8]:

- To produce a high power multi-MeV photon drive beam for positron production (primary positron source only).

- To produce positron bunches by e^+e^- pair production in a metal target. The metal target must reliably handle the beam power and radioactivity (primary positron source only).

- To capture and accelerate the positron beam to 5 GeV.

- To perform energy compression and spin rotation into the vertical plane.

- To transport the positrons through 5km of transport lines, and inject them in to the positron damping ring.

Figure 1.4 shows a schematic of the positron sources. The primary positrons are generated through e^+e^- pair production at the metal target. To produce 10MeV photons required for efficient pair production the electrons from the electron main linac are used. The electrons in the electron main linac are accelerated to 150 GeV and then diverted from the ML into an offset beam line which contains a helical undulator. The undulator generates circularly polarised photons and then returns the electrons back to the electron main linac. The photons hit a Ti-alloy target and produce a beam of electrons and positrons. The electrons and positrons are then captured by an optical matching device (OMD) and accelerated to 125MeV using NC accelerator structures. After acceleration to 125MeV the electrons and remaining photons are separated off and dumped while the positrons are further accelerated to 400MeV. The beam is then transported to the central injector complex and accelerated to 5 GeV using SC accelerating components. The beam's spin vector is then rotated to the vertical plane and the beam undergoes energy compression before injection into the positron damping ring. Table 1.4 shows some of the key parameters of the beam before it is injected in to the positron damping ring.

Parameter	value
Positron per Bunch	2×10^{10}
Bunches per Pulse	2625
Train Repetition Rate	5Hz
Positron Energy	5GeV
Positron Polarisation	>60%
Electron Drive Beam Energy	150 GeV
Electron Drive Beam Energy Loss	3.23 GeV

Table 1.4: Key positron source parameters

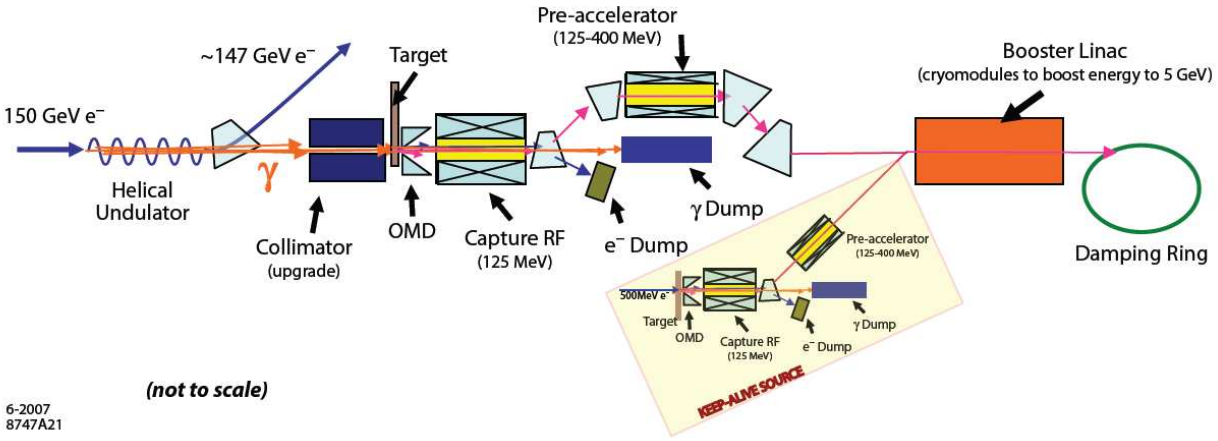

Figure 1.4: Schematic of the positron source [8] (injector complex is not shown).

1.3.5 Damping Rings (DR)

There are two damping rings in the ILC: the positron and electron damping rings. One damping ring is placed on top of the other. The damping rings have the following primary functions [8]:

- To accept e^- and e^+ beams with a betatron amplitude of 0.09 m·rad.
- To damp the beam emittance to 20nm vertically and 8μm horizontally within the 200 ms between machine pulses.
- To inject and extract individual bunches without affecting the emittance or stability of the stored bunches in the DR.

As shown in figure 1.2 the damping rings are located in the middle of the ILC site, with one stacked on top of the other to reduce tunnelling costs. The damping ring tunnel is 10m above the beam delivery system to allow adequate shielding so that the injector system can be operated while other systems are open to human access.

The damping ring lattice (shown in figure 1.5) consists of six arc sections made of theoretical minimum emittance (TME) cells and six straight sections consisting of quadrupole focusing defocusing (FODO) cells. Two of the straight sections are for injection and extraction while the other four contain the RF systems and superconducting wigglers. One ring

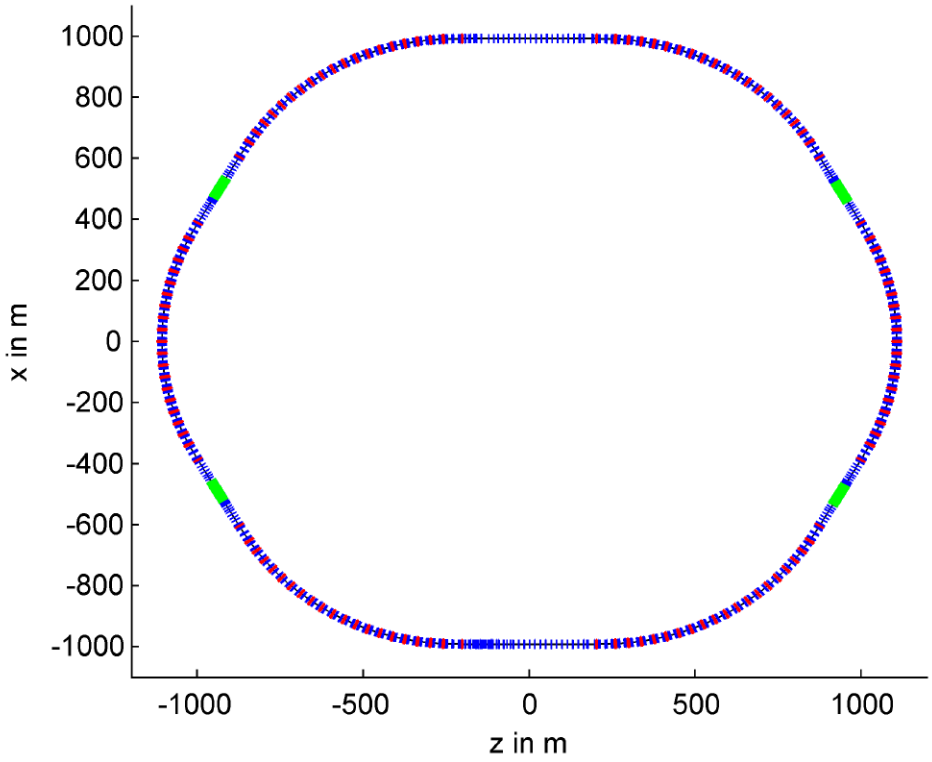

Figure 1.5: The ILC damping ring layout [9].

has 40 wigglers and 18 RF cavities. All of the damping ring magnets, except for the wigglers, are NC. The SC RF cavities run at half the frequency of the cavities in the main linac to accommodate different bunch patterns. Key extraction parameters are shown in table 1.5.

Parameter	value
Extracted bunch separation	330ns
Extracted normalized horizontal emittance	8μm
Extracted normalized vertical emittance	20nm
Extracted energy spread	0.15%
Extracted bunch length	9mm
Maximum extracted beam jitter	1σ
Extracted energy	5GeV

Table 1.5: Key nominal damping ring beam extraction parameters

1.3.6 Ring To Main Linac (RTML)

The RTML has the following functions to perform [8]:

- To transport the beam from the damping ring to the main linac.

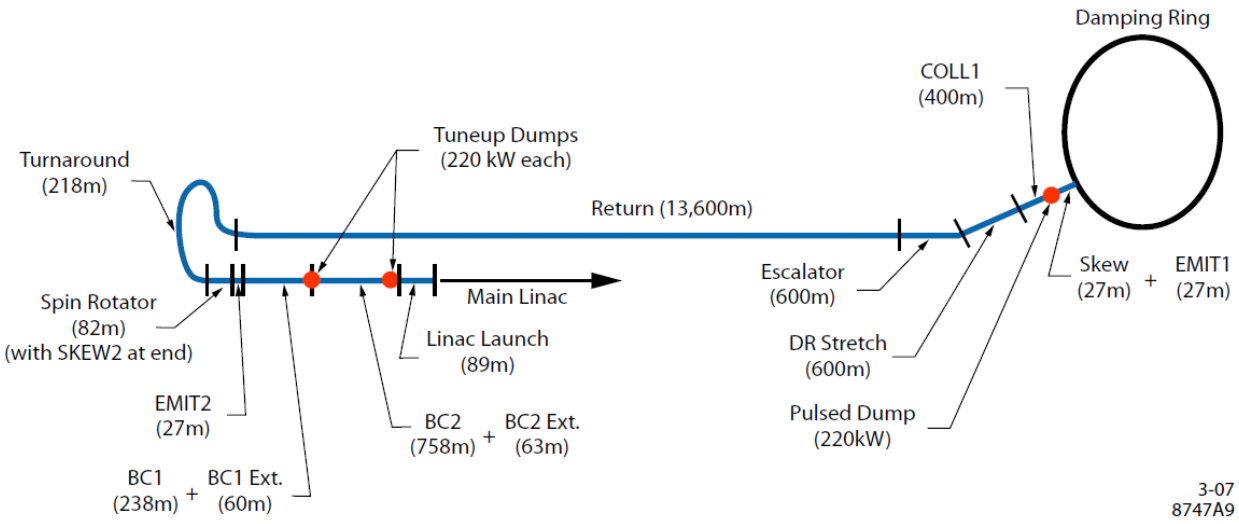

Figure 1.6: The RTML layout [8].

- To collimate the beam halo generated in the damping ring.

- To rotate the polarization from the vertical to any arbitrary angle required at the IP.

- To compress the bunch length from 9mm to 0.3mm .

Figure 1.6 shows a schematic of the RTML. The RTML transports the damped beam through approximately 15km of transport lines, while maintaining the 5GeV energy and the low emittance. The RTML is in the same tunnel as the ML (section 1.3.7) and is vulnerable to ML stray fields. The RTML transports the beam through 180^o turn which enables feed forward beam stabilisation for beam jitter reduction. After the 180^o turn the beam enters spin rotators and then into a two stage bunch compressor. A two stage bunch compressor is used as a single stage bunch compressor will produce an energy spread which is unacceptably high. The bunch compressor accelerates the beam to 15GeV and reduces the longitudinal size to 0.3mm. The bunch compressors also generate the different energy beams required for dispersion matched steering (section 7.1). The key nominal parameters for the RTML are shown in table 1.6

Parameter	value
Final bunch length	0.3 mm
Final energy	15.0GeV
Final energy spread	1.5%
Final horizontal beam jitter	0.1σ
Vertical emittance budget	4nm
Horizontal emittance budget	1μm

Table 1.6: Key nominal RTML parameters

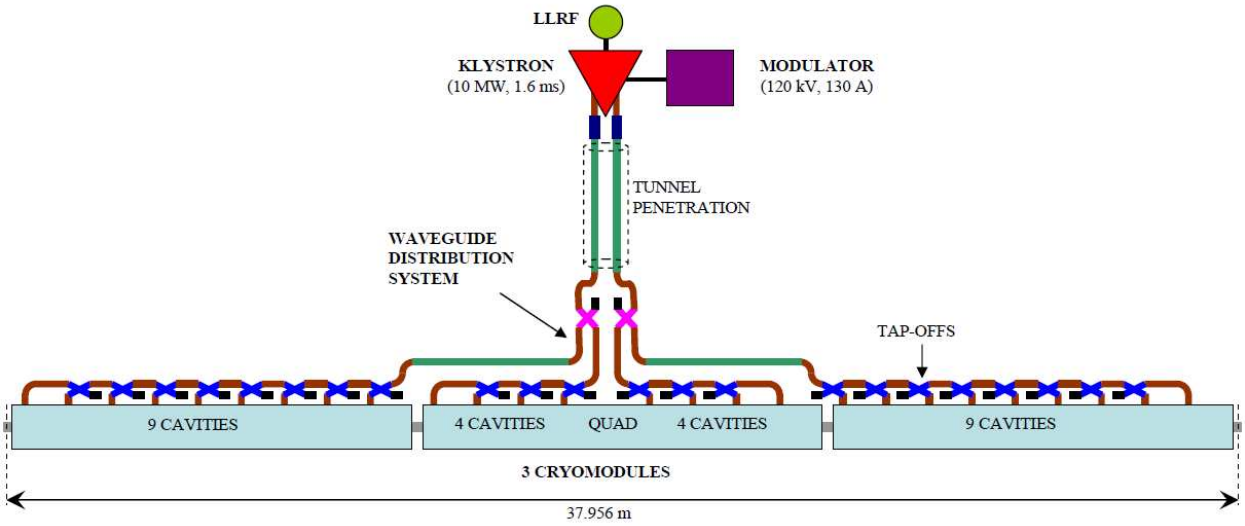

Figure 1.7: The RF unit layout [8].

1.3.7 Main Linac (ML)

The ILC's two main linacs accelerate the electron and positron beams to 250GeV while maintaining emittances below 9.4μm horizontally and 34nm vertically. The main linacs must also maintain the energy spread below 0.1% and not introduce significant longitudinal or transerse jitter, which could cause the e^+ and e^- beams not to collide.

The electron main linac consist of 282 RF units and the positron main linac consists of 278. An RF unit, as shown in figure 1.7, consists of a stand-alone RF source that powers three cryomodules containing a total of 26 RF accelerating cavities; the outer two cryomodules contain nine RF cavities while the middle contains eight. The RF source include a high-voltage modulator, a 10 MW klystron and a waveguide system that distributes the RF power to the cavities.

The RF cavities are nine cell SC standing wave cavities made of pure niobium which

Components	Error Values (RMS)
Cavity Offset	$300\mu m$
Cavity Tilt	$300\mu m$
Quadrupole Offset	$300\mu m$
Quadrupole roll	$300\mu m$
BPM Offset	$200\mu m$

Table 1.7: Component static Gaussian errors with respect to the module axis

sit in a bath of super fluid helium at a temperature of 2K. In the centre of the middle cryomodule in each RF unit there is a quadrupole magnet, combined horizontal and vertical corrector magnets and a cavity beam position monitor (BPM). The BPM will measure the beam position to the micron level. The cryomodules will be fiducialised with the error on the position of the components in the cryomodule, with respect to the fiducial markers, shown in table 1.7. Fiducialisation determines the position of external measurement points on the component with respect to the functional beam axis (often given as the magnetic or electric centre line of the component); allowing the beam axis of all the components to be aligned. The effect of misalignment of the components is discussed in section 1.4.

1.3.8 Beam Delivery System (BDS)

The BDS is responsible for taking the electron and positron beams from the main linacs past the IP and into the dumps. The BDS focuses the beam at the IP and brings them into collision. In addition it must also [9]:

- Protect the beamline and detector against mis-steered beams.
- Remove beam-halo particles to minimise the background in the detectors.
- Measure key beam parameters such as the energy and polarization before and after the collisions.

Figure 1.8 shows a schematic of the BDS. The main subsystems of the BDS are the diagnostics region, the fast extraction and tuneup beamline, the betatron and energy collimation, the final focus, the interaction region and the extraction line all of which are described in

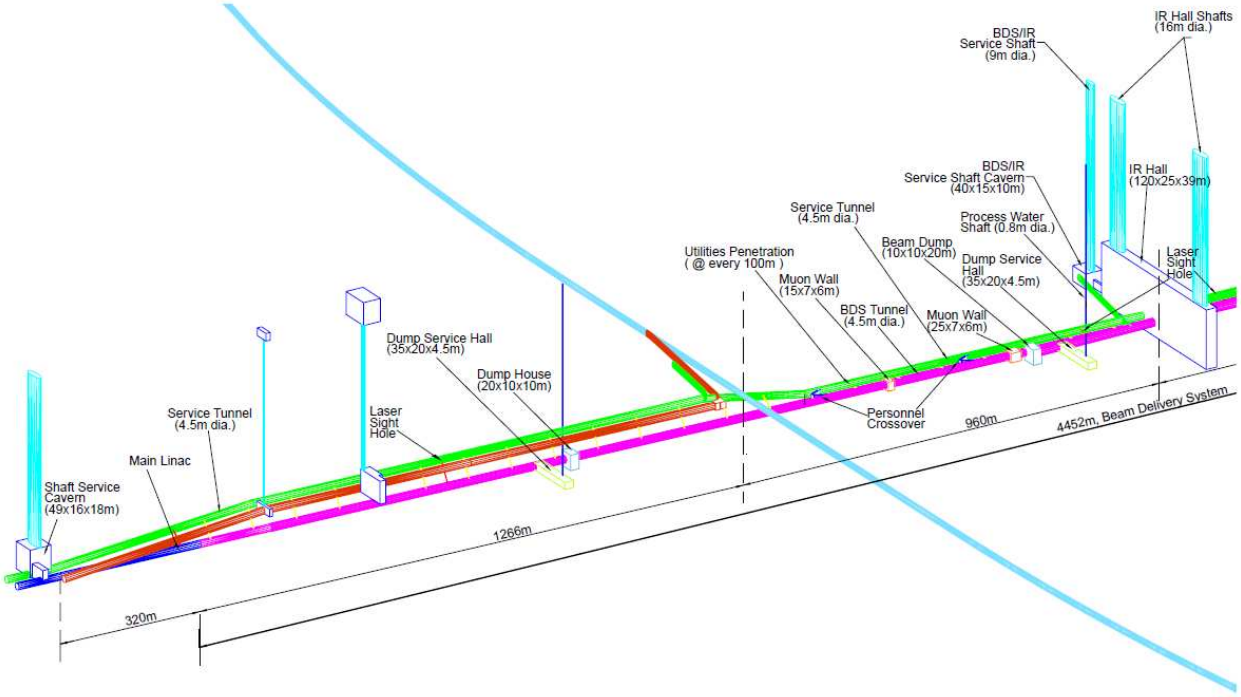

Figure 1.8: Schematic of the BDS [8].

detail in [9]. The BDS is designed to handle 500GeV collisions but can be upgraded to 1TeV with additional magnets. The beams at the IP have a crossing angle of 14mrad and to make the bunches collide head on, while crossing at an angle, crab cavities are used.

1.4 Alignment of the ILC

To achieve the required luminosity at the ILC, a small emittance is required. There are many factors which can cause the beam emittance to increase, one major source is the alignment of the main linac. Miss-aligned cryomodules result in beam trajectory errors which cause emittance growth; the primary factors to consider for alignment of the ML are [9]:

- Dispersion: Unwanted transverse kicks from misaligned quadrupoles, combined with a non-zero energy spread in the beam cause emittance growth.
- Horizontal and vertical coupling: Rotated quadrupoles couple some fraction of the large horizontal emittance into the small vertical emittance leading to vertical beam emittance growth.

- Single-bunch wakefields: An off-axis bunch in a cavity or beampipe generates a dipole wakefield which causes a transverse deflection in the tail of the bunch with respect to its head.

- Multi-bunch wakefields: The wakefield generated by one bunch can cause transverse deflections in the following bunches.

- Cavity tilts: If a bunch passes through an accelerating field at an angle, the transverse component of the accelerating field causes a transverse kick on the beam.

The process of aligning the ILC main linac has four stages. Firstly, all of the components which require alignment are fiducialised as explained in section 1.3.7. Then the reference network (section 1.4.1) for the tunnel is surveyed and the position of the reference markers determined in a suitable co-ordinate system. Next the accelerator components are placed in the tunnel with their fiducial markers aligned to the reference network. The final phase uses beam based methods, such as dispersion matched steering, to adjust correctors in the main linac to produce an optimal orbit resulting in the required beam parameters.

1.4.1 The reference network

The reference network for the ILC may consist of a series of corner cube retro reflectors placed along the length of the tunnel. The exact configuration of the network marker positions, and the accuracy of the knowledge of the marker positions has not yet been specified; some aspects of this will be studied in chapter 7. The reference network has to be surveyed to determine the position of each network marker with respect to all the other network markers.

Conventional reference network surveying

There are many conceivable ways to survey the reference network of the ILC using conventional methods. This may involve the use of tachometers, laser tracers, stretched wires, levels or laser trackers for short range measurements and GPS for long range measurements.

All of the measurements are ultimately combined in a mathematical model which is used to determine the position and position error on each of the markers. This process is explained in detail in chapter 7.

Rapid Tunnel Reference Surveying (RTRS)

The concept of rapid tunnel reference surveying is proposed as a way of measuring the reference network of an accelerator automatically, thereby requiring fewer operators and completing the survey quicker, which will reduce down time. An RTRS may also be operated while the accelerator is running without risk to the operator. The RTRS, conceptually, is a device which will propel itself down the tunnel of the ILC making overlapping measurements on the reference network. All of the measurements from the device will be combined in a mathematical model to determine the position and position error on each of the reference markers. One proposed design for rapid reference network surveying is the Linear Collider Alignment and Survey (LiCAS) Rapid Tunnel Reference Surveyor (RTRS) which is described in detail in chapter 2.

Comparison of conventional surveying and RTRS

There are two major potential problems when using conventional methods to survey the reference network of the ILC. The first problem is that optical measurements over large distances will be subject to systematic errors due to thermal gradients in the tunnel; these effect the refractive index of the air and cause refraction problems with optical measurements. For example a vertical thermal gradient of 0.1 K/m will cause a 4.5mm systematic vertical deflection in a single open air optical beam due to refraction over 600m. An RTRS can overcome this problem by making long range distance measurements in a portable vacuum.

The second problem is the time that a survey takes, coupled with the cost of the survey. It is expected that a conventional surveying team of 3 people can survey the tunnel at a rate of approximately 5 days/km [10] while an RTRS may do this as fast as 0.14 days/km

(optimistic) to 0.42 days/km (pessimistic)[3]. If we are only surveying the main linacs, which form approximately 30% of all beam lines, then the total amount of tunnel to be surveyed is 25km. It is expected that initially there will be two surveys per year decreasing to one per year or even one per two years depending on the stability of the site. If four RTRS's are used the survey will take 3.5 days in the optimistic case and 10.5 in the pessimistic case. For a conventional survey to be completed in the same time, 47 conventional teams are required in the pessimistic regime, and 142 teams in the optimistic regime. An optimistic RTRS system would require one operator for all four trains and a pessimistic would require 2 per RTRS; each conventional survey team would consist of 3 people. Using an RTRS would lead, in the pessimistic case, to a saving of 1396.5 man days per survey and in the optimistic case 1487.5 man days per survey. There are also the set-up costs for each system. A laser tracker costs approximatly 100 Thousand Euro per unit and so the set-up cost in the pessimistic case is 4.7 Million Euro and 14.2 Million Euro in the optimistic, the cost of a LiCAS RTRS (excluding R&D) is 500 Thousand Euro per unit, leading to a set-up cost saving of 2.7 Million Euro in the pessimistic and 12.2 Million Euro in the optimistic. A realistic number of conventional survey teams is ten. Ten surveying teams would take approximately 125 days to survey the main linacs. In the first few years of running, two surveys per year would be required, which would lead to 250 days of surveying per year. This is much more than the three months of down time scheduled per year.

[3]Estimates calculated for LiCAS style RTRS as described in chapter 2

Chapter 2

The LiCAS Rapid Tunnel Reference Surveyor (RTRS)

The LiCAS Rapid Tunnel Reference Surveyor (RTRS) is a device which is intended to survey the reference network of ILC. This chapter describes the design and principle of operation of the prototype LiCAS RTRS.

2.1 The LiCAS RTRS concept

The LiCAS RTRS aims to measure the reference network of the ILC by making overlapping measurements. The reference network is made up of sphere mounted hollow corner cube retro reflectors which are referred to as reference markers. Figure 2.1 shows a diagram of the prototype RTRS and how it will measure the reference network. The prototype described in this chapter and analysed throughout this thesis was designed and built for several purposes. Firstly to develop the metrology techniques required for the surveying of the ILC main linac tunnel, secondly as a proof of principle for robotic surveying of the ILC tunnel and finally to be deployed in the XFEL tunnel, to test its long distance and long term performance in comparison to conventional surveying techniques. The deployment in the XFEL was not achieved due to cancellation of funds. The LiCAS RTRS was constructed at Oxford and

tested in a test tunnel in DESY, Hamburg. The test tunnel is an air conditioned 75m long tunnel of which a 50m segment was to be surveyed.

The reference network in the European XFEL has only a single line of reference markers visible to the RTRS, with the reference markers placed every 5m as sketched in figure 2.1. The visible network in the XFEL tunnel is the minimum possible network that can be surveyed using an RTRS; the ILC, if it were to be surveyed using an RTRS, will require a more complex network of at least two rows of reference markers. The prototype RTRS was built to fit into the constraints of the European XFEL tunnel and so can only measure a single line of reference markers. The prototype is capable of measuring three reference network markers at one stop on the straight line network. Three markers are the minimum number required so that the network can be reconstructed. The design of the RTRS is described in the following sections.

2.2 The LiCAS RTRS design

Figure 2.4 shows a design drawing of the LiCAS RTRS; figures 2.2 and 2.3 show photos of the LiCAS RTRS. Figures 2.4, 2.2 and 2.3 have all the major systems labelled. The major systems are: the three measurement cars (section 2.2.2) and their associated service cars (section 2.2.3), one master car (section 2.2.4), the LSM end caps (section 2.2.7), the vacuum system (section 2.2.13) and the drive motors (section 2.2.14). These major systems, along with their sub-systems, will be described in the following sections.

2.2.1 RTRS co-ordinate system

Throughout this thesis the rotations and translations of the RTRS and its sub-systems are discussed. The co-ordinate system used, unless other wise stated, has the Z direction along the tunnel, the Y direction is vertical and the X direction is horizontal from the train towards the wall; the axes are shown in figure 2.1. When rotations of the measurement units are discussed, the rotations are regarded to be around this co-ordinate system with its origin in the geometric centre of the measurement unit.

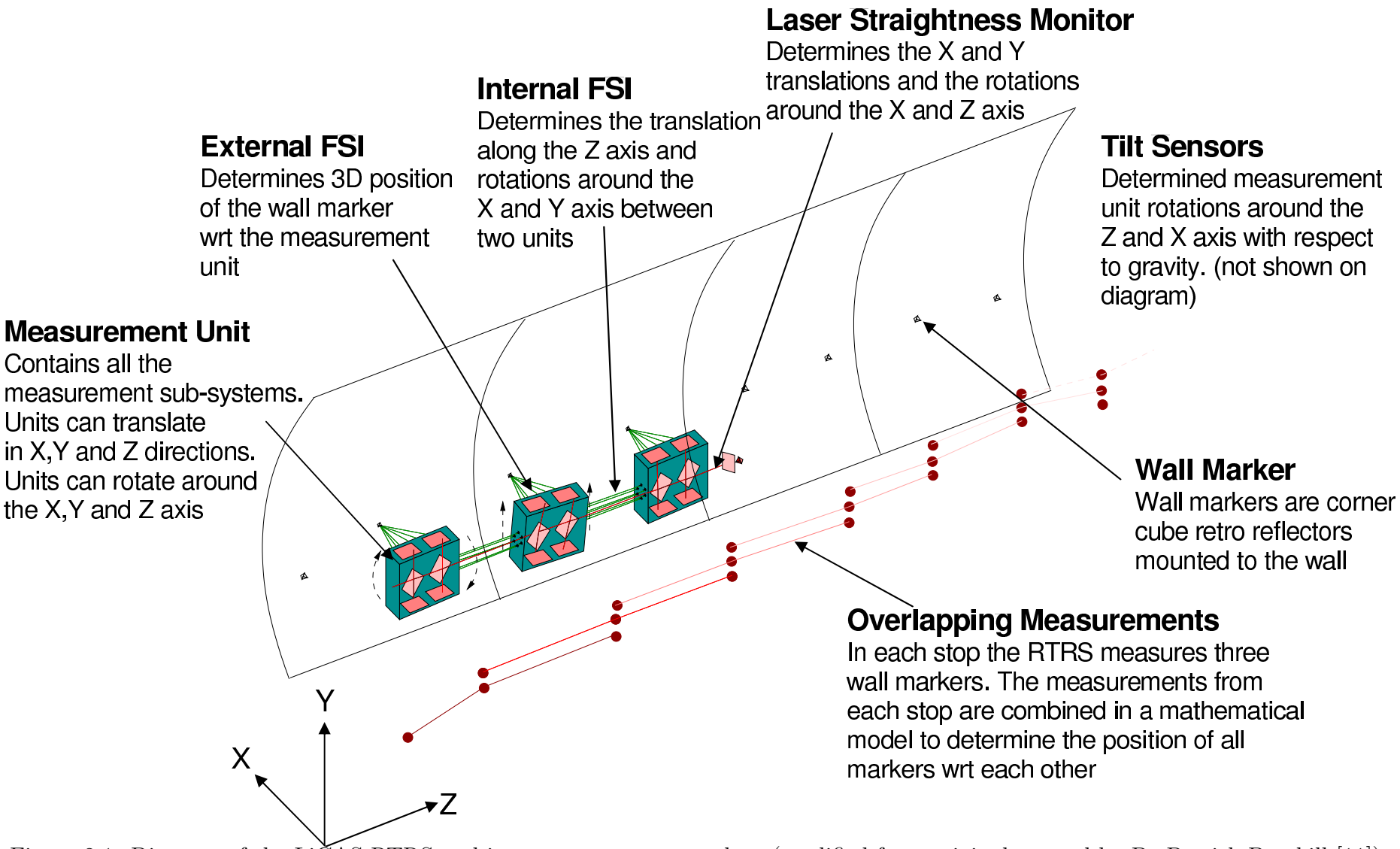

Figure 2.1: Diagram of the LiCAS RTRS and its measurement procedure (modified from original created by Dr Patrick Brockill [11]).

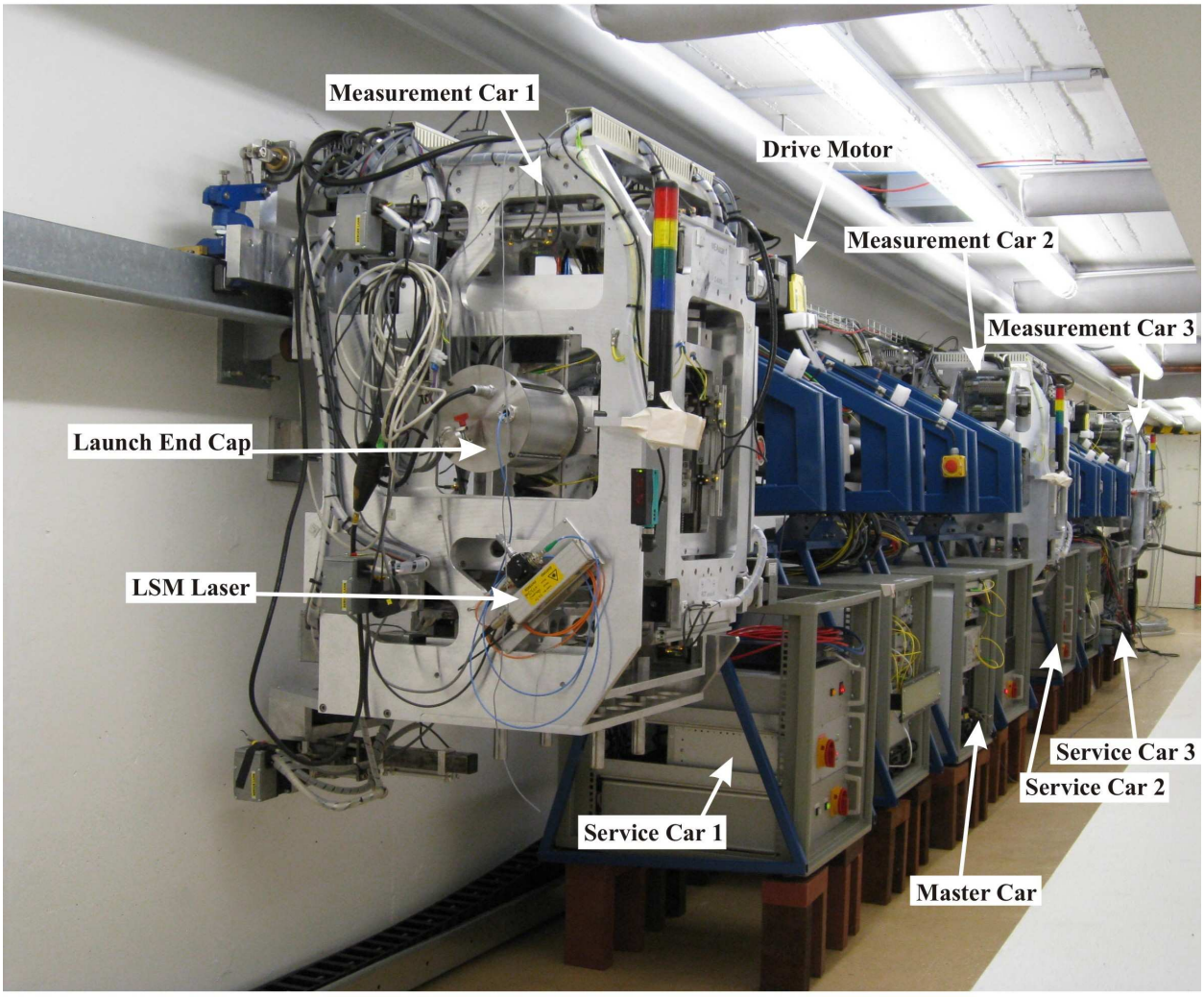

Figure 2.2: Photo of the LiCAS RTRS looking at Measurement Car 1. Reference interferometers are not mounted as they were under calibration at the time the photo was taken. The steel bricks were used to test the effects of service car vibrations on the RTRS

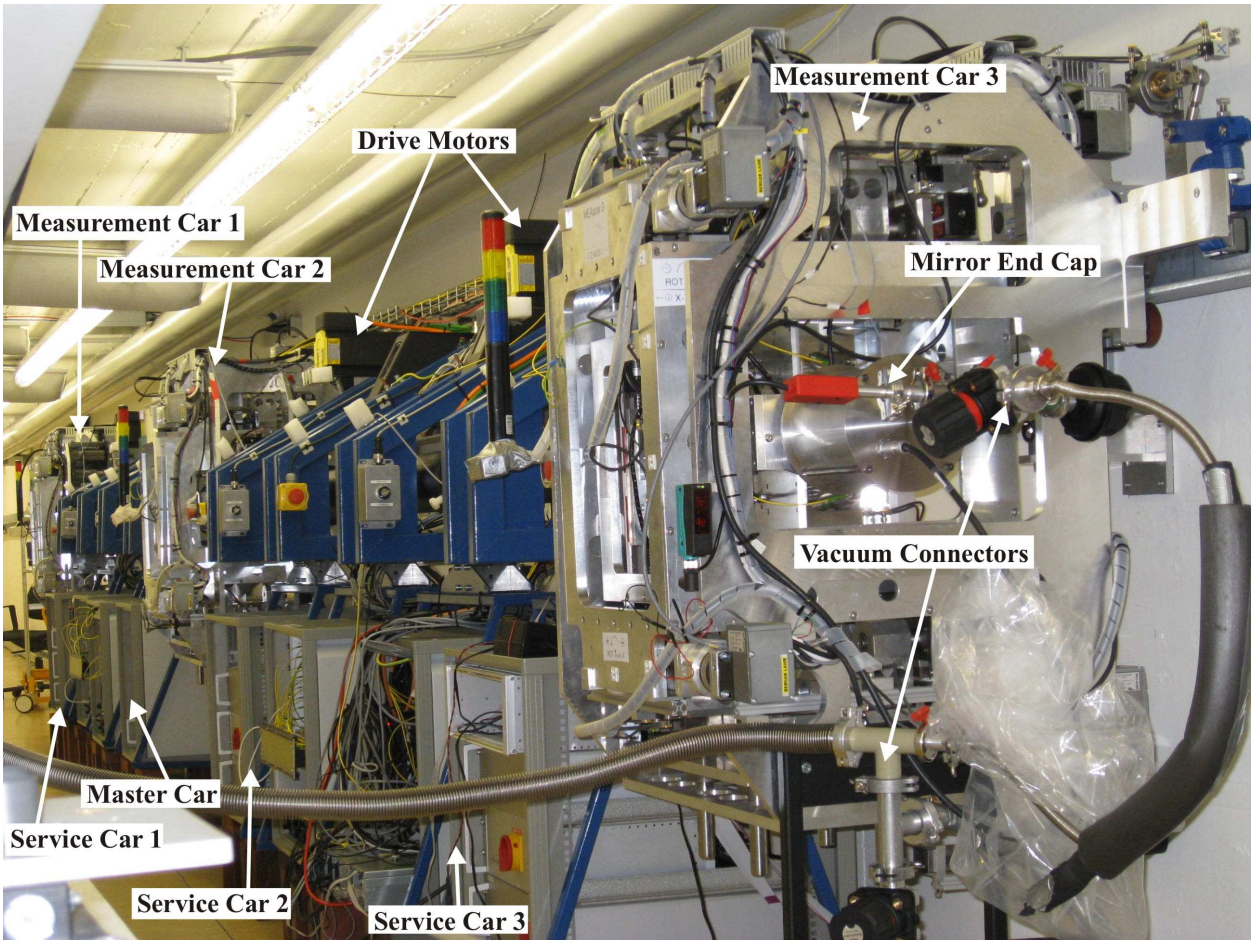

Figure 2.3: Photo of the LiCAS RTRS looking at Measurement Car 3. Reference interferometers are not mounted as they were under calibration at the time the photo was taken. The steel bricks were used to test the effects of service car vibrations on the RTRS

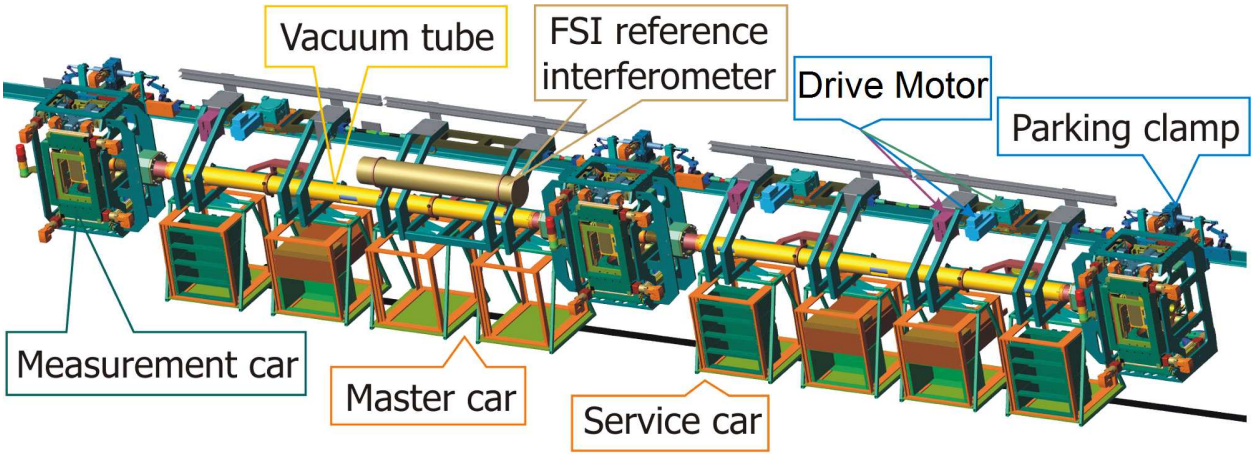

Figure 2.4: Design drawing of the LiCAS RTRS. Image produced by Dr Armin Reichold[10].

2.2.2 Measurement car

The measurement car contains a measurement unit which can be moved in six degrees of freedom by stepper motors (section 2.2.11). The measurement unit is machined from a single piece of Invar 36 with components mounted to the unit (see figures 2.6, 2.11 and 2.22). Invar 36 is used as it has a CTE of the order of 1ppm, allowing sensors to be held in a stable geometry under thermal fluctuations. The measurement units are attached to the vacuum system as described in section 2.2.13. To maintain vacuum all access holes in the unit are closed using o-ring sealed plates. The measurement unit contains several measurement subsystems; these are the FSI systems (section 2.2.5), the LSM system (section 2.2.6), the tilt sensors (section 2.2.8) and the temperature sensors (section 2.2.9).

2.2.3 Service car

Each measurement car has an associated service car consisting of a power crate (figure 2.8) and an electronics crate (figure 2.7). The power crate supplies the electrical power to the electronics crate and the measurement unit. The electronics crate contains the DAQ computer, the FSI measurement car fibre splitter tree and the electronics for the measurement systems.

2.2.4 Master car

The master car consists of two crates: the power crate and the electronics crate. The power crate contains power distribution unit for the master car, and the Interlock Relay Unit (IRU) as shown in figure 2.9. The electronic crate contains the master DAQ computer, the pressure meter and the FSI laser, EDFA and the FSI master splitter tree as shown in figure 2.10. The master DAQ computer is used to control the other DAQ computers during data taking. The master DAQ is also responsible for controlling the LSM end caps and moving the train from one position to the next. The IRU controls the interlock to the LSM laser, the FSI laser and the EDFA. If the interlock is broken then the EDFA is stopped before the FSI laser. This

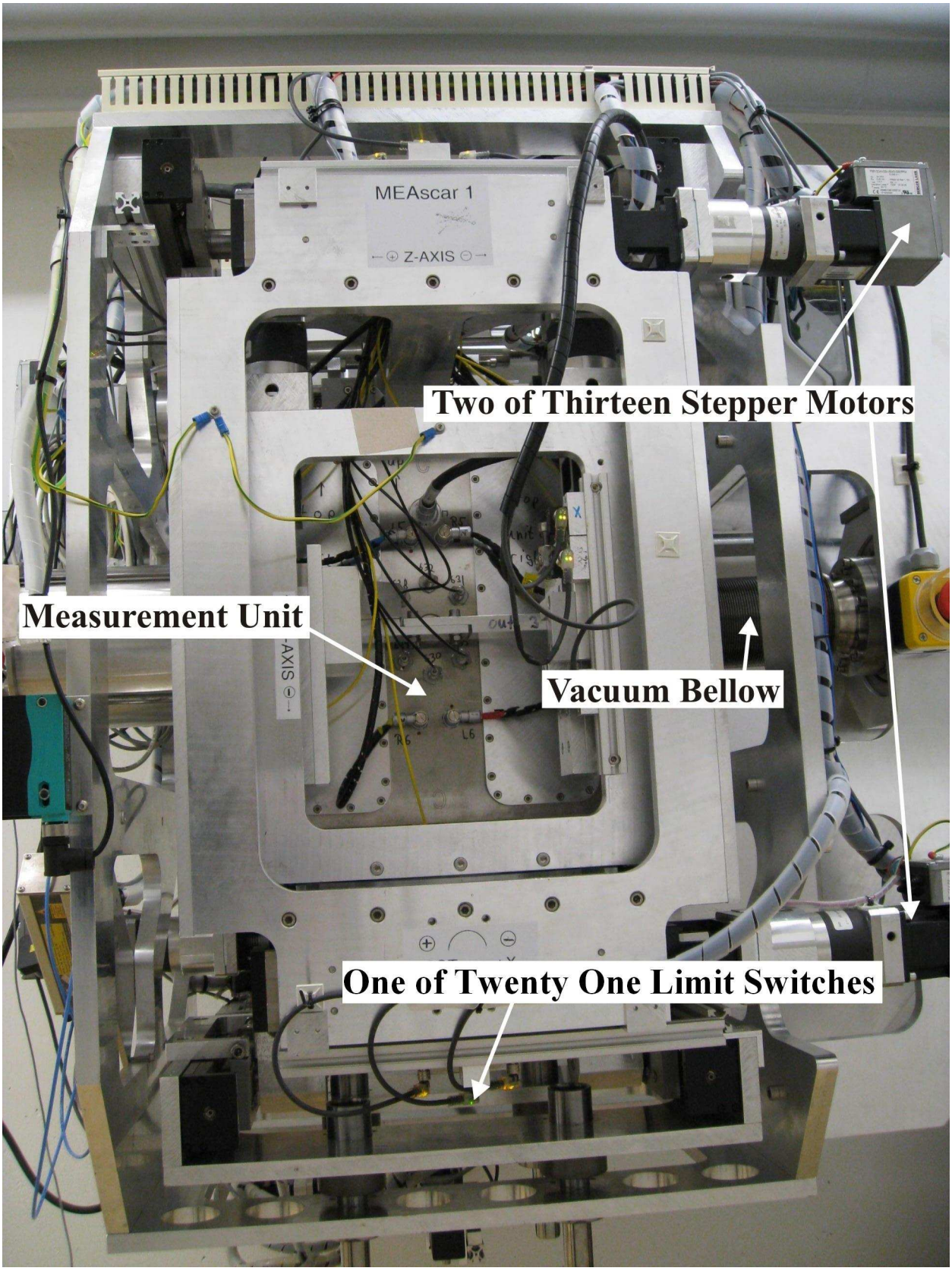

Figure 2.5: Photo of a LiCAS RTRS measurement unit.

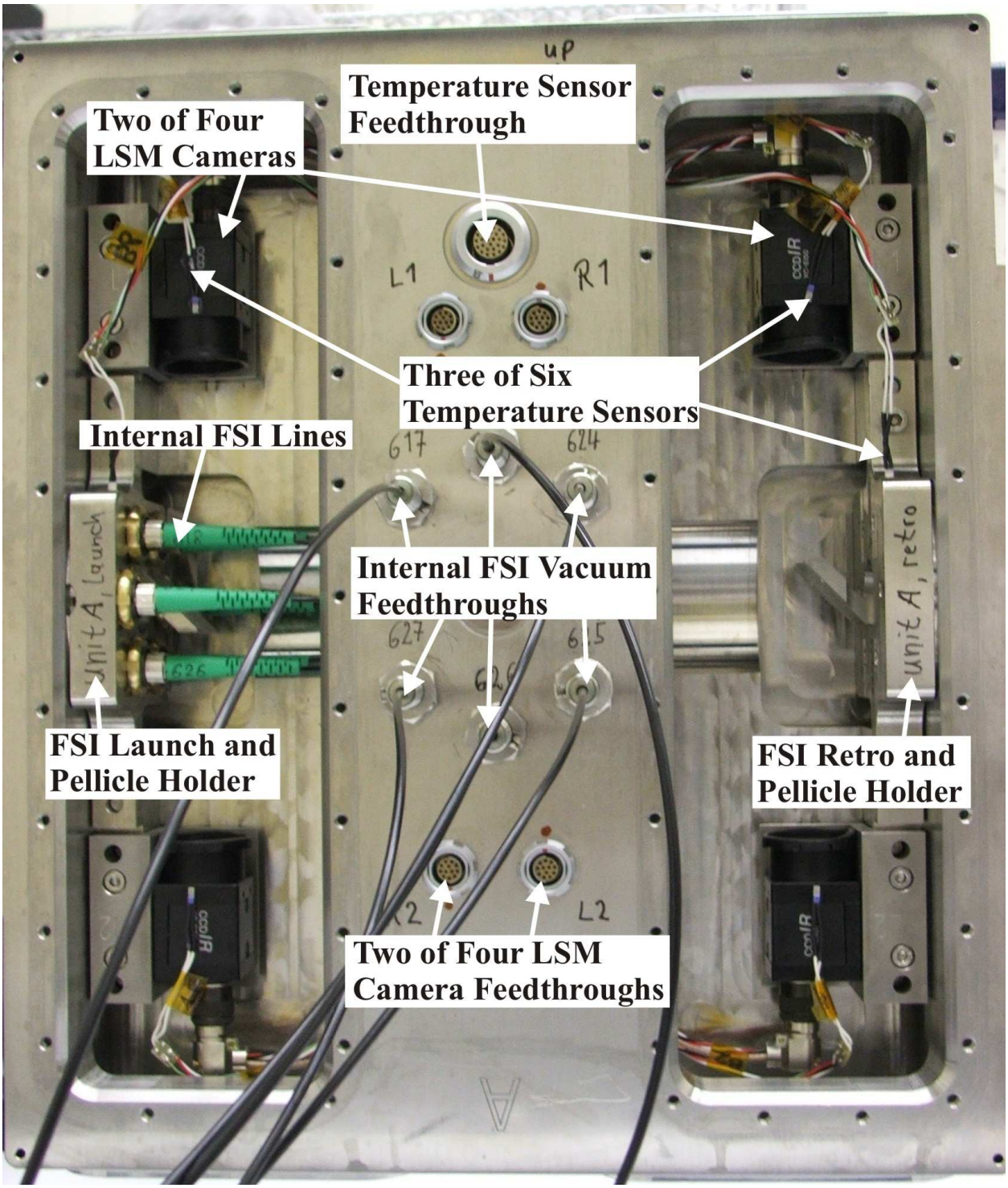

Figure 2.6: Photo of the inside of a measurement unit.

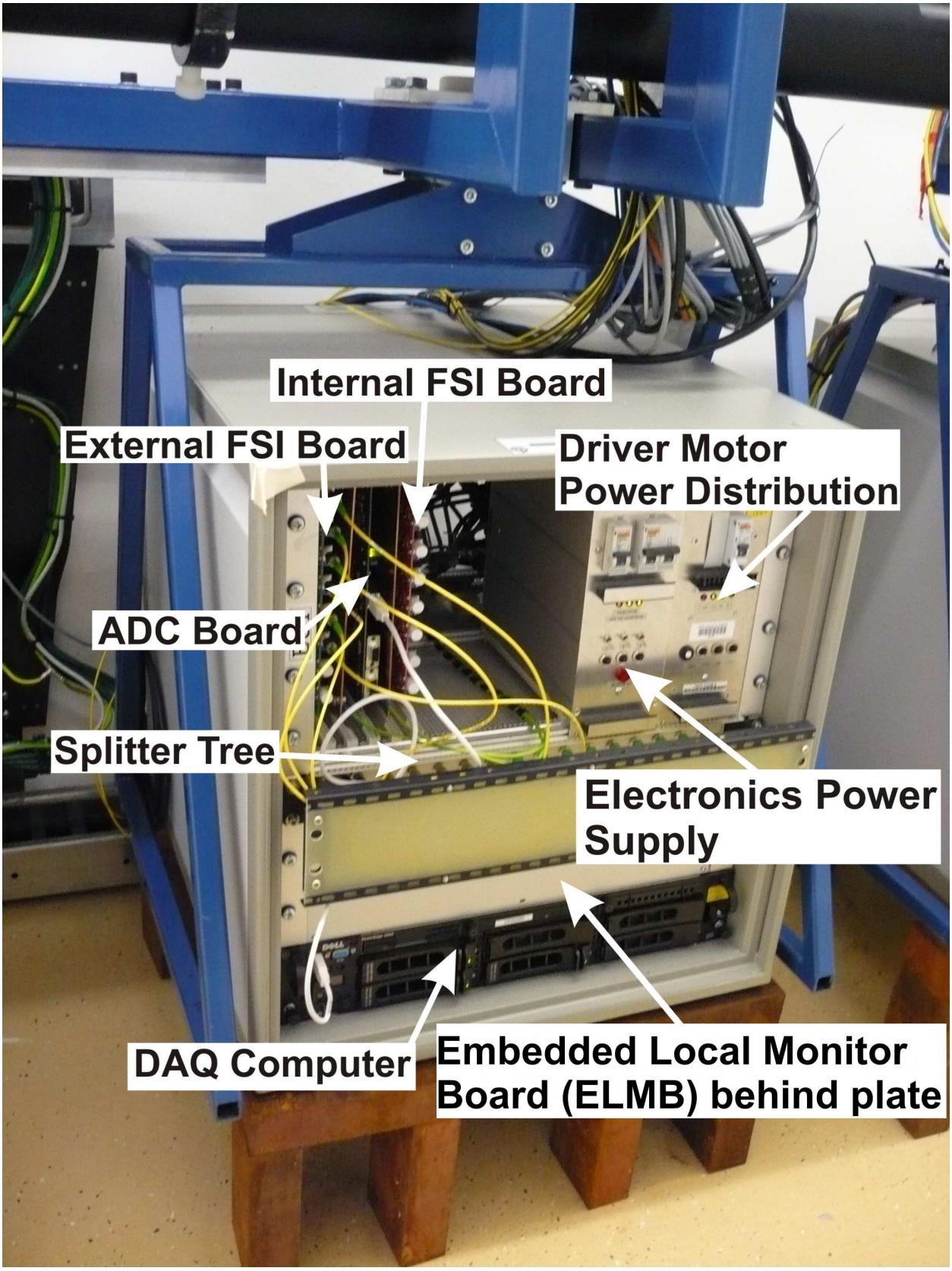

Figure 2.7: Photo of a LiCAS RTRS service car electronics crate.

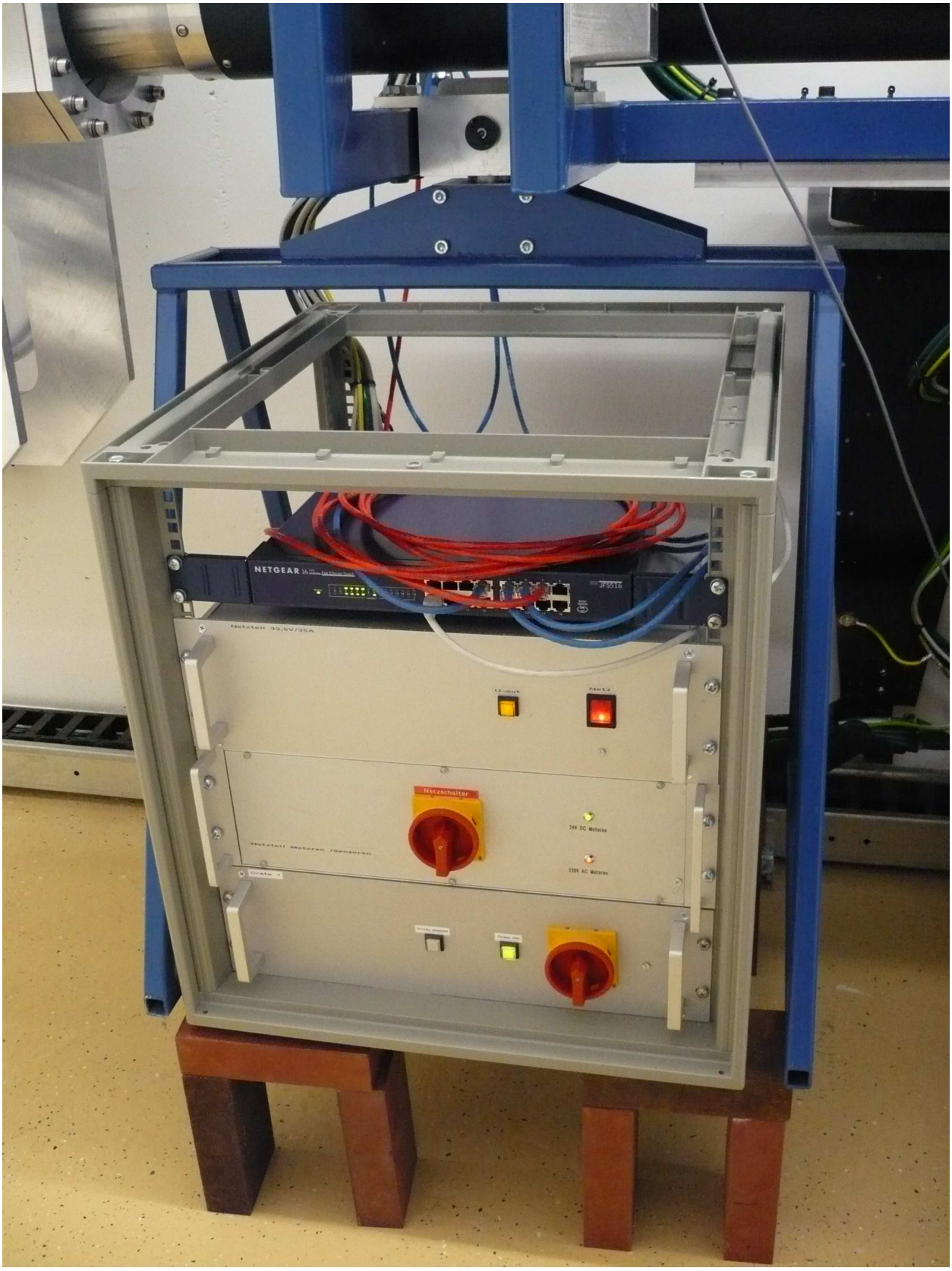

Figure 2.8: Photo of a LiCAS RTRS service car power crate.

prevents damage to the EDFA which could be caused if the EDFA were to amplify without any light at its input.

2.2.5 Frequency Scanning Interferometry (FSI)

The LiCAS RTRS has two absolute length measurement sub-systems: the external and internal FSI sub-systems. For the FSI sub-systems to make absolute distance measurements a reference interferometer is required, as described in the FSI theory chapter (chapter 4). The reference interferometers are described in detail in chapter 5. Depending on the mode of operation there are either one or two reference interferometers in use.

External FSI sub-system

The external FSI sub-system is used to measure the position of the reference network markers with respect to the unit. The six external FSI lines are mounted on the measurement unit so that they are all pointing at a reference marker, which is a distance of approximately 0.42m from the measurement unit's wall side face. Figure 2.11 shows a photo of an installed measurement unit in which five of the six FSI lines are visible along with a reference marker. The position of the fibre tips, with respect to the centre of the measurement unit, are shown in table 2.1. The FSI lines are bare angle polished connector (APC) fibres; there are no collimators or beam splitters. As there is no collimation the laser light leaving the fibre is divergent, which allows a wall marker to be measured by an external FSI line up to 37.5mm off the pointing axis of the fibre [12]. The optical fibres are Corning SMF-28 single mode fibres with a numerical aperture (NA) of 0.14. From the lengths measured by all six FSI lines, the X,Y and Z co-ordinate of the wall marker can be reconstructed using multilateration (see section 6.1.2).

The external FSI fibres are not mounted directly to the unit, they are connected into mounting plates which are fixed to the measurement unit (see figures 2.12 and 2.13). The mounting plate fibre connections are threaded with a key so that the fibres can be screwed

Figure 2.9: Photo of master car power crate.

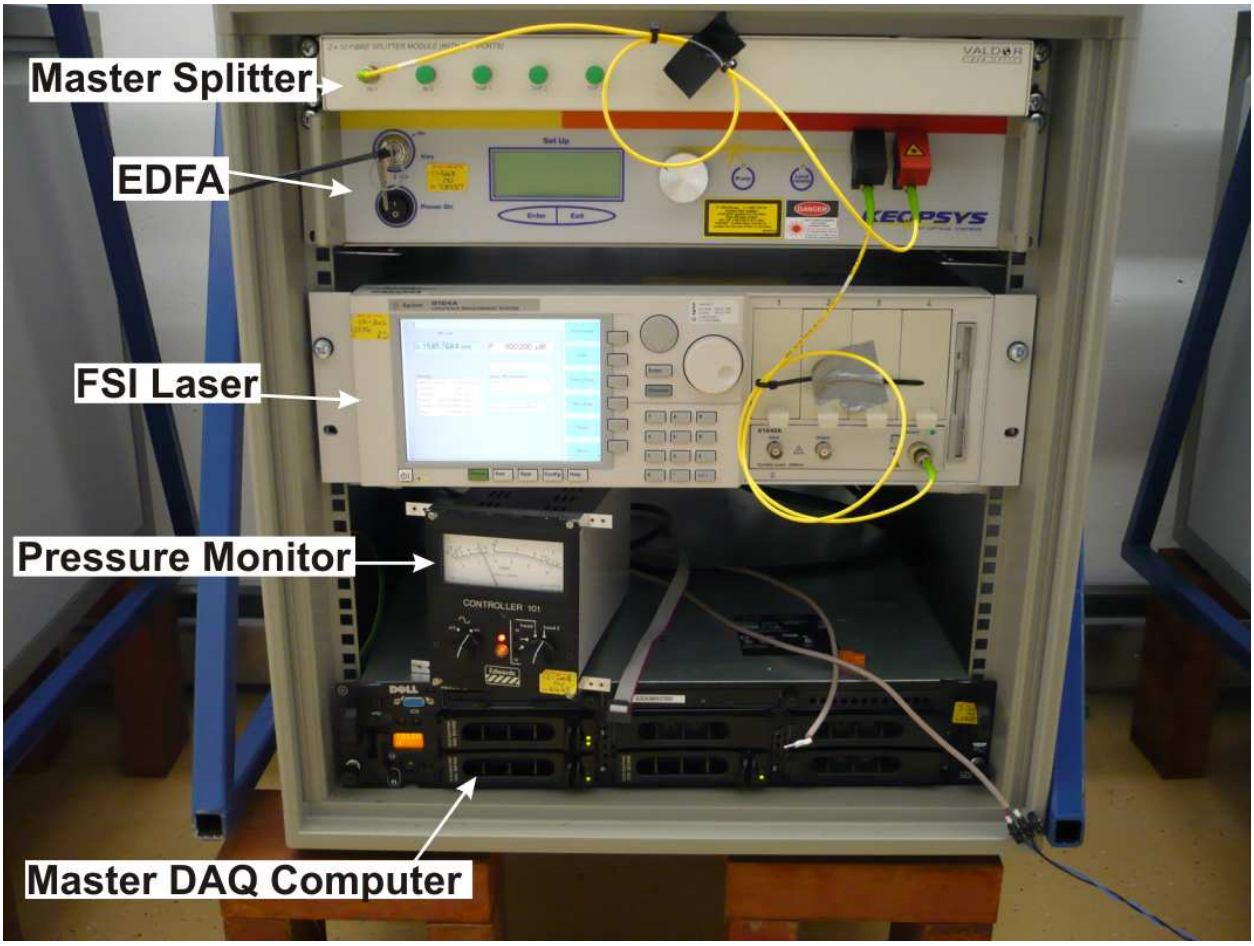

Figure 2.10: Photo of the master car electronic crate.

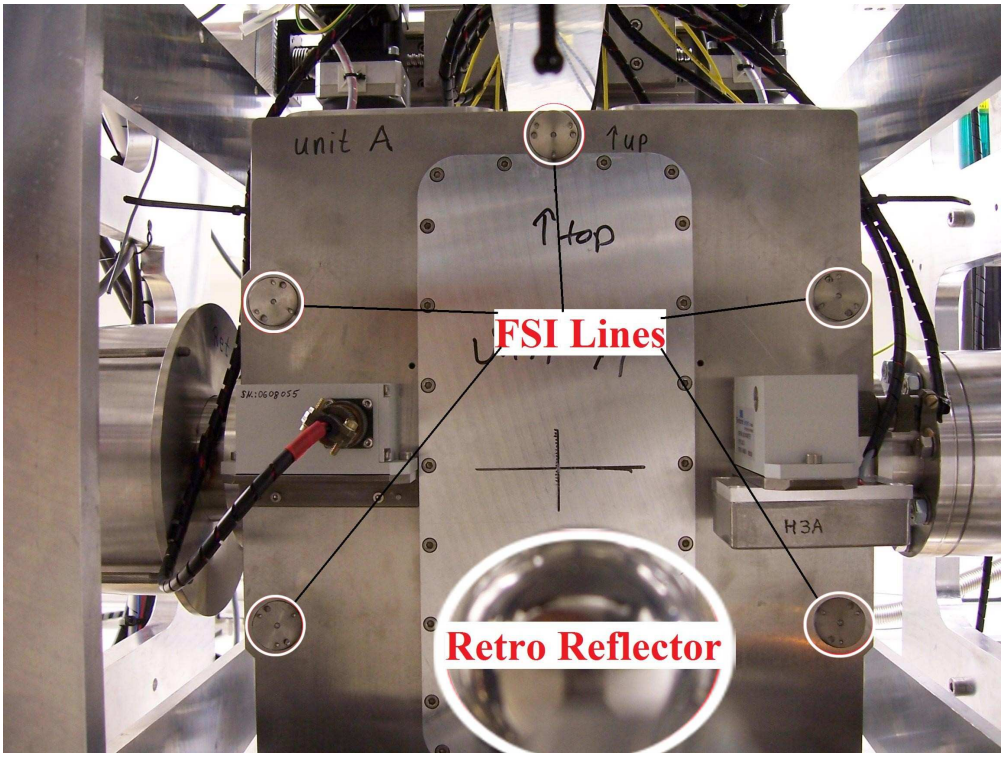

Figure 2.11: Photo of the a measurement unit observing a retro reflector.

Fibre Number	X position	Y position	Z position
1	103mm	168mm	0mm
2	103mm	85mm	146mm
3	103mm	-85mm	146mm
4	103mm	-168mm	0mm
5	103mm	-85mm	-146mm
6	103mm	85mm	-146mm

Table 2.1: The design position of the external FSI fibre ends with respect to the centre of the Invar unit.

into the plate, and cannot move with respect to the plate. The plate is mounted onto the unit with two dowels and three screws so that it remains in a stable position. The six FSI lines are mounted on a circle and are angled to the face of the unit so that they all point at a location 0.36m directly in front of the centre of the unit.

Internal FSI sub-system

The internal sub-system FSI is designed to measure the distance between two units along with the relative rotation around the X and Y axis. Each unit has six collimated angle polished fibres with beam splitters attached, as shown in figure 2.14. The collimating lens is

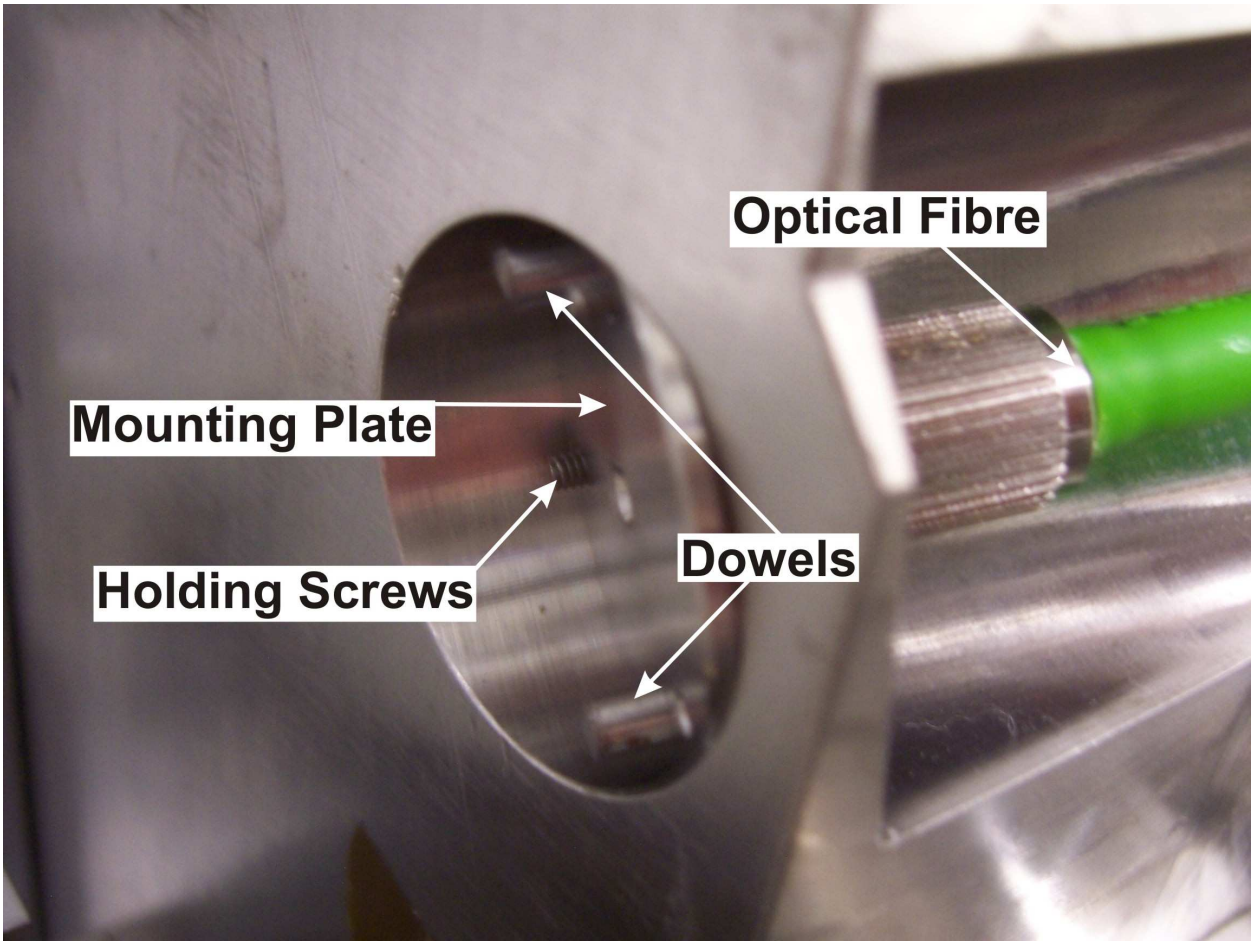

Figure 2.12: Photo of the front of a mounted external FSI line.

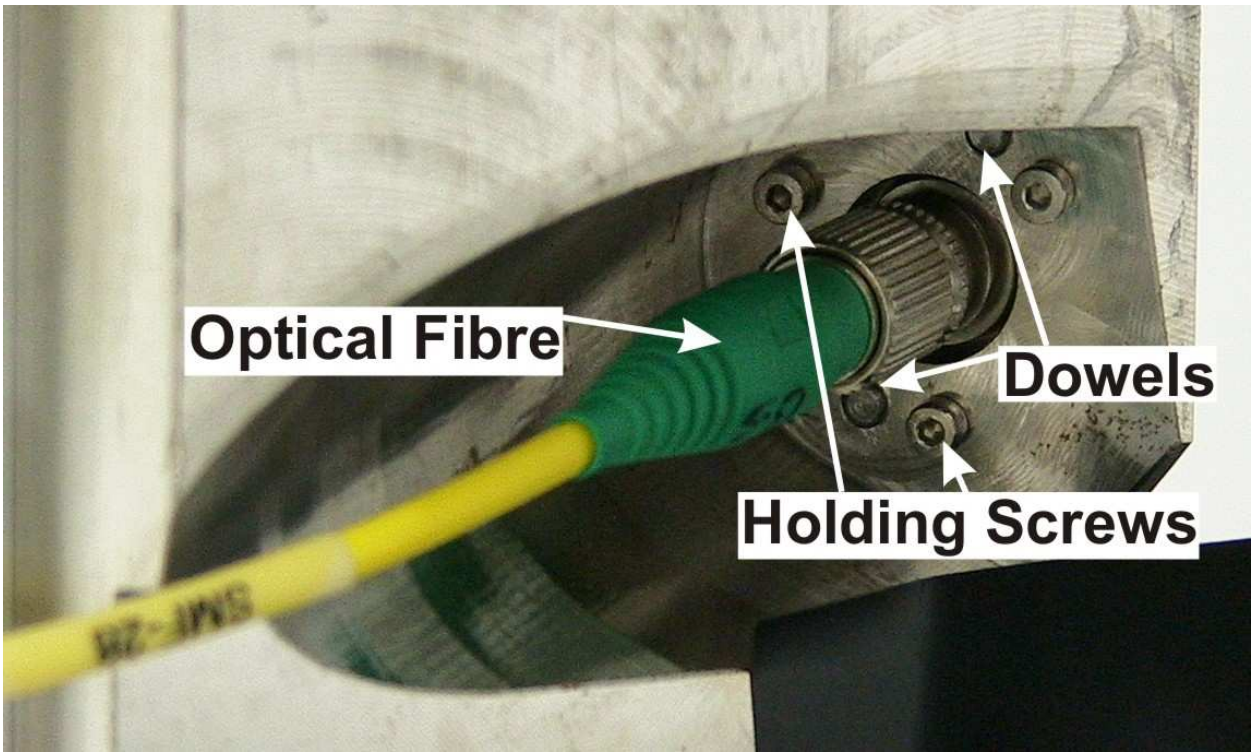

Figure 2.13: Photo of the rear of a mounted external FSI line.

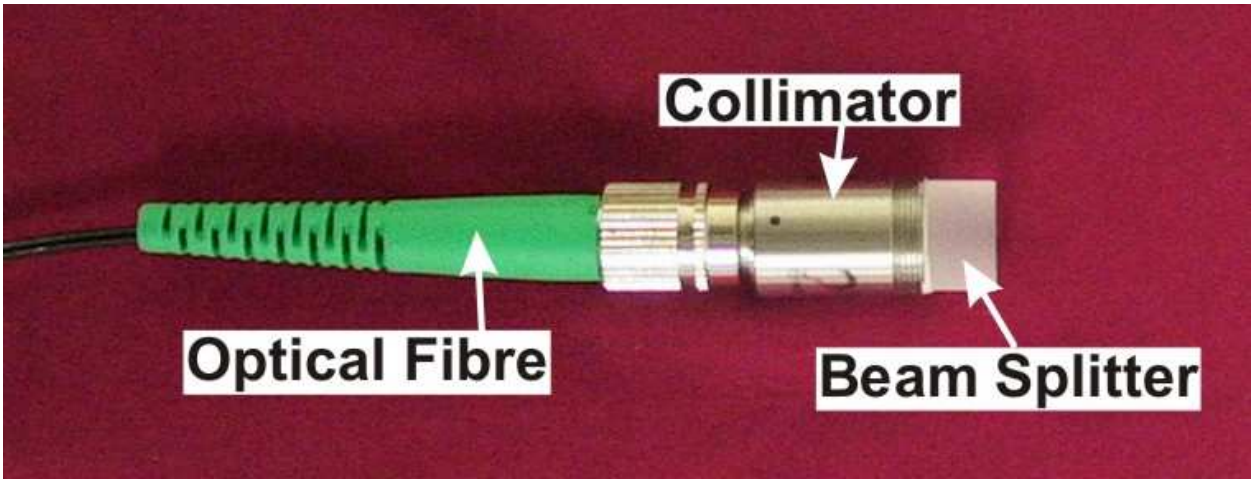

Figure 2.14: Photo of a single collimated FSI line.

made from Corning CO550 glass, and is a graded index lens with a focal length of 11mm; a graded index lens is chosen to allow multiple wavelengths to be focused. The beam splitters are fixed to the collimators with UV curing glue with the glued side of the beam splitter being anti reflection coated. The beam splitter reflects approximately 4% of the beam [13] but only a small fraction of this is coupled back into the fibre. The collimators lead to beam sizes with a range of ±3mm to ±9mm at a distance of 4.5m. The beam size is defined to where the power drops off of by $1/e^3$. The internal FSI sub-system operates within the vacuum, requiring that the fibres have vacuum fibre feedthroughs attached (figure 2.16). The FSI lines are not connected directly to the unit, they are encased in brass spheres which are in turn held in the launch pellicle mount (figures 2.15 and 2.17). The launch pellicle mount is connected to the unit with two dowels and two screws so that it is accurately and stably placed. The launch pellicle mount has a hole in the middle for the LSM beam to pass through and six chamfered holes placed on a circle around the centre hole for the FSI brass spheres to sit in. The positions of the mounted internal FSI lines, with respect to the centre of a measurement unit, are shown in table 2.2.

Figure 2.17 shows six fibres mounted into a unit. To facilitate alignment of the FSI lines' pointing direction, each brass sphere has two small holes on the front to allow an alignment tool to be attached. The brass spheres sit in the launch pellicle mount and a plate is screwed over the top to stop the sphere moving once aligned. To align the internal FSI lines, the

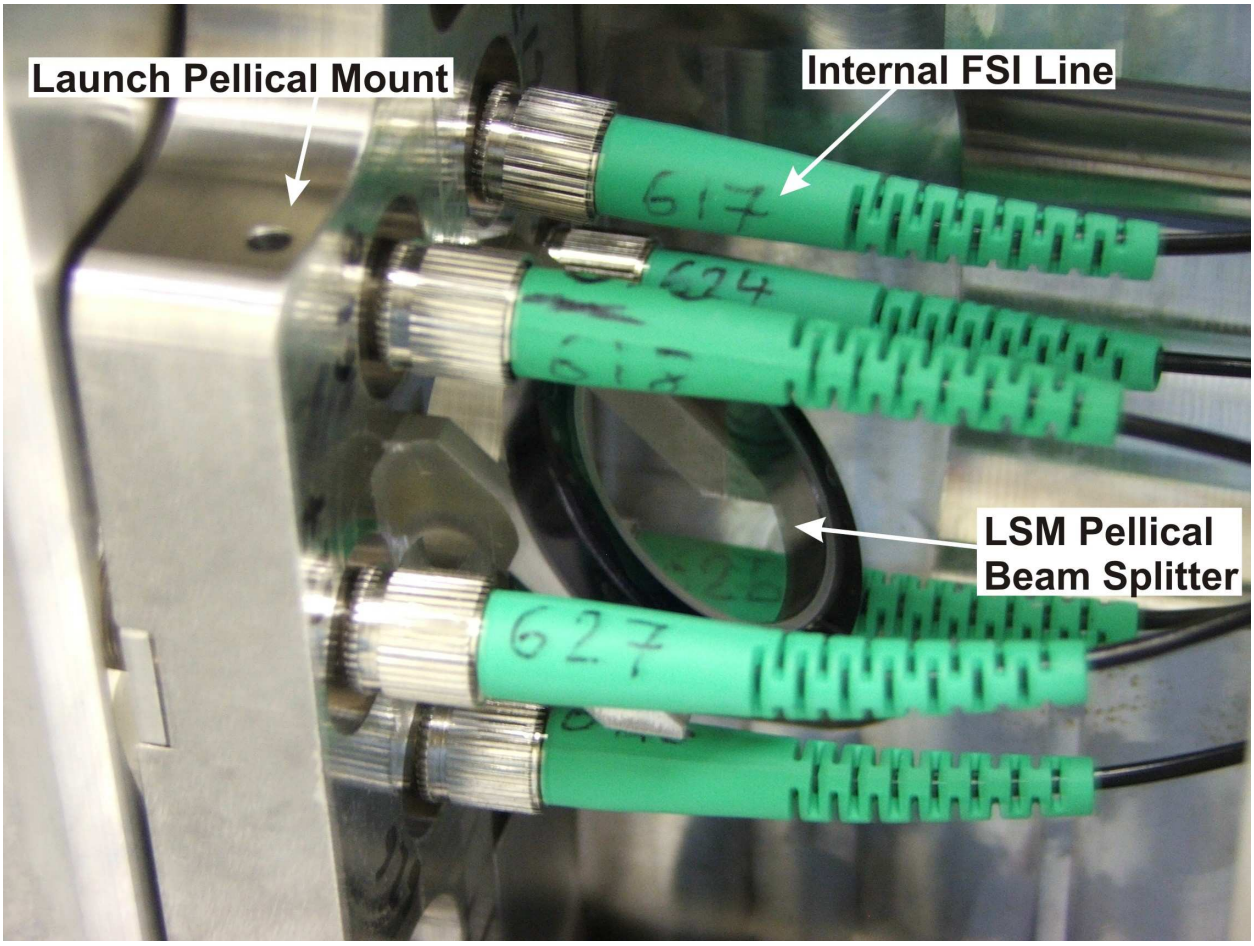

Figure 2.15: Photo of a launch pellicle mount.

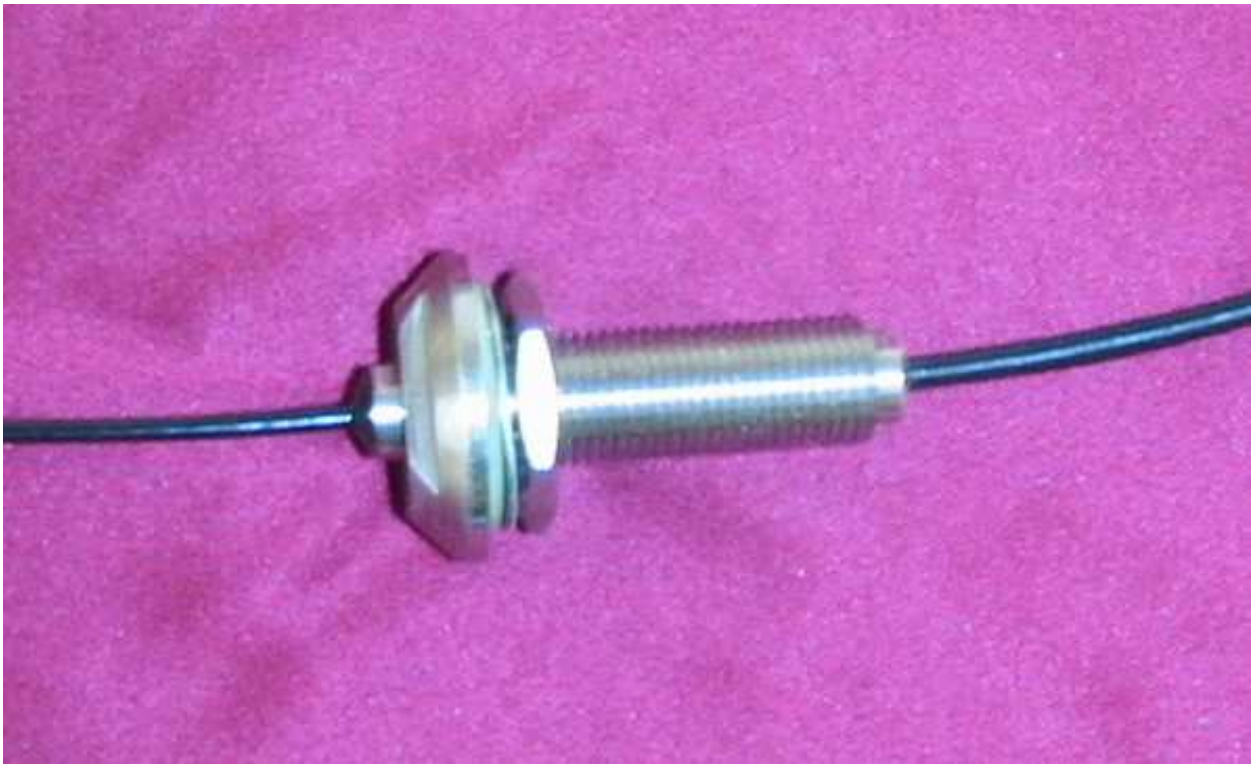

Figure 2.16: Photo of a vacuum fibre feedthrough.

Fibre Number	X position	Y position	Z position (FSI)	Z position (retro)
1	25mm	0mm	-146mm	135.2mm
2	12.5mm	21.7mm	-146mm	135.2mm
3	-12.5mm	21.7mm	-146mm	135.2mm
4	-25mm	0mm	-146mm	135.2mm
5	-12.5mm	-21.7mm	-146mm	135.2mm
6	12.5mm	-21.7mm	-146mm	135.2mm

Table 2.2: The design position of the internal FSI fibre ends and retro reflectors with respect to the measurement unit centre.

cover plate is loosened and the alignment tool attached, the alignment tool can then change the pointing of the line. When the line points correctly, the cover plate is tightened to stop the sphere moving. All six FSI lines on one unit are aligned at the same time so that they are parallel with each other.

Each of the six FSI lines monitor one of six retro reflectors mounted on the next measurement unit (figure 2.18). The six retro reflectors are mounted in a retro pellicle mount. The retro pellicle mount is similar to the launch pellicle mount except that instead of holding FSI lines it holds the retro reflectors. The retro reflectors are gold coated and cylinder mounted with their positions, with respect to the centre of a measurement unit, shown in table 2.2.

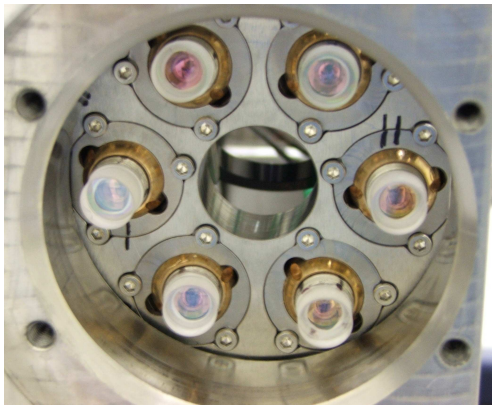

Figure 2.17: Photo of the mounted internal FSI launch optics

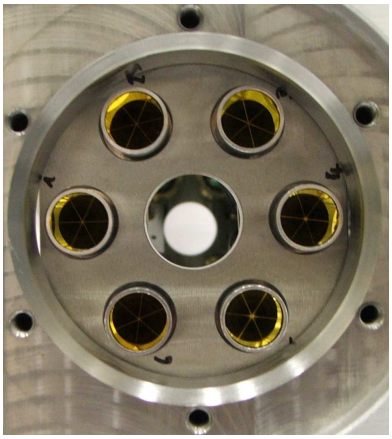

Figure 2.18: Photo of the mounted internal FSI retro reflectors

FSI laser system

The FSI laser system is located in the master car which contains the laser, Erbium Doped Fibre Amplifier (EDFA) and the master splitter tree (see figure 2.10). The laser is an Agilent 81642A tunable laser module [14] in a 8164A light wave measurement system frame; details of the performance of the laser are described in [13]. The laser output is fed into an EDFA to amplify the laser power to 20dBm, a detailed description of the performance of the EFDA is shown in [13]. The output of the EDFA is fed into the master splitter. The layout of the master splitter is shown in figure 2.19. The master splitter splits the laser light to the three measurement cars. The master splitter also has the option of a connecting to a power monitor and also has six outputs (labelled 1-3 A and B) which can be connected to interferometers, with the interferometer return light passing down taps 1-3.

In each of the measurement cars there is a 32 way splitter tree (figure 2.19), fed with laser light from the master splitter tree. The outputs of the measurement car splitter trees (labelled 1-16 A and B) are connected to interferometers; and the taps, which the interferometer return light passes down, are connected to the corresponding channels in the FSI electronics crates. The FSI laser scans from 1535nm to 1565nm at a rate of 40nm/s.

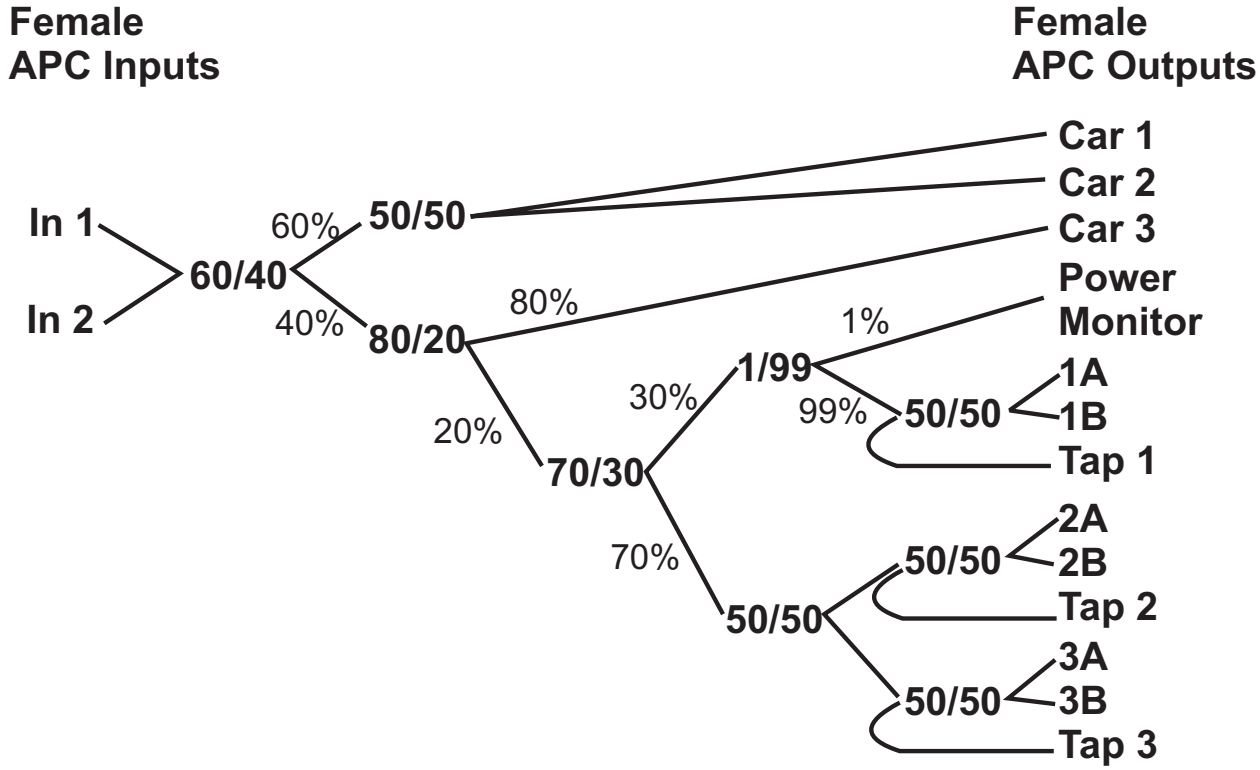

Figure 2.19: Diagram showing the splitter ratios in the master splitter tree.

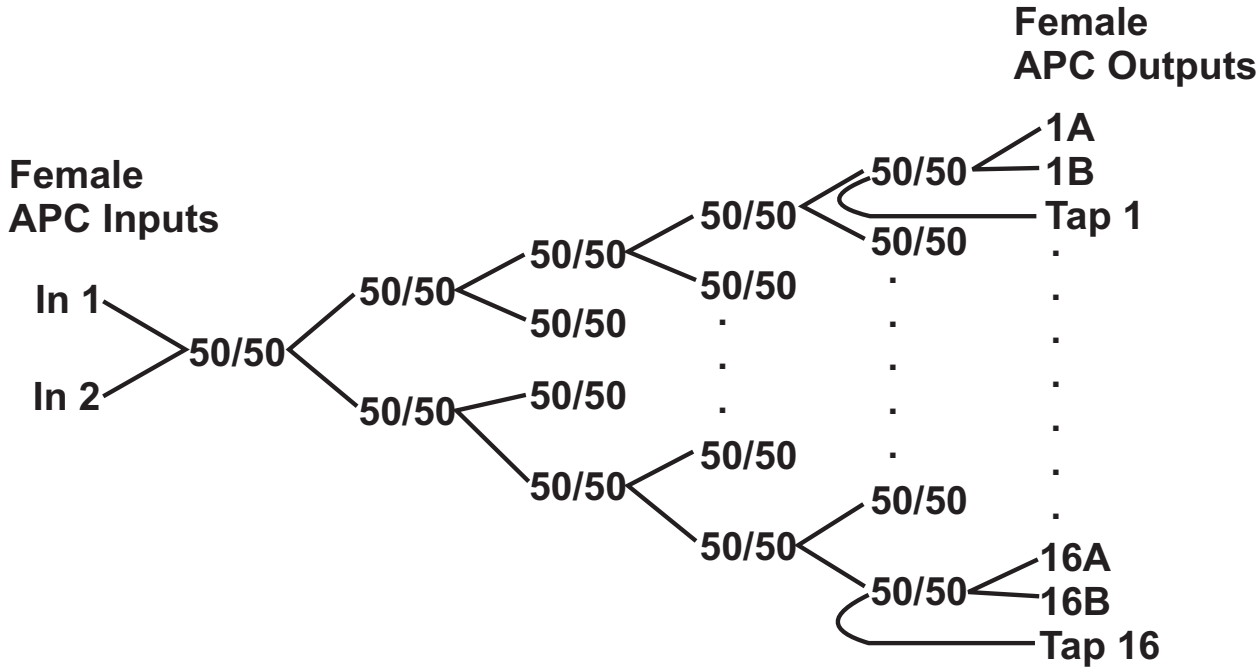

Figure 2.20: Diagram showing the splitter ratios in a measurement unit splitter tree.

FSI electronics crates

Each measurement car has an FSI electronics crate. An FSI electronics crate consists of a backplane, one internal and one external FSI opto amplifier board, and a 16 channel ADC board (figure 2.7). The opto amplifier converts optical signals to electrical via an InGas photo diode, the board also amplifies the signal. The ADC digitises the signal into 14 bits at 2.77MHz and sends data to the DAQ computers via USB. Both of the photo amplifier boards, and the ADC board are custom built, and they plug into the backplane. There are different opto amplifier boards for the internal and external FSI lines because of the different signals they return. The internal FSI lines measure a larger distance causing a higher fringe frequency which requires a higher bandwidth than the external FSI lines. The internal FSI is also collimated and returns more power and requires less amplification in comparison to the external FSI. The reference interferometers are connected to the internal FSI electronics board. The DAQ computer tells the ADC boards which channels to read, how long to take data for and the amplification gain to set in the opto amplifier boards. The ADC board return the digitised data to the DAQ computer. The ADC boards are connected to the laser trigger system. When the laser starts a scan it sends a trigger pulse to the laser trigger system telling the FSI electronics modules to start taking data.

2.2.6 Laser Straightness Monitor (LSM)

The LSM is responsible for determining the unit's rotations around the X and Y axes and the translations along X and Y axes, with respect to the LSM beam. The LSM beam is launched from the launch end cap and travels along the length of the RTRS (referred to as the outgoing beam). The beam is then reflected in the mirror end cap and travels back along the RTRS anti co-linear to the outing beam (referred to as the incoming beam). The end caps are described in section 2.2.7. Inside each measurement unit there are four LSM cameras and two LSM pellicle beam splitters mounted at 45 degrees to the unit, shown in figure 2.21. When the LSM outgoing beam passes through a measurement unit the beam strikes both of the pellicle beam splitters which each splitting off approximately 8% of the

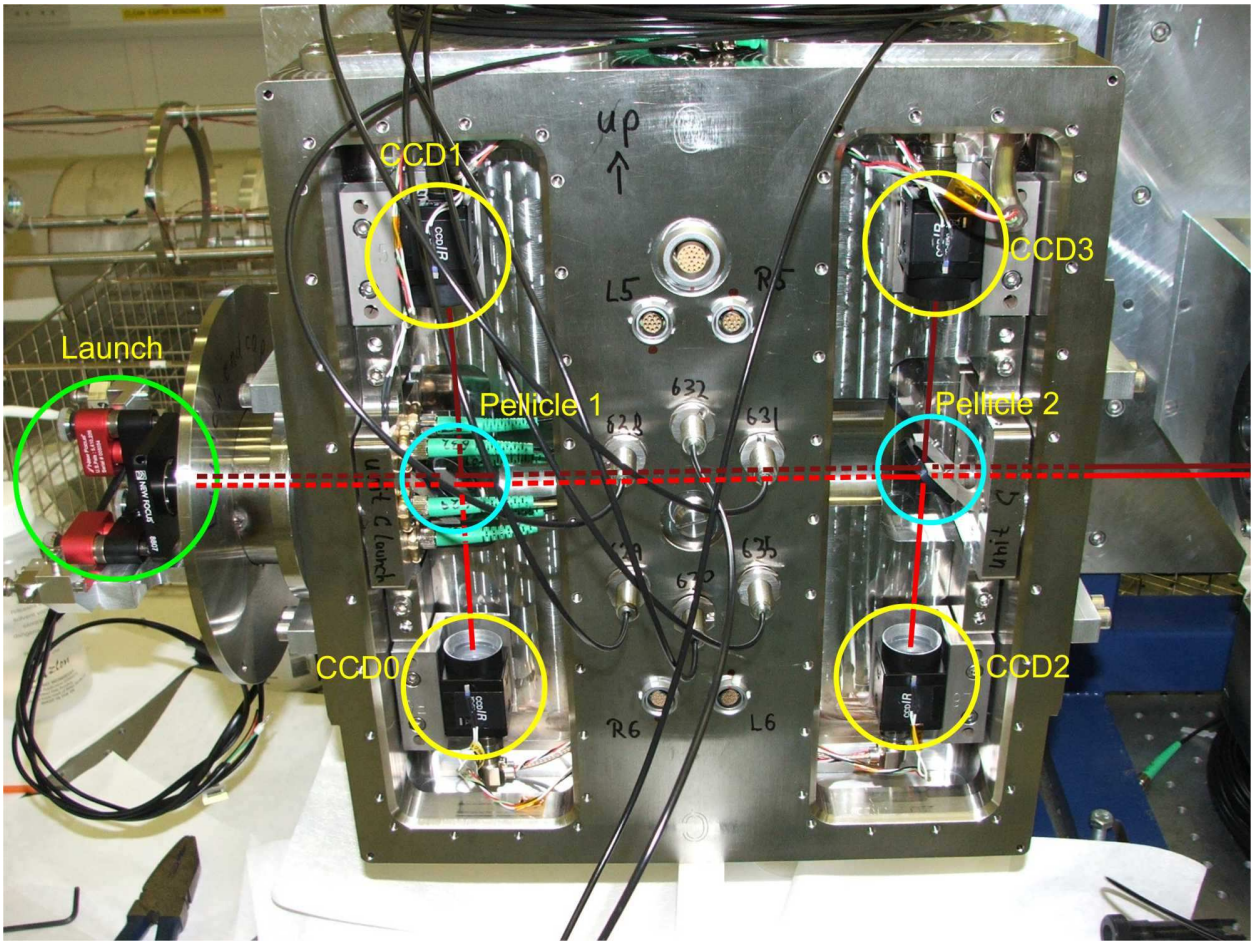

Figure 2.21: Photo of a measurement unit showing the LSM [15]

beam towards the outgoing ccd cameras (ccd0 and ccd2 in figure 2.21). The incoming beam enters the unit from the opposite direction and strikes the pellicles again with approximately 8% of the beam directed towards the incoming ccd cameras (ccd3 and ccd1 in figure 2.21).

Fitting model beams to CCD images gives a beam position for each CCD. From the beam positions, the rotational and translational degrees of freedom can be determined using a geometrical model of the system. More detail about the reconstruction of the LSM and the performance of the system can be found in [15].

2.2.7 LSM laser and end caps

The LSM laser and end caps are described in detail in [15]. A brief description follows.

The LSM laser is a Schäfter and Kirchhoff 57CFM-A-178-20-A-2-28-150 [16] laser which

is connected to a Schäfter and Kirchhoff 60FC-T-4-G25-10 [17] collimator and is launched from the launch end cap. The laser is mounted outside of the launch end cap and is connected to the collimator using an optical fibre. The optical fibre has a vacuum fibre feed through so it can pass into the launch end cap. The launch end cap contains the LSM launch optics which are mounted on pico motors. The pico motors allow the adjustment of the pointing of the collimator around the X and Y axes. The launch end cap is mounted directly to the end unit. The pico motor electronics pass out of the end cap using an electronics feed through. The pico motors are controlled by the master DAQ computer via TCP/IP.

The LSM laser beam passes along the length of the RTRS and is reflected back anti co-linear with the outgoing beam in the mirror end cap. The mirror end cap has a mirror which is mounted on pico motors. The pico motors can adjust the mirror rotation around the X and Y axes along with the translations along the X and Y axes. The LSM has to be aligned such that the return beam is anti co-linear with the launched beam. The launch end cap pico motor electronics pass out of the end cap via an electronic vacuum feed through. The launch end cap pico motors and are controlled by the master DAQ computer via TCP/IP.

2.2.8 Tilt sensors

Each unit has two gravity reference tilt sensors; one measuring the rotation around the X-axis and the other the rotation around the Z-axis. The tilt sensors are Schaevitz LSOP/LSOC DC-Operated, Gravity-Referenced Inclinometers, with the specifications given in [18]. The tilt sensor output voltages are digitised by an embedded electronic monitoring board (ELMB) (section 2.2.10) which is connected to the DAQ computer via CANbus. The sensors are mounted as shown in figure 2.22. Figure 2.23 shows histograms of repeated measurements of the rotation around the X and Y axes tilt sensors while in operation and while the the units are held fixed. Figure 2.23 shows that we typically achieve a precision between 5μrad and 12μrad.

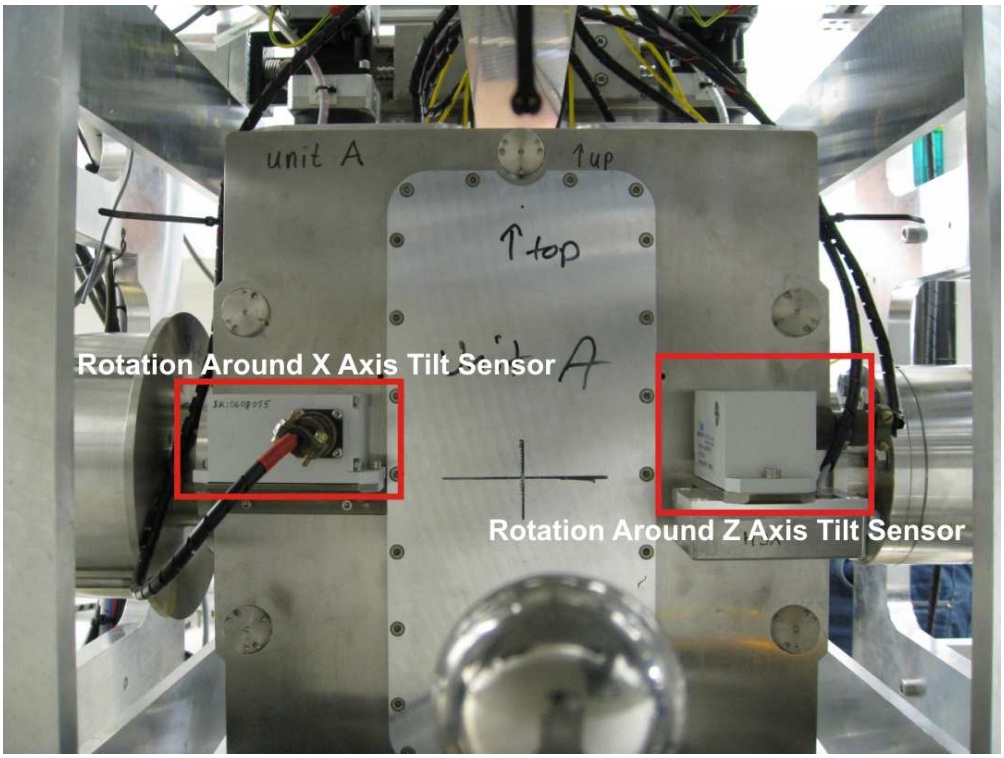

Figure 2.22: Photo of a measurement unit with tilt sensors marked

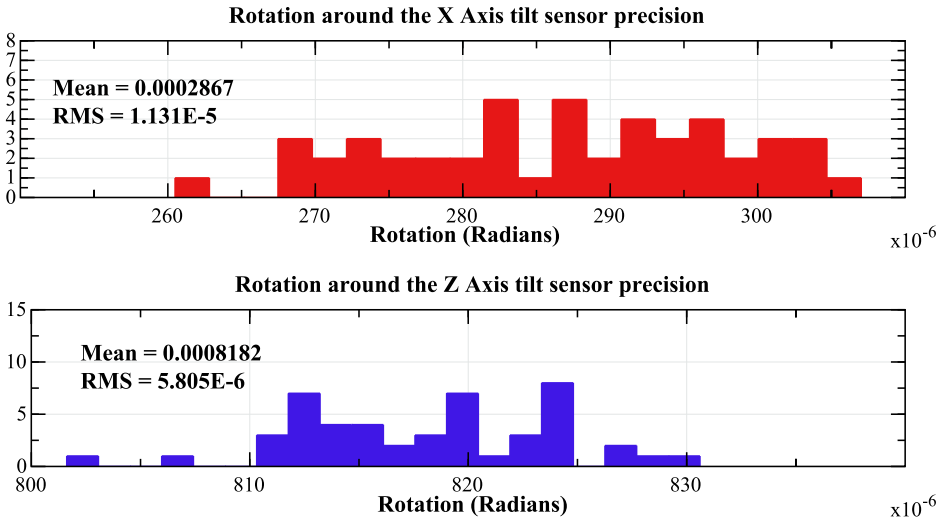

Figure 2.23: Measured tilt sensor precision

2.2.9 Temperature sensors

There are 105 temperature sensors placed throughout the RTRS. There are 15 temperature sensors in each of the reference interferometers, 4 sensors on the rear of each measurement unit, 2 on the front, one on each of the CCD's and the pellicle retro and launch holders. Each unit's stepper motors also have a temperature sensor.

The temperature sensors are PT100's which have been calibrated along with the ELMB's which read them [19]. The ELMB's perform four wire resistance measurements on the sensors. The working range of the sensors are from 0^oC to 50^oC and we achieve an accuracy of 0.05^oC [19].

2.2.10 ELMB

Embedded Local Monitor Board's (ELMB's) [20] are CANbus read, 32 channel 24 bit ADC's with variable signal conditioning boards. The LiCAS RTRS uses ELMB's for reading temperature sensors, tilt sensors, pressure sensors, and for limit switch monitoring in the LSM end caps. The inputs to the ELMB connect via junction boxes as shown in figures 2.24(a) and 2.24(b). An ELMB can digitise a voltage with a range of 0 to 100mV at a sample rate of 15Hz. The ELMB's are connected to the DAQ computers via CANbus.

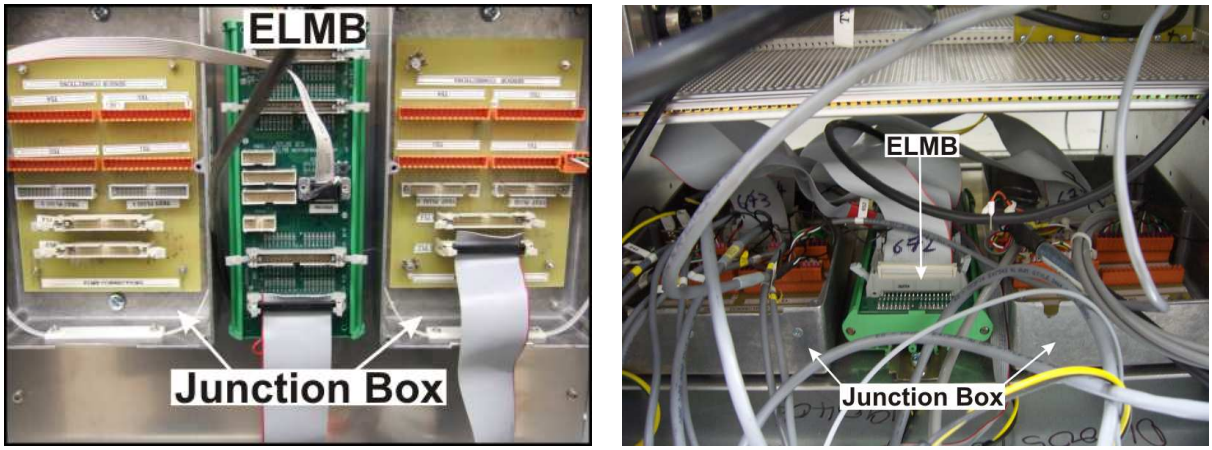

(a) Before installation (b) After installation

Figure 2.24: Photos of an ELMB and junction box before and after installation

2.2.11 Stepper motors

Each measurement unit has thirteen stepper motors: eleven are used to move the measurement unit in its six degrees of freedom, one is for the rail clamp shown in figure 2.26, and one is for the foot shown in figure 2.27. The stepper motors used are ICLA IFA Intelligent Compact Drive Fieldbus servomotor's [21]. Each stepper motor is coupled to its linear bearing via a fail safe brake which only opens when a current is applied. This makes the measurement unit stable when the brakes are applied without incurring vibration from powered brakes.

Figure 2.25 shows a photo of a unit with some of the eleven 6D motors marked. The 6D drive system exists in four shells; the inner shells moving with respect to the other shells. The outer most shell has four motors which translates the unit in the X-axis and rotates it around the Y-axis. The next shell also has four motors which translate the unit in the Z-axis and rotates it around the X-axis . The next shell has one motor which rotates the unit around the Y-axis. The final shell has two motors which translate the unit along the Y-axis. The movement of the system is given using the following equation:

$$Position_{finial} = R_z R_x (R_y (T_y + Position_{initial}) + T_z) + T_x \tag{2.1}$$

Where: R_z, R_x and R_y are the 3×3 rotations matrices around the Z,X and Y axes; T_z, T_x and T_y are the three dimensional translations in Z,X and Y axes and the positions are three dimensional co-ordinates in the measurement car's co-ordinate frame.

The system has three layers of protection to stop damage caused by stepper motors moving too far. The first is software limits which will stop any attempt at movement beyond a predefined range. The next level of protection is the electronic limit switches, which when activated disable the drive circuits for the motors they are connected to. The final system is mechanical stops which do not allow the unit to be driven further.

Before the measurement units can take data they need to be moved into the appropriate positions. This is done by first extending the foot and clamping the rail. By doing this the measurement units are made stable, suppressing vibrations from the rubber wheels. If the

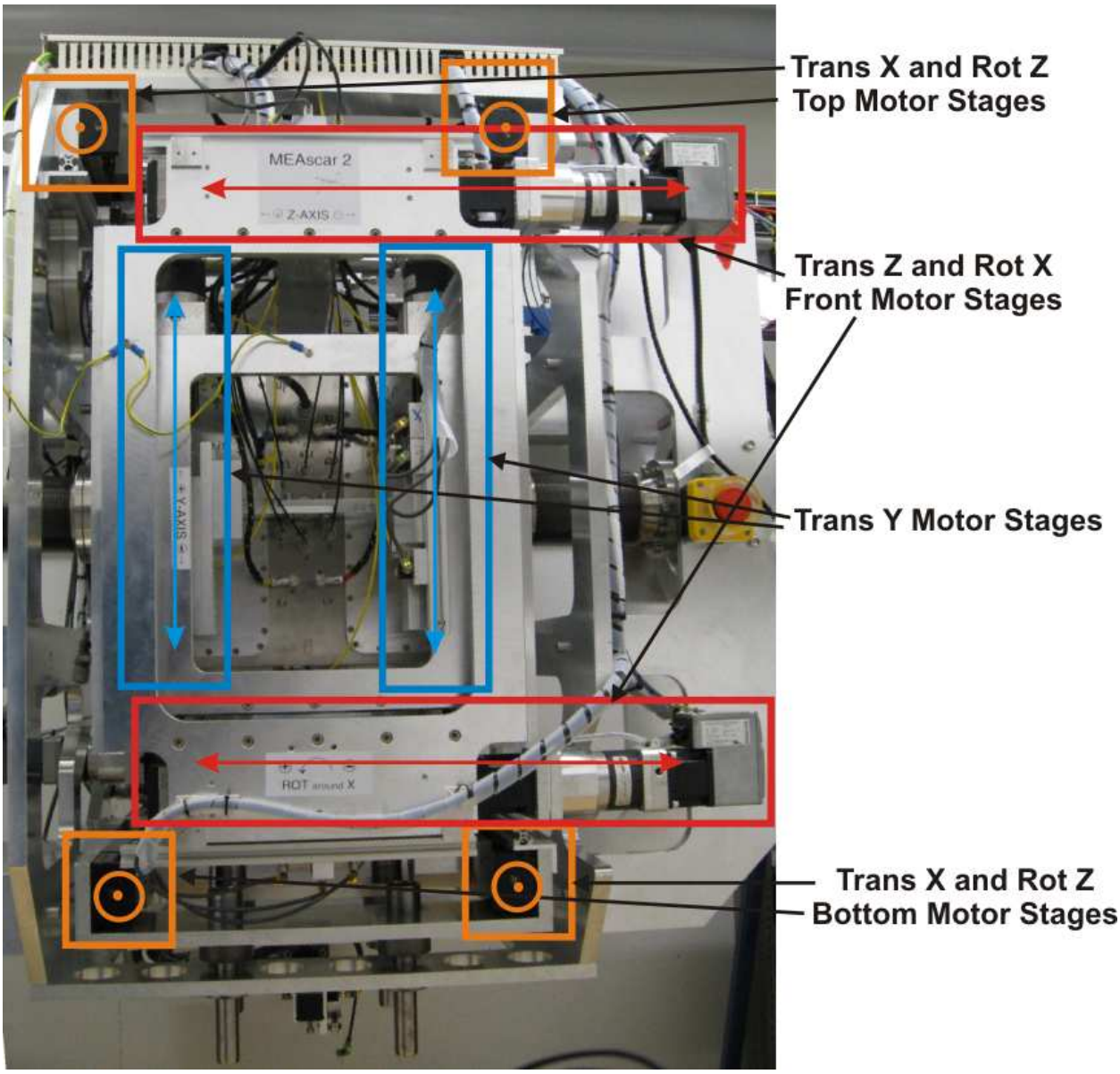

Figure 2.25: Photo of a measurement car with motors marked. Note that translation along the Z axis and rotation around the X axis rear motors, and the rotation around the Y axis motors are not visible.

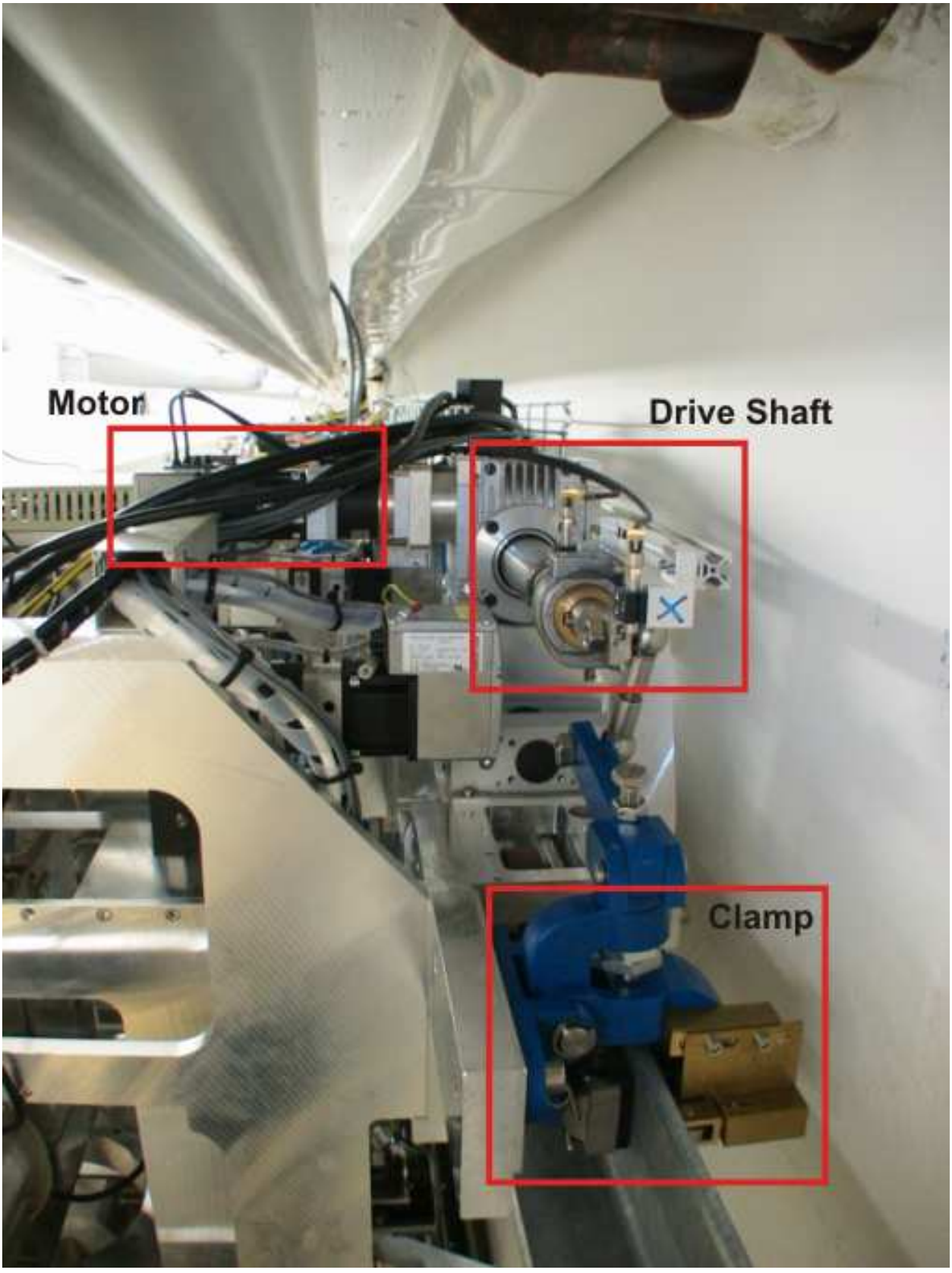

Figure 2.26: Photo of a measurement car rail clamp.

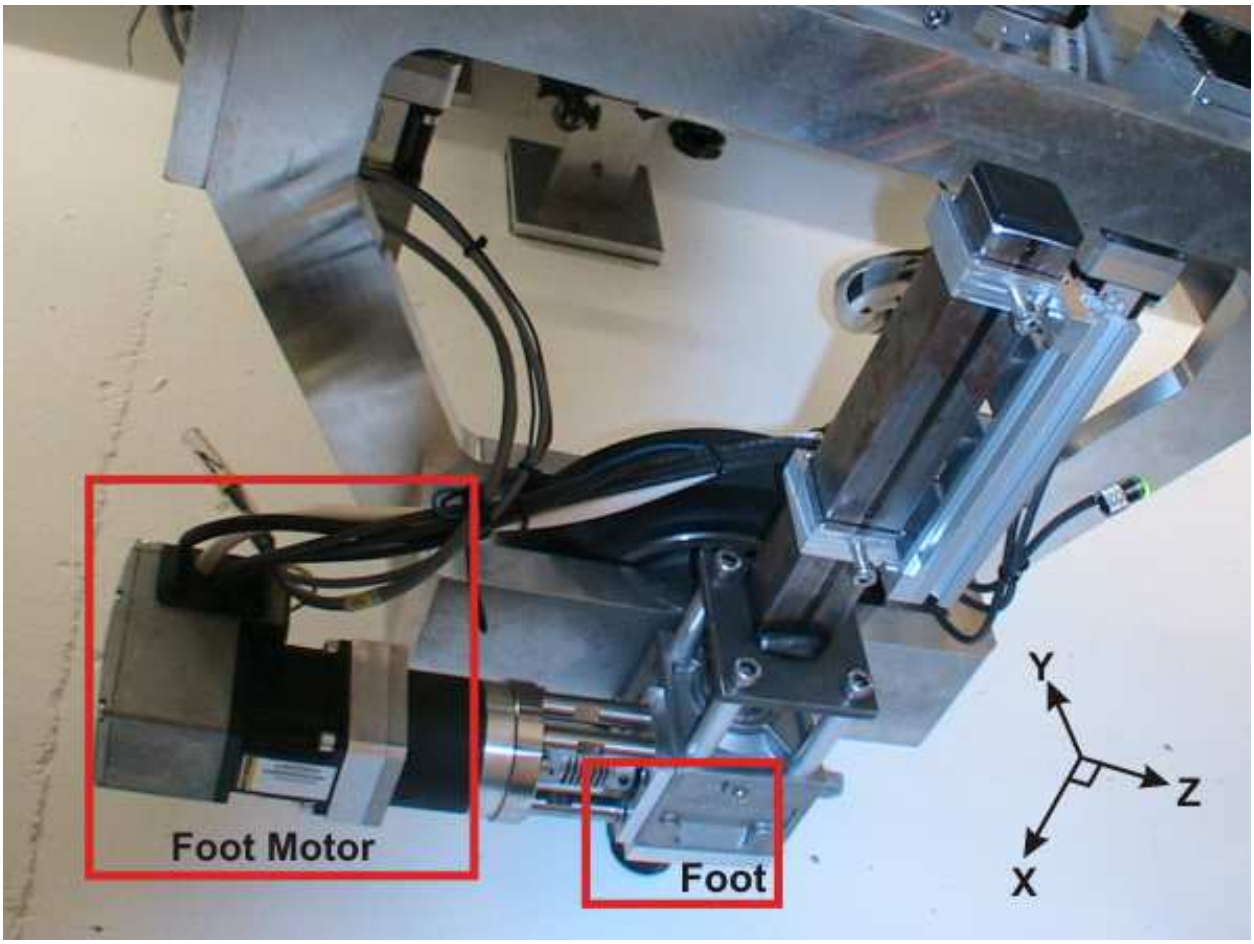

Figure 2.27: Photo of a measurement car foot motor.

rail clap is not applied and the foot not extended, vibrations will degrade the measurements, and the units could creep during the measurement process. The units are then aligned so that all the measurement systems are within their operational ranges.

2.2.12 DAQ computers

Each of the measurement cars is controlled by a DAQ computer. The DAQ computers are responsible for collecting all of the data from the measurement unit's measurement systems, and controlling the stepper motors. The data collecting and the movement of the unit is controlled via the DAQ software (see figure 2.28). The DAQ software controls movement and data taking via scripts. The scripts are time ordered instructions telling the computer what to do. For example, a script might take FSI data, then take temperature data and repeat the process every ten minutes for ten iterations. The scripts that run on the measurement DAQ computers can be controlled by the master DAQ software. The DAQ software needs to take a lot of data very quickly and so the hard disks in the computer are SCSI 360 disks in a RAID zero configuration.

2.2.13 Vacuum system

The internals of the LiCAS RTRS are all in a vacuum. The RTRS has approximately 90 vacuum seals with the LSM and internal FSI system contained in the vacuum. The vacuum flange on each unit is connected to a vacuum rotary seal which is then connected to flexible vacuum bellows as shown in figure 2.29. The bellows are connected to a ball and socket joint which connects to the interconnecting vacuum tubes as shown in figure 2.30. The combination of the vacuum bellows and the vacuum rotary seal allow the unit to move with the six degrees of freedom without breaking vacuum. The ball and socket joints allow the outer frames of the measurement cars to rotate with respect to each other, while keeping a fixed distance apart. The end measurement units only have rotary seals and flexible bellows on the inner vacuum flange, the outer flanges do not as they are attached to the end caps.

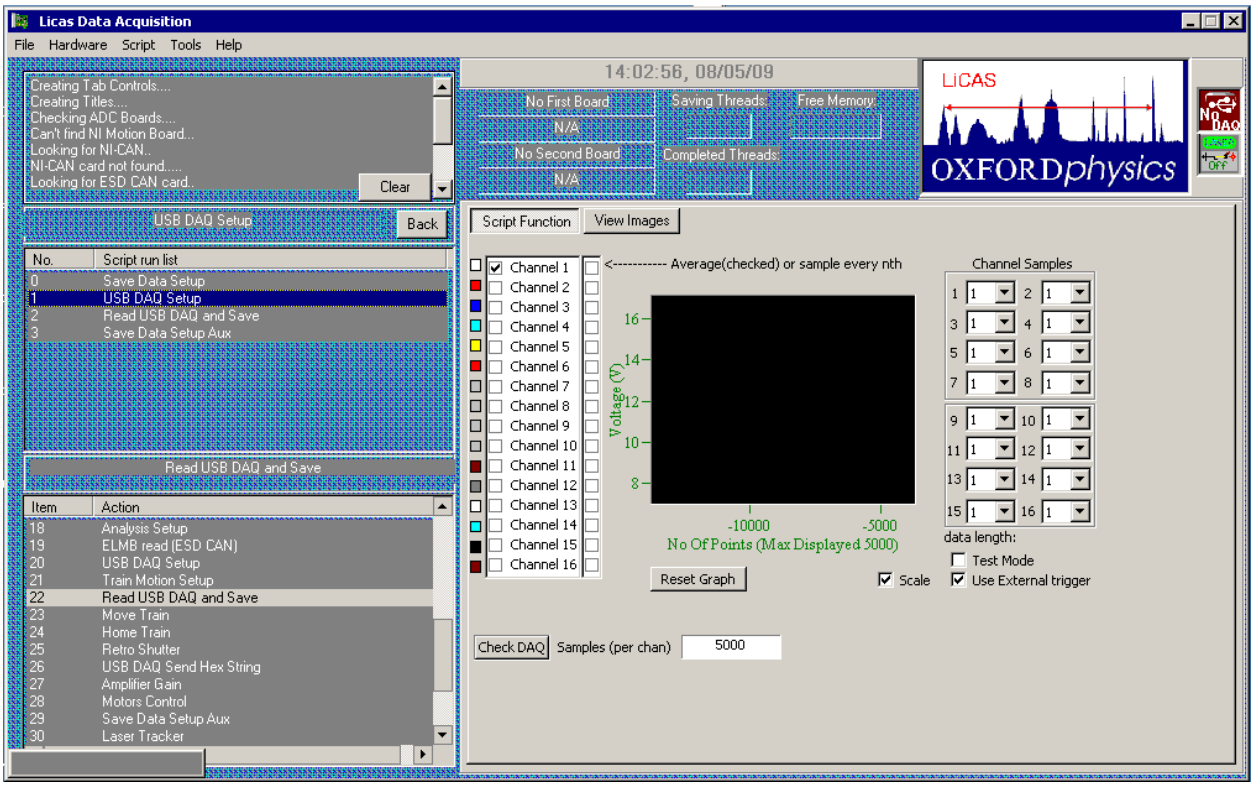

Figure 2.28: Screen shot of the LiCAS RTRS data acquisition software

The LSM retro end cap is also connected to the vacuum pump (see figure 2.31). The vacuum pump is a dry scroll pump mounted on the train. The vacuum system on the train achieved a vacuum of 5.9×10^{-2} mbar with a leak rate of approximately 0.3×10^{-2} mbar/hour.

2.2.14 Drive system

The RTRS drive system is responsible for moving the LiCAS RTRS from one stop to the next. The RTRS drive system has three Baldor BSM90B-275AA drive motors, shown in figure 2.32, which move the RTRS along the rail. Drive motor 1 acts as a master and the others act as slaves. Drive motor 1 receives the commands from the master DAQ computer and communicates with the other drive motors so that they all accelerate and decelerate synchronously. The prototype LiCAS RTRS accelerates and decelerates at $0.2m/s^2$ and travels with a speed of $0.5m/s$. Note that to move the RTRS the rail clamps must be opened and the feet retracted.

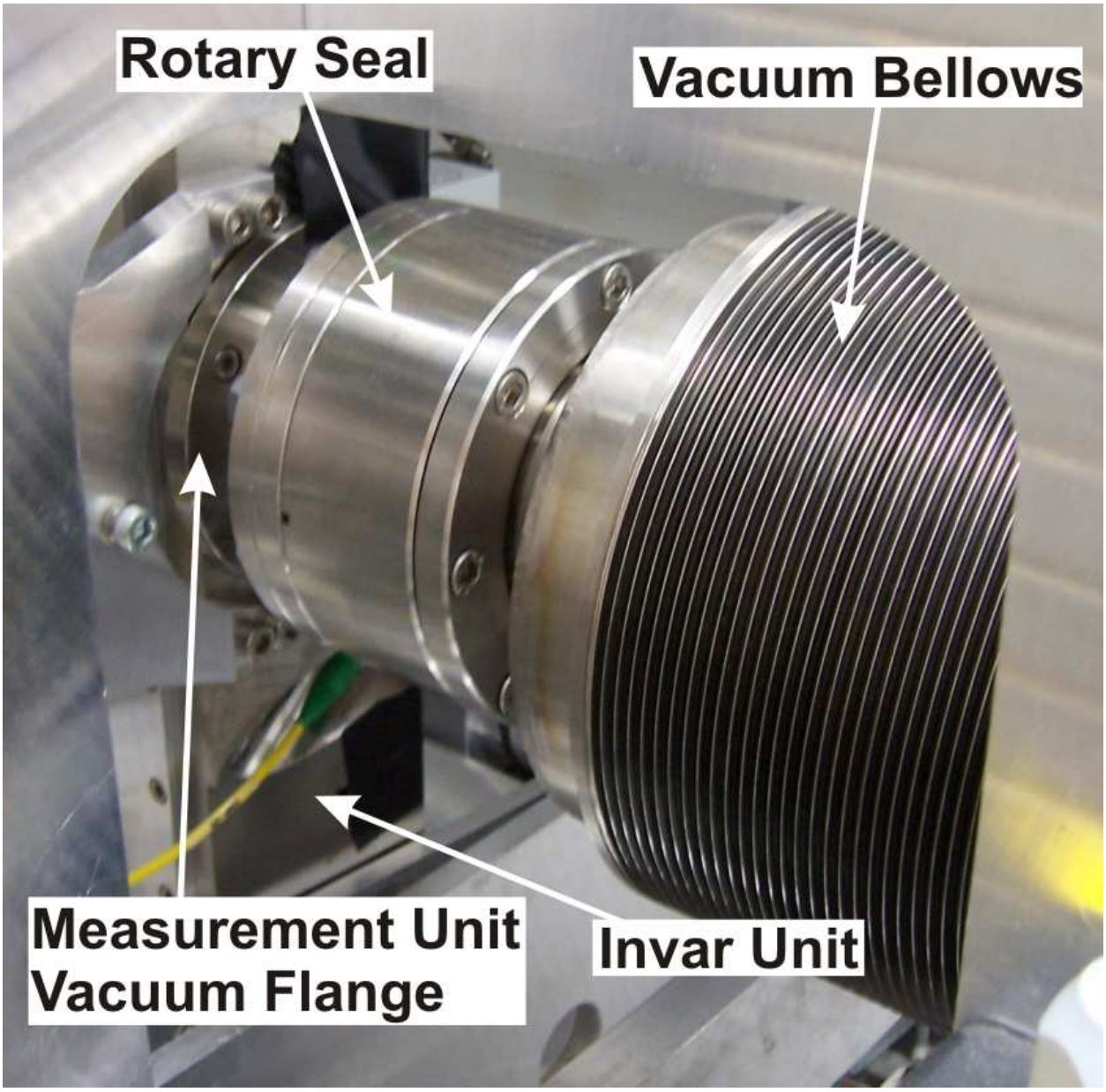

Figure 2.29: Photo of a LiCAS RTRS vacuum bellow and rotary seal

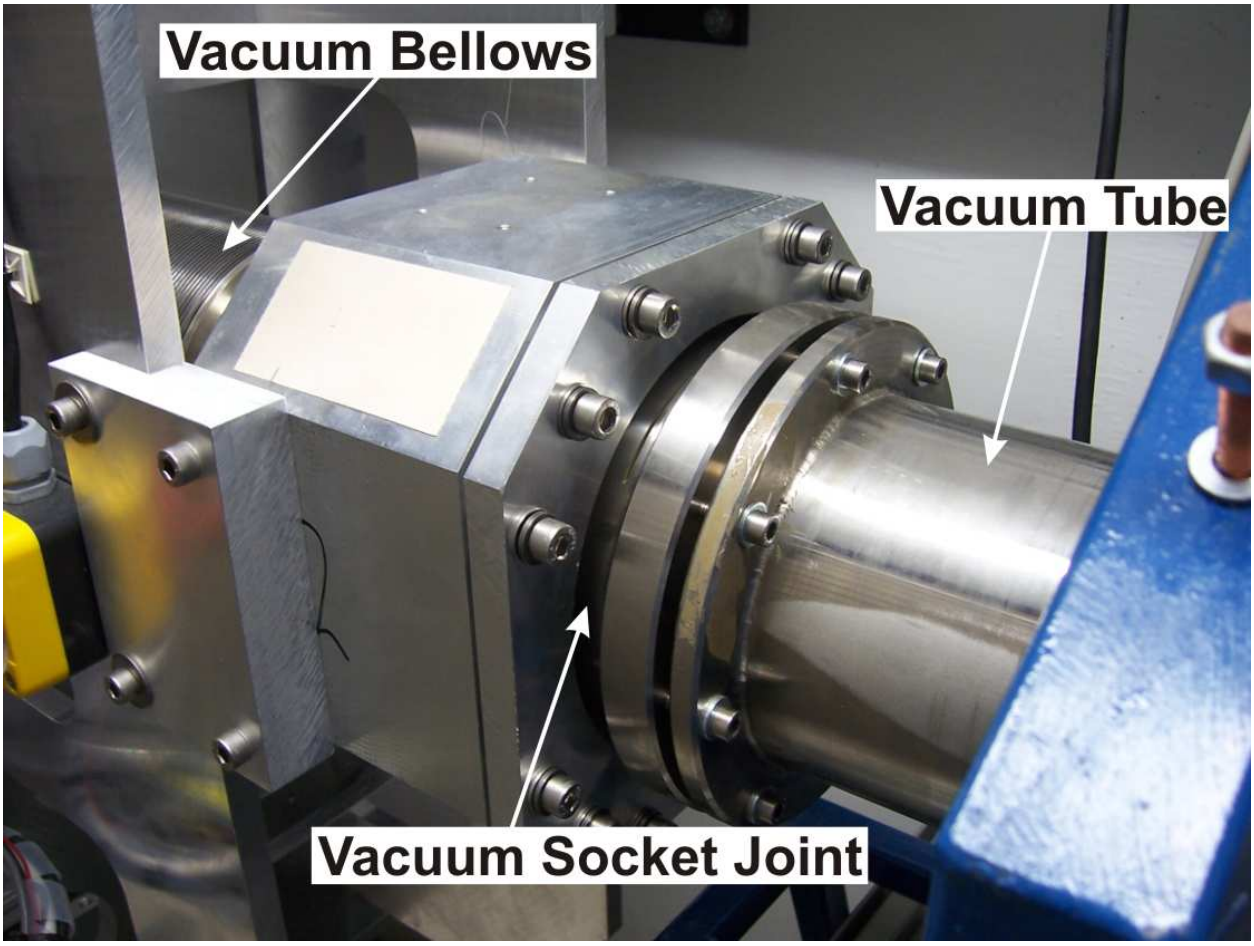

Figure 2.30: Photo of a LiCAS RTRS Vacuum socket joint

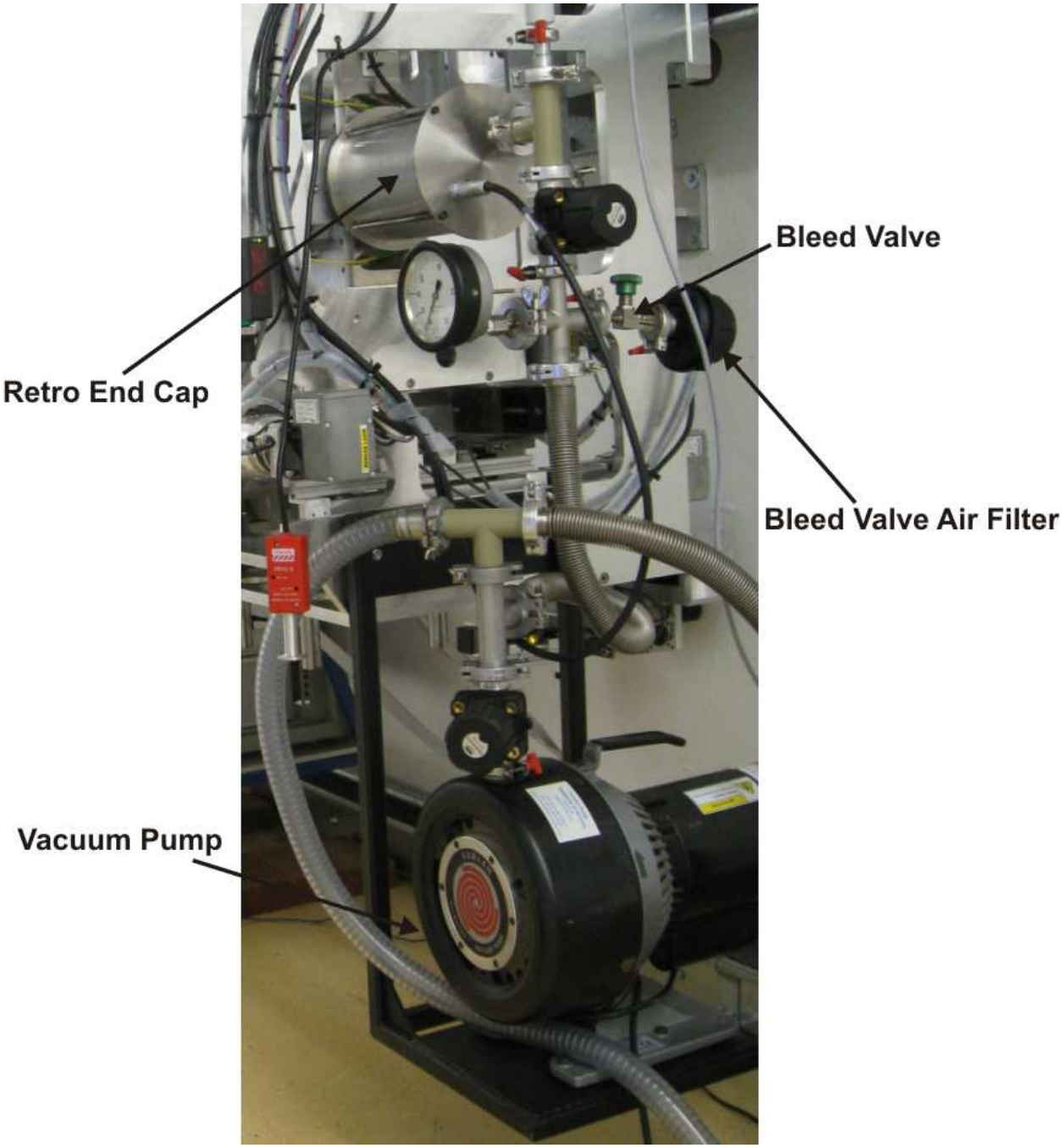

Figure 2.31: Photo of the LiCAS RTRS vacuum pump

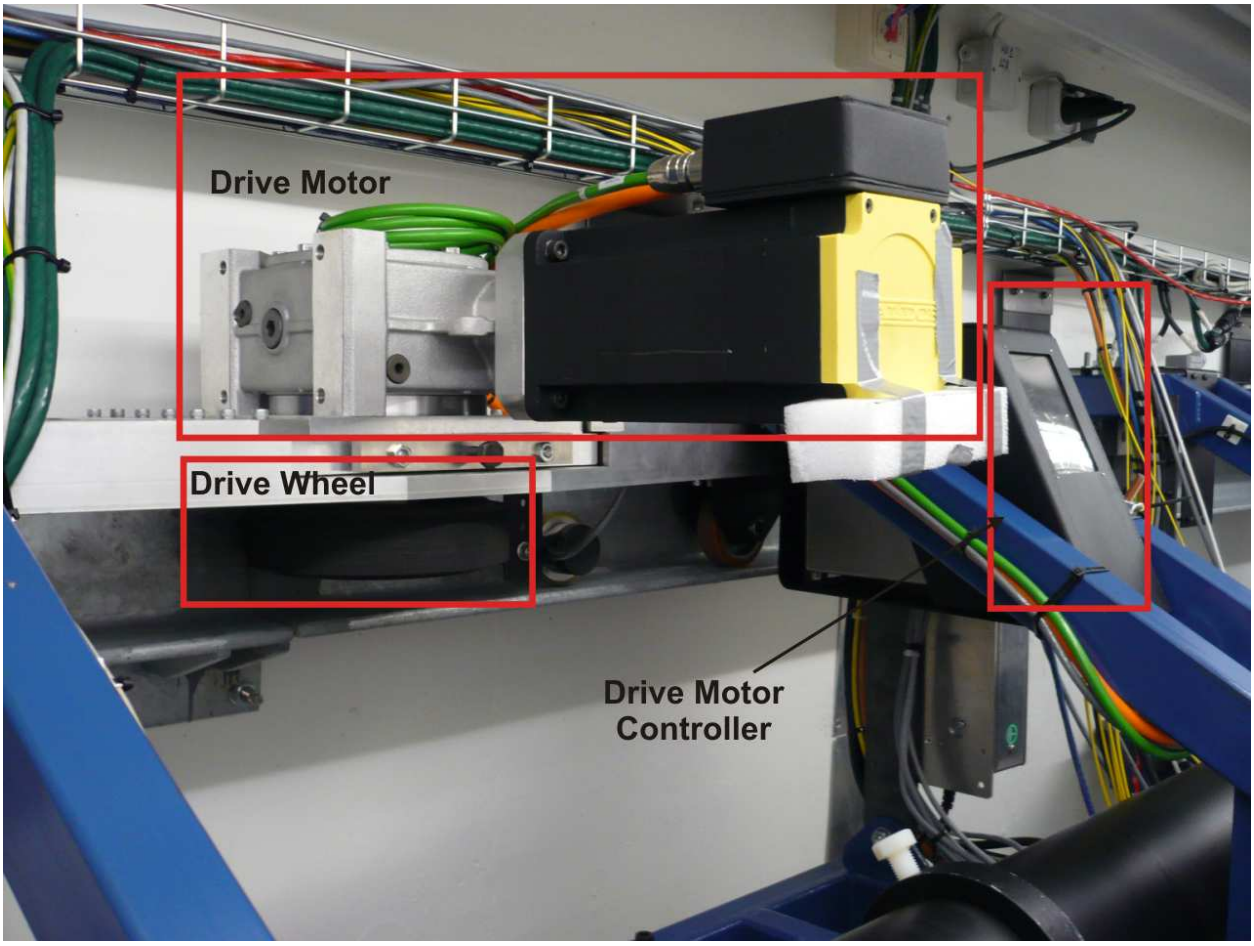

Figure 2.32: Photo of a LiCAS RTRS drive motor

2.3 Current status

At the time of writing the calibration data has been taken for the entire RTRS, and the analysis to determine the calibration constants has begun. Several surveys of the test tunnel were performed but this data is still to be analysed and compared to a conventional survey. Stability runs have been performed and some of the data is presented in this thesis. The RTRS was developed to the point where data could be taken, however this is still a semi manual process. The RTRS can also be aligned to bring all the measurement systems into operational range, but once again this is still a semi manual process.

Chapter 3

Least Squares Point Estimators

Least squares regression is used throughout this thesis to solve many problems ranging from determining the calibration constants of the reference interferometers to solving reference networks for the ILC.

In this chapter the underlying theory of least squares using linear algebra will be described. This chapter draws information from many sources most of which were collated and explained to me by Dr Patrick Brockill [22].

3.1 Linear least squares point estimators

Linear least squares point estimation is well described in chapter 6 of [23]. A summary of the method follows.

In fitting a straight line to data, the parameters for the straight line can be determined using linear least squares. Let us define a vector X which contains the parameters we wish to determine, in this example these are the gradient and the intercept. Let us also define the observation vector L which contains all of the measurements, in this example these are the measured y values. Finally we define the design matrix A which has the first column containing the x values and the second column containing 1 at each element. A linear

mathematical model for this process can be written as:

$$AX - L = V \tag{3.1}$$

Where:

${}_nL_1$ is the observation vector containing all of the measurements.[1]

${}_nV_1$ is the residual vector containing the unknown measurement errors.

${}_uX_1$ is the solution vector containing the unknown parameters.

${}_nA_u$ is the known design matrix or the matrix of coefficients.

n is the number of measurements.

u is the number of parameters.

The least squares criterion is that the weighted sum of the squares of the residuals should be minimized:

$$\hat{V}^T P \hat{V} = minimum \tag{3.2}$$

Where:

$P = \sigma_0^2 \Sigma_L^{-1}$ is the weight matrix.[2]

Σ_L is the measurement covariance matrix.

$\hat{V} = A\hat{X} - L$ where $\hat{}$ indicates the current estimators.

If the least squares condition is applied to equation 3.1 it can be shown that if $A^T PA$ is non-singular, then there is a unique least squares estimator of X given by:

$$\hat{X} = (A^T PA)^{-1} A^T PL \tag{3.3}$$

With the unbiased estimator of the covariance matrix of X given by:

$$\hat{\Sigma}_{\hat{X}} = \hat{\sigma}_0^2 (A^T PA)^{-1} \tag{3.4}$$

[1] lower indices represent matrix dimensions where the pre index is the number of rows and the post index is the number of columns

[2] σ_0^2 is a scaling factor to avoid numerical accuracy problems in Σ_L^{-1}; with the value determined by studying the individual applications.

Where

$$\hat{\sigma}_0^2 = \frac{\hat{V}^T P \hat{V}}{n-u} \tag{3.5}$$

3.2 Non-linear least squares point estimators

Section 3.1 described least squares point estimators for linear models. The theory of non-linear least squares point estimators is well described in chapter 7 of [23]; a summary of the method follows.

There are many different non-linear least squares methods but only two will be addressed here. The first addresses the most general case, and can be used for any non-linear problem. This method is referred to as the combined method, where the non-linear function is expressed in the following form:

$$F(\bar{X}, \bar{L}) = 0 \tag{3.6}$$

Where $\bar{L}$ is the total observation vector given by:

$$\bar{L} = L + V \tag{3.7}$$

L is the observation vector and V is the residual vector. $\bar{X}$ is the true solution vector given by:

$$\bar{X} = X^0 + X \tag{3.8}$$

Where X^0 is the current best guess of the solution vector and X is a correction to X^0 which is to be determined.

This method contains: r equations, n observations, u parameters and a redundancy of (r-u)

The second type is a special case of the combined method which is referred to as the

parametric method; this method can be applied when there is a function of the form:

$$F(\bar{X}) = \bar{L} \tag{3.9}$$

The method can form n equations, n observations, u parameters and a redundancy given by (n-u).

The following descriptions will be based on the combined method with the results for the parametric method given at the end.

To solve a non-linear problem using these methods the redundancy has to be greater than zero, and the problem linearised. Linearisation of the models can be achieved by taking the Taylor's series expansion of F with respect to the elements of X^0 and L leading to:

$$F(\bar{X}, \bar{L}) \approx W + AX + BV = 0 \tag{3.10}$$

Where:

$W = F(X^0, L)$ is the misclosure vector.

$A = \frac{\partial F}{\partial X}\Big|_{X^0,L}$ and $B = \frac{\partial F}{\partial L}\Big|_{X^0,L}$ are the design matrices.

The normal equations (the equations which minimise the sum of the squares) for the expanded functions can now be determined. The normal equations express the relationship between the least squares estimators $\hat{X}$ and $\hat{V}$ to the solution vector X and the residual vector V. The normal equations can be determined by applying the least squares criterion (equation 3.2) leading to the following equations:

$$\hat{X} = -(A^T(BP^{-1}B^T)^{-1}A)^{-1}A^TPW \tag{3.11}$$

$$\hat{V} = -P^{-1}B^T(BP^{-1}B^T)^{-1}(A\hat{X} + W) \tag{3.12}$$

$$\Sigma_{\hat{X}} = \sigma_0^2(A^T(BP^{-1}B^T)^{-1}A)^{-1} \tag{3.13}$$

Where:

$P = \sigma_0^2 \Sigma_L^{-1}$ is the weight matrix.

Σ_L is the measurement covariance matrix.

$A^T(BP^{-1}B^T)^{-1}A$ is non-singular.

With $\hat{X}$ determined, the updated estimate for the solution vector is given by:

$$\hat{\bar{X}} = X^0 + \hat{X} \tag{3.14}$$

and the process can be iterated to determine the best values for the estimate of the solution vector.

The equations for $\hat{X}$, $\hat{V}$ and $\Sigma_{\hat{X}}$ given above stem from the combined method. If however the parametric method is used, it can be shown that $B = -I$, which lead to the following equations for the parametric method:

$$\hat{X} = -(A^T P A)^{-1} A^T P W \tag{3.15}$$

$$\hat{V} = A\hat{X} + W \tag{3.16}$$

$$\Sigma_{\hat{X}} = \sigma_0^2 (A^T P A)^{-1} \tag{3.17}$$

3.3 Constraints

In the following discussion only the combined method will be considered. In many problems the matrix $A^T(BP^{-1}B^T)^{-1}A$ is singular and can not be inverted, therefore $\hat{X}$ cannot be determined. To overcome this problem, constraints can be applied. The number of constraints is equal to the rank deficiency of $A^T(BP^{-1}B^T)^{-1}A$.

If the required constraint equations can be determined and written as a function of the form:

$$F_2(\bar{X}) = 0 \tag{3.18}$$

and then Taylor's series expanded to get:

$$F_2(\bar{X}) \approx W_2 + A_2 X = 0 \tag{3.19}$$

where:

$W_2 = F_2(X^0)$

$A_2 = \frac{\partial F_2}{\partial \vec{X}}\Big|_{X^0}$ it can then be shown, as described in [23], that applying the constraint equation to the problem leads to the following normal equations:

$$\begin{bmatrix} \hat{X} \\ \hat{K}_2 \end{bmatrix} = \begin{bmatrix} A^T(BP^{-1}B^T)^{-1}A & A_2^T \\ A_2 & 0 \end{bmatrix}^{-1} \begin{bmatrix} A^T(BP^{-1}B^T)^{-1}W \\ W_2 \end{bmatrix} \tag{3.20}$$

Where $\hat{K}_2$ is the estimator of the vector of Lagrange multipliers for the constraint equations.

This can then be solved to determine $\hat{X}$ and the solution vector value updated as shown in equation 3.14. The process can then be iterated to determine the best value for $\hat{X}$ with A_2 and A_2^T recalculated each iteration.

3.3.1 Fixed constraint

One way to constrain a problem is to fix certain parameters in the model to a value. An example of this is the internal unit reconstruction discussed in section 6.2.3, where the parametric method is used to determine translations in the X,Y and Z-axis and the rotations around the X and Y-axis between two units. There is a problem however that the translations in the X and Y axis cannot be determined, they must be constrained. These values are therefore measured by other systems, and used to constrain their degrees of freedom in the model.

3.3.2 Free network constraint

There are some problems which require constraining, where no obvious choice for fixed constraints can be found. An example of this are the solutions of geodetic networks as described in section 7.3. This is a common and old problem in Geodesy, and is solved using Free Network Adjustment as discussed in [24], [25], [26], [27] and [28]; this problem is also addressed in computer vision under the term bundle adjustment [29]. The methods all try to minimise the trace of the output covariance matrix to determine the best choice of constraint.

Below we describe several methods for implementing free network constraints. These methods all try to determine the matrix A_2 of equation 3.20.

Singular Value Decomposition (SVD) method

Chapter 12 of [28] gives a worked example of how to solve the problem of a three dimensional network using a singular value decomposition (SVD). Since the matrix $A^T(BP^{-1}B^T)^{-1}A$ cannot be inverted, there can not be an unbiased least squares estimator. However, there are linear combinations of the elements of X for which unbiased estimates exist. As $A^T(BP^{-1}B^T)^{-1}A$ is singular, there must be unconstrained degrees of freedom in the direction of the singular vectors; so the singular vectors with zero or very small singular values are the degrees of freedom which require constraints. An SVD determines all of the singular vectors and singular values of a matrix. An SVD of a matrix M is defined as:

$$M = U\Lambda V^T \tag{3.21}$$

Where:

The columns of V are the eigenvectors of M^*M.[3]

The columns of U are the eigenvectors of MM^*.

The diagonal values in matrix Λ are the singular values. The singular values are the square

[3] M^* represents the complex conjugate of M

root of the eigenvalues of U and V. By convention the singular values are ordered by decreasing value from the upper left to the lower right element.

If a singular value decomposition is performed on $M = A^T(BP^{-1}B^T)^{-1}A$ to determine U and V, it is shown in [28] that the optimally constrained form of the matrix A_2 is:

$$A_2 = \begin{pmatrix} 0 & -I \end{pmatrix} V^T \tag{3.22}$$

Where the size of I is the rank deficiency of $A^T(BP^{-1}B^T)^{-1}A$, or the number of constraints required, or the number of singular vectors with zero eigenvalues.

Now that A_2 and A_2^T have been re-defined in a constrained form, W_2 also needs to be re-defined. Because the constraints are determined by the singular vectors along which the model requires constraints, W_2 can simply be re-defined to be zero.

Eigenvalue Decomposition (EVD) method

A singular value decomposition can be performed on any shape matrix. However, as we are interested in the SVD of $A^T(BP^{-1}B^T)^{-1}A$ which has to be square, an Eigenvalue Decomposition can be used instead of an SVD. An EVD of a square matrix M is defined as:

$$M = Q\Lambda Q^{-1} \tag{3.23}$$

Where:
M must be a square matrix.
Λ is a diagonal matrix containing all of the eigenvalues.
Q contains the eigenvectors corresponding to the eigenvalues in Λ.

In a similar way to the SVD approach, the zero or small eigenvalues can be used to determine the required eigenvectors to use in A_2 and A_2^T, with $W_2 = 0$ as described above.

An EVD can have computational advantages over an SVD if $A^T(BP^{-1}B^T)^{-1}A$ has certain

structures. When $A^T(BP^{-1}B^T)^{-1}A$ has, for example, a band diagonal structure, there are algorithms which will calculate the EVD faster than the SVD.

Inner constraint method

Another method to determine the matrix A_2 is described in [27]. In this method we take the matrix $A^T(BP^{-1}B^T)^{-1}A$ and divide it up into the form of:

$$A^T(BP^{-1}B^T)^{-1}A = N = \begin{bmatrix} N_{11} & N_{12} \\ N_{21} & N_{22} \end{bmatrix} \tag{3.24}$$

where N_{11} is non-singular and the number of columns in N_{12} equals the number of rows in N_{21} which equals the number of constraints required. Note to make N_{11} non-singular the rows and columns of N in general need shifting. The parameter vector is also split:

$$X = \begin{bmatrix} X_1 \\ X_2 \end{bmatrix} \tag{3.25}$$

And the constraint is then defined as:

$$\begin{bmatrix} (N_{11}^{-1}N_{12})^T & -I \end{bmatrix} \begin{bmatrix} X_1 \\ X_2 \end{bmatrix} = 0 \tag{3.26}$$

Where I is the size of the number of required constraints. Equation 3.26 can be written as:

$$(N_{11}^{-1}N_{12})^T X_1 - X_2 = 0 \tag{3.27}$$

which leads to the constraint matrix

$$A_2 = ((N_{11}^{-1}N_{12})^T - I) \tag{3.28}$$

The values for W_2 can simply be defined as 0 as explained above. Note that $A^T(BP^{-1}B^T)^{-1}A$ will normally have to be re-arranged so that N_{11} becomes non-singular. The determination of which rows and columns form N_{11} is achieved by analysis of the problem.

The inner constraint method has one weakness in comparison to the SVD or EVD method referred to as the selection problem [25]. The selection problem refers to the fact that often the choice of N_{11} is not unique, but only one choice will lead to the trace of the output covariance matrix being minimum. Therefore the incorrect choice may not lead to the best minimum.

3.4 Line search

In non-linear least squares point estimation, described in 3.2, the process has to be iterated to get the best solution. It can take several iterations to get to the best solution, and at times the process can oscillate around the ideal solution. The iterative procedure can converge quicker, and any problems with oscillation around the best solution can be avoided by using a line search algorithm.

One line search algorithm which is well described in [26] and [25] is the Damped Gauss-Newton method. For each iteration we determine $\hat{X}$, then using our initial guess for the solution vector X^0, the following condition is evaluated:

$$\begin{aligned}(F(X^0)-L)^TP(F(X^0)-L)-(F(X^0+\alpha\hat{X})-L)^TP(F(X^0+\alpha\hat{X})-L)\\ \geq \frac{1}{2}\alpha\hat{X}^T(A^T(BP^{-1}B^T)^{-1}A)\hat{X}\end{aligned} \tag{3.29}$$

The value of α starts at 1, if the condition is false then α is halved and the condition re-evaluated, and if it is true then the process stops. Note that this is a fast approximation

to the exact line search in which α is found as the solution to the following condition:

$$min|_{\alpha}((F(X^0 + \alpha\hat{X}) - L)^T P(F(X^0 + \alpha\hat{X}) - L)) \tag{3.30}$$

With the value of α determined we can optimally update the estimate of the parameter vector using the following equation:

$$\hat{\hat{X}} = X^0 + \alpha\hat{X} \tag{3.31}$$

3.5 Computation

Solving linear and non-linear least squares problems is mostly done using computers, and often involves using specialist software packages. Throughout this thesis many linear and non-linear point estimator problems will be approached and solved using Java [30] package Matrix Toolkits for Java [31] (MTJ). MTJ is a collection of wrapper classes around the JLapack and JBlas libraries [32]. The JLapack and JBlas libraries are java implementations of the Lapack [33] and Blas [34] Fortran libraries.

Chapter 4

Frequency Scanning Interferometry

Frequency scanning interferometry (FSI) is an interferometric method for absolute distance measurements. FSI is used in two of the RTRS measurement systems. This chapter discusses the theory of FSI and the FSI data analysis method.

4.1 Theory

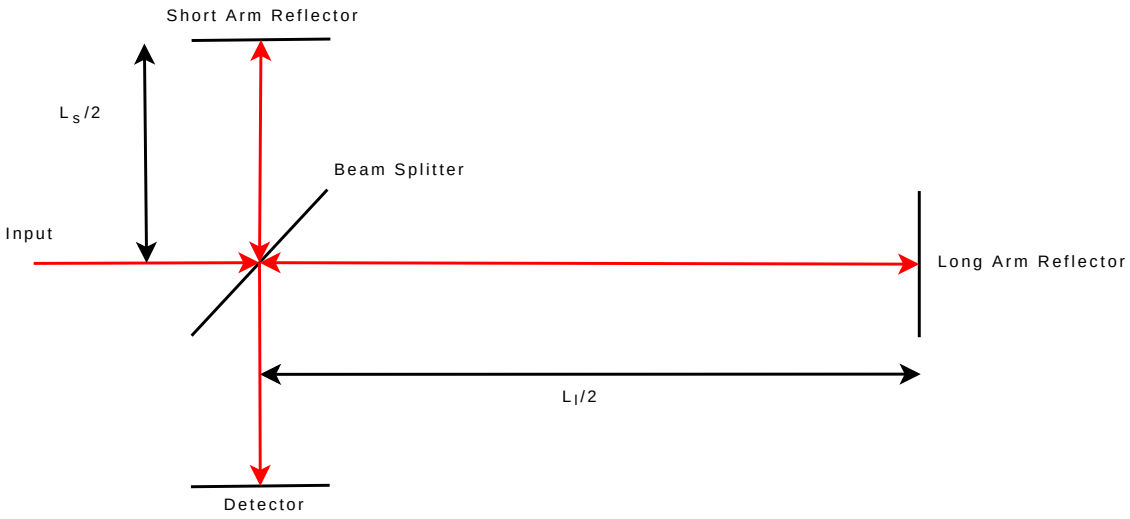

Figure 4.1: A diagram of a two arm interferometer

The interferometers described here are amplitude splitting two arm interferometers. The interferometers have a long and a short arm of geometric length l_l and l_s respectively, and are

fed with light from a frequency scanning laser. The frequency scanning laser has a frequency of $\nu(t)$ at a time t and scans from an initial time t_i to a final time t_f. The light from the frequency scanning laser enters the interferometer and is split into the two arms as shown schematically in figure 4.1. The light passes down each arm, reflects and recombines at the beam splitter. At recombination the electric field of the light in each arm is represented by the following equations:

$$E_l = a_l * E_0 * e^{i(k(T_l)*l_l - 2*\pi*\nu(T_l)*T)}, \tag{4.1}$$

$$E_s = a_s * E_0 * e^{i(k(T_s)*l_s - 2*\pi*\nu(T_s)*T)}. \tag{4.2}$$

Where T_l and T_s are the time the light entered the two arms of the interferometer, $\nu(T_l)$ and $\nu(T_s)$ are the frequencies of the laser light when it enters the respective arms of the interferometer, $k(T_l)$ and $k(T_s)$ are the wave numbers of the laser light when it enters respective arms of the interferometers, T is the time at which the light recombines at the beam splitter and a_l and a_s are the amplitude coupling constants of the two arms of the interferometer. The intensity of the recombined beams, at time T, is given by:

$$\begin{aligned} I(T) =& \left(E_l + E_s\right)\left(E_l + E_s\right)^*, \\ I(T) =& a_l a_s e^{i(k(T_l)l_l - 2\pi\nu(T_l)T) - i(k(T_s)l_s - 2\pi\nu(T_s)T)} {E_0}^2 \\ &+ a_l a_s e^{i(k(T_s)l_s - 2\pi\nu(T_s)T) - i(k(T_l)l_l - 2\pi\nu(T_l)T)} {E_0}^2 \\ &+ {a_l}^2 {E_0}^2 + {a_s}^2 {E_0}^2, \\ I(T) =& E_0^2\left(a_l^2 + a_s^2 + 2a_l a_s \cos(\phi(T))\right). \end{aligned} \tag{4.3}$$

Where the phase $\phi(T)$ given by:

$$\phi(T) = (k(T_l)l_l - 2\pi\nu(T_l)T) - (k(T_s)l_s - 2\pi\nu(T_s)T). \tag{4.4}$$

Given that:

$$k(t) = \frac{2\pi\nu(t)}{c} \tag{4.5}$$

and:

$$\nu(T_l) = \nu(T_s) + \Delta\nu(\Delta l, T), \tag{4.6}$$

$$\Delta l = l_l - l_s. \tag{4.7}$$

the phase can be expressed as:

$$\phi(T) = \frac{2\pi}{c}\left(\nu(T_l)l_l - \nu(T_s)l_s - T\Delta\nu(\Delta l, T)c\right) \tag{4.8}$$

If $T_s - T_l$ and $\dot{\nu(t)}$ are small then $\Delta\nu(\Delta l, T)$ is small, a typical value in our system is 3.14×10^{-3}Hz, then:

$$\nu(T_l) \approx \nu(T_s) \approx \nu(T), \tag{4.9}$$

Given these simplifying assumptions, the phase at time T in the interferometer is:

$$\phi(T) \approx \frac{2\pi\nu(T)\Delta l}{c}. \tag{4.10}$$

The total phase advanced during the scan is then:

$$\phi_{total} \approx \frac{2\pi\Delta l}{c}\int_{T=t_i}^{T=t_f}\nu(T). \tag{4.11}$$

The interferometers studied in this thesis are Fizzeau interferometers. In a Fizzeau interferometer the short arm length is zero and the interferometer's optical path length difference Δl is the long arm length l_l assuming that the refractive index in the long arm is 1. In the rest of this discussion l_l will be referred to as l. If there are two Fizzeau interferometers fed simultaneously with the same light, as shown in figure 4.2, the ratio of the total phases of the two interferometers shown in figure 4.2 is given by:

$$\frac{\phi_{total_1}}{\phi_{total_2}} = \frac{l_1}{l_2} = \phi_{2,1}. \tag{4.12}$$

Subject to the approximation made in 4.9, and if l_2 is known, the length of l_1 can be

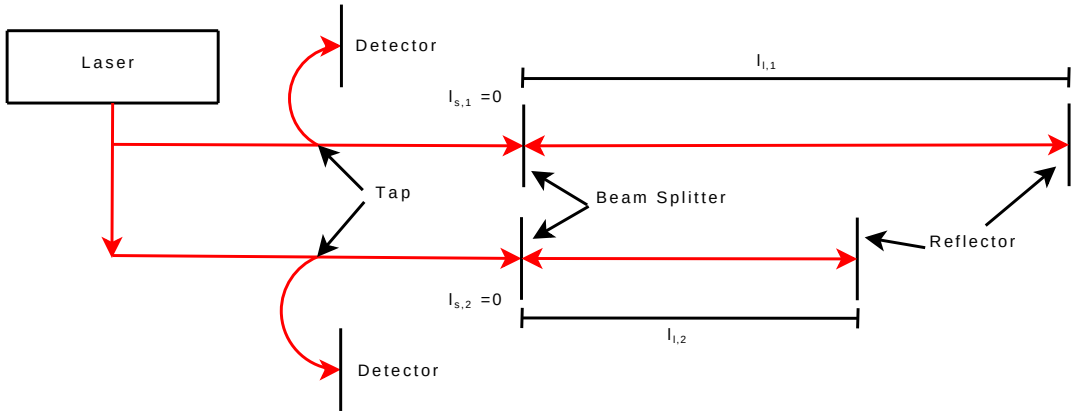

Figure 4.2: A diagram of two Fizzeau interferometers connected to the same laser

determined if the total phase advance ratio can be measured.

4.2 Phase ratio measurement algorithm

Section 4.1 shows that the ratio of the lengths of two Fizzeau interferometers is equal to the ratio of the phase advanced during a laser frequency scan. If one of the interferometers has a well known length (referred to as the reference interferometer r), the other interferometer has an unknown length (referred to as the measurement interferometer m) and $\phi_{r,m}$ can be measured, the length of the measurement interferometer can be determined. To determine $\phi_{r,m}$ the data from both interferometers has to be filtered to clean the signal (section 4.2.1). We then extract the phase from the reference interferometer $\phi_r(t)$ (section 4.2.2), which can be used to express the measurement interferometer phase $\phi_m(t)$:

$$\phi_m(t) = \frac{l_m}{l_r}\phi_r(t). \tag{4.13}$$

The intensity of the measurement interferometer is of the form:

$$I_m(t) = I_m(0) + A_m \cos(\phi_m(t)) = I_m(0) + A_m \cos(\frac{l_m}{l_r}\phi_r(t)). \tag{4.14}$$

Plotting I_m vs ϕ_r will give a periodic function with a phase frequency of:

$$\nu_\phi = \frac{l_m}{l_r}\frac{1}{2\pi}. \tag{4.15}$$

This implies that if ν_ϕ is measured, l_m can be determined by knowing l_r. Note that if the measurement interferometer is also the reference interferometer then $\nu_\phi = \frac{1}{2\pi}$.

4.2.1 Data filtering

The first stage of the analysis is to filter the data in frequency space. A band pass butterworth filter [35] is used to isolate the required frequencies of the spectrum. A Butterworth filter is used as its frequency response is maximally flat in the passband and rolls towards zero in the stopband. The equation for the band pass butterworth filter is:

$$\frac{\mathrm{M}^2}{\left(\left(\frac{\omega}{\omega_h}\right)^{-2n_h}+1\right)\left(\left(\frac{\omega}{\omega_l}\right)^{2n_l}+1\right)} \tag{4.16}$$

Where M is the magnitude of the filter, n_h is the high pass order, n_l is the low pass order, ω is the frequency, ω_h is the high pass cut off frequency and ω_l is the low pass cut off frequency. The effect of a filter of order 10 is shown in figure 4.3. The values of ω_h and ω_l are based on the expected length of the measurement interferometer. The value of $M = 1$ and $n_h = n_l = 10$ are used throughout this thesis unless otherwise stated.

The filter has the effect of removing back ground noise along with signals from any multiply reflected paths and any interferometric signals caused by reflections in the fibre connections between the laser, interferometer and detector.

4.2.2 Reference interferometer phase extraction

The next stage in the analysis is to extract the phase of the reference interferometer. The phase is extracted using a modified Carré algorithm followed by a phase unwrapping proce-

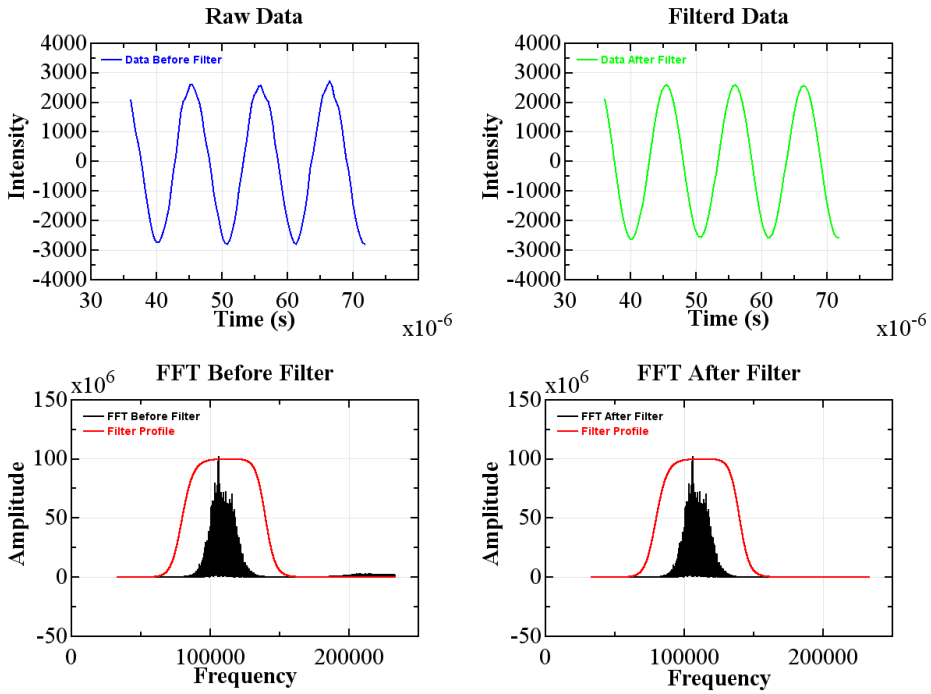

Figure 4.3: Data from a reference interferometer before and after filtering with the spectrum before and after filtering also shown.

dure. The Carré algorithm was first described in [36], with modifications to it described in [37]. The implementation used by the analysis in this thesis is a Java version of the software developed in [13]. The phase output by the Carré algorithm is the wrapped phase (phase values between 0 and 2π). The output wrapped phase is unwrapped using an algorithm described in [13]; the unwrapped phase is a monotonic function (see figure 4.4 top). In figure 4.4 1% of the phase extracted from the reference interferometer, ϕ_r, is shown. From equation 4.10 it can be seen that the $\phi_r \propto \nu$ and so figure 4.4 top is proportional to the tuning curve of the laser. The tuning curve is approximately linear with time, but with small deviations as shown in figure 4.4 bottom. In fact the entire tuning curve is hyperbolic, as the lasers are designed to tune linearly in wavelength not frequency, as shown in figure 4.5. The deviations from the straight line shown in figure 4.4 and the hyperbolic nature shown in figure 4.5 lead to the broadending of the spectral peak shown in figure 4.3.

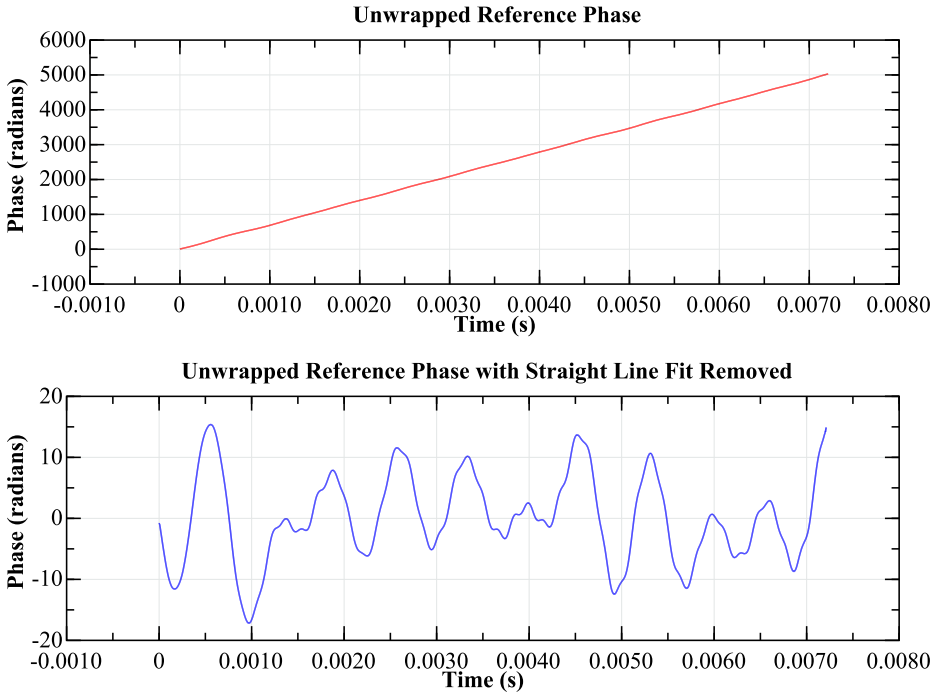

Figure 4.4: Top: 1% of the extracted phase of a LiCAS Reference Interferometer. Bottom: Top with straight line fit removed.

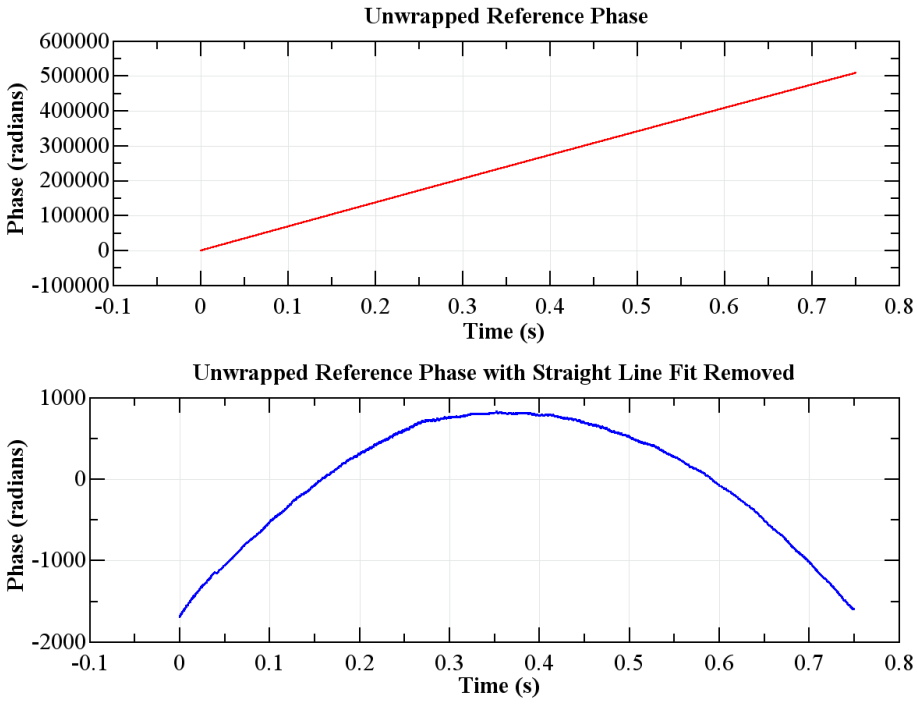

Figure 4.5: Top: Total extracted phase of a LiCAS reference interferometer. Bottom: Top with straight line fit removed.

4.2.3 Spectral analysis

Spectral analysis is used to determine ν_ϕ from equation 4.15. Since ν_ϕ is the frequency with respect to the reference interferometer phase and the data is not evenly sampled with respect to ϕ_r, a standard Fast Fourier Transform (FFT) cannot be used in the reference phase domain. A spectral analysis method which can work on unequally spaced data is required. To do this a Lomb periodogram [38] is used. The Lomb periodogram uses least-squares frequency analysis to determine the spectral power at certain frequencies. The procedure described in [38] is regarded as "slow" requiring 10^2N^2 operations to analyse N data points [39]. Instead of using the method described in [38] a fast method described in [39] and [40] is used. The methods described in [39] and [40] are modified as described in [13] for use in FSI analysis. A Java version of the fast Lomb periodogram described in [13] is used throughout the analysis in this thesis. Figure 4.6 shows an example of the Lomb spectrum produced by a LiCAS reference interferometer. The data input into the Lomb periodogram is the extracted reference phase and the measurement interferometer intensity as a function of time, the expected length ratio $\frac{l_m}{l_r}$, the frequency step parameter and the MACC parameter. The frequency step parameter sets the frequency resolution of the output Lomb periodogram. The MACC value is the number of interpolation points per 1/4 cycle of highest frequency [39] and is proportional to the number of elements in the two FFT's used by the algorithm; the effect of varying these parameters is discussed in chapter 6.

4.2.4 Peak locating and length determination

The Lomb periodogram used in the spectral analysis produces a spectrum which has a number of peaks. Peaks are identified by finding three or more consecutive phase frequencies which are at least 5σ above the mean spectral level. All of the peaks located are fitted with a Marquardt non-linear least square fitting technique [13]. The fitted function is a Gaussian, and the peak height, width and mean position ν_ϕ are determined. With the mean position

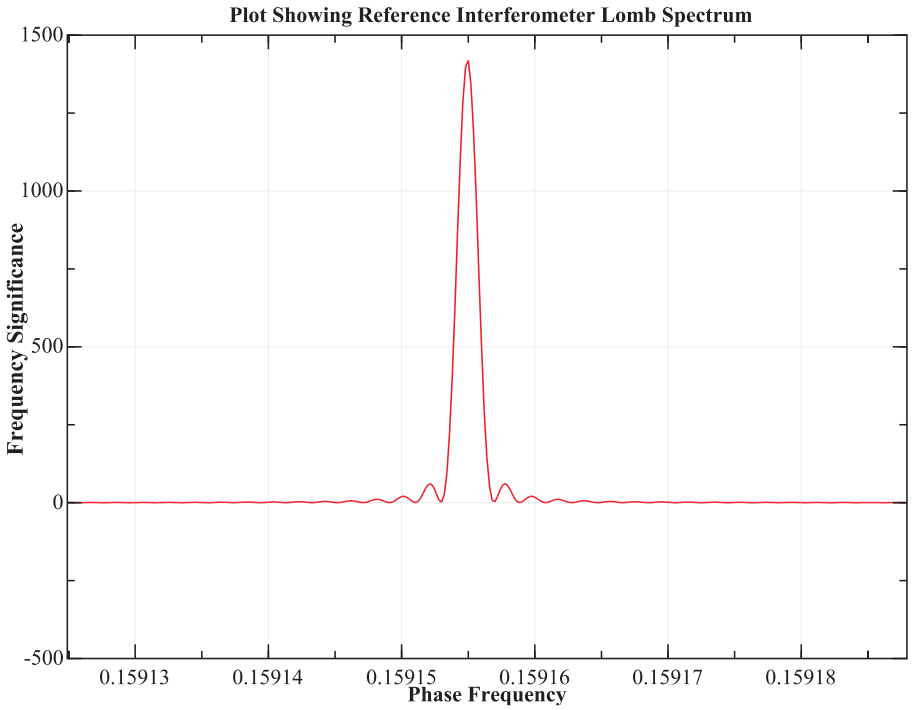

Figure 4.6: The Lomb spectrum for one of the LiCAS reference interferometers.

for each peak determined the length corresponding to that position can be calculated by:

$$l_m = \nu_\phi \times 2\pi \times l_r. \tag{4.17}$$

The above process generates a number of possible lengths for the measurement interferometer. The length which corresponds to the peak with the largest peak height is the length l_m. The analysis in this thesis is a Java implementation of this method described in [13].

4.3 Atmospheric length corrections

Section 4.1 describes how the lengths are determined if the interferometers are in a vacuum, where the refractive index is one. When the measurement interferometers are in air, a correction is required because the refractive index in air causes a lower speed of light and the measured lengths appears longer. Note that dispersion in air at 1550nm is small enough to be neglected in the method described in this chapter. To correct the length the refractive

index of air, n, has to be calculated and this can be done by using the Ciddor equations [41]. The Ciddor equations are developed from the Edlén equations [42],[43] and [44]. The calculated refractive index, n, can be used to correct the measured length using:

$$l_{m,c} = \frac{l_m}{n}. \tag{4.18}$$

The Ciddor equations require the laser wavelength, air temperature (^{o}C), the relative humidity (%RH) and air pressure (Pa) to be input. The CO2 content is always taken as that of standard air (450ppm). The largest distance to which the corrections are applied is 2m, during the reference interferometer length calibration. Assuming all other factors to be measured perfectly, then, if the temperature is measured to $\pm 0.1^o$C a correction error of 0.2μm is caused; if pressure is measured to ± 0.05 Pa a correction error of 0.2μm is caused; if relative humidity is measured to ± 10 %RH a correction error of 0.2μm is caused. These errors combine quadraticially to give an error of 0.35μm.

Chapter 5

Reference Interferometer

For the LiCAS RTRS FSI system to measure unknown lengths, a reference interferometer is required (see section 4.1). The design, calibration and performance of the LiCAS reference interferometers are discussed in this chapter.

5.1 Design

The LiCAS reference interferometers are evacuated folded path Fizzeau interferometers with a optical path length (referred to as length) of approximately 6m. The design of the reference interferometer is shown in figure 5.1 and a photo of the interferometer under construction shown in figure 5.2. The reference interferometers contain one internal FSI line (section 2.2.2), three mirrors, mounted on what are referred to as the launch and mirror end plate, and 15 PT100 temperature sensors (section 2.2.2).

The LiCAS reference interferometers are designed to meet the following design specifications: Low thermal expansion, zero dispersion, high long term stability and high thermal stability when in operation. This will enable accurate determination of the reference interferometers' lengths.

The internal FSI line and mirror number two, are mounted on the launch end plate;

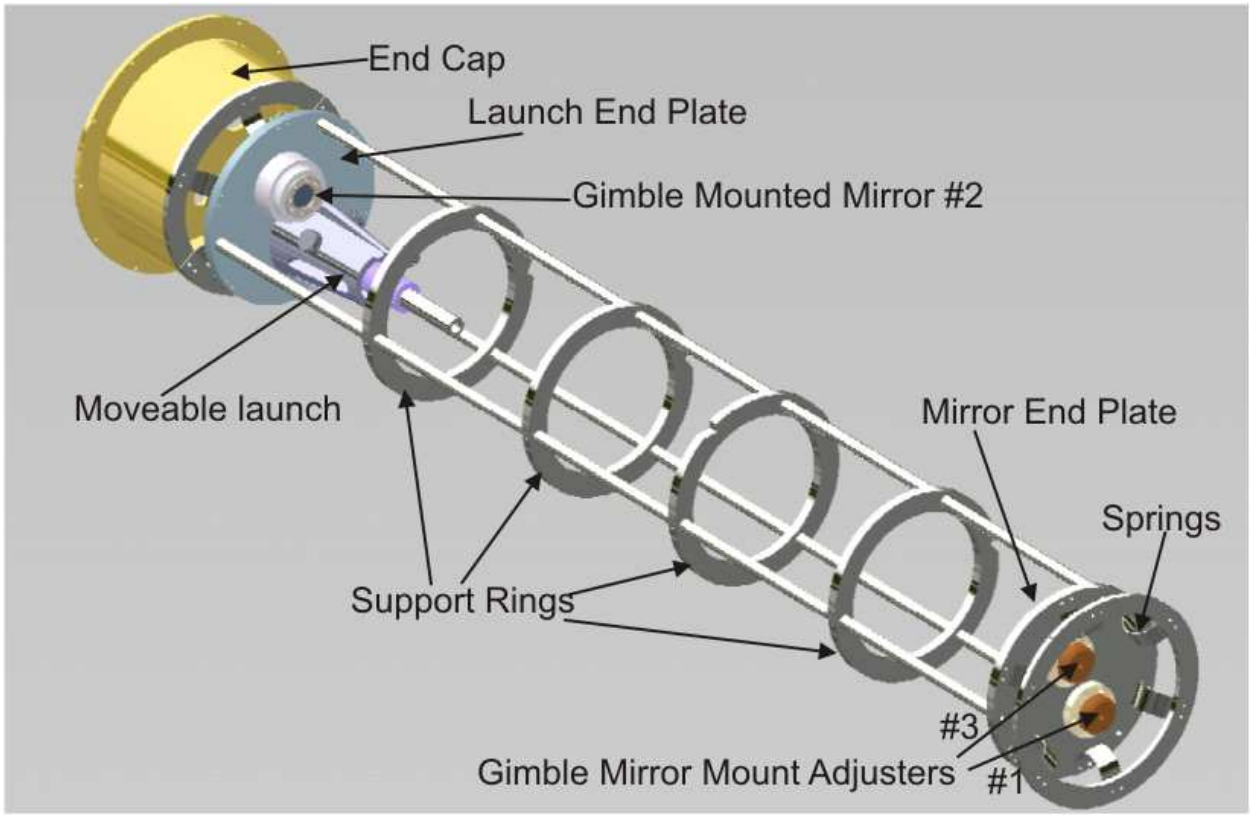

Figure 5.1: CAD design of the reference interferometer. Vacuum chamber, FSI line, temperature sensors, temperature sensor cables and feed through omitted.

mirrors number one and three are mounted on the mirror end plate. The end plates are held apart by three bars, with the bar's supported by four support rings; the bars support rings and end plates are all machined from Invar 36. The internal FSI line is aligned so that the laser beam hits the centre of the first mirror; the first mirror is aligned so that the reflected laser hits the centre of the second mirror; the second mirror is aligned so that the reflected laser hits the centre of the third mirror; the third mirror is aligned so that the laser beam is reflected back along the path it has come from and couples back down the internal FSI line.

The mirrors are circular and not mounted directly to the end plates; they are held within gimble mounts, which are fixed to the end plates as shown in figure 5.3. The gimble mounts have a socket made of aluminium and a half sphere made of phosphor bronze. The mirrors are fixed such that the centre of the mirrors are in the centre of the phosphor bronze sphere, thereby enabling the mirrors to be rotated but with the centre remaining at a fixed position. Phosphor bronze is used as it will not jam with the aluminium. The internal FSI line

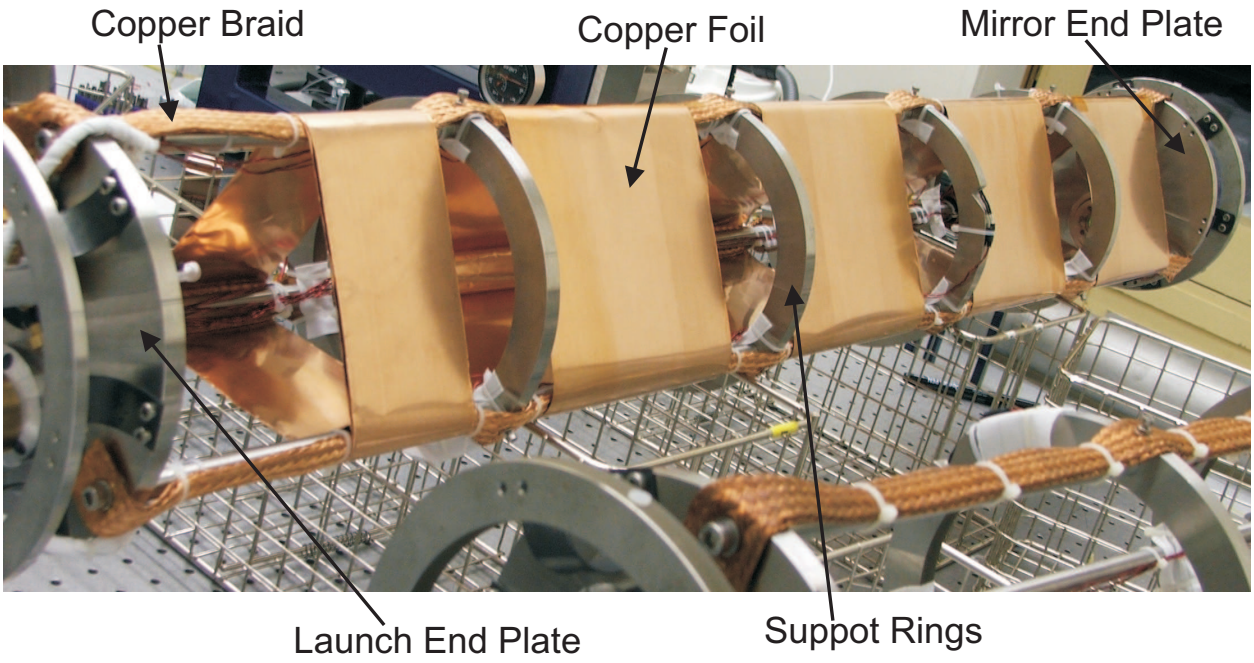

Figure 5.2: Photo of the reference interferometer under construction. The copper sheets and braid are not part of the initial design but added to increase thermal stabilisation.

is mounted in an adjustable aluminium launch tube. The launch tube is mounted in an aluminium holder on the launch end plate which allows the launch tube to be moved in and out of the interferometer, as shown in figure 5.3.

The temperature of the interferometer is measured by 15 PT100 temperature sensors; a temperature sensor is placed on each of the gimble mounts, the end plates, the launch tube and each of the support rings; the remaining sensors are placed on the connection bars between the support rings.

To give the interferometer low thermal expansion, the end plates and the bars connecting them are made of Invar 36 which has a coefficient of thermal expansion (CTE) of 1.6ppm. This is, however, not the CTE of the interferometer. If the interferometer heats up, the Invar bars will expand, causing the surface of the launch and end plates to move apart. If the mirrors and launch optics were connected directly to the inner surfaces of the plates, the length would increase with the Invar 36 CTE, however, they are mounted in aluminium which is connected to the plates. When the Invar bars expand, making the length longer, the aluminium expands making the length smaller. The launch tube which contains the FSI optics can be moved to vary the amount of aluminium inside the interferometer and,

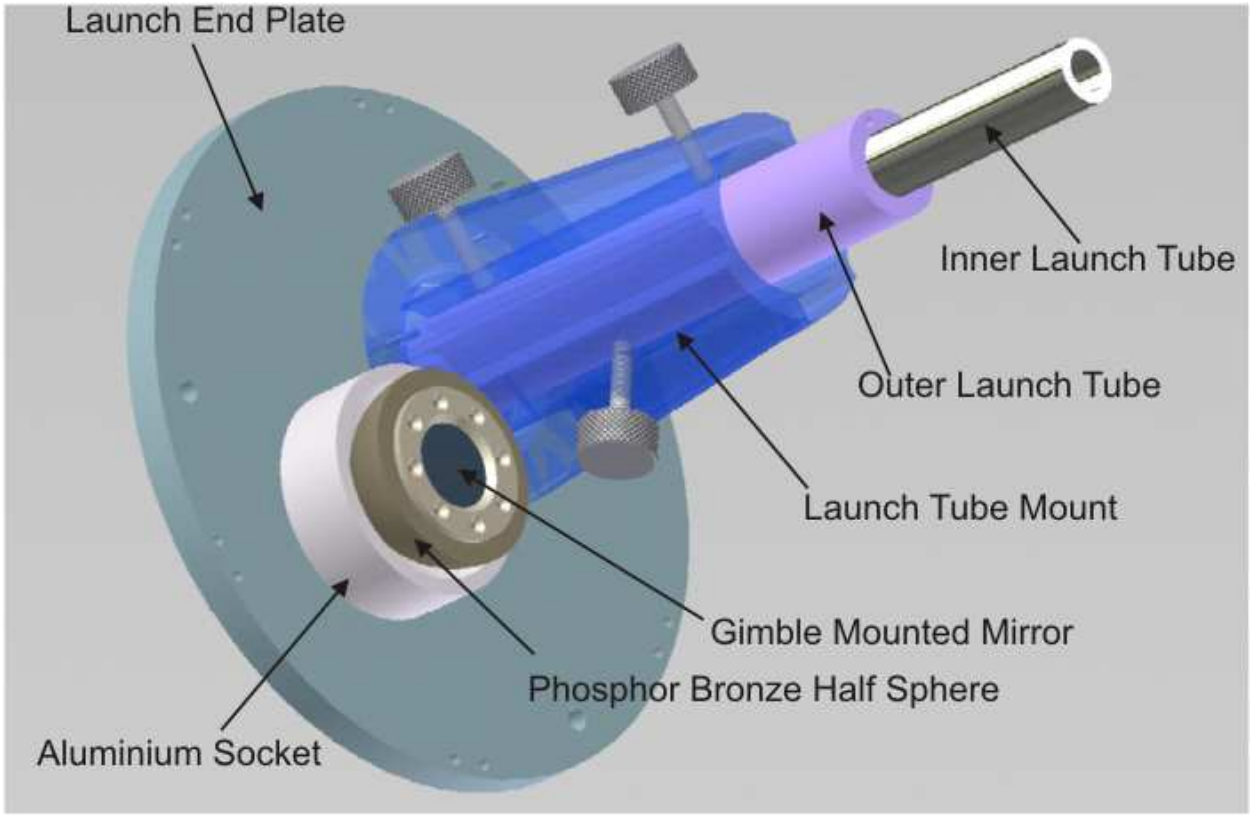

Figure 5.3: Figure showing the adjustable launch tube and gimble mounted mirror for the reference interferometers

therefore, the thermal expansion of the interferometer can be minimised.

The interferometers require zero optical dispersion and to achieve this, the interferometers are operated in a vacuum. The interferometers are placed within vacuum tubes, with the temperature sensor cables and optical fibres passing through vacuum feed throughs in the reference interferometer end cap (see figure 5.4). The fibre feed throughs are described in chapter 2. There are two temperature sensor feed throughs: a Lemo 36 way connector and a Fischer 24 way connector. The vacuum flange is connected to the end cap and the end cap is bolted to the vacuum tube with an O-ring seal to maintain the vacuum.

To maintain the mechanical stability of the reference interferometer's length, the mirrors are gimble mounted; this ensures that, as long as the laser is aligned to hit the middle of the mirrors, any movement of the mirror's rotation will minimally change the interferometer length. The end plates are also connected to spring's (see figure 5.1); the interferometer springs press against the end cap and the bottom of the interferometer tube. The springs

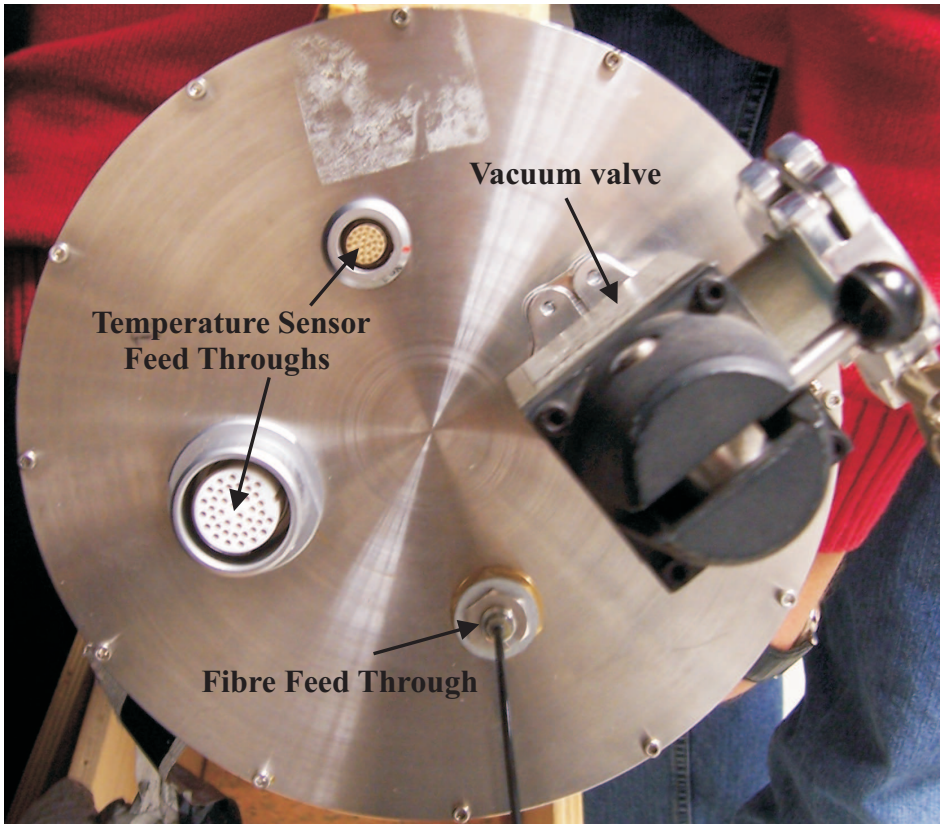

Figure 5.4: Photo of the reference interferometer end cap

primary purpose is to fix the interferometer into positions, to ensure that it does not rattle around; they also stop the thermal expansion of the vacuum tube compressing the interferometer.

To stop thermal gradients forming from one end of the interferometer to the other, the connection bars have copper braid running along them. Copper foil is wrapped around the interferometer to increase thermal conductivity as shown in figure 5.2. To stop rapid thermal changes outside the interferometer affecting the thermal stability, the outside of the vacuum tube is insulated with insulation foam (see figure 5.5) and then placed within a sleeping bag. Note that the insulation foam was only attached after thermal calibration was completed (see section 5.5.1).

Figure 5.5: Photo of an insulated reference interferometer

5.2 Laser tracker measurements for reference interferometer length calibration

During the length calibration of the reference interferometers, a laser tracker is used to measure the position of a retro reflector. Here it will be explained how the laser tracker was used and what the expected accuracies are. The laser tracker used is a Leica LTD 800. It is operated in two different modes during the calibration; single layer mode and double layer mode. In Single layer mode the laser tracker takes one reading on the position (distance, azimuth and zenith) of the retro reflector which gives a 3D measurement error of approximately $16\mu m$[1]. In double layer mode the laser tracker takes one measurement on the markers position (as above), the laser tracker head then rotates 180^0 in the azimuth and zenith directions, so that it is pointing at the marker again and repeats the measurement. This gives a measurement resulting in a error of approximately $3\mu m$[2] as the systematic errors in the angle encoders are cancelled. The double layer measurements are more accurate than the single layer but takes more time and requires that the retro reflector is stationary during the measurement. The laser tracker also measures the air temperature, pressure and humidity during operation; it uses these atmospheric measurements to correct its distance measurements.

[1]Error from experienced DESY operators[45]
[2]Error from repeated measurement test

5.3 FSI measurement

An FSI system measurement consists of taking data with both reference interferometers and all selected measurement interferometers. When the reference interferometers take data all of their temperatures sensors also take data. The temperature of a reference interferometer is taken as the average of all of the temperature sensors in the interferometer. The interferometers were in thermal equilibrium when the RMS of the temperature sensors was less than 0.05 K

5.4 Reference interferometer length calibration

5.4.1 Length calibration experiment

The reference interferometer's length (L_{ref}) needs to be known to the sub-micron level. A sub-micron reference length error is required to allow micron level measurement interferometer errors. To determine L_{ref}, a motion stage with two retro reflectors mounted back to back is used. One retro reflector is monitored by a collimated FSI line; the other is monitored by a laser tracker as shown in figure 5.6. The collimated FSI line is set up as collinear as possible with the motion of the stage; this is achieved by adjusting the FSI launch so that the power returned is maximised at both the start and end of the stage. The laser tracker is also set-up to be collinear with the stage motion, which reduces the influence of the angle measurement and minimises laser tracker measurement errors. The motion stage is moved to a series of positions: at each position the FSI system measures the ratio of the the stage interferometer length (L_{stage}) to the reference interferometer length (L_{ref}); note that the length ratio is equal to the phase ratio as described in section 4.1. The laser tracker measures the three dimensional co-ordinate of the retro reflector, which is used to calculate ΔL, the displacement of the stage with respect to the initial stage position ($L_{initial}$).

Because the stage neither moves in a perfectly straight line, nor are the FSI and laser tracker measurements perfectly collinear, the change in distance measured by FSI and the

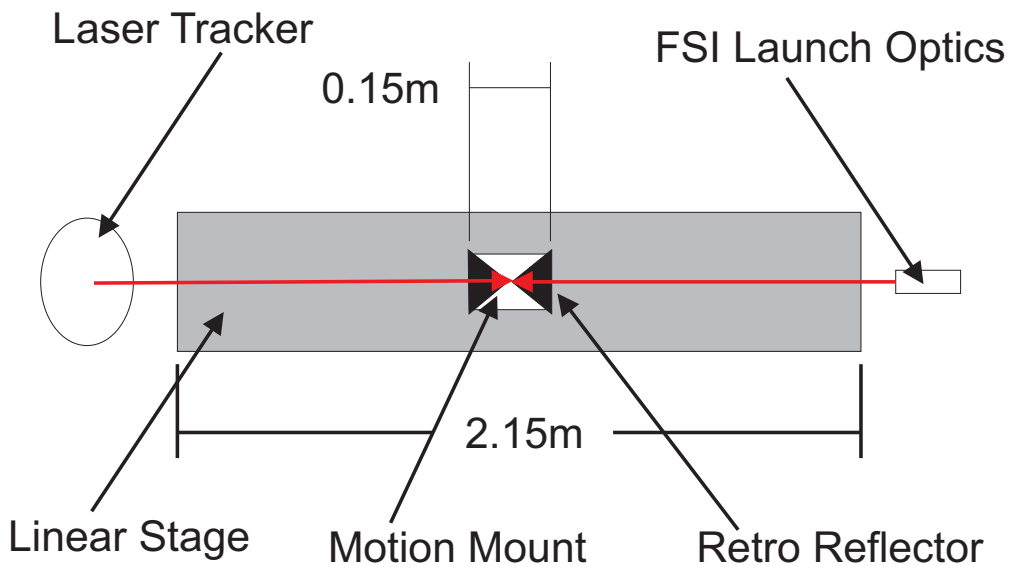

Figure 5.6: Diagram of the length calibration experimental set-up

laser tracker can be different, as shown in figure 5.7. The FSI system measures the distance to the retro reflector at each position giving a length difference of:

$$\Delta L_{FSI} = L_2 - L_1 \tag{5.1}$$

The laser tracker determines the distance moved from the first measured point to the current measurement point:

$$\Delta L = \sqrt{L_2^2 + L_1^2 - 2L_2L_1\cos\theta} \tag{5.2}$$

This leads to an error if θ is large. As it is a cosine error, a sufficiently small θ leads to a negligible error.

Figure 5.8 shows vertical and horizontal movements of the stage, as measured by the laser tracker with respect to the distance travelled along the stage, along with the residuals to straight line fits. Note that the motion mount was moved from one end of the stage to the other, and then back again. From figure 5.8 the most significant deviation from the straight line is in the vertical plane; the stage is bowed in the middle. From figure 5.8 the largest offset in the vertical plane is approximately 0.9mm, which is in the middle of the stage. As the stage FSI line is aligned to the start and end of the stage to significantly better than 0.9mm, the stage bending is the dominant source of deviation from $\theta = 0$. Since the smallest

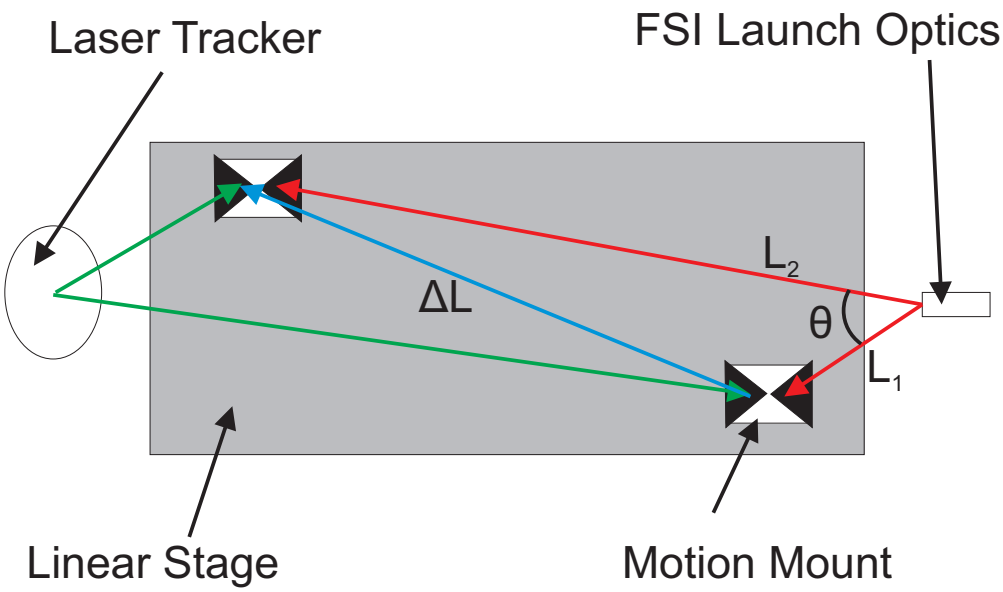

Figure 5.7: Diagram showing measurements made during calibration experiment. The laser tracker measures ΔL and the FSI measures $L2 - L1$

distance measured by the FSI is 0.03m, and the middle of the stage is at approximately 0.75m, the angle θ will be 1.3 milli radians leading to a maximum discrepancy ($\Delta L - \Delta L_{fsi}$) error of 25nm. The discrepancy is small enough to be neglected in the following analysis.

The length ratio measured at each position by the FSI is expressed by equation 5.3 and can be rearranged to give equation 5.4.

$$L_{ratio,i} = \Phi_{ref,stage,i} = \frac{L_{stage,i}}{L_{ref}} = \frac{L_{StageInitial} + \Delta L_i}{L_{ref}}. \tag{5.3}$$

$$\Delta L_i = \Phi_{ref,stage,i} L_{ref} - L_{StageInitial}. \tag{5.4}$$

Where: $\Phi_{ref,stage} = \Delta\Phi_{stage}/\Delta\Phi_{ref}$ is the phase advance ratio between the stage and measurement interferometers.

The stage interferometer operates in open air and so requires atmospheric corrections as shown in section 5.6.2. The length of the reference interferometer is temperature dependent, therefore, when the reference interferometers components are in thermal equilibrium, and using only linear expansion coefficients, the lengths can be re-written as:

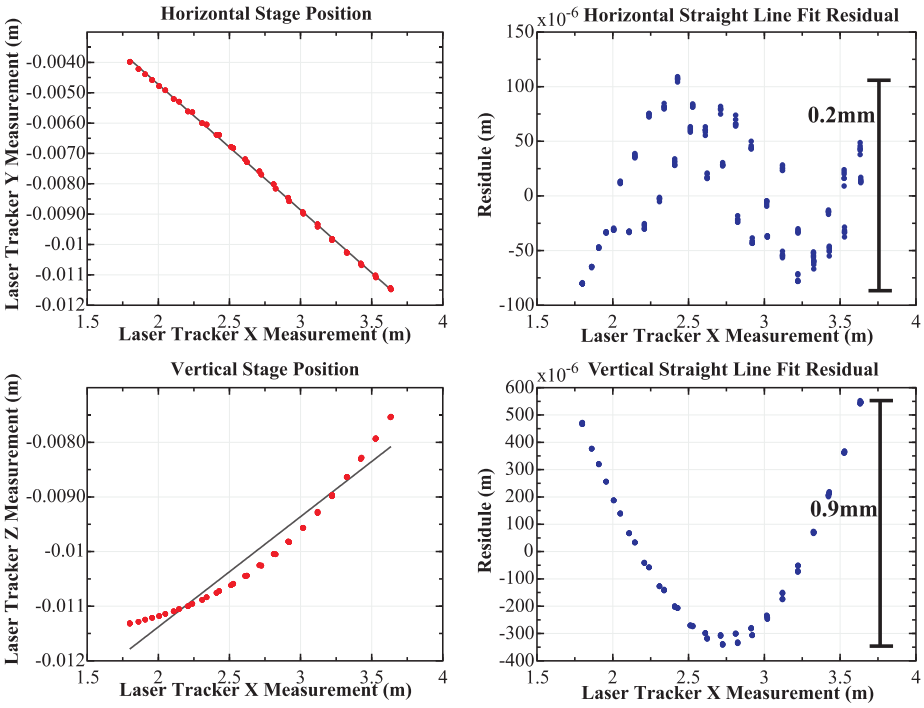

Figure 5.8: The movement of the linear stage as measured by the laser tracker fitted with a straight line with the residues shown

$$L_{ref} = L_{ref}(T_{ref,i}) = L_{ref}(T^0_{ref}) + RTE_{ref} \times (T_{ref,i} - T^0_{ref}). \tag{5.5}$$

Where:

T^0_{ref} is the temperature at which the interferometer is calibrated.

$T_{ref,i}$ is the measured temperature of the interferometer.

$L_{ref}(T_{ref,i})$ is the length of the interferometer at temperature $T_{ref,i}$.

$L_{ref}(T^0_{ref})$ is the length of the interferometer at the calibration temperature.

RTE_{ref} is the relative thermal expansion of the interferometer given in mK^{-1}. The RTE is determined by the thermal calibration experiment in section 5.5.1.

There are two reference interferometers which require calibrating. The experiment was set up such that both reference interferometers and the stage interferometer took data simultaneously. The interferometers in the equations are referred to by the numbers shown in table 5.1. If the data is taken simultaneously, the following three equations describe the measurements for a single position.

Number	Interferometer
1	Reference Interferometer 1
2	Reference Interferometer 2
3	Stage Interferometer

Table 5.1: Length Calibration Interferometer Numbers

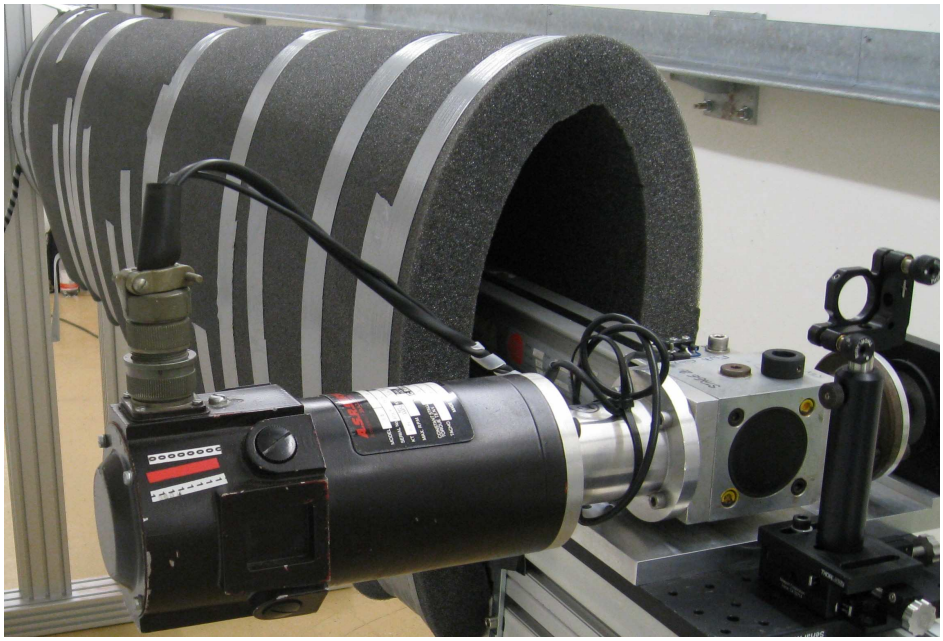

Figure 5.9: A photo of the covered stage used for FSI length calibration experiment

$$0 = \Delta L + \Phi_{1,3} \times (L_1(T_1^0) + RTE_1 \times (T_1 - T_1^0)) - L_{StageInitial} \tag{5.6}$$

$$0 = \Delta L + \Phi_{2,3} \times (L_2(T_2^0) + RTE_2 \times (T_2 - T_2^0)) - L_{StageInitial} \tag{5.7}$$

$$0 = \frac{L_1(T_1)}{L_2(T_2)} - \Phi_{2,1} = \frac{(L_1(T_1^0) + RTE_1 \times (T_1 - T_1^0))}{(L_2(T_2^0) + RTE_2 \times (T_2 - T_2^0))} - \Phi_{2,1} \tag{5.8}$$

Two length measurement experiments were performed. Length calibration experiment 1 had data taken at fourteen different stage positions; at each stage position one single layer laser tracker measurement and five FSI measurements were taken. The average and standard deviation of each set of FSI measurements was determined at each stage position. This first experiment was used as a test of the technique, hence the low number of data points and low statistics. The error assigned to the laser tracker measurements is described in section 5.2.

Length calibration experiment 2 had data taken at thirty nine different stage positions. At

each stage position a set of six double layer laser tracker and a set of five FSI measurements were taken. For each of the sets taken at any stage position, the average and standard deviation is determined. The average laser tracker measurement is used to determine ΔL with the standard deviation taken as the error. During data taking for length calibration experiment 2, the stage was covered with a thick sheet of insulating foam to stop air motion effecting the FSI and laser tracker measurements (see figure 5.9). The laser tracker errors are in agreement with those stated in section 5.2.

The stage interferometer is in open air and, therefore, the measurements require the application of atmospheric corrections as described in section 4.3. The atmospheric measurements (humidity, temperature and pressure) were taken by the laser tracker.

The length calibration experiment aims to determine the constants $L_1(T_1^0)$ and $L_2(T_2^0)$. The values for T_1^0 and T_2^0 are the average of the temperatures of the reference interferometers during the length experiment. $L_1(T_1^0)$ and $L_2(T_2^0)$ are determined by solving equations 5.6-5.8 for all the data taken during the length calibration experiment, using a non-linear least squares method as described in chapter 3.

The equations 5.6-5.8 are of the form $F(\bar{X}, \bar{L}) = 0$ and so the combined non-linear least squares method is used (see section 3.2). The measurement vector L, shown in equation 5.9, contains all the laser tracker length change measurements, reference interferometer temperature measurements and phase ratio measurements. Atmospheric measurements are applied as explained in section 5.6.2.

$$L = \begin{bmatrix} \Phi_{1,3}^1 \\ \Phi_{2,3}^1 \\ \Phi_{2,1}^1 \\ \Delta L^1 \\ T_1^1 \\ T_2^1 \\ \vdots \\ \Phi_{1,3}^n \\ \Phi_{2,3}^n \\ \Phi_{2,1}^n \\ \Delta L^n \\ T_1^n \\ T_2^n \end{bmatrix} \tag{5.9}$$

Where $\Phi_{1,3}^i$ is the average of the phase ratio measurements at stop i and T_1^i is the average of the reference interferometer temperatures at stop i. The variable vector, X, contains the reference lengths and the initial stage length:

$$X = \begin{bmatrix} L_1(T_{T_1^0}) \\ L_2(T_{T_2^0}) \\ L_{StageInitial} \end{bmatrix} \tag{5.10}$$

The prediction vector, $F(X, L)$, in the model is:

$$F(X,L) = \begin{bmatrix} \Delta L^1 + \Phi^1_{1,3} \times (L_1(T^0_1) + RTE_1 \times (T^1_1 - T^0_1)) - L_{StageInitial} \\ \Delta L^1 + \Phi^1_{2,3} \times (L_2(T^0_2) + RTE_2 \times (T^1_2 - T^0_2)) - L_{StageInitial} \\ \frac{L_1(T^1_1)}{L_2(T^1_2)} = \frac{(L_1(T^0_1)+RTE_1\times(T^1_1-T^0_1))}{(L_2(T^0_2)+RTE_2*(T^1_2-T^0_2))} - \Phi^1_{2,1} \\ \Delta L^2 + \Phi^2_{1,3} \times (L_1(T^0_1) + RTE_1 \times (T^2_1 - T^0_1)) - L_{StageInitial} \\ \Delta L^2 + \Phi^2_{2,3} \times (L_2(T^0_2) + RTE_2 \times (T^2_2 - T^0_2)) - L_{StageInitial} \\ \frac{L_1(T^2_1)}{L_2(T^2_2)} = \frac{(L_2(T^0_1)+RTE_1\times(T^2_1-T^0_1))}{(L_2(T^0_2)+RTE_2\times(T^2_2-T^0_2))} - \Phi^2_{2,1} \\ \vdots \\ \Delta L^n + \Phi^n_{1,3} \times (L_1(T^0_1) + RTE_1 \times (T^n_1 - T^0_1)) - L_{StageInitial} \\ \Delta L^n + \Phi^n_{2,3} \times (L_2(T^0_2) + RTE_2 \times (T^n_2 - T^0_2)) - L_{StageInitial} \\ \frac{L_1(T^n_1)}{L_2(T^n_2)} = \frac{(L_1(T^0_1)+RTE_1\times(T^n_1-T^0_1))}{(L_2(T^0_2)+RTE_2\times(T^{3,9}_2-T^0_2))} - \Phi^1_{2,1} \end{bmatrix} \tag{5.11}$$

The design matrices A and B are then defined as $A = \frac{\delta F(X,L)}{\delta X}$ and $B = \frac{\delta F(X,L)}{\delta L}$. The covariance matrix P contains the standard deviations of the averages used in the L vector; the covariance matrix is a diagonal matrix with off axis elements being zero, assuming no correlation between measurements. The model was solved to determine the calibration constants $L_1(T^0_1)$ and $L_2(T^0_2)$. The errors on the parameters are computed using the non-linear model.

5.4.2 Length calibration data

The data used to determine the reference interferometer lengths is described in this section. Figures 5.10(a) and 5.10(b) shows $\Phi^i_{1,3}$ and $\Phi^i_{2,3}$ plotted against ΔL^i for length calibration experiment 1 and 2. The error bars in both figures are multiplied by 100000, and the ranges the figures cover are similar. The larger error bars in figure 5.10(a) are due to the experimental set-up of length calibration experiment 1 using only single layer measurements, and the stage not being covered, leading to movements in the air reducing the precision of the stage FSI and laser tracker measurements.

The thermal stability of the reference interferometers during the experiments will now be discussed. Figures 5.11(a) and 5.11(b) show $\Phi^i_{2,1}$ plotted against index and figures 5.12(a) and 5.12(b) show T^i_1 and T^i_2 plotted against index for length calibration experiments 1 and 2. T^i_1 and T^i_2 is the average of the temperatures measured by all the temperature sensors in a particular reference interferometer. Figure 5.12(a) shows that the temperatures of the reference interferometers change by less than 0.02^oC during length calibration experiment 1 and figures 5.12(b) shows that they change by less than 0.07^oC during length calibration experiment 2. The effect of the temperature changes can be seen from figures 5.11(a) and 5.11(b); which show that the ratio of the lengths change by less than 7.5×10^{-8} in length calibration experiment 2 and 1×10^{-8} during length calibration experiment 1. These thermal changes are small but are still taken into account in the linear algebra model by incorporating the RTE of both interferometers. The results of the length calibration is discussed in section 5.6. Note here that if the calibration constants in section 5.6 are used in conjunction with the data in figure 5.12(b) it does not explain the movement seen in figure 5.11(b), this shows that there is some internal life in the reference interferometer which will be discussed in later sections.

5.5 Reference interferometers thermal calibration

5.5.1 Thermal calibration experiment

The aim of the thermal calibration is to determine the values of RTE_1 and RTE_2. For thermal calibration both reference interferometers are required: one interferometer is held at a constant temperature while the second has its temperature varied in an environmental chamber. The interferometer with the changing temperature is the interferometer being calibrated; the other acts as the reference. The temperature of the interferometer under calibration is varied in steps of approximately 2^oC; the interferometers take approximately 24 hours to thermally stabilize. When the interferometer under calibration is at thermal equilibrium, its phase ratio with respect to the reference is measured. The phase ratio measured at each point equals the length ratio and leads to the following equation if reference

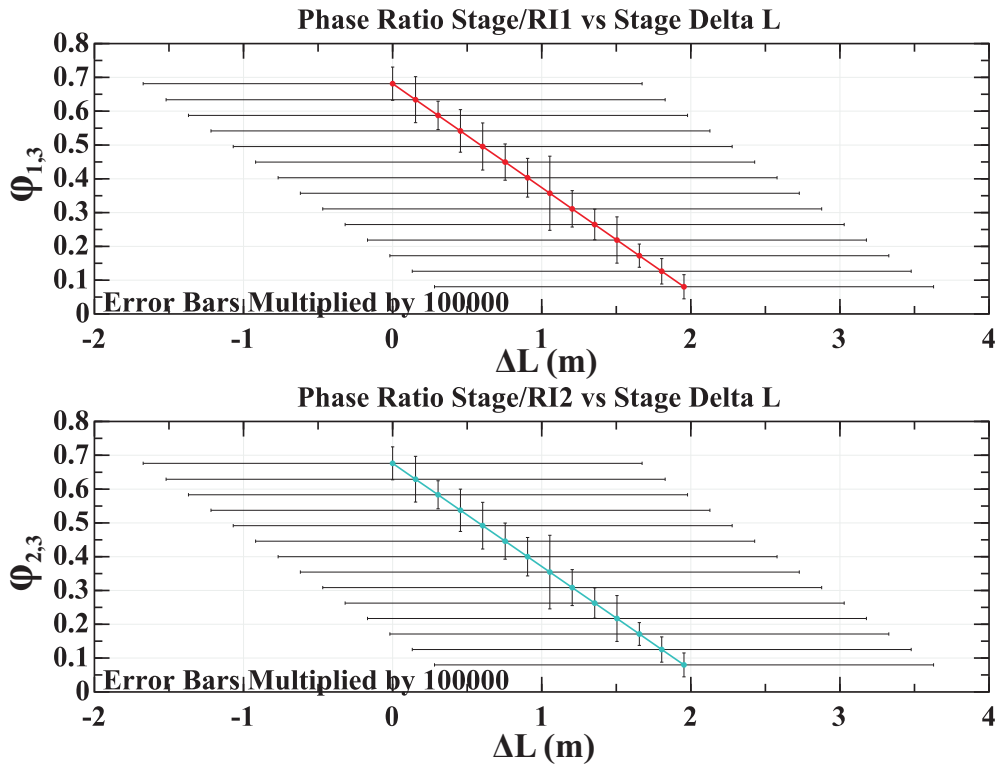

(a) Length calibration experiment 1 data

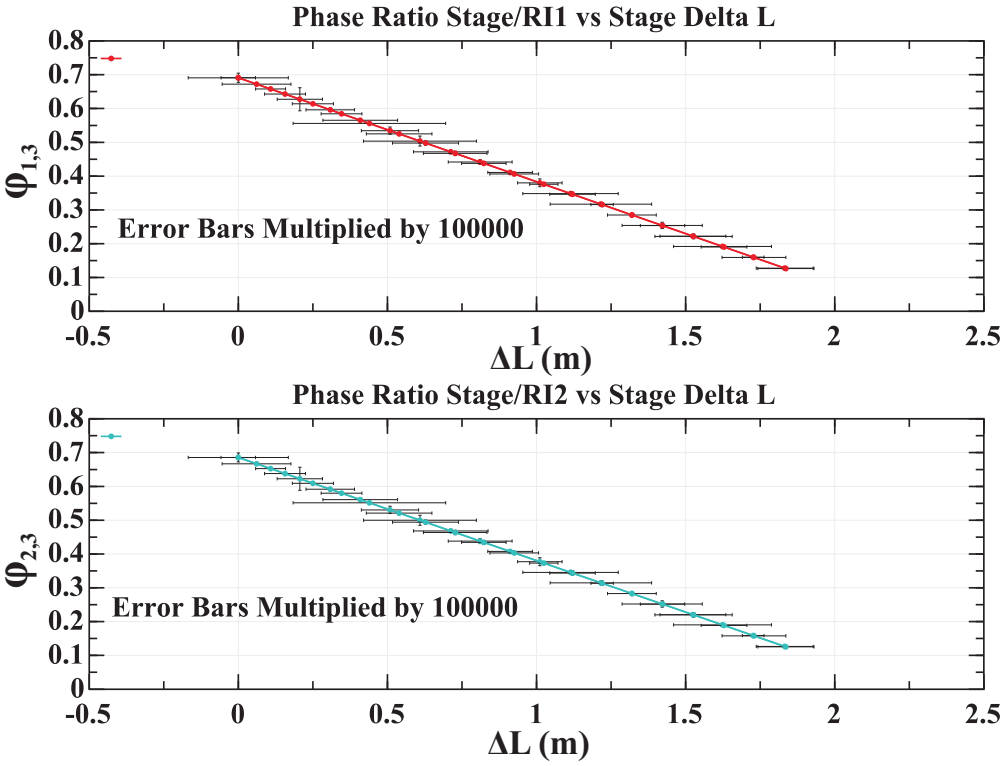

(b) Length calibration experiment 2 data

Figure 5.10: $\Phi^i_{1,3}$ and $\Phi^i_{2,3}$ against ΔL^i for length calibration experiments 1 and 2

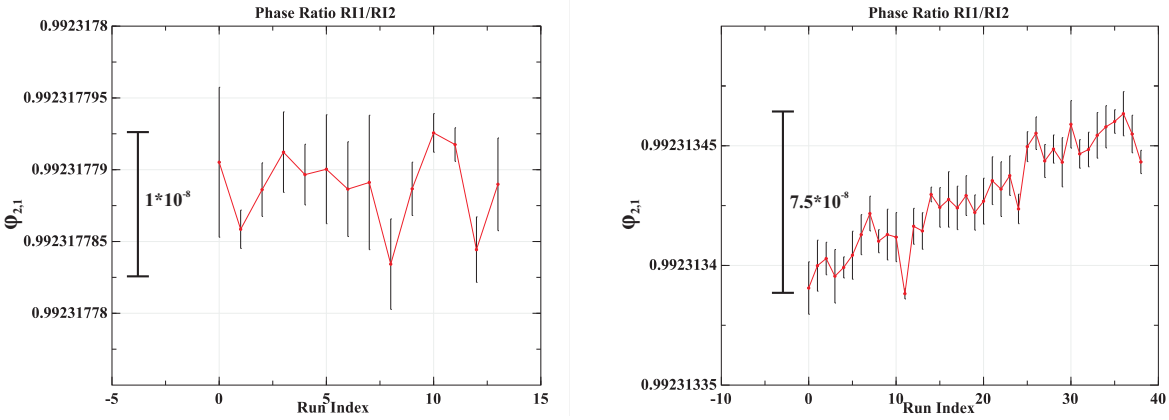

(a) Length calibration experiment 1 (b) Length calibration experiment 2

Figure 5.11: $\Phi^i_{2,1}$ vs index for length calibration experiments 1 and 2

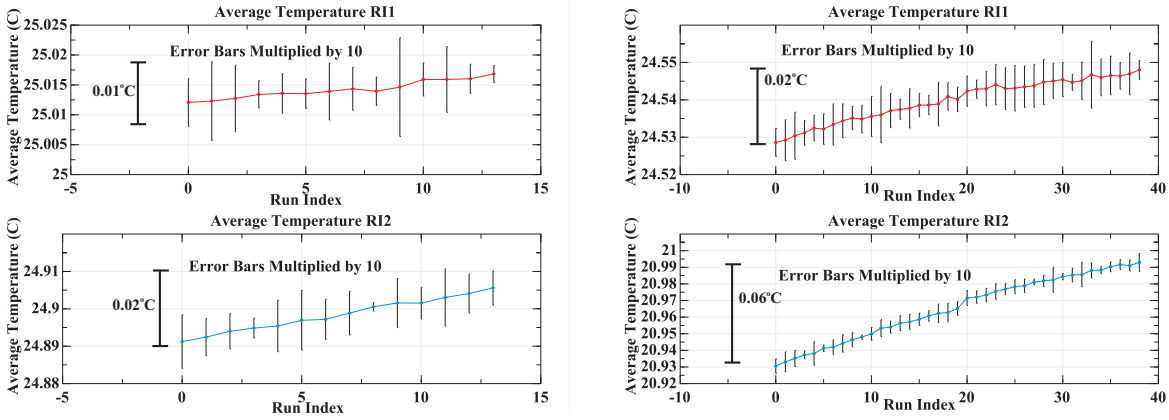

(a) Length calibration experiment 1 (b) Length calibration experiment 2

Figure 5.12: The average temperatures of reference interferometers 1 and 2 during the length calibration experiments 1 and 2

interferometer 1 is being calibrated:

$$0 = RTE_1 \times (T_1 - T_1^0)) + L_1(T_1^0) - \Phi_{2,1} \times (L_2(T_2^0) + RTE_2 \times (T_2 - T_2^0))) \tag{5.12}$$

At each temperature 50 FSI scans were taken and the temperature of both reference interferometers recorded. The average and standard deviation of the measured phase ratios and temperatures is then calculated. The measured values are used in a non-linear least squares process, as described in section 3.2, to determine RTE_1 using the combined method. The measurement vector L is:

$$L = \begin{bmatrix} \Phi^1_{2,1} \\ T^1_1 \\ T^1_2 \\ \vdots \\ \Phi^n \\ T^n_1 \\ T^n_2 \\ L_1(T^0_1) \end{bmatrix} \tag{5.13}$$

The variable vector X is:

$$X = \begin{bmatrix} RTE_1 \end{bmatrix} \tag{5.14}$$

The prediction vector, $F(X, L)$, is given by:

$$F(X,L) = \begin{bmatrix} RTE_1 \times (T^1_1 - T^0_1)) + L_1(T^0_1) - \Phi^1 \times (L_2(T^0_2) + RTE_2 \times (T^1_2 - T^0_2))) \\ RTE_1 \times (T^2_1 - T^0_1)) + L_1(T^0_1) - \Phi^2 \times (L_2(T^0_2) + RTE_2 \times (T^2_2 - T^0_2))) \\ \vdots \\ RTE_1 \times (T^n_1 - T^0_1)) + L_1(T^0_1) - \Phi^n \times (L_2(T^0_2) + RTE_2 \times (T^n_2 - T^0_2))) \end{bmatrix} \tag{5.15}$$

The design matrices A and B are then defined as $A = \frac{\delta F(X,L)}{\delta X}$ and $B = \frac{\delta F(X,L)}{\delta L}$. The covariance matrix P contains the standard deviations of the averages used in the L vector. The errors on the parameters are computed using the non-linear model.

This experiment is repeated with reference interferometer 2 under calibration and reference interferometer 1 as reference.

The analysis is run separately for the different experiments so only one RTE is varied in each experiment. The data taken in the experiment to find RTE_1 has a very weak correlation

to RTE_2 and so allowing this parameter to vary could cause instability in the non-linear least squares solution.

5.5.2 Thermal calibration data

The data used in the thermal calibration of the reference interferometers is described in this section. Figures 5.13(a) and 5.13(b) show the phase ratio measurements against the temperature of the calibrating interferometer. The time order in figures 5.13(a) and 5.13(b) is from the bottom left following the line anti clockwise. Figures 5.14(a) and 5.14(b) show the temperature of the reference interferometer during the calibration of reference interferometers 1 and 2.

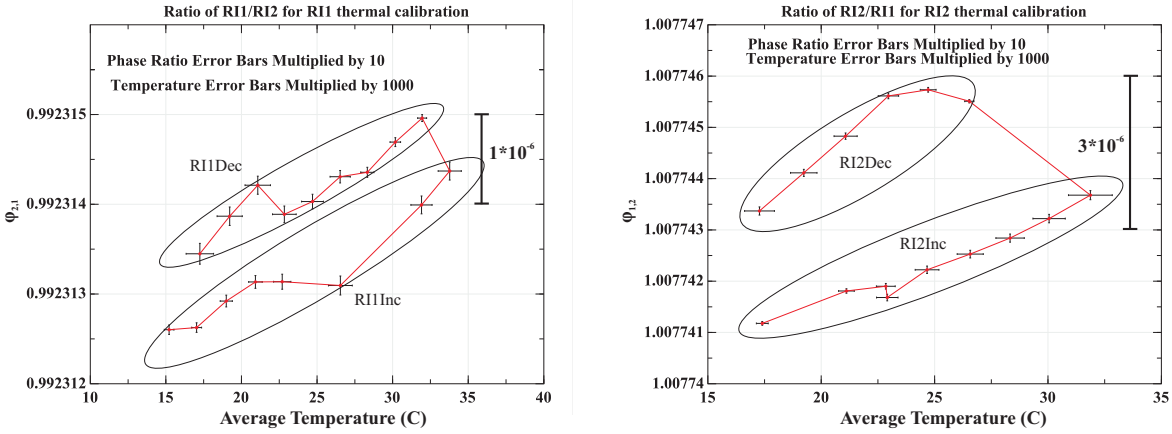

(a) Thermal calibration of reference interferometer 1 (b) Thermal calibration of reference interferometer 2

Figure 5.13: Phase ratio of reference interferometers during the thermal calibration experiments against average temperature of the reference interferometer under calibration.

In figures 5.13(a) and 5.13(b) there is a difference between the warming up data and the cooling down data. The data can be treated as separate sets in the analysis, this is because the thermal calibration experiments are only concerned with determining RTE_1 and RTE_2; so offsets in the data should only cause minimal effects. The hysteresis on the length of the reference interferometer lengths is discussed in section 5.7.

From figure 5.13(b) the cooling data appears to curve significantly, this will cause any analysis which uses this data to generate poor accuracy values for RTE_2. The values generated by this data and the cause of the problem will be discussed in later sections.

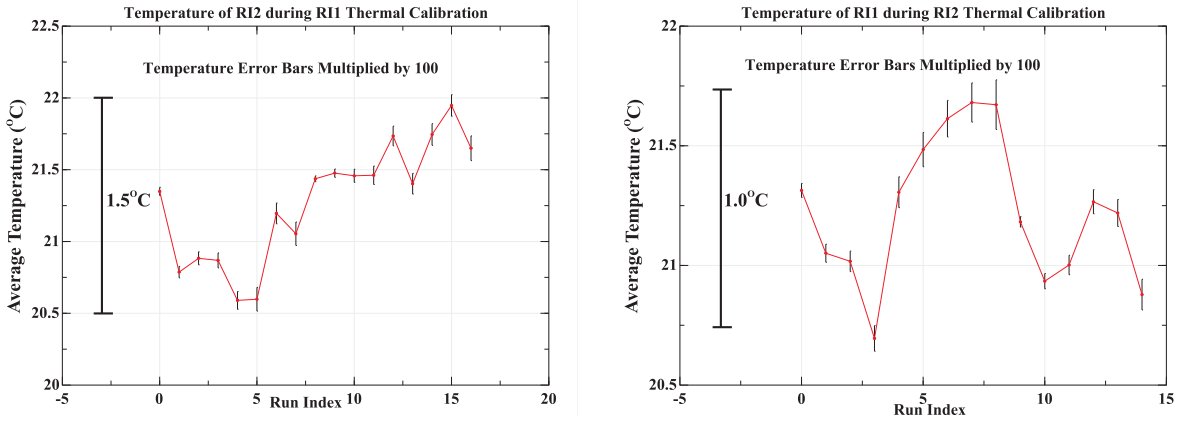

(a) Reference Interferometer 2 Temperature (b) Reference Interferometer 1 Temperature

Figure 5.14: Average temperature of the reference interferometer not under calibration during the thermal calibration experiments

5.6 Reference interferometer calibration results

5.6.1 Temperature constants

To calibrate both reference interferometers two temperature constants must first be defined for each length calibration experiment, these are $T_1^{0,I}$ and $T_2^{0,I}$ for length calibration experiment 1 and $T_1^{0,II}$ and $T_2^{0,II}$ for length calibration experiment 2; the subscripts identify which reference interferometer is being referred to. The values are defined as the average temperature of the corresponding reference interferometer during the length calibration experiment and are given in table 5.2

Length Calibration Experiment	Parameter	Value (Centigrade)	RMS (Centigrade)
1	$T_1^{0,I}$	25.01	0.001
1	$T_2^{0,I}$	24.90	0.004
2	$T_1^{0,II}$	24.54	0.006
2	$T_2^{0,II}$	20.97	0.019

Table 5.2: Values for T_1^0 and T_2^0 for length calibration experiments 1 and 2

5.6.2 Effect of atmospheric corrections on the length calibration

FSI length measurements in air require atmospheric corrections (see section 4.3). To evaluate the magnitude of these corrections the length calibration analysis was performed, using data

from length calibration experiment 2, with and without atmospheric corrections. For both calibrations, the constants in table 5.2 and $RTE_1 = RTE_2 = 0.0$ were used. The results of both calibrations are shown in table 5.3.

Parameter	With Correction	Error	Without Correction	Error	Difference
$L_1^{II}(T_1^{0,II})$	3.252174805 m	6.4×10^{-7} m	3.252088642 m	6.4×10^{-7} m	8.6×10^{-5} m
$L_2^{II}(T_2^{0,II})$	3.277366540 m	6.4×10^{-7} m	3.277279709 m	6.4×10^{-7} m	8.7×10^{-5} m
$L_{StageInitial}^{II}$	2.247227610 m	2.1×10^{-7} m	2.247227604 m	2.1×10^{-7} m	6.0×10^{-9} m

Table 5.3: Table showing the effect of atmospheric corrections on the results from length calibration experiment 2

From table 5.3 it can be seen that the atmospheric correction is an important correction as it has an effect of 86 μm on the length of the reference interferometers.

5.6.3 Determination of the reference interferometer calibration constants

The process of determining the calibration constants for the reference interferometers is iterative. A flow diagram of the process is shown in figure 5.15, the flow diagram corresponds to one length calibration experiment, one reference interferometer 1 thermal calibration experiment and one reference interferometer 2 thermal calibration experiment.

The data from the thermal calibration experiments is broken into the four time continuous sections as shown in figures 5.13(a) and 5.13(b). Breaking up the data leads to eight sets of calibration constants being determined, four for each of the length calibration experiments as shown in table 5.4. The results of the calibrations are shown in table 5.5 for length calibration experiment 1 and table 5.6 for length calibration experiment 2.

As discussed in section 5.5.2, the RI2Dec data used for RI2 RTE calibration shows a curve where a straight line is expected. The calibration constant sets α_2, α_4, β_2 and β_4 use the RI2Dec data and will therefore be excluded from further analysis (the values are shown in italics); the reason for the RI2Dec curvature will be discussed in section 5.7.

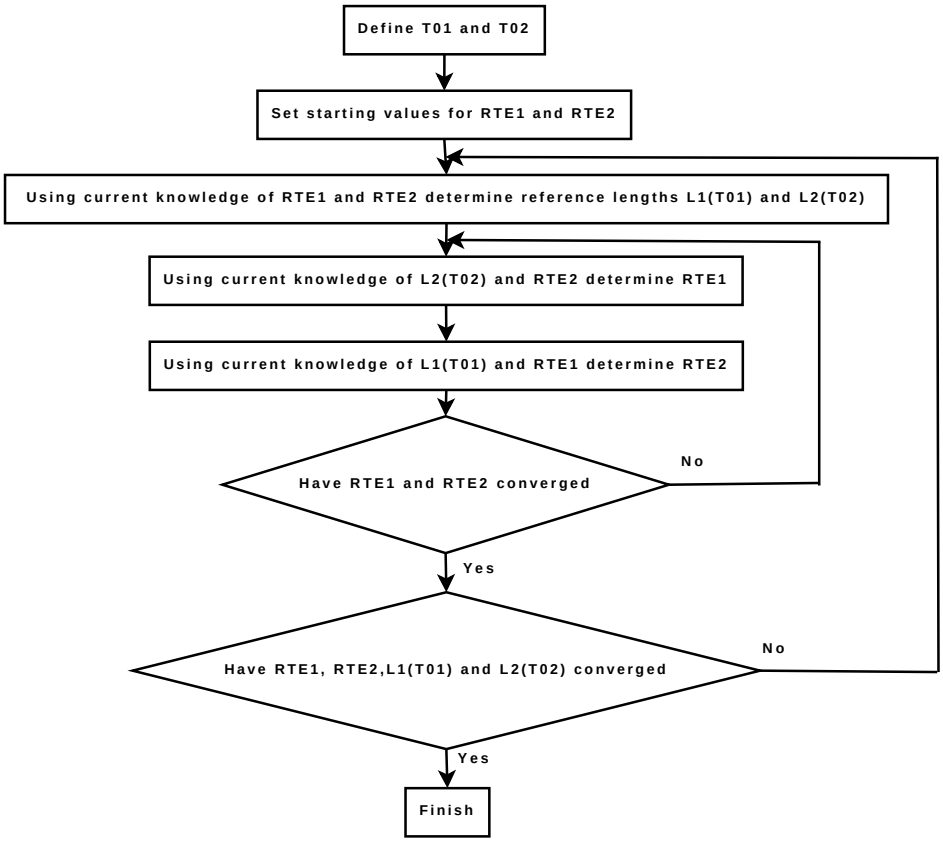

Figure 5.15: Flow diagram showing the reference interferometer calibration process

Excluding the RI2Dec data, tables 5.5 and 5.6 show a variation in RTE_1^I and RTE_1^{II} of 0.018μm/K (6% of the largest value) and in RTE_2^I and RTE_2^{II} of 0.001μm/K (0.2% of the largest value). The large variation in RTE_1 corresponds to the different data groups in figure 5.13(a), and is most likely a result of mechanical hysteresis between the warming and cooling of the interferometers.

The results in tables 5.5 and 5.6 show that the values for $L_1^I(T_1^{0,I})$, $L_1^{II}(T_1^{0,II})$, $L_2^I(T_2^{0,I})$, $L_2^{II}(T_2^{0,II})$, $L^I_{StageInitial}$ and $L^{II}_{StageInitial}$ do not vary at the nm level across the whole range of RTE values found. This is expected as each of the values for $L_1^I(T_1^{0,I})$, $L_1^{II}(T_1^{0,II})$, $L_2^I(T_2^{0,I})$, $L_2^{II}(T_2^{0,II})$, $L^I_{StageInitial}$ and $L^{II}_{StageInitial}$ use the same length calibration experiment data; therefore, as $T_1^{0,I}$, $T_1^{0,II}$, $T_2^{0,I}$ and $T_2^{0,II}$ are defined by these experiments, a change in the RTE can only have a small effect. To compare reference interferometer lengths across the different calibration sets, we need to calculate the reference interferometer lengths at the same temperature. If we use the calibration constant sets α_1 and β_1 and determine the length of reference interferometer 1 at temperature $T_1^{0,I}$ and the length of interferometer

Calibration Set	Length Calibration Experiment	RI1 Thermal Calibration Section	RI2 Thermal Calibration Section
α_1	1	RI1Inc	RI2Inc
α_2	1	RI1Inc	RI2Dec
α_3	1	RI1Dec	RI2Inc
α_4	1	RI1Dec	RI2Dec
β_1	2	RI1Inc	RI2Inc
β_2	2	RI1Inc	RI2Dec
β_3	2	RI1Dec	RI2Inc
β_4	2	RI1Dec	RI2Dec

Table 5.4: The calibration constant sets

Calibration Set Parameter	α_1 RI1Inc RI2Inc	α_2 *RI1Inc RI2Dec*	α_3 RI1Dec RI2Inc	α_4 *RI1Dec RI2Dec*
$L_1^I(T_1^{0,I})$ (m)	3.252275974 $\pm 2.41\times10^{-5}$	*3.252275974* $\pm$*2.41*$\times10^{-5}$	3.252275974 $\pm 2.41\times10^{-5}$	*3.252275974* $\pm$*2.41*$\times10^{-5}$
$L_2^I(T_2^{0,I})$ (m)	3.277454065 $\pm 2.43\times10^{-5}$	*3.277454066* $\pm$*2.43*$\times10^{-5}$	3.277454066 $\pm 2.43\times10^{-5}$	*3.277454066* $\pm$*2.43*$\times10^{-5}$
$L^I_{StageInitial}$ (m)	2.216238477 $\pm 1.02\times10^{-5}$	*2.216238477* $\pm$*1.02*$\times10^{-5}$	2.216238477 $\pm 1.02\times10^{-5}$	*2.216238477* $\pm$*1.02*$\times10^{-5}$
RTE_1^I mK^{-1}	2.798×10^{-7} $\pm 1.5\times10^{-9}$	*2.787*$\times10^{-7}$ $\pm$*1.5*$\times10^{-9}$	2.963×10^{-7} $\pm 1.8\times10^{-9}$	*2.935*$\times10^{-7}$ $\pm$*1.7*$\times10^{-9}$
RTE_2^I mK^{-1}	5.24×10^{-7} $\pm 1.5\times10^{-9}$	*6.48*$\times10^{-7}$ $\pm$*2.3*$\times10^{-9}$	5.25×10^{-7} $\pm 1.5\times10^{-9}$	*6.48*$\times10^{-7}$ $\pm$*2.3*$\times10^{-9}$

Table 5.5: Different calibration constants extracted from length calibration experiment I in combination with the four segments of the two thermal calibration experiments

2 at temperature $T_2^{0,I}$, we will get the values $L_1^I(T_1^{0,I})$, $L_1^{II}(T_1^{0,I})$, $L_2^I(T_2^{0,I})$ and $L_2^{II}(T_2^{0,I})$. It is expected that $L_1^I(T_1^{0,I})$ and $L_1^{II}(T_1^{0,I})$, and $L_2^I(T_2^{0,I})$ and $L_2^{II}(T_2^{0,I})$ would agree within errors, however, they do not. The difference between $L_1^I(T_1^{0,I})$ and $L_1^{II}(T_1^{0,I})$ is 0.1mm, and the difference between $L_2^I(T_2^{0,I})$ and $L_2^{II}(T_2^{0,I})$ is 0.087mm. Since the error on $L_1^I(T_1^{0,I})$ is 0.0241mm and on $L_2^I(T_2^{0,I})$ is 0.0243mm[3], the difference between the two length calibration experiments is significant; this problem is addressed further in section 5.7. Comparing the length calibration constants in table 5.6 and table 5.3, which uses $RTE_1 = RTE_2 = 0.0$, shows that the RTE's have an effect at the 1nm level on the determination of the values of $L_1^I(T_1^{0,I})$, $L_1^{II}(T_1^{0,II})$, $L_2^I(T_2^{0,I})$, $L_2^{II}(T_2^{0,II})$, $L^I_{StageInitial}$ and $L^{II}_{StageInitial}$.

Splitting the two length calibration experiments and the thermal calibration data into different sections has led to the discovery of inconsistencies in the data. By separating the

[3]The errors on $L_1^{II}(T_1^{0,I})$ and $L_2^{II}(T_2^{0,I})$ are much smaller and can be ignored

Calibration Set Parameter	β_1 RI1Inc RI2Inc	β_2 *RI1Inc RI2Dec*	β_3 RI1Dec RI2Inc	β_4 *RI1Dec RI2Dec*
$L_1^{II}(T_1^{0,II})$ (m)	3.252174806 $\pm 6.35\times10^{-7}$	*3.252174806* $\pm 6.35\times10^{-7}$	3.252174806 $\pm 6.35\times10^{-7}$	*3.252174806* $\pm 6.35\times10^{-7}$
$L_2^{II}(T_2^{0,II})$ (m)	3.277366541 $\pm 6.40\times10^{-7}$	*3.277366541* $\pm 6.40\times10^{-7}$	3.277366541 $\pm 6.40\times10^{-7}$	*3.277366541* $\pm 6.40\times10^{-7}$
$L_{StageInitial}^{II}$ (m)	2.247227611 $\pm 2.12\times10^{-7}$	*2.247227611* $\pm 2.12\times10^{-7}$	2.247227611 $\pm 2.12\times10^{-7}$	*2.247227611* $\pm 2.12\times10^{-7}$
RTE_1^{II} mK^{-1}	2.798×10^{-7} $\pm 1.5\times10^{-9}$	2.787×10^{-7} $\pm 1.5\times10^{-9}$	2.963×10^{-7} $\pm 1.8\times10^{-9}$	2.935×10^{-7} $\pm 1.7\times10^{-9}$
RTE_2^{II} mK^{-1}	5.24×10^{-7} $\pm 1.5\times10^{-9}$	6.48×10^{-7} $\pm 2.3\times10^{-9}$	5.25×10^{-7} $\pm 1.5\times10^{-9}$	6.48×10^{-7} $\pm 2.3\times10^{-9}$

Table 5.6: Different calibration constants extracted from length calibration experiment II in combination with the four segments of the two thermal calibration experiments

two length calibration experiments, a shift in the lengths of the reference interferometers has been detected (discussed further in section 5.7). Splitting the thermal data into sections has shown problems with the mechanical stability in the interferometers.

The final values used for the RTE's are taken as the averages of the RTE values in calibration sets α_1, α_3, β_1 and β_3, and are shown in table 5.7. The final length calibration constants and errors are given for both of the length calibration experiments; the reason for this is discussed in section 5.7. The final values are shown in table 5.7.

In the length calibration experiment equations (equations 5.6 and 5.7) the parameter $L_{StageInitial}$ is defined to be constant. To study if this is true, the value of $L_{StageInitial}$ is determined for each data point in length calibration experiment 1 and 2 using the other calibration constants. The value of $L_{StageInitial}$ determined for each data point is then subtracted from the value of $L_{StageInitial}$ determined by the fit, with the differences for length calibration experiment 1 and 2 shown in figures 5.16(a) and 5.16(b) respectively.

Comparing figure 5.16(a) and the error on $L_{StageInitial}$ in table 5.5 it can be seen that the error on $L_{StageInitial}$ is larger than the spread of the data in figure 5.16(a). This implies that the changes in $L_{StageInitial}$ are unlikely to effect the length calibration experiment 1 results.

Comparing figure 5.16(b) and the error on $L_{StageInitial}$ in table 5.6 it can be seen that the error on $L_{StageInitial}$ is significantly smaller than the spread of the data in figure 5.16(b).

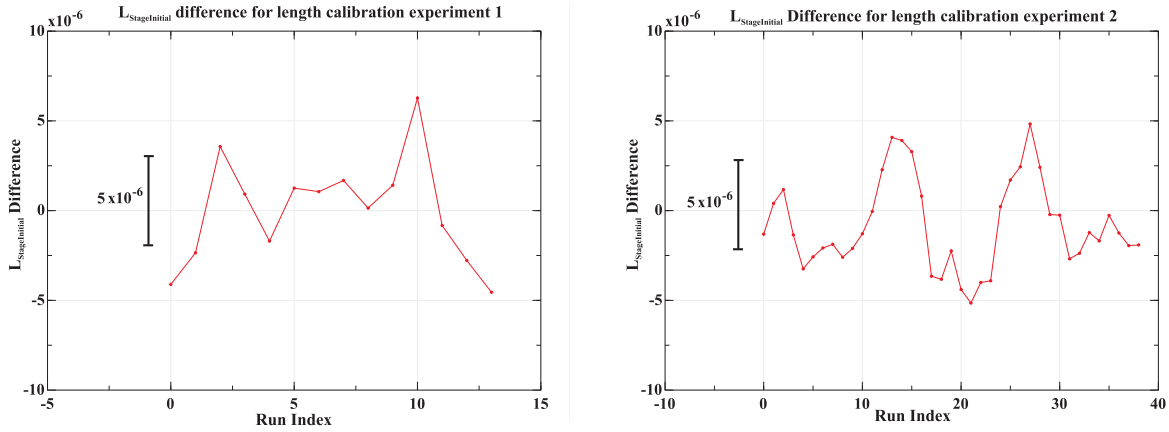

(a) $L_{StageInitial}$ difference for length calibration experiment 1

(b) $L_{StageInitial}$ difference for length calibration experiment 2

Figure 5.16: The difference between the value of $L_{StageInitial}$ from the fitting procedure and the value determined from the data and other calibration constants for length calibration experiment 1 and 2

Figure 5.16(b) also shows that $L_{StageInitial}$ is systematically moving. This implies that the value $L_{StageInitial}$ is not constant during the experiment, and that the errors in table 5.6 could be improved if this movement could be taken account of.

5.6.4 Length prediction, ratio prediction and associated errors

From the calibration constants it is possible to predict the length of either of the reference interferometers at a temperature T, and to estimate an error on the prediction. The length of a reference interferometer at a temperature T is given by:

$$L_{ref}(T) = (L_{ref}(T^0_{ref}) + RTE_{ref} \times \Delta T_{ref}). \tag{5.16}$$

Where:

$$\Delta T_{ref} = T - T^0_{ref}. \tag{5.17}$$

Using Gaussian error propagation [46] and ignoring errors on the measurement of T, the error on the reference interferometer length is given by:

$$\sigma^2_{L_{ref}(T)} = \Delta T^2_{ref}\sigma^2_{RTE} + \sigma^2_{L_0} \tag{5.18}$$

It is not possible to measure the length of one interferometer using FSI alone, however, it is possible to measure the ratio of the lengths of two interferometers. From the predicted reference interferometer lengths it is possible to predict the ratio of reference interferometer lengths. The ration of the lengths is given by:

$$\Phi_{2,1} = \frac{L_1(T)}{L_2(T)}. \tag{5.19}$$

With an error of:

$$\sigma^2_{\Phi_{2,1}} = \frac{\sigma^2_{L_1(T)}}{[L_2(T)]^2} + \frac{[L_1(T)]^2\sigma^2_{L_2(T)}}{[L_2(T)]^4}. \tag{5.20}$$

If we assume a ΔT of 10 K then the error on the length ratio for length calibration experiment 1 would be 1.04E-5 and for length calibration experiment 2 it would be 2.75E-7.

To study the uncertainty of the predicted error, a set of data was rapidly taken with both reference interferometers to minimise any environmental changes; there were approximately 5 seconds between scans. The ratio of the length of the reference interferometers was determined from the measurements and is shown in figure 5.17. Figure 5.17 shows that the measurement precision of the length ratio of the reference interferometers is 2.3×10^{-8} which is much smaller than the error on the predicted length ratios. This also shows that the dominant source of error when determining the length of a measurement interferometer is the error on the length of the reference interferometer.

5.7 Time variation of reference interferometer length ratios

The results from section 5.6.3 show a disagreement between in the values of $L_1^I(T_1^{0,I})$ and $L_1^{II}(T_1^{0,I})$, and also between $L_2^I(T_2^{0,I})$ and $L_2^{II}(T_2^{0,I})$. To study this further, all of the data taken by the reference interferometers over an eight month period is analysed. The phase ratio of the reference interferometers, $\Phi_{2,1}$, is determined from the data, and predicted using the thermal data and the calibration constants give in table 5.7. Figure 5.18(a) shows the

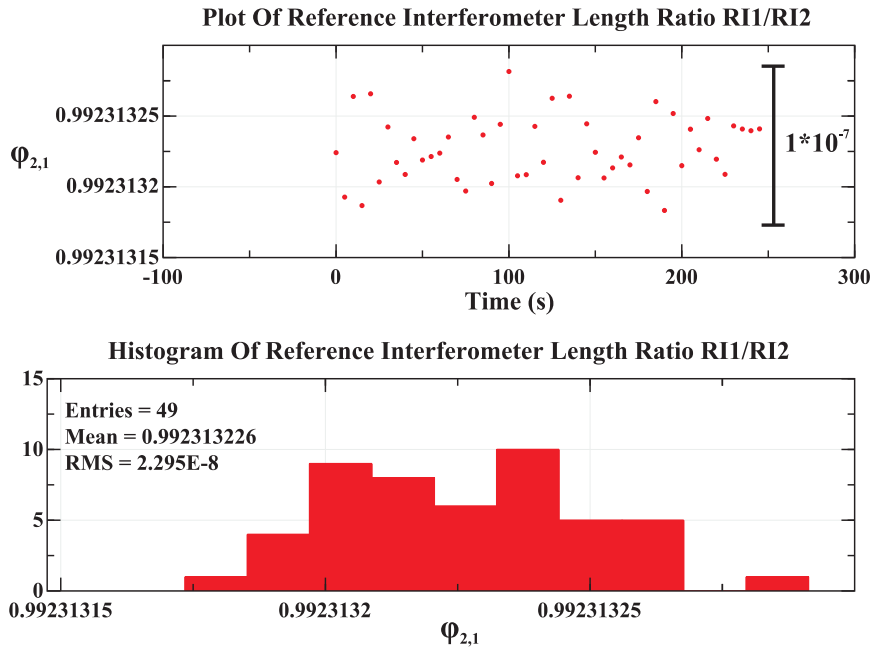

Figure 5.17: The rapid scan length ratios, $\Phi_{2,1}$

measured $\Phi_{2,1}$, the predicted $\Phi_{2,1}$ (using length calibration experiment 1 calibration constants) and the difference between them; figure 5.18(b) shows the same but using constants from length calibration experiment 2.

From figures 5.18(a) and 5.18(b) it can be seen that there is a jump in the difference between the predicted length ratio and the measured length ratio at an index of 2710. It can also be seen that the calibration constants from length calibration experiment 1 fit the first half of the data, and length calibration experiment 2 fits the second half of the data; this is expected because length calibration 1 experiment was performed before the event and length calibration 2 after. The reason for this event, where the length of both of the reference interferometers have changed, is unknown, however, different calibration constant sets can be used before and after the event. The event explains the difference between the values for $L_1^I(T_1^{0,I})$ and $L_1^{II}(T_1^{0,I})$, and also between $L_2^I(T_2^{0,I})$ and $L_2^{II}(T_2^{0,I})$. The RI2Dec data was taken during this jump which may be the cause of the curve seen in that data. This data is not reliable and is removed from the analysis as explained earlier in section 5.6.3.

The data can be split at the event, and the length prediction before and after the event

can be carried out with the corresponding calibration constants. The difference between the predicted and measured length ratio before and after the event is shown in histograms in figures 5.19(a) and 5.19(b) respectively.

Figures 5.18(a) and 5.18(b) also show the errors on the predicted length ratios (calculated using equation 5.20); the errors using calibration constants before the event are much larger. From the calibration constants before the event, the smallest length ratio prediction error achieved is when $\Delta T_1 = \Delta T_2 = 0$, giving an error on the length ratio of $\sigma_{\Phi_{2,1}} = 1.04 \times 10^{-5}$. From figure 5.19(a) the RMS spread is 8.21×10^{-7}. Since the errors on the length ratio prediction before the event are larger than the RMS spread before the event, this implies that the errors on the length ratio prediction are over estimated and any data taken before the event can take the value 7.51×10^{-7} multiplied by the length of the reference interferometer, as the error on the reference lengths. From the calibration constants after the event, using a large value of $\Delta T_1 = \Delta T_2 = 10$ K [4], the error on the predicted length ratio is $\sigma_{\Phi_{2,1}} = 2.75 \times 10^{-7}$. From figure 5.19(b) the RMS spread is 3.49×10^{-7}. The spread of the difference between the predicted and the measured length ratios after the event are larger than the error prediction after the event. This shows that the calibration constants we have measured do not fully describe the reference interferometers. For example the effect of hysteresis is not taken into account of in the prediction. The spread of the difference is the larger of the two errors, therefore, we can take the value 3.49×10^{-7} multiplied by the length of the reference interferometer, as the error on the reference lengths. In figures 5.19(a) and 5.19(b) it can also be seen that the distributions are not centred on zero. This is because the calibration constants do not fully describe the reference interferometers, leading not only to a spread in the predicted length ratios, but also a systematic shift in the predicted length ratios.

The calibration constants determined for both interferometers are summarized in table 5.7. From the constants in table 5.7 it is possible to determine the length of the reference interferometers at any temperature using equation 5.16. The calculations to determine the error on the reference interferometer lengths are also shown in table 5.7.

[4] The test tunnel in DESY is air conditioned and the temperature variation should not exceed ±10K.

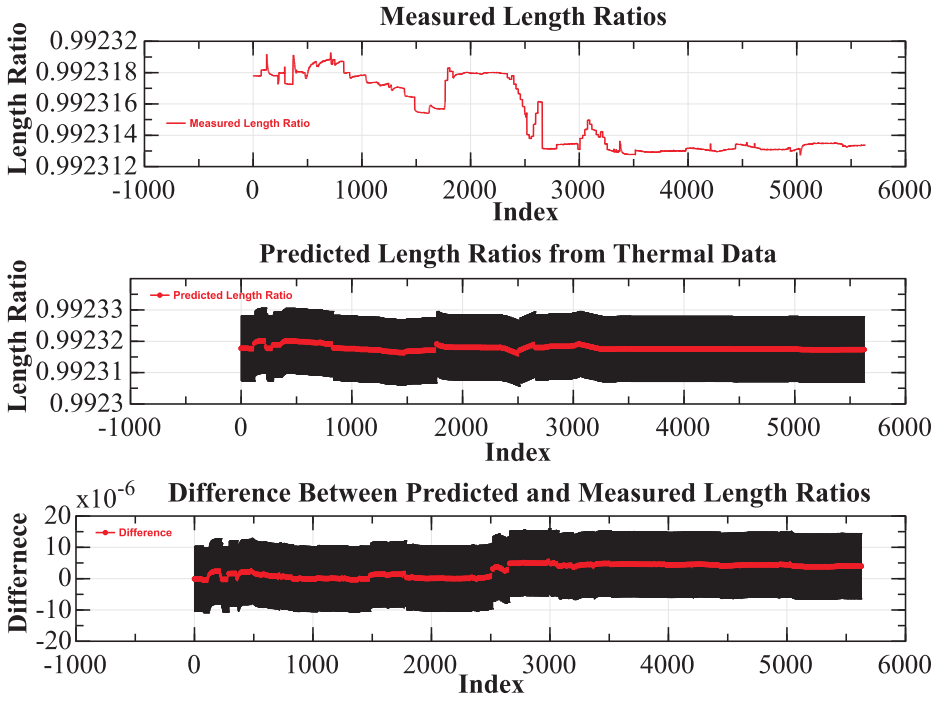

(a) Length calibration experiment 1 calibration constants

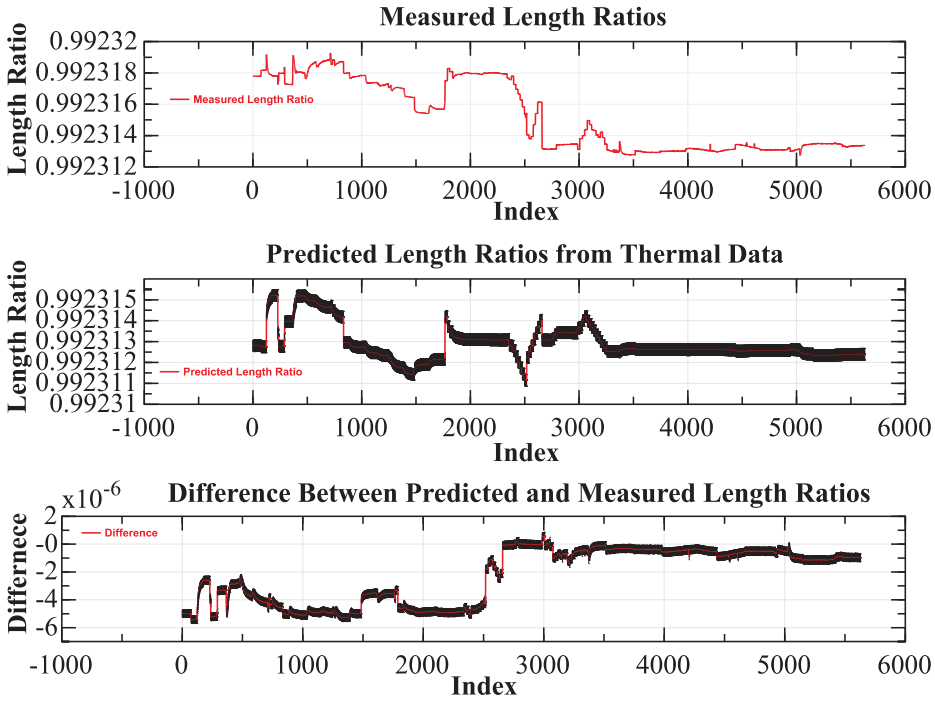

(b) Length calibration experiment 2 calibration constants

Figure 5.18: The measured $\Phi^i_{2,1}$, predicted $\Phi^i_{2,1}$ and their differences using length calibration experiment 1 and length calibration experiment 2 calibration constants shown in table 5.7

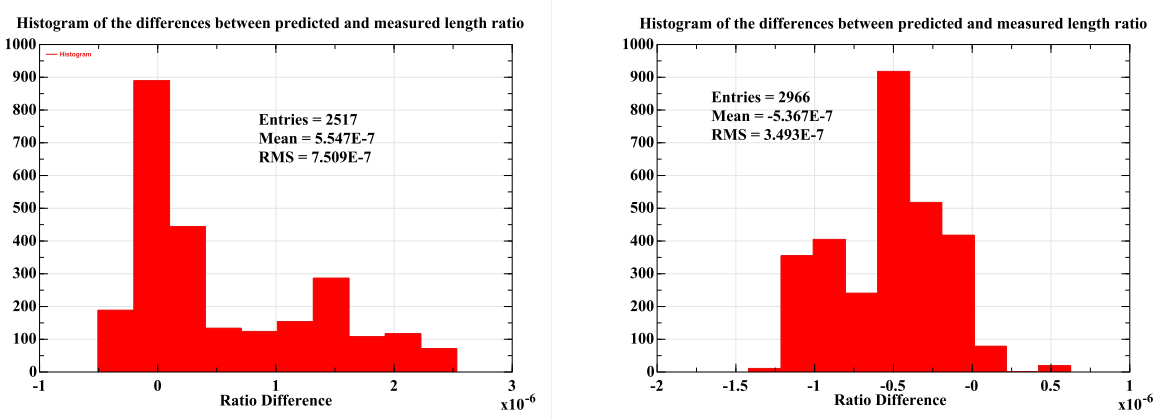

(a) Data and calibration constants before the event (b) Data and calibration constants after the event

Figure 5.19: difference in predicted and measured $\Phi^i_{2,1}$ before and after the event

Before or After Event	RI Number	$T_{0,ref}$ (^{O}C)	$L(T_{0,ref})$ (m)	RTE_{ref} (m/k)	Error (m)
Before	1	25.01	$3.252275974 \pm 2.41\times10^{-5}$	$2.87\times10^{-7} \pm 8.11\times10^{-9}$	$7.51 \times 10^{-7} \times (L_1(T_{0,1}) + RTE_1 \times \Delta T_1)$
Before	2	24.90	$3.277454065 \pm 2.42\times10^{-5}$	$5.25\times10^{-7} \pm 0.50\times10^{-9}$	$7.51 \times 10^{-7} \times (L_2(T_{0,2}) + RTE_2 \times \Delta T_2)$
After	1	24.54	$3.252174806 \pm 6.35\times10^{-7}$	$2.87\times10^{-7} \pm 8.11\times10^{-9}$	$3.49 \times 10^{-7} \times (L_1(T_{0,1}) + RTE_1 \times \Delta T_1)$
After	2	20.97	$3.277366541 \pm 6.40\times10^{-7}$	$5.25\times10^{-7} \pm 0.50\times10^{-9}$	$3.49 \times 10^{-7} \times (L_2(T_{0,2}) + RTE_2 \times \Delta T_2)$

Table 5.7: The final reference interferometer calibration constants and errors

Chapter 6

Measurement Interferometer Performance

As described in chapter 2 the LiCAS RTRS has two different types of absolute distance measurement systems: the internal and the external FSI systems. The performance of these two FSI systems will be discussed in this chapter.

6.1 External FSI systems

The design of the external FSI system, along with its readout electronics is described in chapter 2. The external FSI system has six uncollimated FSI lines. The system is responsible for determining the three dimensional position of a wall marker with respect to a measurement unit.

6.1.1 External FSI data

Figure 6.1 shows the raw data as a function of time, and the corresponding Fourier transform of the time domain data before and after filtering. The power returned is low but a peak in the Fourier spectrum is visible. Figure 6.2 shows the Lomb periodogram after transformation

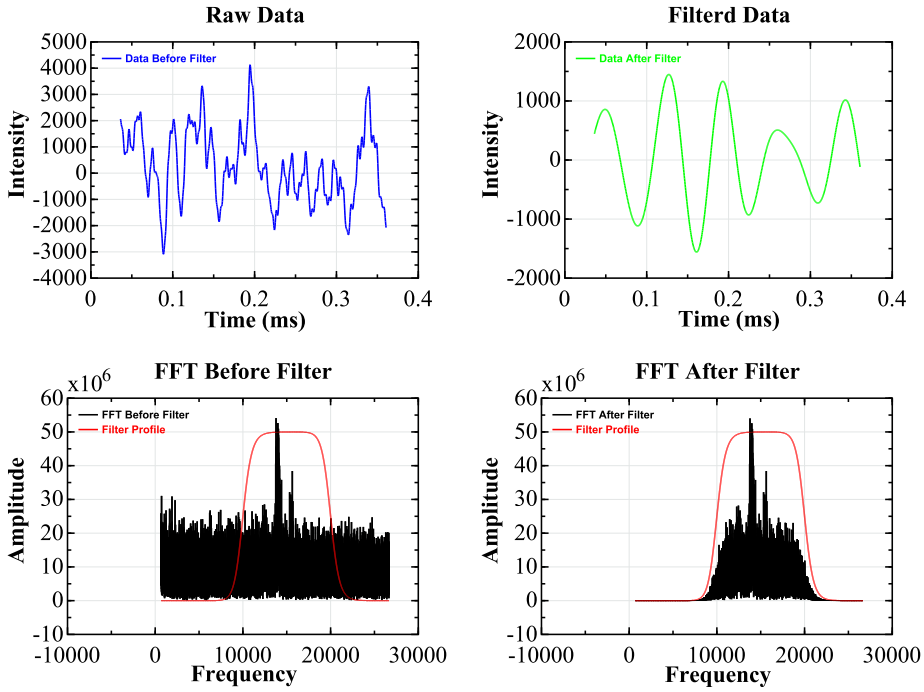

Figure 6.1: External FSI data and Fourier spectrum before and after Fourier filtering. FFTs are of 0.75s of data

into the reference phase domain for an external FSI line. This peak is much clearer than the peak in the Fourier spectrum of the time domain data. The peak in the Lomb periodogram can then be used to determine the length of the measurement interferometer as described in chapter 4.

6.1.2 External FSI wall marker reconstruction

The external FSI system has six FSI lines arranged as shown in chapter 2. Each external FSI line measures the distance from the fibre tip to the wall marker apex. If the position of all the reference interferometer tips are known, then it is possible to reconstruct the 3D position of the wall marker. This problem is referred to as external FSI wall marker reconstruction. To do this we build a linear algebra model, using the parametric method (section 3.2) as we can write explicit prediction equations for the measured distances. If the reference marker has the co-ordinates (R_x,R_y,R_z) and the fibres tips have the co-ordinates (E_{xi},E_{yi},E_{zi}), where i

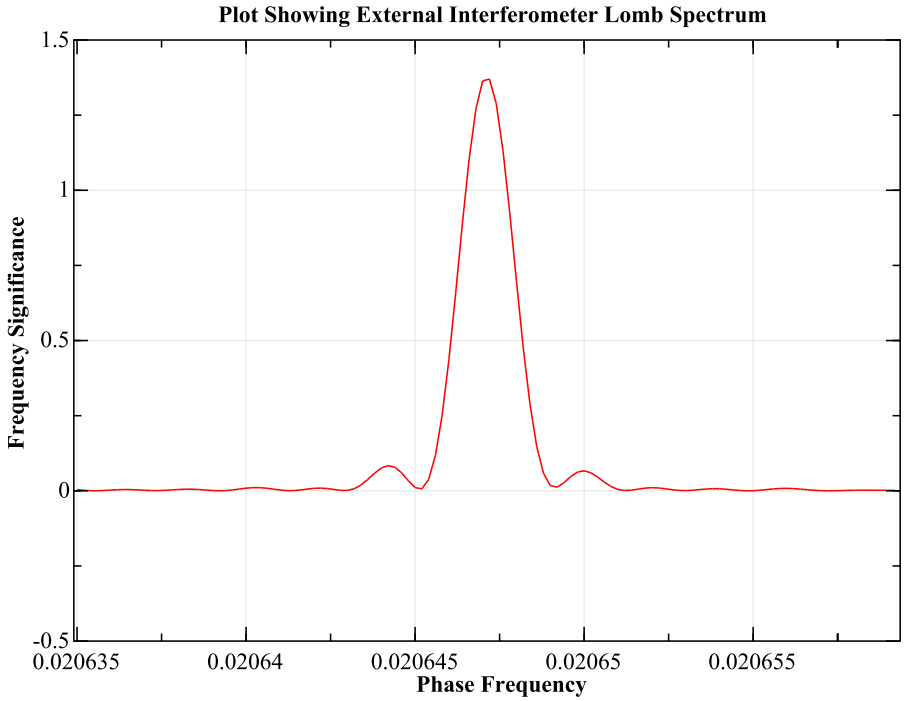

Figure 6.2: The Lomb periodogram of an external FSI line.

is the fibre number, the measured distances are:

$$D_i = \sqrt{(R_x - E_{xi})^2 + (R_y - E_{yi})^2 + (R_z - E_{zi})^2}. \tag{6.1}$$

The vector $F(\bar{X})$ is:

$$F(\bar{X}) = \begin{bmatrix} \sqrt{(R_x - E_{x1})^2 + (R_y - E_{y1})^2 + (R_z - E_{z1})^2} \\ \sqrt{(R_x - E_{x2})^2 + (R_y - E_{y2})^2 + (R_z - E_{z2})^2} \\ \sqrt{(R_x - E_{x3})^2 + (R_y - E_{y3})^2 + (R_z - E_{z3})^2} \\ \sqrt{(R_x - E_{x4})^2 + (R_y - E_{y4})^2 + (R_z - E_{z4})^2} \\ \sqrt{(R_x - E_{x5})^2 + (R_y - E_{y5})^2 + (R_z - E_{z5})^2} \\ \sqrt{(R_x - E_{x6})^2 + (R_y - E_{y6})^2 + (R_z - E_{z6})^2} \end{bmatrix} \tag{6.2}$$

The vector $\bar{X}$ contains the marker position:

$$\bar{X} = \begin{bmatrix} R_x \\ R_y \\ R_z \end{bmatrix} \tag{6.3}$$

The vector L contains the distances measured by each FSI line and the design matrix A consists of the partial derivatives $A = \frac{\partial F}{\partial X}\Big|_{X^0,L}$.

Note that there are two solutions to the reconstruction problem, one either side of the plane on which the fibres lie. To avoid this problem, the initial choice for the marker position has to be distinctly one side of the plane of the fibres. The precision of the reconstruction is discussed in section 6.5.1.

6.2 Internal FSI system

The design of the internal FSI system, along with its readout electronics is described in chapter 2. The internal FSI systems has six collimated FSI lines in each measurement unit except, for unit 1. The internal FSI system is responsible for measuring the distance and the relative rotations around the X and Y axis from one unit to the next.

6.2.1 Internal FSI data

Figure 6.3 shows a sample of internal FSI data along with the time domain Fourier spectrum of a single FSI scan. The oscillatory signal is clearly visible in the data and the spectrum.

Figure 6.4 shows the Lomb periodogram for an internal FSI line after transformation into the reference phase domain after Fourier filtering. There is a clear peak in the Lomb spectrum which can then be used to determine the length of the reference interferometer as described in chapter 4.

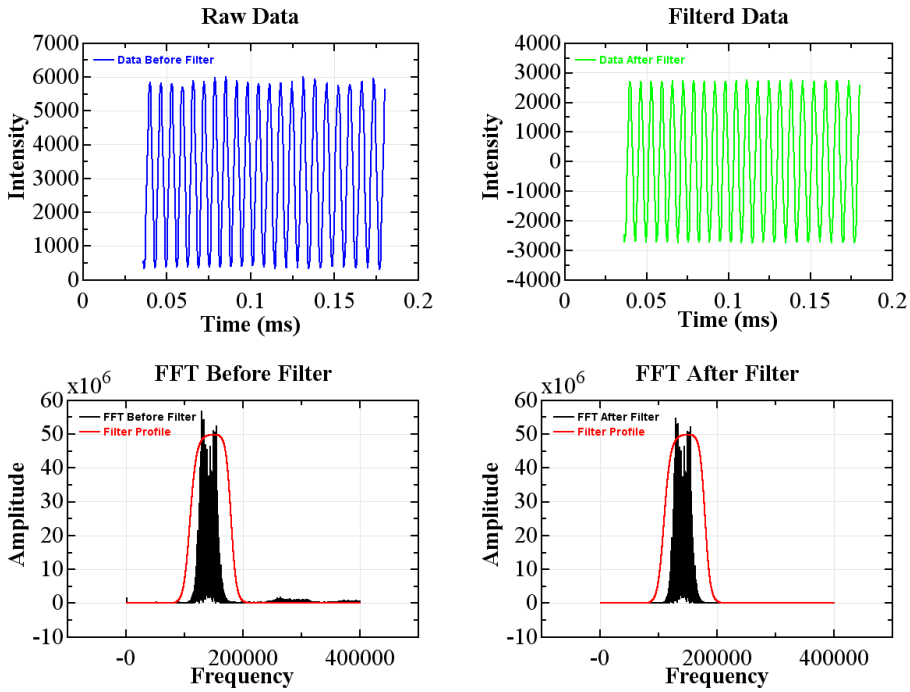

Figure 6.3: Internal FSI data and Fourier spectrum before and after Fourier filtering. FFTs are of 0.75s of data

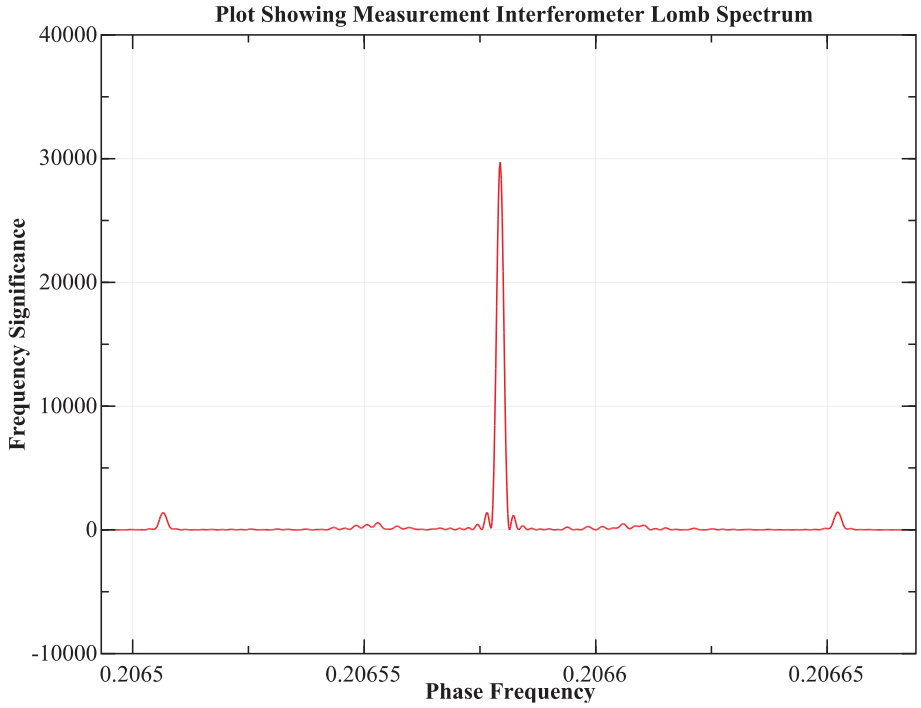

Figure 6.4: The Lomb periodogram of an internal FSI line.

6.2.2 Unit alignment

The internal FSI lines are collimated. To get a return signal on all lines, the internal FSI system on one unit requires alignment with the corresponding retro reflectors on a second unit. All of the individual internal FSI lines in a unit are initially aligned with each other at construction time. They are aligned so that they all point in the same direction as described in chapter 2. The alignment here is to make all the internal FSI lines on one measurement unit point at the correct retro reflector on the observed unit. The system is inside a vacuum and so alignment is achieved by scanning the unit containing the internal FSI lines through a series of stepper motor moves; this is referred to as an alignment scan. There are two types of alignment scans: the coarse scan and the fine scan. The coarse scan is used to find the correct retro reflectors to align to; the fine scan is used for the precise final alignment. The coarse scans cover a range of ±6mrad in steps of 0.6mrad in both rotations around the X and Y axis. The fine scans cove a smaller range of ±2mrad in steps of 0.4mrad in both rotations around the X and Y axis. The measurement units co-ordinate system is described in chapter 2. At each stop during a scan 50176 intensity measurements are taken by each FSI line and the RMS of the intensity measurements is determined. The larger the RMS the more power is being returned and the better the alignment.

Figure 6.5 shows the results of a coarse scan using car 3; each line is in a different plot. The size of the symbol represents the ratio of the RMS of the FSI data to the max RMS during the alignment scan for an individual line. Figure 6.5 shows that during the coarse scan, each of the FSI lines pass over several retro reflectors. A retro reflector group is determined by consecutive points with an RMS above the scans mean RMS. To determine the correct orientation of the units, so that all of the FSI lines are aligned with the correct retro reflectors, the RMS weighted average rotations for each retro reflector group is determined for all lines. The retro reflector groups which have similar rotations on all lines is the correct group to align to. Note that not all of the retro reflectors are covered by every FSI line during the coarse alignment scan.

Figure 6.6 shows the same data as all the plots from figure 6.5 but with the rotations

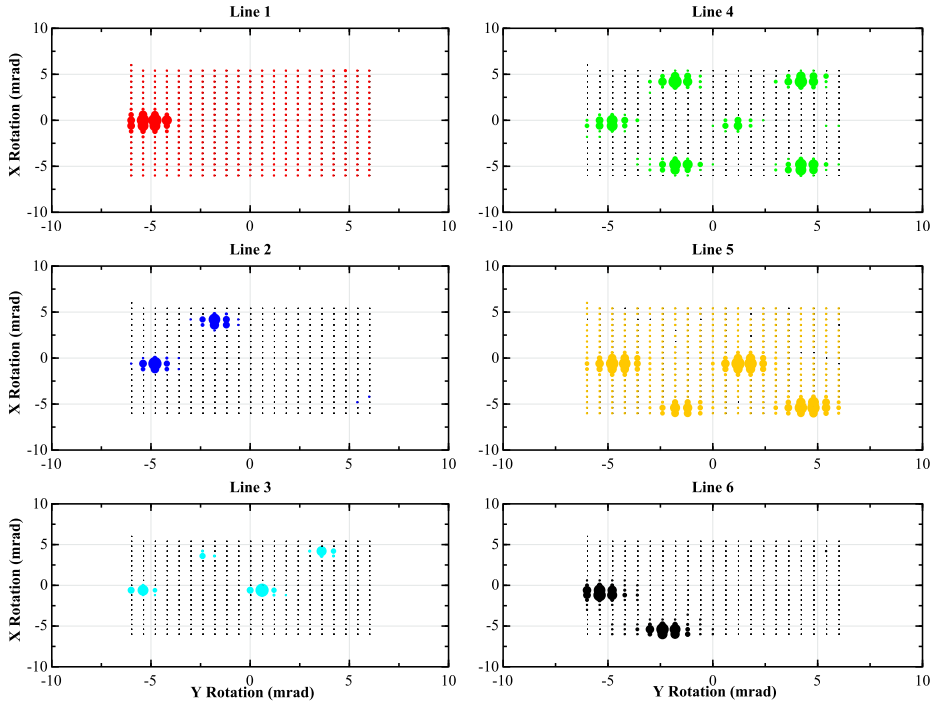

Figure 6.5: Results of a coarse internal FSI alignment scan. The size of the symbol represents the ratio of RMS of the FSI scan to the max RMS during the alignment scan.

adjusted by hand so that retro reflector groups which correspond to the same retro reflector are on top of each other; this is referred to as a staggered plot. From figure 6.6 the position of all the retro reflectors can be seen. We would only expect to see six retro reflector groups but there are seven groupings shown. The central grouping corresponds to the retro reflectors on car 1. During the scan the centres of the three measurement units were approximately on a straight line and this allowed the internal FSI laser light, at certain angles, to pass through car 2 and onto car 1.

With the coarse scan completed all of the FSI lines are pointing at the correct retro reflector and the fine scan can be run to determine the best position to optimize the power return. Figure 6.7 shows the results of a fine alignment scan using car 3 with the staggered plot show in figure 6.8. For each line the best rotations are found by calculating the RMS weighted average in rotations around the X and Y axis. The best rotations are the average over all lines. Note that line 3 has much stronger collimation (the beam size is smaller) than the other lines which is why its retro reflector group is smaller.

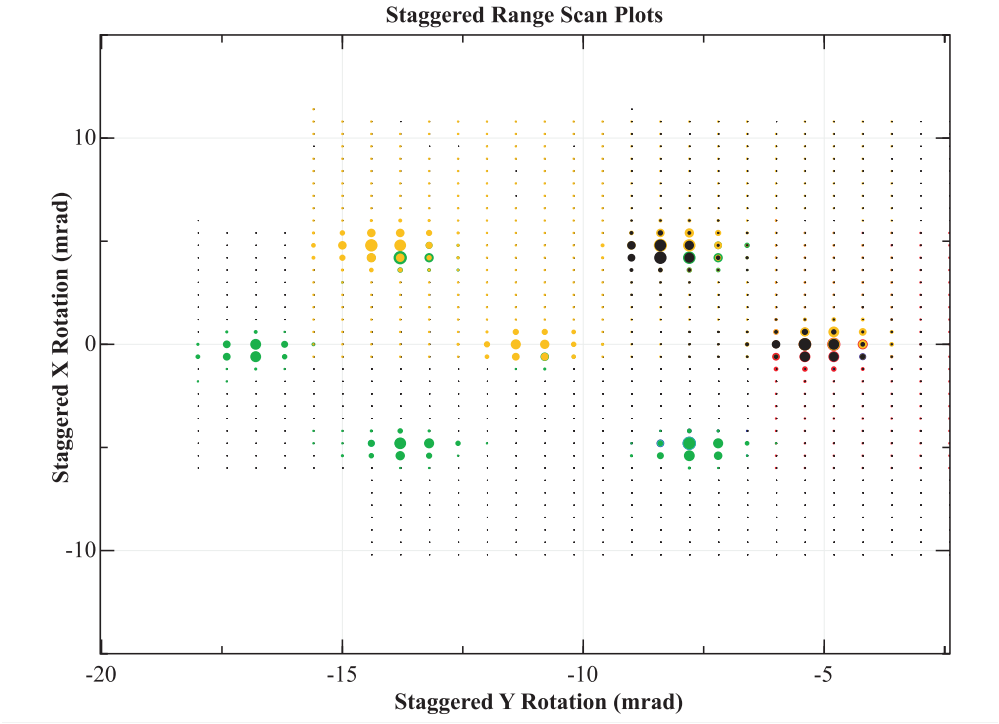

Figure 6.6: Results of a coarse internal FSI alignment scan with each lines results staggered to represent the position of the retro reflector on the observed unit. The size of the symbol represents the ratio of RMS of the FSI scan to the max RMS during the alignment scan.

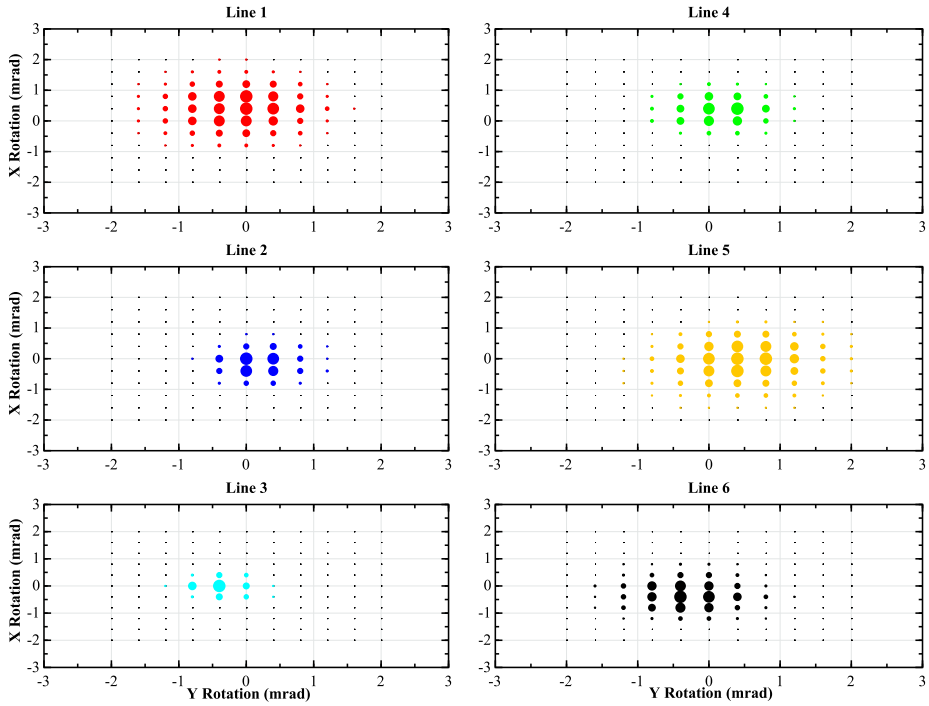

Figure 6.7: Results of a fine internal FSI alignment scan. The size of the symbol represents the ratio of RMS of the FSI scan to the max RMS during the alignment scan.

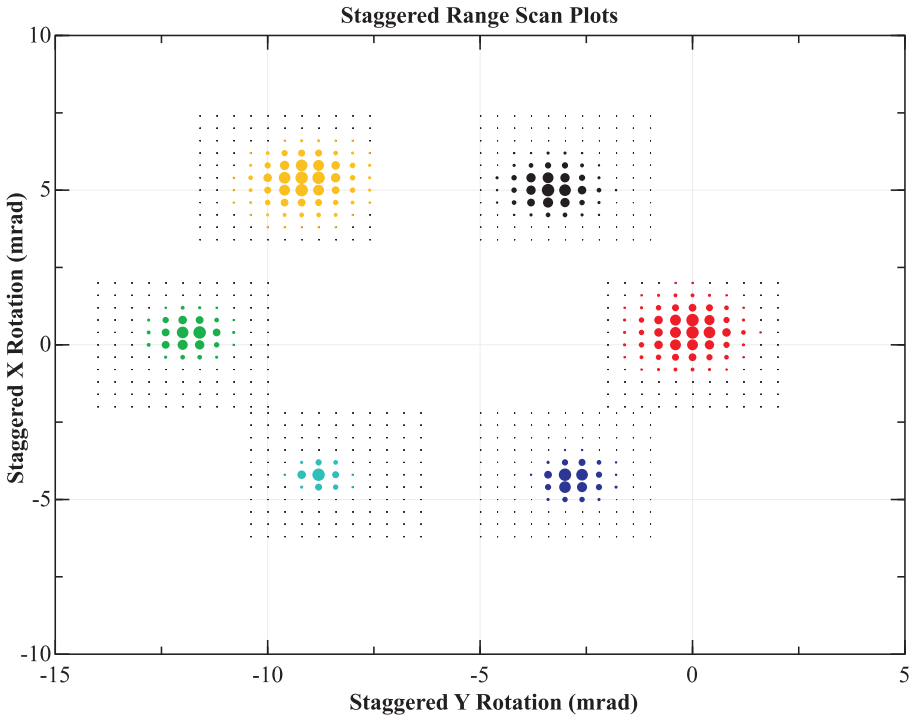

Figure 6.8: Results of a fine internal FSI alignment scan with each lines results staggered to represent the position of the retro reflector on the observed unit. The size of the symbol represents the ratio of RMS of the FSI scan to the max RMS during the alignment scan.

Figure 6.9 shows the optimal position for each FSI line and the final alignment point. The error bars represent the RMS falling off by $1/e^3$. From figure 6.9 it can be seen that there is an operational range of approximately ± 0.75mrad.

6.2.3 Reconstruction of relative measurement unit co-ordinates from internal FSI measurements

The internal FSI system on one unit has six FSI lines monitoring six retro reflectors on the next. The position of the FSI lines, $F_i = (F_{xi}, F_{yi}, F_{zi})$, are given in a local frame located at $Pf = (Pf_x, Pf_y, Pf_z)$ in the global frame. The position of the corresponding retro reflectors, $R_i = (R_{xi}, R_{yi}, R_{zi})$, are given in a second local frame located at $Pr = (Pr_x, Pr_y, Pr_z)$ in the global frame. Both of the local frames, Pf and Pr, are free to translate in all directions and rotate around their own X-axis and Y-axis. Note that small rotations around the Z-axis are irrelevant to this discussion. If the difference in the rotations around the X-axis of both

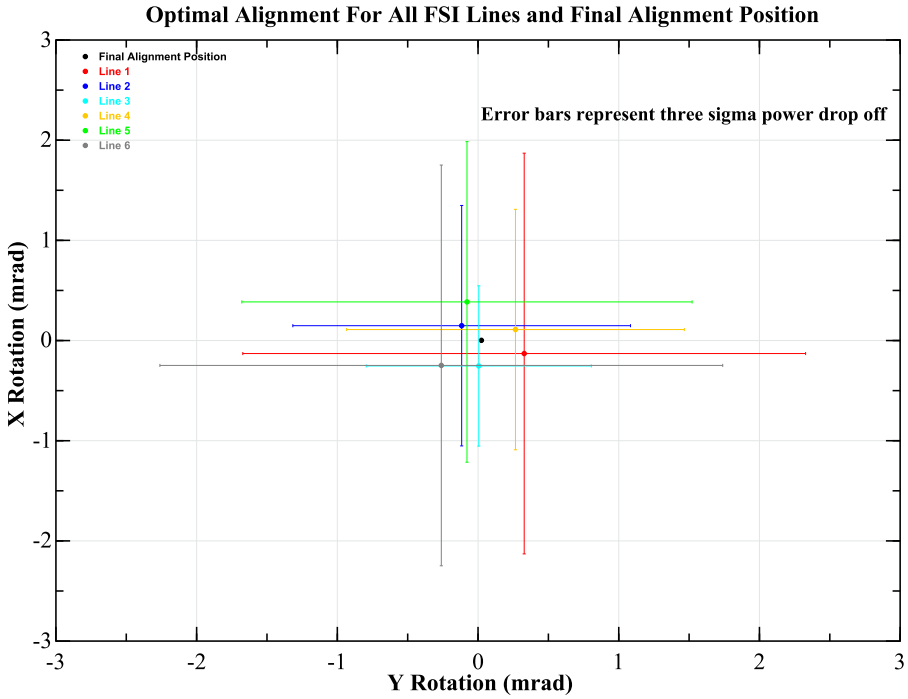

Figure 6.9: The optimal alignment position for each internal FSI line along with the final alignment point. The error bars represent three sigma power drop off.

local frames is θ and the Y-axis is ϕ; the distance between a fibre and its respective retro reflector is give by:

$$\begin{aligned} D_i^2 =& (Pf_x - Pr_x - R_{xi} + F_{xi}\cos(\phi) + F_{zi}\sin(\phi))^2 \\ &+ (Pf_z - Pr_z - R_{zi} + F_{zi}\cos(\theta)\cos(\phi) + F_{yi}\sin(\theta) - F_{xi}\cos(\theta)\sin(\phi))^2 \\ &+ (Pf_y - Pr_y - R_{yi} + F_{yi}\cos(\theta) - F_{zi}\cos(\phi)\sin(\theta) + F_{xi}\sin(\theta)\sin(\phi))^2 \end{aligned} \tag{6.4}$$

If Pr is defined to be $(0, 0, 0)$; then Pf_z becomes the distance between the two units (D) in the Z direction and the distance measured between the fibre and the corresponding retro reflector is:

$$\begin{aligned} D_i^2 =& (Pf_x - R_{xi} + F_{xi}\cos(\phi) + F_{zi}\sin(\phi))^2 \\ &+ (D - R_{zi} + F_{zi}\cos(\theta)\cos(\phi) + F_{yi}\sin(\theta) - F_{xi}\cos(\theta)\sin(\phi))^2 \\ &+ (Pf_y - R_{yi} + F_{yi}\cos(\theta) - F_{zi}\cos(\phi)\sin(\theta) + F_{xi}\sin(\theta)\sin(\phi))^2 \end{aligned} \tag{6.5}$$

If Pf_x, Pf_y, F_i and R_i are known, non-linear least squares methods can be used to determine D,θ and ϕ. This process is known as internal FSI reconstruction. We use the parametric non-linear least squares method described in section 3.2. For the method the vector $F(X)$ is:

$$F(\bar{X}) = \begin{bmatrix} D_1 \\ D_2 \\ D_3 \\ D_4 \\ D_5 \\ D_6 \end{bmatrix} \tag{6.6}$$

The vector $\bar{X}$ contains the relative unit rotations and the distance between the units:

$$\bar{X} = \begin{bmatrix} \theta \\ \phi \\ D \end{bmatrix} \tag{6.7}$$

The vector L is the lengths measured by each FSI line and the design matrix A, is the matrix of partial derivatives, $A = \frac{\partial F}{\partial X}\Big|_{X^0,L}$. The precision of the reconstruction is discussed in section 6.5.2.

6.3 Internal vs external FSI data comparison

The internal and external FSI systems have three major differences which effect their data. The first is that the internal FSI system is collimated where the external uses only bare

fibres. The second difference is that the internal FSI operate in vacuum while the external FSI operate in open air. The third difference is that the distance measured by an internal FSI line is approximately 4.5m and an external FSI line is 0.45m. The effect of collimation is to increase the signal to noise but decrease the acceptance range. The signal to noise seen in the time domain FFTs of the external and internal FSI lines are shown in figures 6.1 and 6.3 respectively. The external FSI lines's time domain FFT peak height to FFT mean is approximately 2:1 where as for an internal FSI line it is approximately 250:1. When the data is shifted into reference interferometer phase space the effect of the signal to noise can be seen on the Lomb periodograms (figures 6.2 and 6.4). An external FSI line produces a peak frequency significance of approximately 1.3 but the internal FSI line produces one of 30000. The acceptance range of an external FSI line is much greater than that of an internal FSI line; the transverse acceptance range of a single FSI line is ±35.5mm at a distance of 0.45m (±79mrad), where as for internal FSI lines this varies from ±3mm to ±9mm at a distance of 4.5m (±0.7mrad to ±2mrad). The effect this has on length measurement precision is discussed in section 6.5. The distance measured by the lines effects the fringe frequency, the longer the distance measured the higher the fringe frequency. At a sampling rate of 2.77MHz and a tuning speed of 40nm/sec the internal FSI line has approximately 18 points per fringe where as the external FSI line has approximately 180.

6.4 Analysis parameter optimisation

In this section the effects of the analysis parameters on the internal and external length measurements will be studied. The aim is to adjust the parameters to get the best performance with the quickest processing time. Note that unless stated, the parameters used are the same for both internal and external FSI lines. To determine the optimal parameters a set of data was taken using the LiCAS RTRS. Fifty scans were taken rapidly (5 seconds between scans) so that the effect of environmental changes, such as temperature and air pressure, were minimized. The data was analysed with different parameters and the effects on precision and processing time determined. The processing time is taken as the time to

analyse one reference, one external and one internal FSI line; this is because we wish to optimise across the system. The analysis parameters were initially set as shown in table 6.1 and the lengths determined using the reference interferometer calibration constants shown in chapter 5.

Parameter	Value
Start Index	0
End Index	2077690
reference Filter Frequency Low	80000.0 Hz
reference Filter Frequency High	140000.0 Hz
internal Filter Frequency Low	110000.0 Hz
internal Filter Frequency High	180000.0 Hz
external Filter Frequency Low	7500.0 Hz
external Filter Frequency High	20000.0 Hz
Filter Magnitude	1.0
Filter Order	10
Carre Scale Factor	0.8
Carre Window Size	5000
MACC	4
Lomb Frequency Step, Δf	2E-7

Table 6.1: Initial Parameters Used For FSI Analysis

6.4.1 Variation of start and end index

The FSI scans take data for three quarters of a second at 2.77MHz and thus acquire 2077696 data points per scan. The amount of data used in the analysis is varied from 519422 to 2077690 points. The unused data is always cut equally from both of ends of the scan by adjusting the start and end index parameters. Figure 6.10 shows the results of the variation of the number of points. The data points in figure 6.10 are the difference between the average length determined with the current parameters and the lengths determined with the nominal parameters. The error bars are the standard deviations of the measured lengths and is an estimator of the measurement precision.

It is seen from figure 6.10 that reducing the number of points causes some reduction in the processing time, but only with deteriorating resolution as indicated by the increasing error bars. The number of points used in the analysis remains at 2077690 for all further

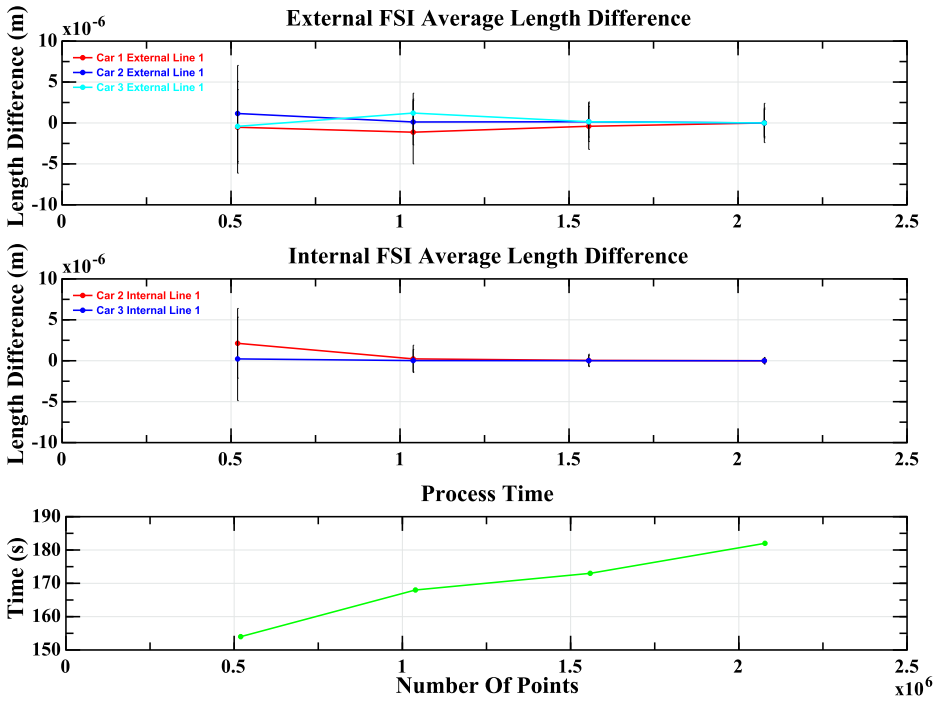

Figure 6.10: Figure showing the variation of the number of data points used in an FSI analysis. Points are the average measured length minus the nominal average.

analysis.

6.4.2 Variation of Lomb MACC and frequency step

The Lomb Periodogram has two input parameters which will be studied here. The MACC value is the number of interpolation points per 1/4 cycle of highest frequency [39] and is proportional to the number of elements in the two FFT's used by the algorithm. The frequency step parameter Δf defines the output frequency spacing and the number of output points $N_{out} \propto \frac{1}{\Delta f}$.

Figure 6.11 shows the ratio of the Lomb peak height to Lomb RMS at different values of Δf with MACC=4 for internal, external and reference interferometers. We see that there are regions where the peak height is small, these regions will be avoided when Δf is varied in the following analysis. With a frequency step value of 2×10^{-7} there are approximately twenty points in a lomb peak, so the frequency step value is not varied beyond 8×10^{-7} as

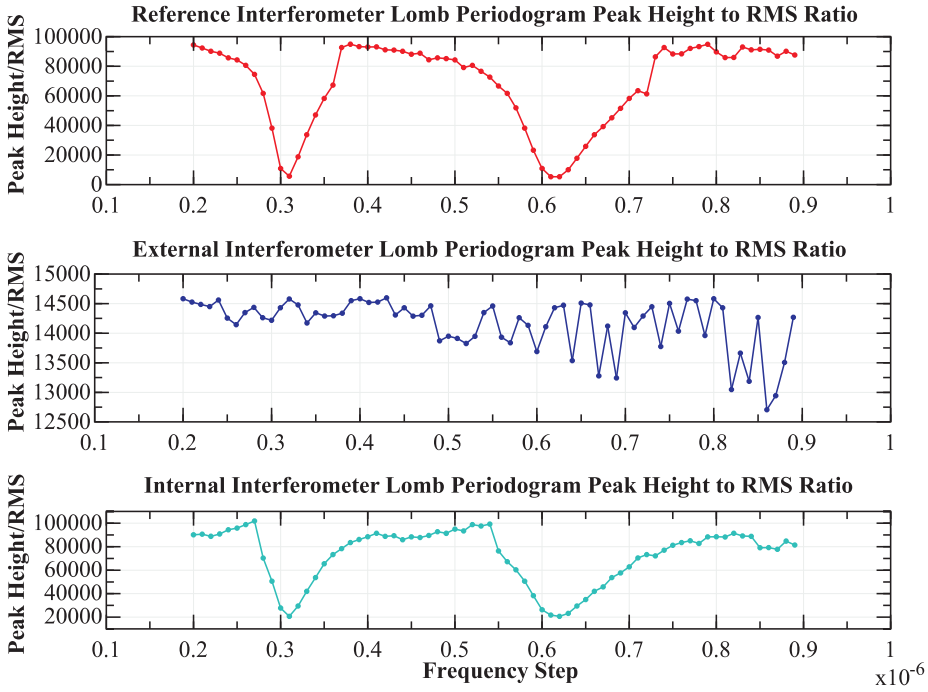

Figure 6.11: Figure shows, Lomb peak height/Lomb RMS, at different values of Δf for MACC = 4.

this will reduce the number of points in the peak below five and could lead to peak fitting problems.

Figure 6.12 and 6.13 show the effect of varying the MACC and frequency step parameter on the first external and internal FSI line in each unit; the bottom right plot shows the process times. Figure 6.12 shows the results with MACC=1 included; it is clear that there is a large systematic caused by this parameter at frequency step 4×10^{-7} and 5×10^{-7}. Figure 6.13 shows the results with MACC=1 removed.

From figures 6.12 and 6.13 it can be seen that MACC=1 should be excluded as this can cause systematics. Taking the frequency step value above 4×10^{-7} starts to cause systematic shifts in the internal FSI measured lengths which are still below the standard deviations, but are increasing. If we take the parameters to use in the future analysis to be MACC=2 and frequency step = 4×10^{-7} we get significant process time improvement without risking systematic errors.

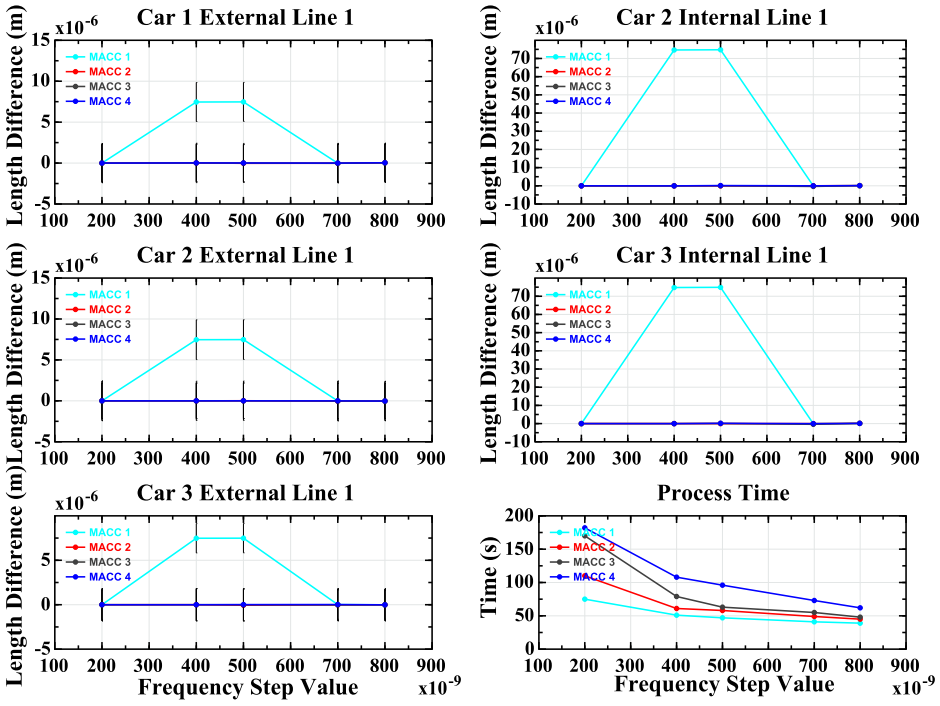

Figure 6.12: Frequency step and MACC parameter scans showing effect of varing MACC and Δf. Points are the average measured length minus the nominal average.

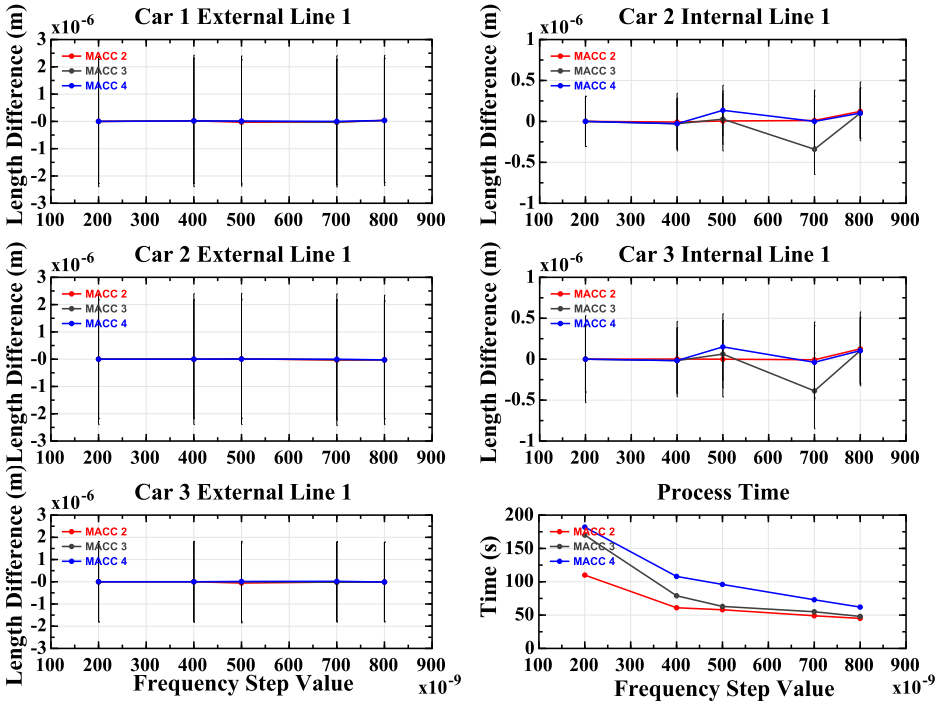

Figure 6.13: Frequency step and MACC parameter scans showing effect of varying MACC and Δf with MACC=1 removed. Points are the average measured length minus the nominal average.

6.4.3 Variation of parameters conclusion

The sections above have shown how parameters can be adjusted to reduce the processing time from 180 seconds to 58 seconds, but with almost no reduction in performance. The optimal parameters are shown in table 6.2 and will be used for all further analysis in this thesis, unless otherwise stated.

Parameter	Value
Start Index	0
End Index	2077690
reference Filter Frequency Low	80000.0 Hz
reference Filter Frequency High	140000.0 Hz
internal Filter Frequency Low	110000.0 Hz
internal Filter Frequency High	180000.0 Hz
external Filter Frequency Low	7500.0 Hz
external Filter Frequency High	20000.0 Hz
Filter Magnitude	1.0
Filter Order	10
Carre Scale Factor	0.8
Carre Window Size	5000
MACC	2
Lomb Frequency Step, Δf	4E-7

Table 6.2: Final optimal parameters used for FSI analysis

6.5 Precision of the internal and external FSI systems

To understand the statistical performance of the FSI system a set of fifty FSI scans for each FSI line was taken rapidly (five seconds between measurements). The rapid data was taken as quickly as the system could to avoid any ambient changes effecting the data. The data is analysed in the following sections to understand precisions of the system. The parameters used for the FSI analysis are shown in table 6.2.

6.5.1 External FSI precision

Figure 6.14 shows a histogram of the lengths measured by the external FSI system during the burst data taking run. Figure 6.15 shows histograms of the results of the external FSI

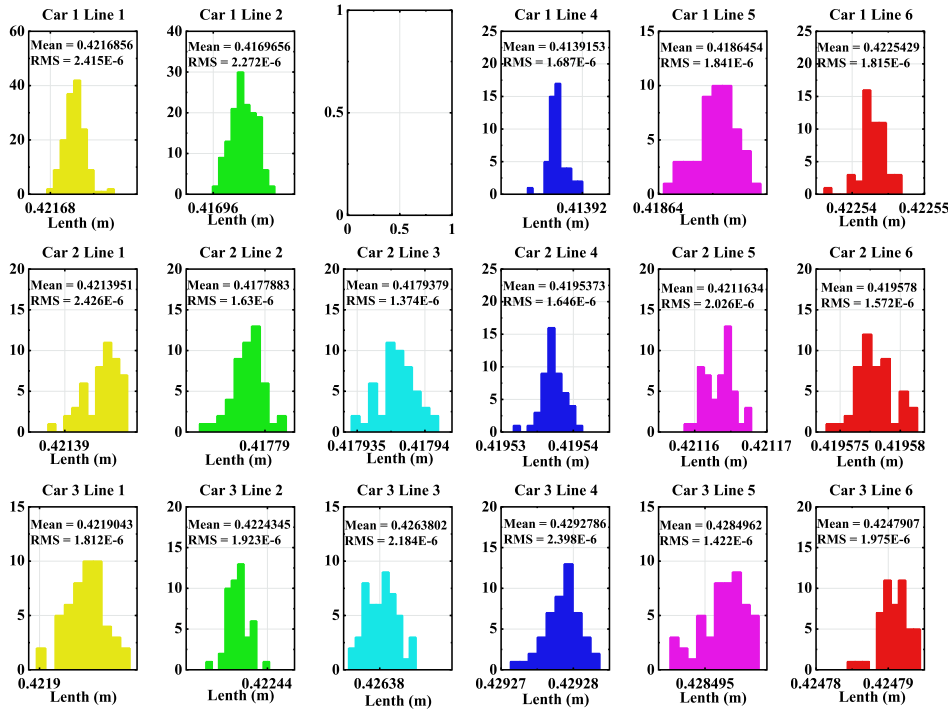

Figure 6.14: Figure showing histograms of the measured external FSI lengths during the burst data taking.

wall marker reconstruction (section 6.1.2) using the external FSI fibre positions from the design drawings as shown in table 2.1.

The RMS values in figure 6.14 can be taken as an upper limit of the measurement precision of the external FSI lines. The results for all external FSI lines are summarised in table 6.3. The RMS of the external FSI wall marker reconstruction (section 6.1.2), shown in figure 6.15, can be taken as an upper limit on the precision of the reconstruction with the results summarised in table 6.4. Note that in figure 6.14 external FSI line 3 on car 1 had failed and that the external FSI wall marker reconstruction for car 1 does not take this line into account. Using fewer FSI lines reduces the accuracy of the reconstruction, thus explaining why the car 1 reconstruction errors are larger than those of the other cars.

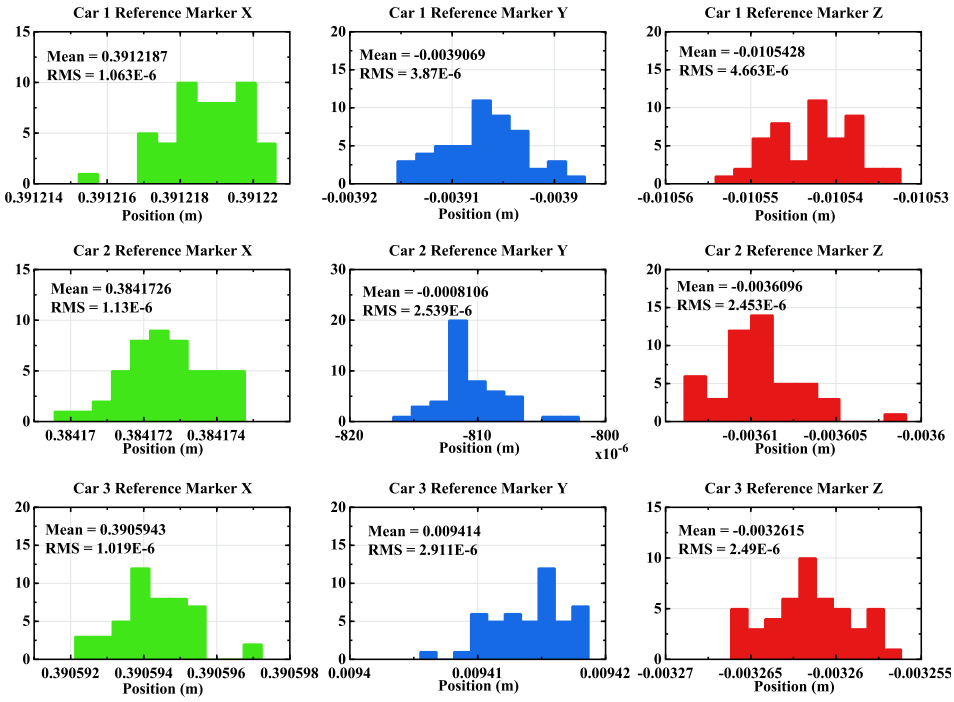

Figure 6.15: Figure showing histograms of the reconstructed external FSI reference marker during the burst data taking.

6.5.2 Internal FSI precision

Figure 6.16 shows a histogram of the lengths measured by the internal FSI system during the rapid data taking. Figure 6.17 shows histograms of the internal FSI reconstruction (section 6.2.3) results during the rapid data taking. For the internal FSI reconstruction the values of Pf_x, Pf_y are set to zero and the fibre and retro positions are set to their design values as shown in table 2.2.

The RMS values in figure 6.16 can be taken as the upper limit on the measurement precision of the internal FSI lines and are summarised in table 6.5. The RMS of the internal FSI reconstruction (section 6.2.3), shown in figure 6.17, can be taken as an upper limit on the precision of the reconstruction with the results summarised in table 6.6.

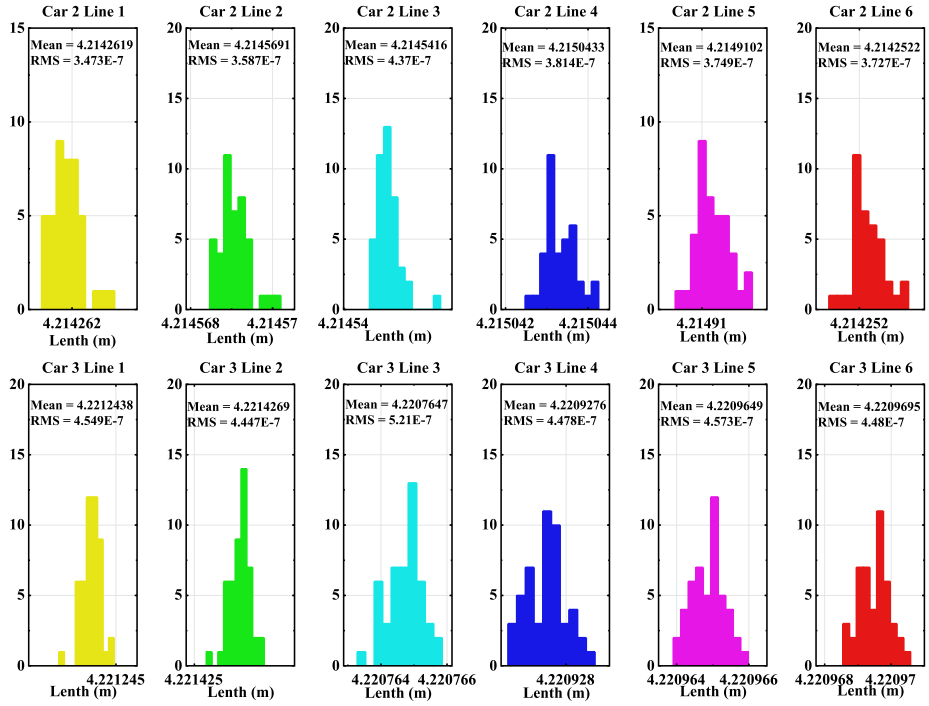

Figure 6.16: Figure showing histograms of the measured internal FSI lengths during the burst data taking.

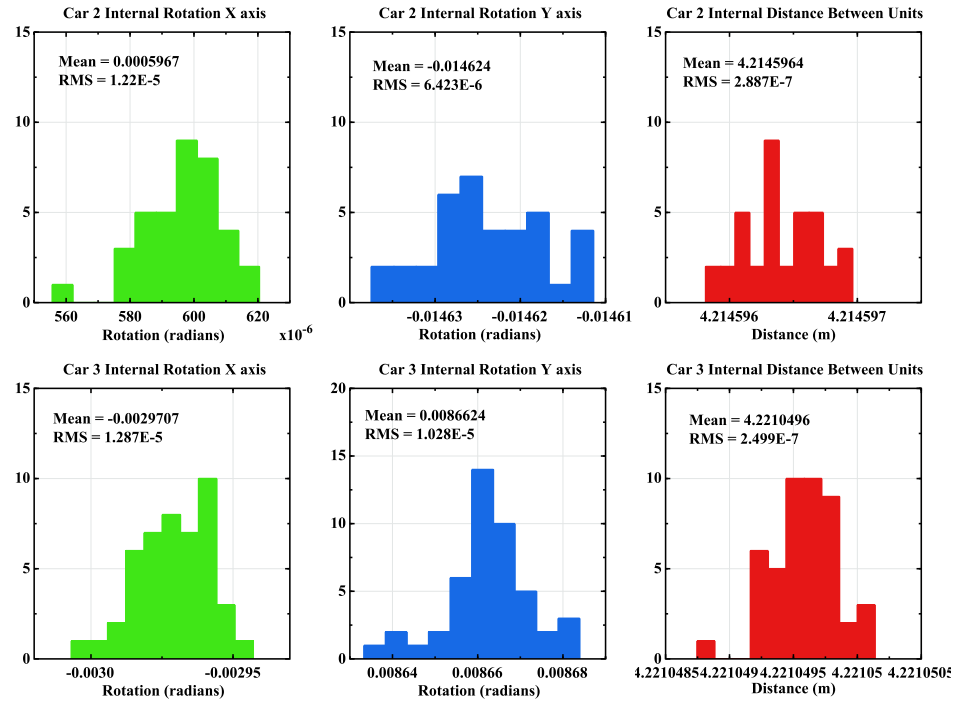

Figure 6.17: Figure showing histograms of the internal reconstructed values during the burst data taking.

Car Number	Line Number	Precision (m)
1	1	2.41×10^{-6}
1	2	2.27×10^{-6}
1	4	1.69×10^{-6}
1	5	1.84×10^{-6}
1	6	1.82×10^{-6}
2	1	2.43×10^{-6}
2	2	1.63×10^{-6}
2	3	1.37×10^{-6}
2	4	1.65×10^{-6}
2	5	2.03×10^{-6}
2	6	1.57×10^{-6}
3	1	1.81×10^{-6}
3	2	1.92×10^{-6}
3	3	2.18×10^{-6}
3	4	2.40×10^{-6}
3	5	1.42×10^{-6}
3	6	1.98×10^{-6}

Table 6.3: The upper limit on the external FSI line precision

Car Number	Parameter	Precision (m)
1	Translation in X axis	1.06×10^{-6}
1	Translation in Y axis	3.87×10^{-6}
1	Translation in Z axis	4.66×10^{-6}
2	Translation in X axis	1.13×10^{-6}
2	Translation in Y axis	2.54×10^{-6}
2	Translation in Z axis	2.45×10^{-6}
3	Translation in X axis	1.02×10^{-6}
3	Translation in Y axis	2.91×10^{-6}
3	Translation in Z axis	2.49×10^{-6}

Table 6.4: The upper limit on the external FSI reconstruction precision

6.6 Measurement interferometer systematic errors

The results in section 6.5.1 and 6.5.2 give the upper limit on the precision of the FSI lines during rapid data taking. The precision can be taken as the statistical error on a measurement. To calculate the length measured by the FSI lines, a reference interferometer is required. The length of the reference interferometer, $l_r(T_r)$, has an error on it as shown in chapter 5. The error is primarily a function of temperature, and this error leads to a systematic error on the length measured by the FSI lines. The length measured by an FSI

Car Number	Line Number	Precision (m)
2	1	3.47×10^{-7}
2	2	3.59×10^{-7}
2	3	4.37×10^{-7}
2	4	3.81×10^{-7}
2	5	3.75×10^{-7}
2	6	3.72×10^{-7}
3	1	4.55×10^{-7}
3	2	4.45×10^{-7}
3	3	5.21×10^{-7}
3	4	4.48×10^{-7}
3	5	4.57×10^{-7}
3	6	4.48×10^{-7}

Table 6.5: The upper limit on the internal FSI line precision

Car Number	Parameter	Precision
2	Rotation around X axis	1.22×10^{-5} radians
2	Rotation around Y axis	0.64×10^{-5} radians
2	Translation along Z axis	2.89×10^{-7} m
3	Rotation around X axis	1.29×10^{-5} radians
3	Rotation around Y axis	1.03×10^{-5} radians
3	Translation along Z axis	2.50×10^{-7} m

Table 6.6: The upper limit on the external FSI reconstruction precision

line, l_m, is give by:

$$l_m = \phi_{r,m} \times l_r(T_r) \tag{6.8}$$

If the error on $l_r(T_r)$ is, σ_{l_r}, then the systematic FSI measurement error is:

$$\sigma_{l_m,Sys} = \phi_{r,m} \times \sigma_{l_r} \tag{6.9}$$

From equation 6.9 it can be seen that, as $\phi_{r,m} = l_m/l_r$, the longer the measured length, the larger the systematic error. As the error on the reference interferometer length is of the order 1.1μm, the systematic errors on the external FSI lines are of the order 0.16μm and on the internal FSI are of the order 1.6μm. This shows that the systematic error on the external FSI lines is negligible compared to the statistical error of approximately 1.9μm; but on the internal FSI lines the systematic error is the dominating error as it is greater than statistical error of approximately 0.42μm.

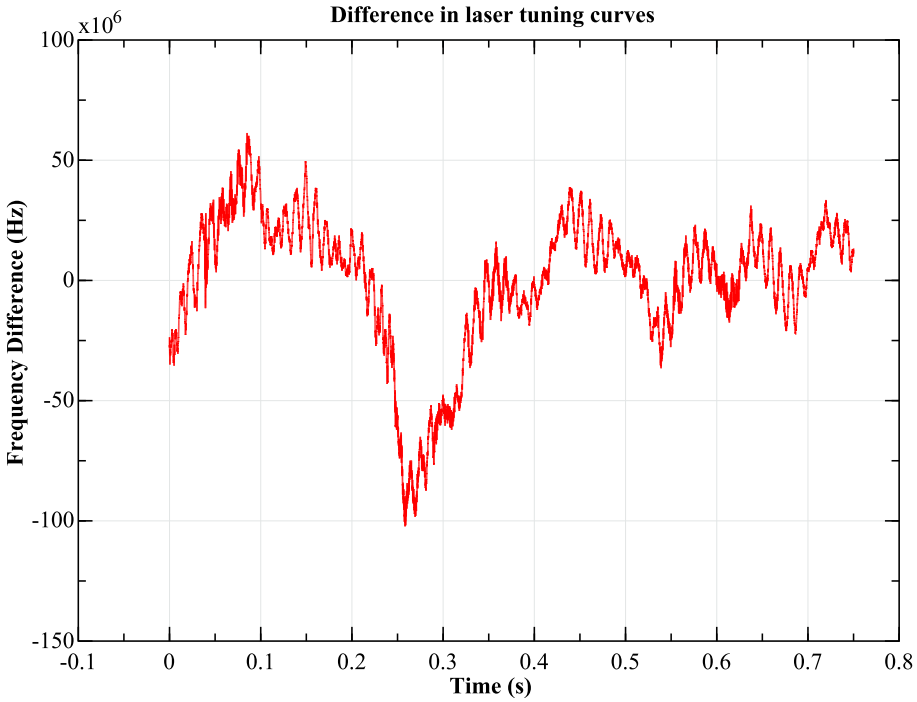

Figure 6.18: The difference in the laser tuning curves from one scan to the next.

6.7 FSI analysis using a reference from a different run

During the operation of the LiCAS RTRS data is taken on three different computers synchronously, however occasionally the DAQ computers become asynchronous. As described in chapter 4, for FSI to be used to measure unknown lengths the reference interferometer and the measurement interferometer need to be measured simultaneously because the laser tunes differently from one scan to the next. The difference between two laser scans is shown in figure 6.18. The reference interferometer is only read by one of the DAQ computers and so if the DAQ computers become asynchronous, there will be a problem with the data analysis of the asynchronous measurement interferometers.

To study the above effect the rapid scan data described in the previous sections is used; however instead of using the synchronous reference interferometer, the reference interferometer data from the previous run is used. Figure 6.19 shows the lengths measured by the external FSI lines on car 2 during the rapid scan experiment analysed with the synchronous and asynchronous reference interferometer; the differences are shown in figure 6.20. The

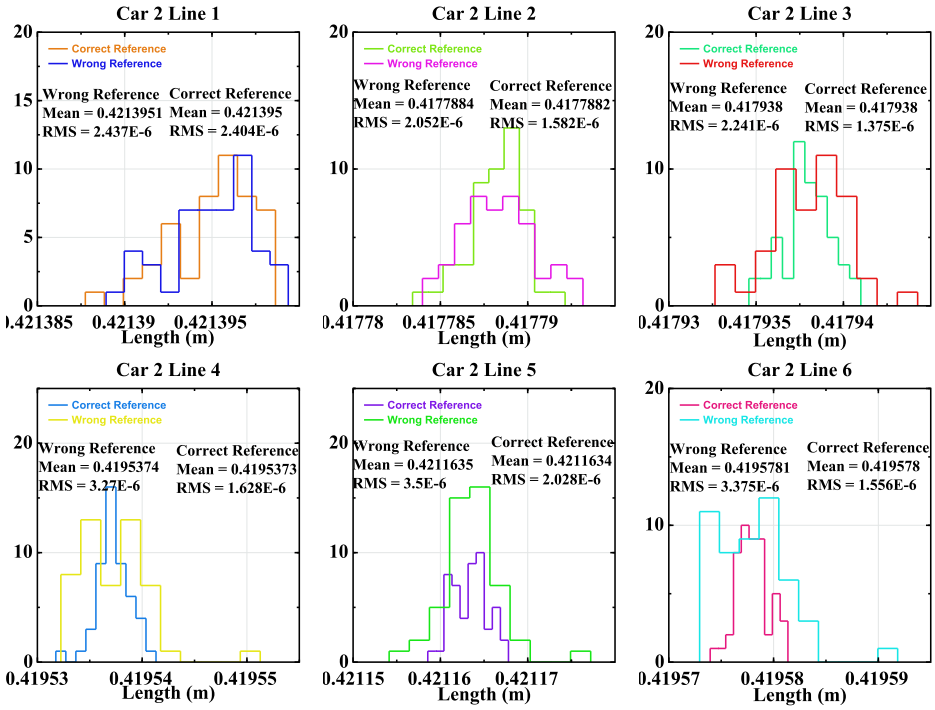

Figure 6.19: Histograms showing the external FSI lengths measured by Car 2 during the rapid scan analysed with the synchronous and asynchronous reference interferometer

results for all other lines are shown in table 6.7. The results in table 6.7 show that the effect of using the incorrect reference interferometer only has a small effect on the precision of the external FSI measurements with no systematic shifts.

When an asynchronous reference interferometer is used in the same way as above but with the internal FSI lines the analysis fails. To understand why we need to look at the length being measured. As described in section 6.3, the distance measured by the internal FSI is approximately 4.5m which leads to 18 data points per fringe as the tuning speed of 40nm/s. The external FSI lines measure a distance of approximately 0.45m leading to 180 points per fringe. As the total phase advanced of the reference interferometer is approximately 500000 radians and there are 2077690 data points in the scan, the phase advance from one point to the next is 0.24 radians. The reference phase advance for one internal FSI fringe is therefore 4.33 radians and for one external FSI fringe is 43.3 radians. Figure 6.18 shows that the frequency variation from one laser scan to the next can be as large as 50 MHz in laser frequency which is equivalent to 7 radians in reference interferometer phase. As the

		Synchronous		Asynchronous		Difference	
Car	Line	Average (m)	RMS (m)	Average (m)	RMS (m)	Average (m)	RMS (m)
1	1	0.42168561	2.39×10^{-6}	0.42168563	3.09×10^{-6}	-1.08×10^{-8}	2.54×10^{-6}
1	2	0.41696555	2.21×10^{-6}	0.41696568	2.91×10^{-6}	-1.11×10^{-7}	2.11×10^{-6}
1	4	0.4139153	1.71×10^{-6}	0.41391539	3.14×10^{-6}	-8.61×10^{-8}	2.83×10^{-6}
1	5	0.41864544	1.85×10^{-6}	0.4186455	3.47×10^{-6}	-6.25×10^{-8}	2.82×10^{-6}
1	6	0.42254292	1.81×10^{-6}	0.42254303	3.58×10^{-6}	-1.11×10^{-7}	2.89×10^{-6}
2	1	0.42139504	2.4×10^{-6}	0.42139507	2.44×10^{-6}	-2.22×10^{-8}	1.54×10^{-6}
2	2	0.41778822	1.58×10^{-6}	0.41778835	2.05×10^{-6}	-1.54×10^{-7}	2.24×10^{-6}
2	3	0.41793795	1.37×10^{-6}	0.41793795	2.24×10^{-6}	3.56×10^{-8}	1.93×10^{-6}
2	4	0.41953731	1.63×10^{-6}	0.41953736	3.27×10^{-6}	-4.7×10^{-8}	2.81×10^{-6}
2	5	0.42116343	2.03×10^{-6}	0.42116351	3.5×10^{-6}	-5.67×10^{-8}	3.33×10^{-6}
2	6	0.41957802	1.56×10^{-6}	0.4195781	3.37×10^{-6}	-8.08×10^{-8}	2.85×10^{-6}
3	1	0.42190429	1.81×10^{-6}	0.42190452	2.48×10^{-6}	-2.35×10^{-7}	1.77×10^{-6}
3	2	0.42243448	1.91×10^{-6}	0.42243459	2.52×10^{-6}	-1.13×10^{-7}	1.82×10^{-6}
3	3	0.42638026	2.18×10^{-6}	0.42638029	2.5×10^{-6}	-2.77×10^{-8}	1.72×10^{-6}
3	4	0.42927866	2.38×10^{-6}	0.42927868	3.89×10^{-6}	-6.31×10^{-8}	5×10^{-6}
3	5	0.4284962	1.44×10^{-6}	0.42849604	2.95×10^{-6}	2.04×10^{-7}	3.25×10^{-6}
3	6	0.42479075	1.95×10^{-6}	0.42479073	3.25×10^{-6}	1.99×10^{-8}	2.78×10^{-6}

Table 6.7: The external FSI asynchronous analysis results

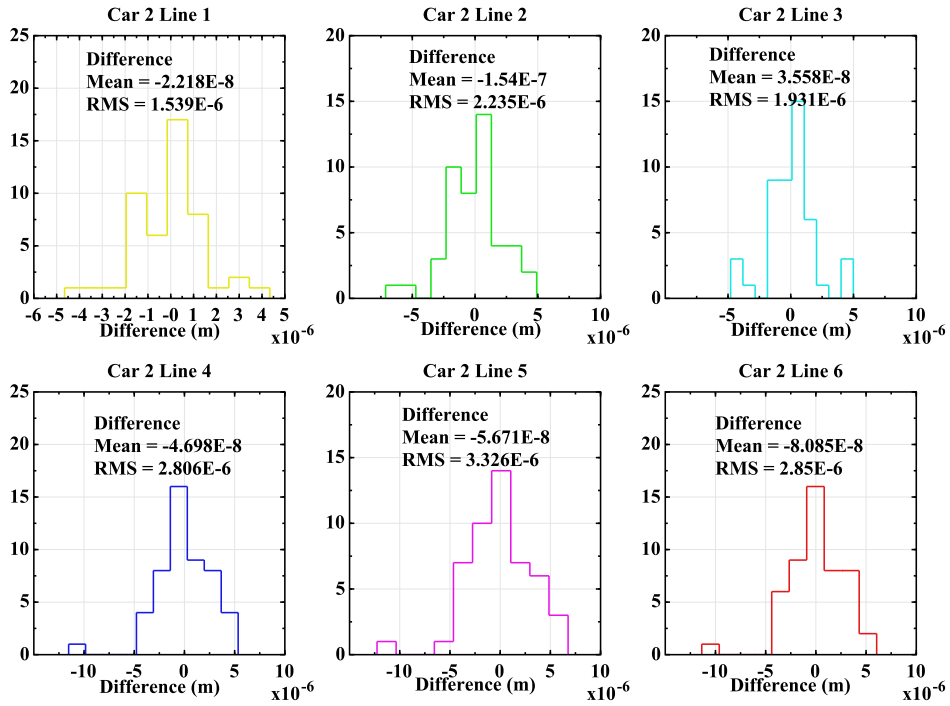

Figure 6.20: Histograms showing the difference between the external FSI lengths measured by Car 2 during the rapid scan analysed with the synchronous and asynchronous reference interferometer

internal FSI fringe phase advance is only 4.33 radians the fringes will be heavily warped by using the incorrect reference phase which will degrade the peak in the reference phase space Lomb periodogram as shown in figure 6.21. If figure 6.21 is compared to figure 6.4 which is the Lomb periodogram with the correct reference, the range covered by figure 6.21 is six times figure 6.4; the sharp peak in figure 6.4 is washed out. The external FSI has a phase advance of 43.3 radians per fringe and so the effect is much weaker.

If however there is a reference, external and internal interferometer, with the reference data being asynchronous (the external and internal are synchronous) a length measurement for the internal FSI can still be determined. In the analysis, the external FSI line is analysed against the asynchronous reference and its length ($L_{external}$) determined. In the next step the internal FSI line can be treated in the analysis as a reference interferometer and analysed against the external line to find, L_{ext}/L_{int}, and so L_{int} can be determined. This will however lead to a larger error on L_{int}; if $\sigma_{L_{ext,Async}}$ is of the order 2.5μm then the error on L_{int} will be of the order of 25μm, as the internal FSI is approximately ten times longer than the external

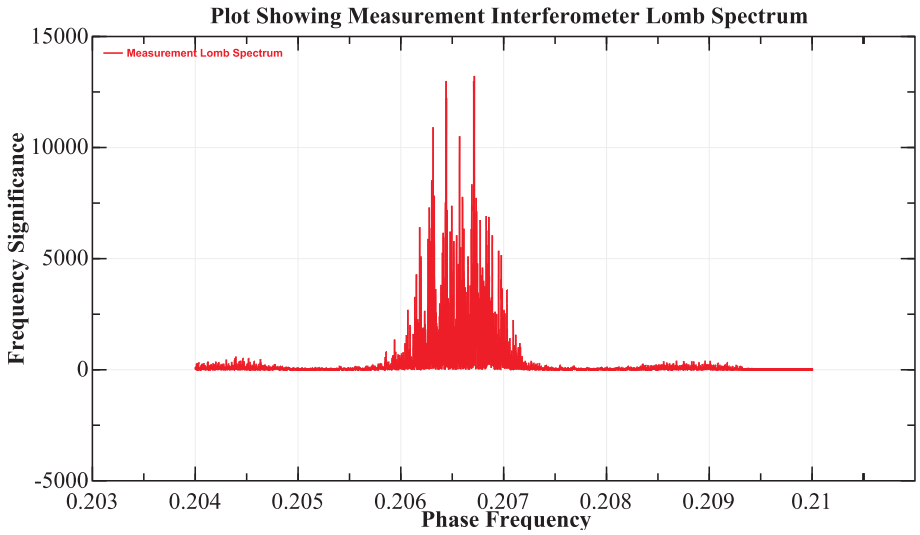

Figure 6.21: The Lomb periodogram of an internal FSI line using an asynchronous reference interferometer.

FSI.

6.8 FSI subsystem comparison

In this section the internal FSI, external FSI and tilt sensor subsystems are compared. To do this an experiment was performed where all of the LiCAS RTRS subsystems took data every 10 minutes. Nothing on the LiCAS RTRS was actively moved during the experiment and any movement is due to mechanical creep. This experiment is referred to as "stability run 27/10/2008". Figure 6.22 shows the tilt sensor measurements during the stability run. Note that car 3 rotation around X tilt sensor has failed during this run. Figure 6.23 shows the internal FSI reconstruction during the stability run from car 2 to car 1 and from car 3 to car 2. For the internal FSI reconstruction the values for Pf_x, Pf_y are set to zero. Figure 6.24 shows the external FSI wall marker reconstruction during the stability run for all three units.

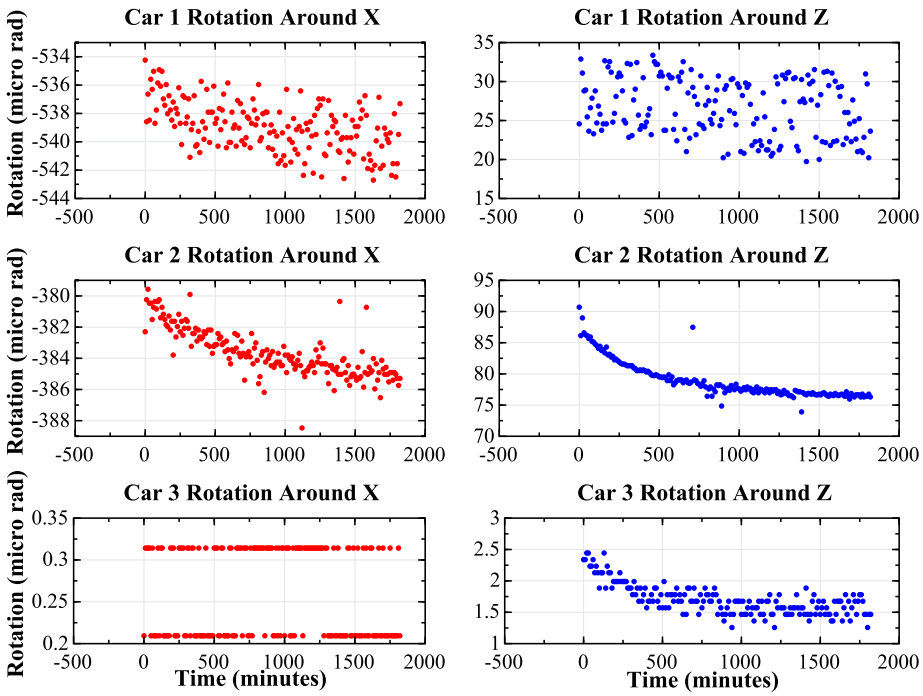

Figure 6.22: Tilt sensor measurements during the stability run 27/10/2008.

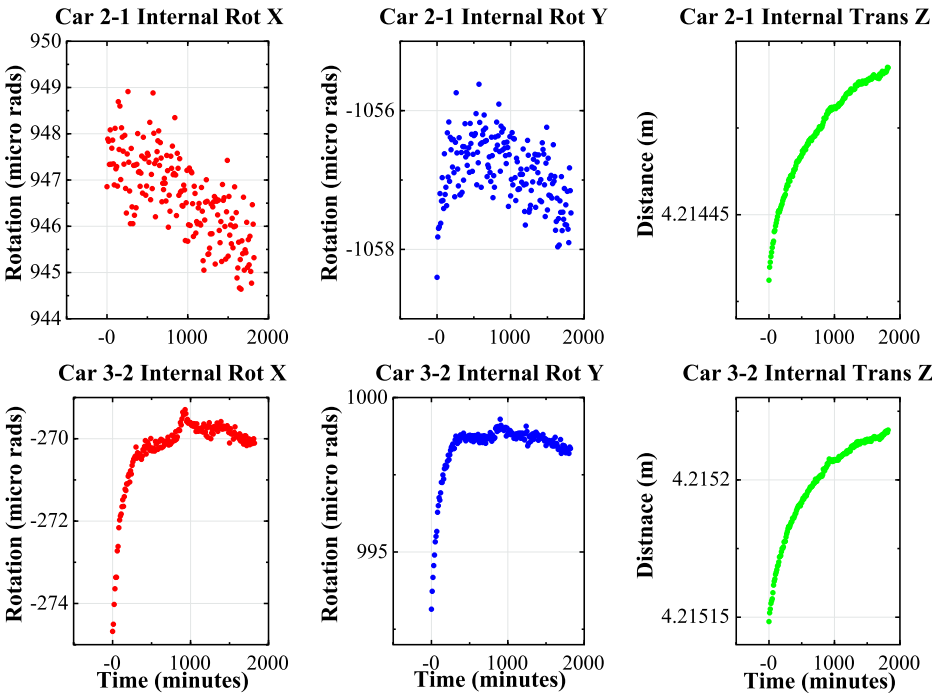

Figure 6.23: Unit co-ordinate reconstruction during the stability run 27/10/2008 using internal FSI.

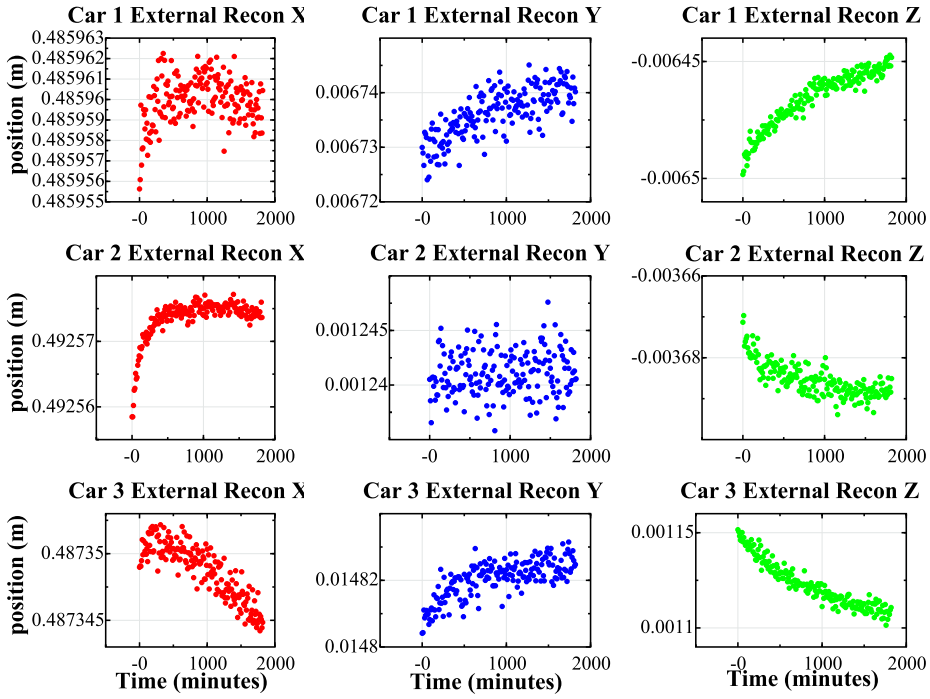

Figure 6.24: Wall marker reconstruction during the stability run 27/10/2008 using external FSI.

6.8.1 Internal vs external Z translation comparison

The internal FSI system on the LiCAS RTRS can determine the Z distance and rotations around the X and Y axis (section 6.2.3) between two units. The external FSI system can determine the position of a wall marker with respect to the unit (section 6.1.2). If there are two units, which monitor separate wall markers (M_1 and M_2), and the internal FSI measures the distance between the two units (D); if the retro reflectors do not move during data taking, the following equation holds:

$$M_{1,z} - M_{2,z} - D = constant. \tag{6.10}$$

Where $M_{1,z}$ and $M_{2,z}$ are the Z components of M_1 and M_2. If the measurement systems are functioning correctly then the above equation should be true within the measurement errors.

The external FSI wall marker reconstruction obtains wall marker co-ordinates in its own frame, and this frame co-rotates with the units. Any rotation round the Y axis will appear

in the external FSI wall marker reconstruction as a shift in the X and Z wall marker position. The shift in the X measurement will be small as it is dependant on the cosine of the angle, however the Z measurement will be affected significantly as it is dependent on the sine of the angle. For this reason we want to compare the Z translations when rotations around the Y axis are small. Figure 6.23 shows that during the stability experiment, the relative rotation around the Y axis between cars 2 and 3 is approximately 60μradians in the first 500 minutes. The first 500 minutes will therefore be ignored for car 2 to 3 analysis. Figure 6.23 shows that during the stability run experiment the rotations around the Y axis for cars 1 and 2 has no significant rotations and all the data is used for the analysis.

Figure 6.25 shows the difference between the Z-translations determined by the internal and external FSI systems for cars 1 to 2 and cars 2 to 3 during the stability run 27/10/2008 experiment. Data from the first 500 minutes is removed in the cars 2 to 3 analysis as explained above. The data for both analysis is plotted against time and histogrammed. From the histograms in figure 6.25 the agreement between the internal and external FSI is 3.4μm and 4.0μm for cars 1 to 2 and cars 2 to 3 respectively. If the external FSI has a precision of approximately 2.5μm and the internal FSI a precision of approximately 0.29μm, then combining the errors of the two external FSI systems and the Internal FSI system will give an approximate error of 3.5μm. This shows that the internal and external FSI systems agree with the expected errors for the car 1 to 2 analysis, but for the car 2 to 3 analysis there is a slight discrepancy of 0.5μm. An error of 0.5μm in the reconstruction of the wall maker corresponds to a unit rotation around the Y-axis of 1.1μrad which is smaller than the precision of the internal reconstruction rotation around Y axis and so the discrepancy could be explained by the residual unit rotations around the Y axis.

6.8.2 Internal vs tilt sensor X rotation comparison

The internal FSI system can reconstruct the relative rotation around the X-axis between two units (section 6.2.3). The rotation around the X-axis tilt sensors for car 1 and car 2 can be combined and compared to the internal FSI reconstruction between units 1 and 2.

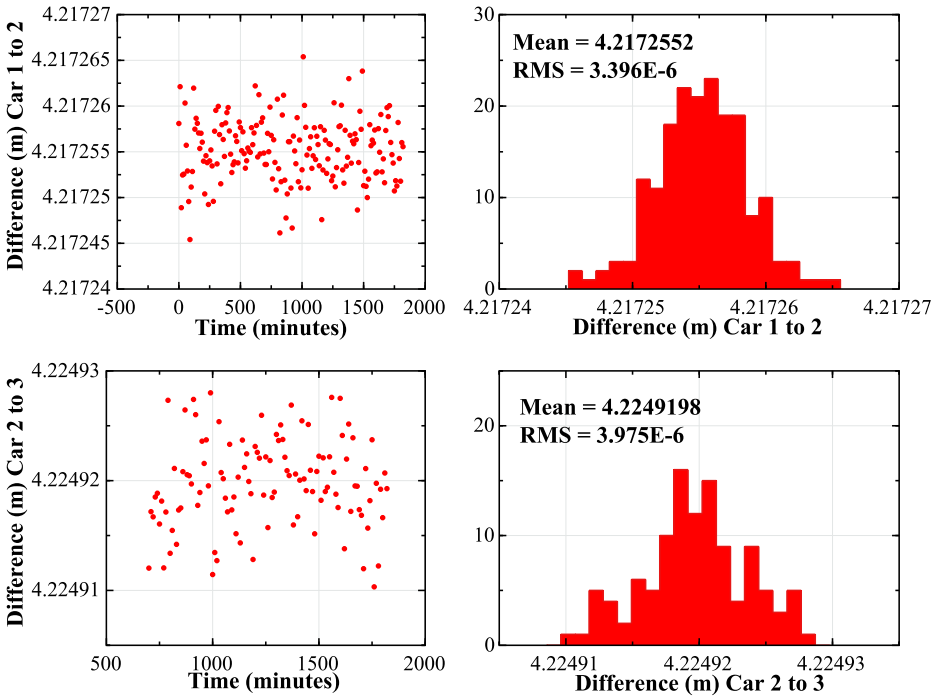

Figure 6.25: Figure shows the difference between the internal and external Z translation measurements during the stability run 27/10/2008.

Figure 6.26 shows the difference between the relative rotations measured by the internal FSI system from car 2 to car 1 and the difference between the rotations around the X axis on car 1 and car 2. As shown in chapter 2 the expected error of the tilt sensors is $\pm 11.3 \mu$radians, the error on the internal FSI rotation around the X axis is $\pm 12 \mu$radians leading to a combined error of $\pm 20.0 \mu$radians. The RMS shown in figure 6.26 is 18.1μradians showing the systems agree within errors.

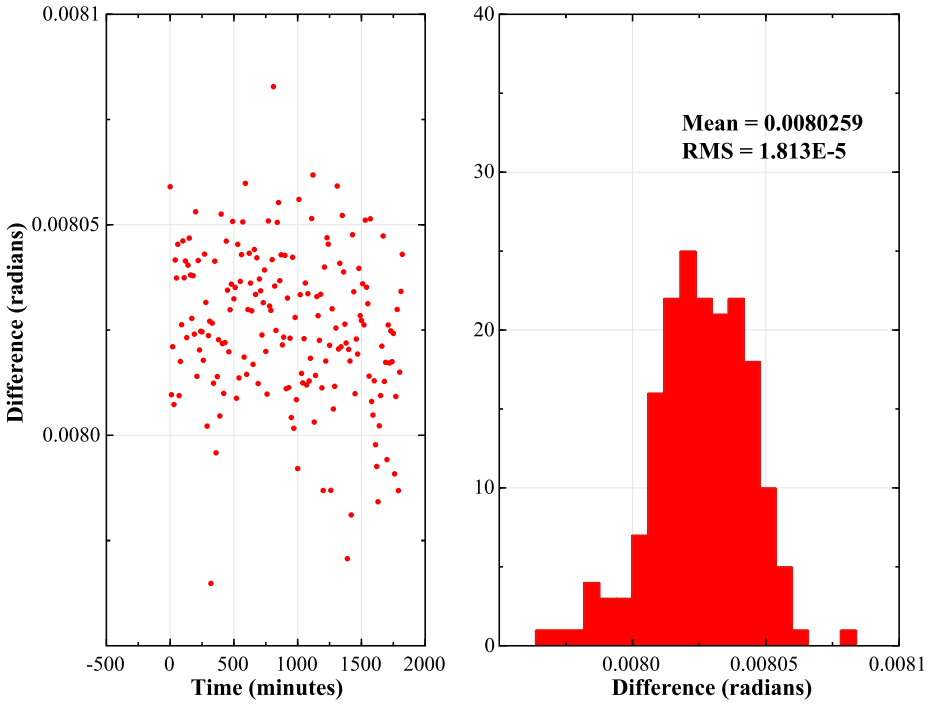

Figure 6.26: Figure shows the difference between the internal and tilt sensor X rotation measurements during the stability run 27/10/2008.

Chapter 7

Reference Network Simulations

For the design of the ILC, the effects of the misalignment of the main linac on the emittance, needs to be studied. In this chapter the survey process of the ILC main linac will be simulated using conventional surveying techniques. To simulate conventional surveying techniques a reference network has to be simulated along with measurements on that network. A reference network is a series of markers placed along the tunnel with their positions measured by a device such as a laser tracker. These device measurements are used to determine the position of all the markers in the network with respect to each other. The simulated networks are used to misalign a simulated ILC for the study of the performance of beam-based alignment (BBA). A simplified network simulation software capable of simulating reference networks measured with conventional, as well as novel techniques will also be presented and compared to full conventional simulations.

7.1 Dispersion matched steering (DMS)

Dispersion free steering (DFS) [47] is a BBA technique which can be used to minimize emittance growth in linear colliders. The technique requires that at least two different beams are injected into the main linac. The beams will have either different initial energies (initial energy adjustment), different accelerating gradient along the main linac (constant

gradient adjustment) or a combination of the two. The technique then adjusts the dipole correctors to minimize the difference in the trajectory of the two beams.

The ILC will be built to follow the earth's curvature; therefore the ideal beam trajectory will have non-zero dispersion, leading to the dispersion in the ILC being matched to the design specifications [48], not eliminated. Dispersion matched steering (DMS) achieves the optimum trajectory by minimizing the following merit function [49]:

$$\chi^2 = \sum w_{diff}^2[\Delta y_i(\delta) - \Delta\tilde{y}_i(\delta)]^2 + w_{abs}^2[y_i(0) - \tilde{y}_i(0)]^2. \tag{7.1}$$

Where $y_i(\delta)$ is the measured beam trajectory at the i^{th} BPM with relative momentum deviation from the nominal beam of $\delta = \Delta p/p$, $\Delta y_i(\delta) = y_i(\delta) - y_i(0)$ is the difference in the trajectories of the two different energy beams at the i^{th} beam position monitor (BPM), $\tilde{}$ represents the design values and w_{diff} and w_{abs} are weight parameters, with w_{diff} representing the RMS BPM position error and w_{abs} representing the RMS BPM offset error.

To measure the performance of DMS an estimation of the corrected emittance is calculated. The corrected emittance is the normalized emittance with the linear energy correlation numerically removed[1]; it is given by:

$$\gamma\epsilon_{yc} = \gamma\sqrt{\langle y^2\rangle_c\langle y'^2\rangle_c - \langle yy'\rangle_c^2}. \tag{7.2}$$

Where y and y' represent the vertical phase space coordinates of the particles in the beam and:

$$\langle y^2\rangle_c = \langle y^2\rangle - \frac{\langle y\delta\rangle^2}{\langle\delta^2\rangle}, \tag{7.3}$$

$$\langle y'^2\rangle_c = \langle y'^2\rangle - \frac{\langle y'\delta\rangle^2}{\langle\delta^2\rangle}, \tag{7.4}$$

$$\langle yy'\rangle_c = \langle yy'\rangle - \frac{\langle y\delta\rangle\langle y'\delta\rangle}{\langle\delta^2\rangle}. \tag{7.5}$$

[1] In practice the correction of the energy correlation is done using a closed trajectory dispersive bump, the numerical approach is equivalent to perfect corrective bump [49]

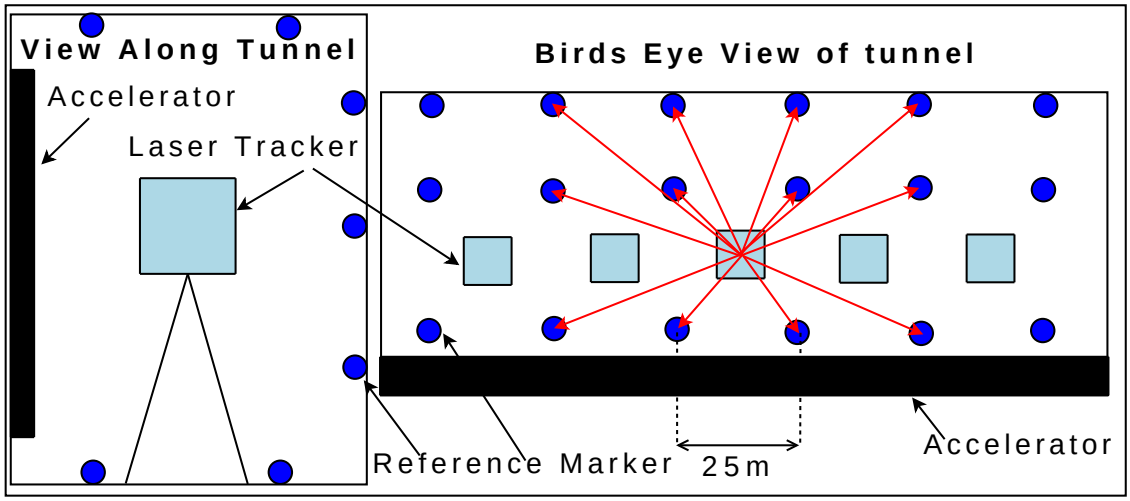

Figure 7.1: The reference marker configuration, for conventional network measurements, shown looking down the tunnel and looking along the tunnel.

7.2 Conventional survey methods

There are many possible techniques for the measurement of the ILC reference network. The conventional reference network measurement method studied here uses a laser tracker to measure reference markers (section 7.2.2), a small number of reference markers are linked using GPS measurements transferred from the surface (section 7.2.3). These are referred to as primary reference markers (PRMs). All of the measurements are described by a linear algebra model and processed by a solver (adjusted) to determine the marker positions (section 7.2.4). The adjusted network is then used to align a simulated ILC (section 7.2.5) for beam dynamics studies.

7.2.1 Reference network layout

The reference network used in the simulations is made up of rings of RMs. A ring consists of 7 RMs: 2 on the ceiling, 2 on the floor and 3 on the wall away from the accelerator (see figure 7.1). It is assumed that the accelerator will block the view to any RMs on the wall behind it and for simplicity the tunnel is assumed to be rectangular; which is not expected to affect the results significantly. One such ring is placed every 25m along the tunnel.

7.2.2 Laser tracker measurements

The laser tracker is placed between two reference marker rings in the tunnel and measures two RM rings in both directions as shown in figure 7.1. It is then moved 25m along the tunnel and measures a different set of RM rings, which overlaps with the previous. This is repeated down the entire length of the main linac tunnel. The laser tracker is only capable of short range measurements of approximately 40m. Overlapping short range measurements can cause long range error growth. The long range error growth can be reduced with the use of primary reference markers as described in section 7.2.3.

7.2.3 Primary reference marker measurements

Primary Reference Marker (PRM) measurements are long range (approximately 2.5km) measurements between RMs. These measurements are less accurate than, for example, the laser tracker measurements and are to reduce long range error growth. The method simulated here uses GPS measurement stations on the surface which can determine their position with respect to each other. The GPS position information is then transferred down into the tunnel via access shafts. The transferred GPS information is then used to determine the position of a PRM at the bottom of each access shaft with respect to the PRMs at the bottom of the other access shafts. The solution of the GPS stations and the transfer process through the shafts are not simulated here in detail, instead an error for the combined GPS measurement and transfer is assumed (see table 7.1). The PRM measurements are modelled as vector difference measurements between PRMs.

7.2.4 Network adjustment

The final RM positions can be determined by a process called network adjustment. Network adjustment takes all of the measurements in the network (for example GPS and laser tracker measurements) and uses a linear algebra model to determine the best fit RM positions. The network adjustment is performed by PANDA [50]. PANDA is a software package which

can design, optimize, adjust (solve for positions) and assess 3D networks. It is commercial software used by, for example, the DESY geodesy group [45]. PANDA produces the position and position errors of all the RMs.

7.2.5 Main linac alignment against the reference network

With the reference network determined, the components of the main linac can be aligned with respect to it. In practice this is done by placing a laser tracker in the tunnel near the component to be aligned. The laser tracker measures its position with respect to several local RMs, and using the knowledge of the adjusted network, determines its own position in the tunnel. The laser tracker then uses this information to determine the components position which is then moved to the required location. The accelerating components of the ILC will be fiducialised as described in section 1.3.7.

For the simulations covered in this chapter a simplified method is used; this method simply uses the 3 closest RM rings (see section 7.2.1) and fits a straight line to them. The fitted straight line is then used to determine the position of the component. Note that the misalignment of the rotation around the longitudinal axis is not simulated here.

In practice the entire ILC reference network will be surveyed in one go, however, in the simulations below only the main linac section is simulated. The simulated network's first point will not be at (0,0,0) and this will lead to the start of the ML being offset from the end of the RTML. An offset in the positions of the RTML and ML can cause a kink in the beam line, which in turn can cause emittance blow up. As the connection from the ML to the RTML should be smooth, the simulated networks are shifted vertically and horizontally so the start of the ML matches with the RTML. The RTML is not misaligned during the simulations.

7.2.6 PANDA reference network simulations

Two groups of reference network simulations were performed using PANDA, one without and one with PRMs. The simulations consisted of first generating all of the laser tracker measurements and/or PRM measurements using a JAVA program. The program requires the nominal reference network geometry and all measurement errors to be input; the program does not apply any systematic errors. Systematic errors would be expected because the refractive index of air varies along the tunnel due to temperature variations, as described in section 1.4.1. Not taking account of systematic errors will make the simulations optimistic. The simulated measurements have Gaussian noise added (see table 7.1 for values) and PANDA is used to determine the final RM positions.

Laser Tracker Parameters			PRM parameters
Distance	Azimuth	Zenith	PRM uncorrelated errors Δx, Δy, Δz
0.1mm+0.5ppm	0.3 mgon (4.7 μrad)	0.3 mgon (4.7 μrad)	10mm

Table 7.1: Simulation error parameters. Note errors are assumed to be uncorrelated. (Errors are give by experienced DESY surveyors [45])

Simulations without primary reference marker measurements

The simulations were initially performed without PRMs. PANDA was used to determine the errors on the adjusted network (see figure 7.2). The error curves shown in figure 7.2 follow a double minima curve as expected.

Twenty reference networks were simulated and adjusted in this way; the difference from the truth in the horizontal and vertical plane for each run is shown in figures 7.3 and 7.4 respectively. Figure 7.3 appears as expected, given the horizontal errors shown in figure 7.2. Figure 7.4, does not appear as expected, given the vertical errors shown in figure 7.2; it has a large systematic curvature and clearly indicates a problem with the PANDA network adjustment. The incorrect systematic curvature could lead to problems as we wish to study the vertical emittance using DMS; however, if we compare the horizontal and vertical errors from figure 7.2, we see that they have similar shape and size. This allows us to use the

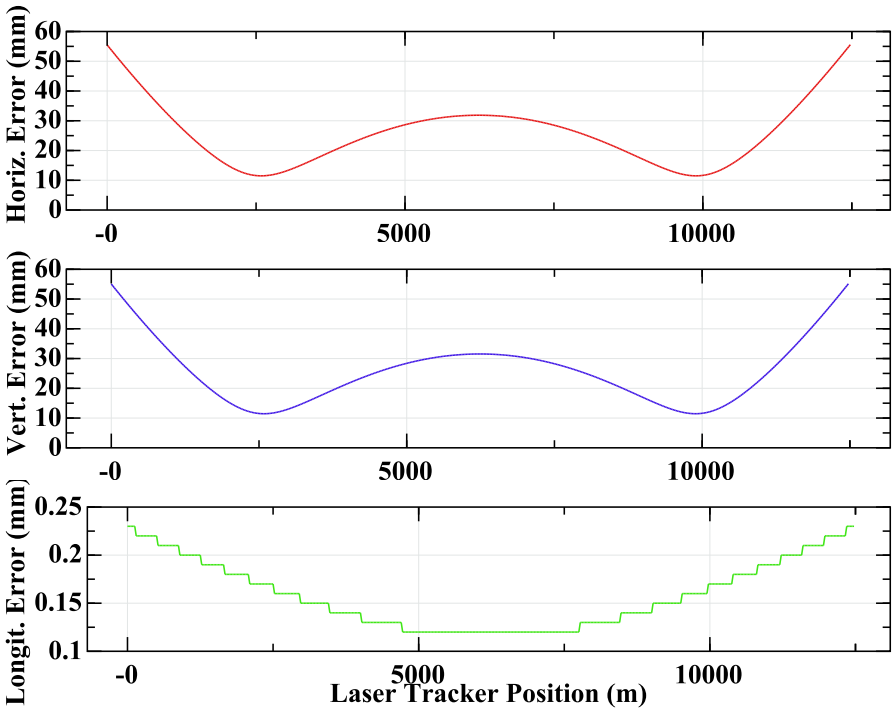

Figure 7.2: The horizontal, vertical and longitudinal errors on the reference network simulated by PANDA without PRM

horizontal adjusted network positions as the vertical adjusted network positions in the DMS simulations and work around the PANDA problem. Note that this problem has been reported to the producers of PANDA.

Simulations with PRM

A second set of simulations with PRM's were also performed. As before PANDA was used to determine the errors on the adjusted network (see figure 7.5). The error curves shown in figure 7.5 follow the expected double minima curve, with a pull down effect caused by the PRMs. They also show the expected similarity between horizontal and vertical errors.

Twenty reference network simulations with PRMs were performed. The truth was subtracted from the horizontal and vertical reconstructed positions and the difference plotted in figures 7.6 and 7.7 respectively.

The horizontal difference, shown in figure 7.6, appears again as expected given the hor-

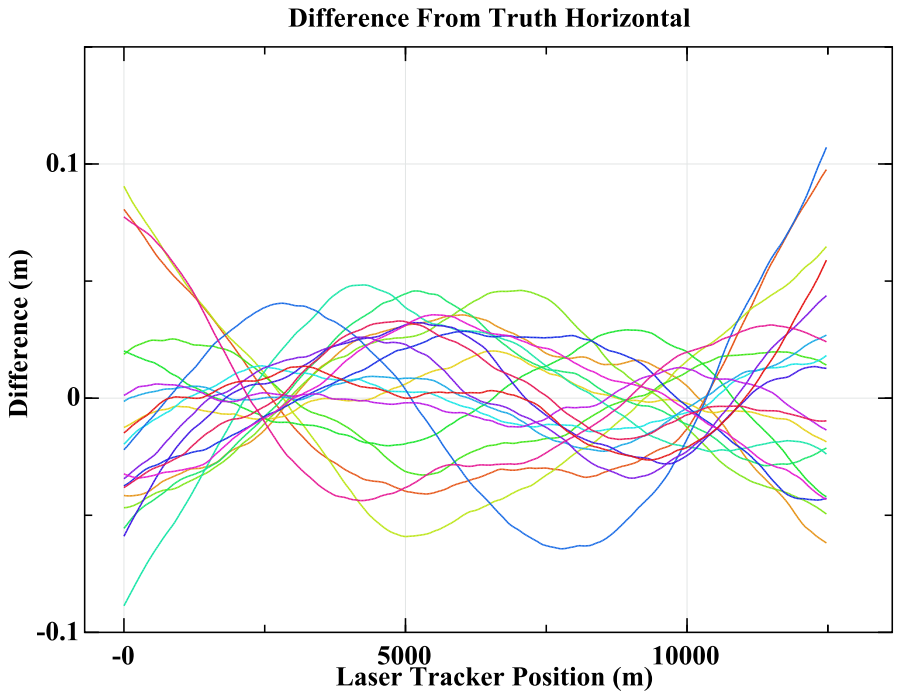

Figure 7.3: The horizontal difference from truth simulated by PANDA without PRM

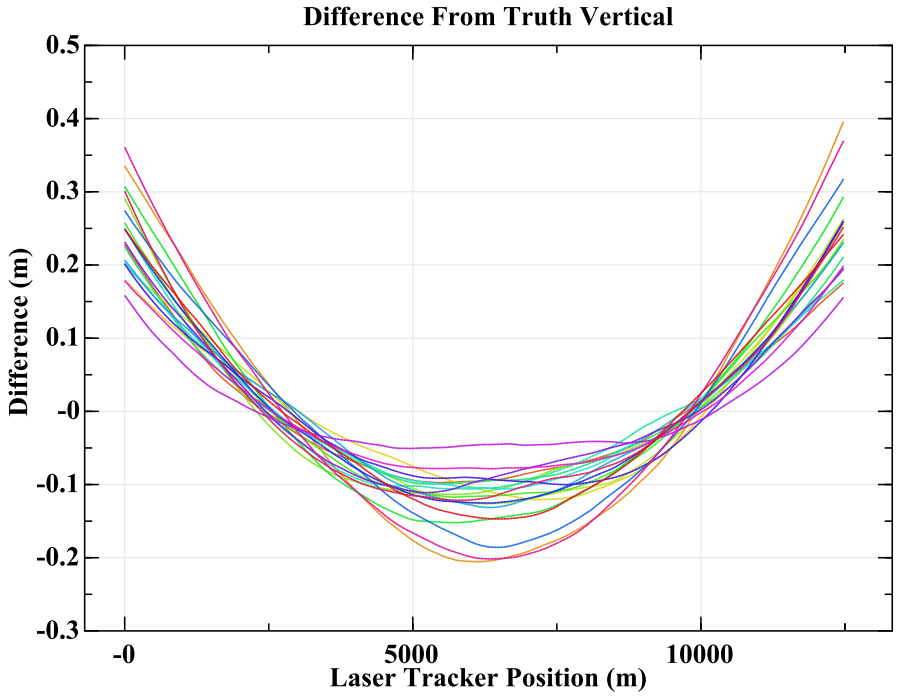

Figure 7.4: The vertical difference from truth simulated by PANDA without PRM

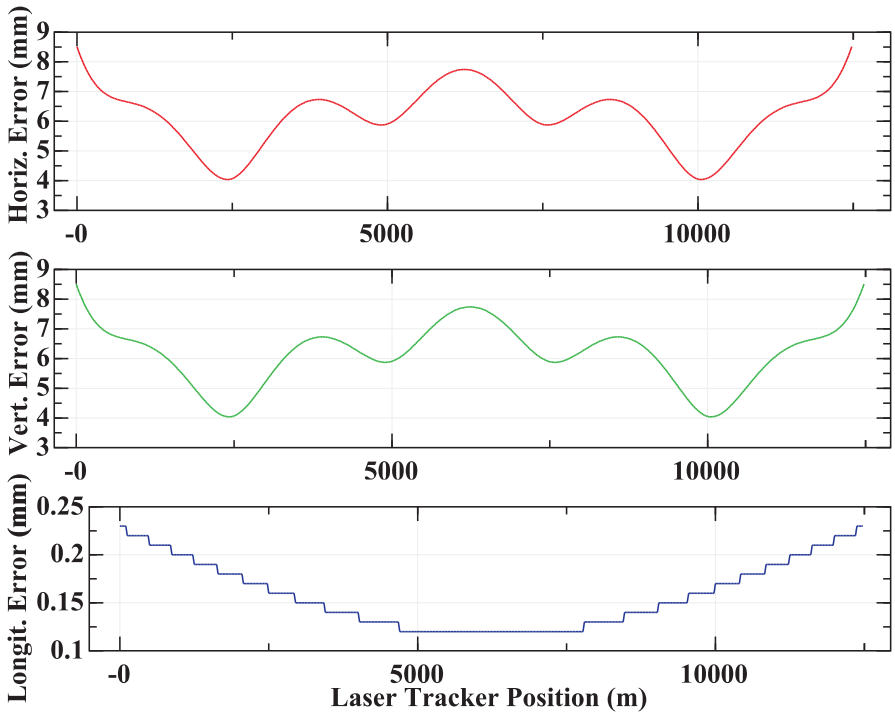

Figure 7.5: The horizontal, vertical and longitudinal errors on the reference network simulated by PANDA with PRM

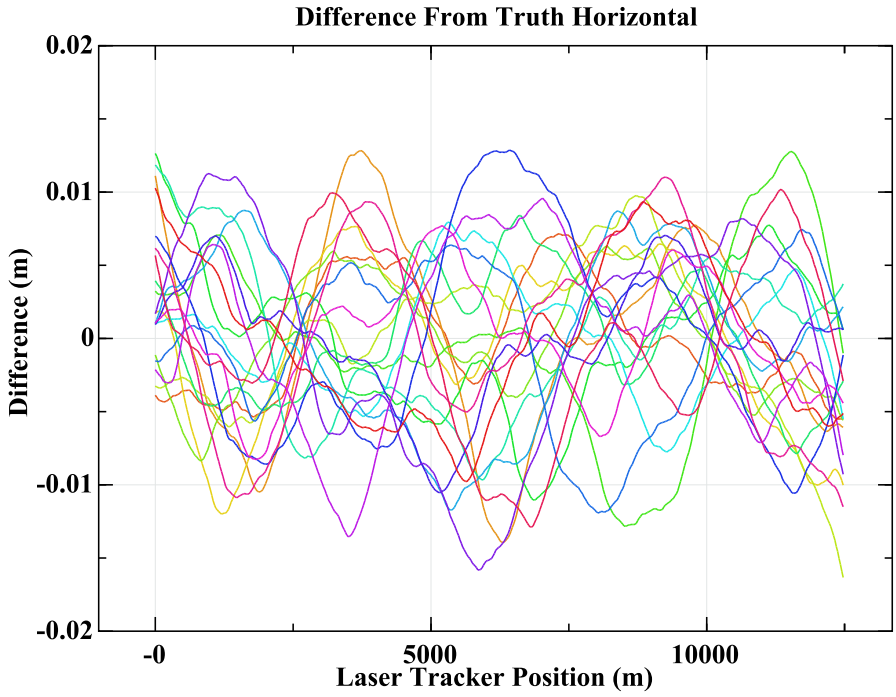

Figure 7.6: The horizontal difference from truth simulated by PANDA with PRM

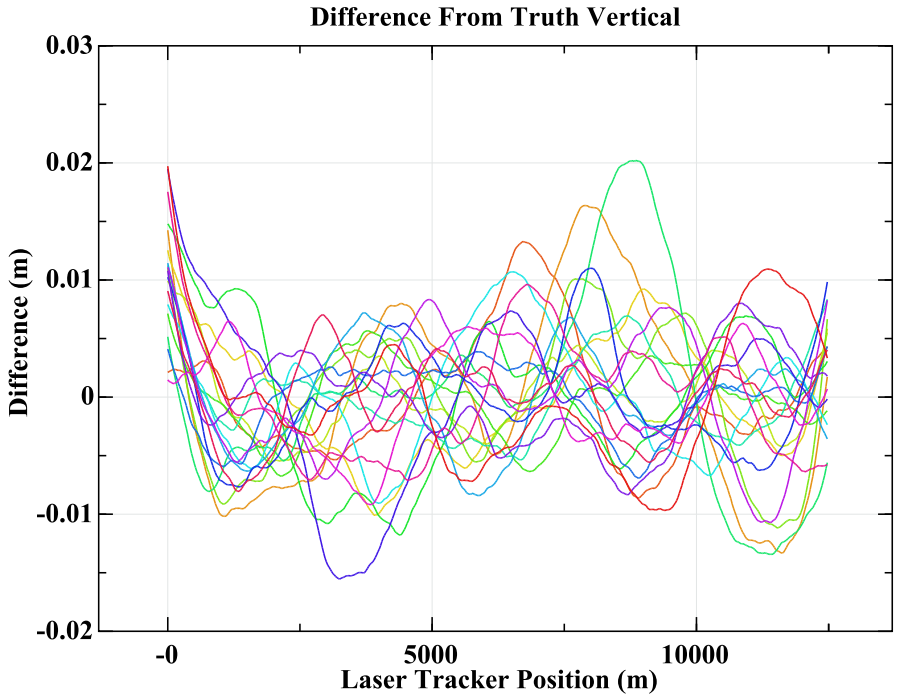

Figure 7.7: The vertical difference from truth simulated by PANDA with PRM

izontal errors shown in figure 7.5; however the vertical difference from the truth, shown in figure 7.7, again do not appear as expected. Figure 7.7 has a systematic curvature at the start indicating the same problem with the PANDA software seen in section 7.2.6. Although the systematic curvature is a problem, the horizontal network can again be used to misalign the vertical plane of the simulated ILC.

7.2.7 Dispersion matched steering on a conventional aligned ILC main linac

To perform DMS simulations the positron side of the ILC main linac is simulated using the ILCDFS package [51] which is part of the Merlin C++ library [52]. Simulated components are positioned within cryomodules with the random errors given in table 1.7. These errors represent the error with respect to the functional beam axis. The supports of the cryomodules are aligned with respect to the reference network as described in section 7.2.5.

The DMS was set up with the parameters shown in table 7.2, these parameters have been

Parameter	Value
Initial Beam Emittance	20nm
Nominal Beam Starting Energy	15GeV
Nominal Beam Final Energy	250GeV
Initial energy of the Test Beam	-20%
Constant Gradient Adjustment	-20%

Table 7.2: Dispersion matched steering initial parameters

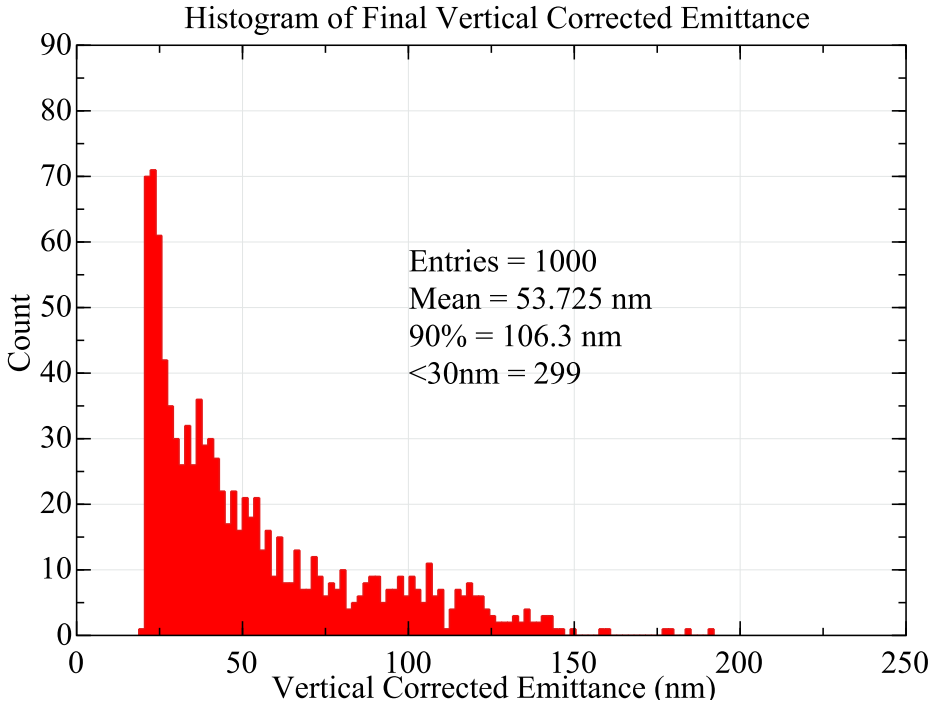

Figure 7.8: DMS results using PANDA simulated networks without PRM

shown to be effective in obtaining low emittance [49]. The simulations use two beams, one at nominal energy and one with the reduced energy and constant gradient adjustment.

Simulations without PRM

One hundred networks were simulated without PRMs and on each network ten DMS simulations were performed. In each DMS simulation a different random seed is used to determine the accelerator component positions and the beam make up, we will refer to one DMS simulation as a run. The final vertical corrected emittance for each run is shown in the histogram in figure 7.8.

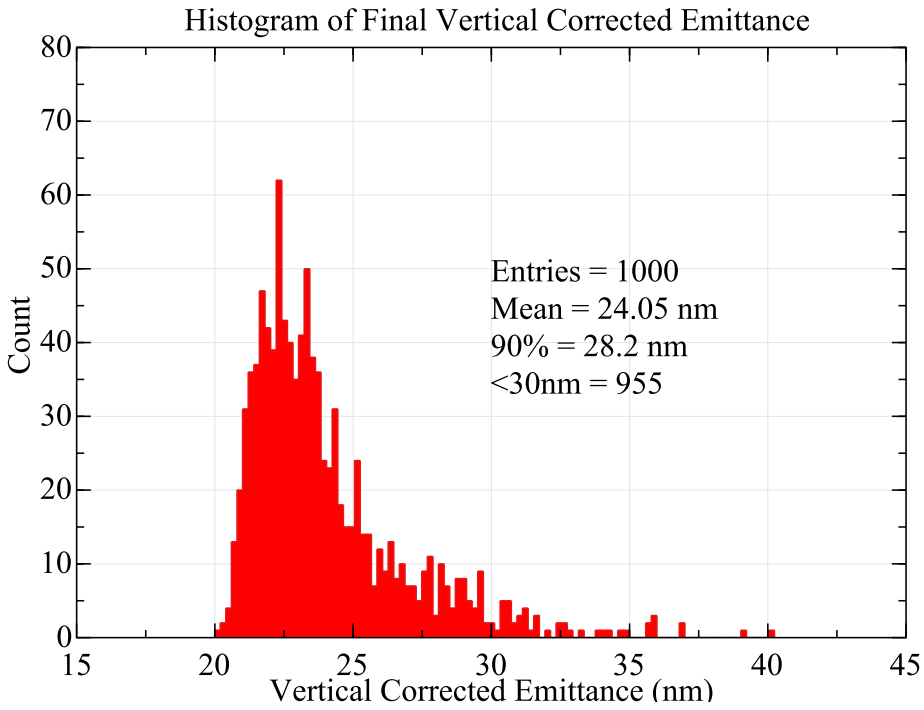

Figure 7.9: DMS results using PANDA simulated networks with PRM

From figure 7.8 it is shown that without using PRM's only 30% of the simulations give a final corrected vertical emittance of less than 30nm. It is required that at least 90% are below 30nm and so without PRMs the ILC can not achieve the required performace. Note that the simulations use the low bunch population regime and so the beam emittance is required to be 30nm not the nominal 40nm.

Simulations with PRM

One hundred networks were simulated with PRMs and on each ten DMS simulations were performed. The final vertical corrected emittance for each run is shown in the histogram in figure 7.9.

Figure 7.9 shows that with PRM's 95% of the simulations give a final corrected vertical emittance of less than 30nm; which is better than the 90% required. This shows that if systematic errors are ignored then this process has the precision required to align the ILC.

7.3 Simplified network simulations

The PANDA software can be used to do reference network simulations as described above. However; there are some problems using PANDA for the large number of networks simulations required for the ILC. PANDA is a commercial software and so understanding of its internal workings is not possible, and from the problems with the residues shown in figures 7.4 and 7.7 such an understanding is needed. To use PANDA licences are required; to purchase a license for all researchers doing beam dynamics simulations is prohibitably expensive. PANDA can only do simulations using conventional techniques; any novel techniques for measuring the reference network can not be simulated using the software. There are also some questions about the reliability of PANDA, as shown by the systematic errors in figure 7.7.

To simulate reference networks measured with novel techniques, and to generate the large number of networks required for beam dynamics simulations a simplified network simulation software has been produced. This software should: be able to be used by people without detailed surveying knowledge, give similar DMS and error curve results to PANDA, not involve the use of any commercial software and be capable of generating the large number of networks required beam dynamics simulations.

7.3.1 Reference network layout

The networks simulated in the simplified network simulation software have rings of four markers placed every 25m along the tunnel. The layout of the markers in a ring is shown in table 7.3. Four markers are used in a ring instead of seven (as used in the PANDA simulations) as the simplified simulation software has not been optimised for memory performance and seven markers requires more memory than is available.

Marker Number	X Coordinate (m)	Y Coordinate (m)
1	0.0	0.0
2	3.0	0.0
3	0.0	3.0
4	3.0	3.0

Table 7.3: Layout of a marker ring in the simplified network simulation software

7.3.2 The measurement simulations

There are two types of measurements simulated in the software: Long range measurements of PRMs and short range measurements of regular RMs.

There are 6 PRMs in the network, placed 2.5km apart. At the ILC these measurements may take the form of GPS measurements on the surface which are transferred to the reference markers in the tunnel via access shafts. PRM measurements are simulated as vector differences in the global frame, the measurements have Gaussian noise added with no correlation.

Standard network measurements, as made by devices such as a laser tracker or a LiCAS RTRS, are simulated as follows. The device makes overlapping measurements on the network, measuring four rings in one position and then advancing along the tunnel by one ring. The measurements at one position are simulated as vector differences between all adjacent markers as shown in figure 7.10.

The vector differences are measured in the device's frame of reference. The device frame of reference has three possible rotations with respect to the global frame: rotations around the x-axis (θ), the y-axis (ϕ) and the z-axis (ω). The vector difference between two adjacent markers in the global frame is given by:

$$\begin{bmatrix} \Delta X \\ \Delta Y \\ \Delta Z \end{bmatrix} = \begin{bmatrix} X_{n+1} - X_n \\ Y_{n+1} - Y_n \\ Z_{n+1} - Z_n \end{bmatrix}. \tag{7.6}$$

Where (X_n,Y_n,Z_n) represent the n^{th} reference marker position in the global co-ordinate

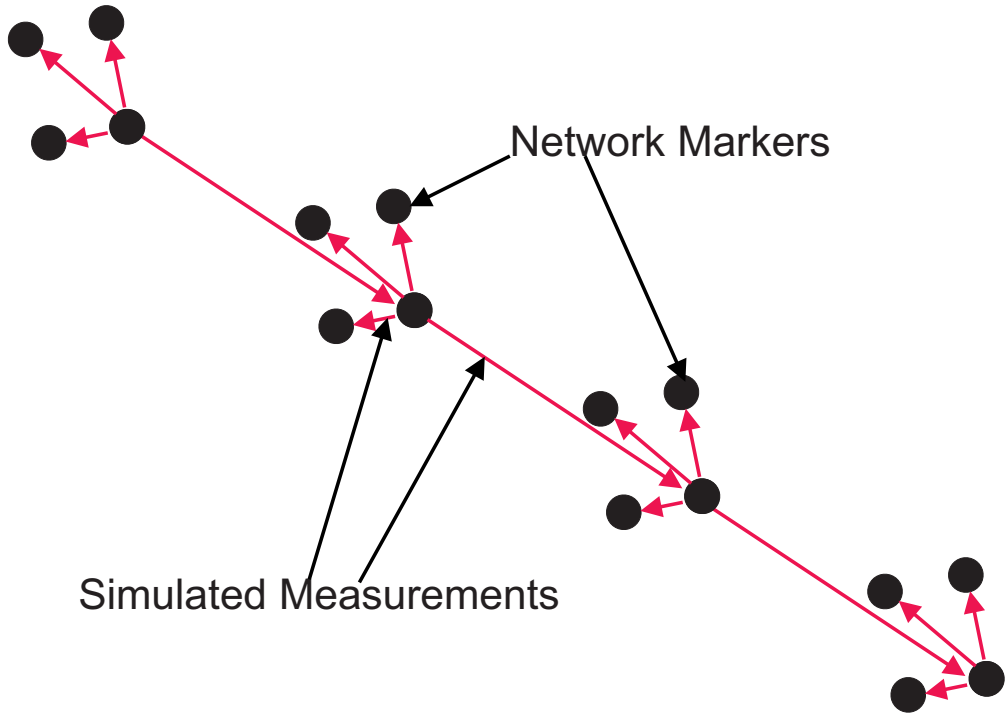

Figure 7.10: Simplified simulation model network measurement procedure for one stop. The arrows show the vector difference measurements taken.

system. To get the vector difference in the device frame we need to allow three rotations between the global and device frame. The rotation matrix for one device position is R:

$$R = \begin{bmatrix} \cos(\omega)\cos(\phi) & -\cos(\phi)\sin(\omega) & \sin(\phi) \\ \cos(\theta)\sin(\omega)+\cos(\omega)\sin(\theta)\sin(\phi) & \cos(\omega)\cos(\theta)-\sin(\omega)\sin(\theta)\sin(\phi) & -\cos(\phi)\sin(\theta) \\ \sin(\omega)\sin(\theta)-\cos(\omega)\cos(\theta)\sin(\phi) & \cos(\omega)\sin(\theta)+\cos(\theta)\sin(\omega)\sin(\phi) & \cos(\theta)\cos(\phi) \end{bmatrix}. \tag{7.7}$$

Leading to difference measurements in the devices frame, for one vector difference being:

$$\begin{bmatrix} \Delta X' \\ \Delta Y' \\ \Delta Z' \end{bmatrix} = R \begin{bmatrix} \Delta X \\ \Delta Y \\ \Delta Z \end{bmatrix}. \tag{7.8}$$

The measurement errors are simulated by adding Gaussian noise with no correlations.

7.3.3 The linearised mathematical model

The vector difference measurements described in the above sections, for all stops, are combined in a linearised mathematical model; which is used to determine the best fit marker positions. The linearised model used for the simulations is a parametric model (see section 3.2). For the parametric model several matrices and vectors need to be defined: vector L contains the PRM and RM measurements, vector X contains all of the current best estimate for the positions of the RMs and the device rotations (Note that the initial values for X are the design values), the function vector $F(X) = L$, the residual vector $W = F(X) - L$, the matrix of partial derivatives $A = \frac{\partial F(X)}{\partial X}$ and the covariance matrix for all measurements P. P is modelled as a single diagonal matrix as we assume no correlation between the errors.

7.3.4 Constraints

In the simplified simulation model described above, $A^T PA$ is singular and therefore the model requires constraints. Several different methods to constrain the simplified simulation model are described in the following sections.

Eigenvalue Decomposition (EVD) at each iteration

The standard way to constrain this type of problem is described in section 3.3 and involves using an eigenvalue decomposition of $A^T PA$ on each iteration, as this will minimise the trace of the output covariance matrix at each iteration. It is however very slow for our purposes as it takes up to one hour per iteration and up to 10 hours to generate a network. Different ways to constrain the network are discussed in the next sections and compared to this method. The simulations all use the same random seed.

This method is regarded as the best method as it will minimise the trace of the covariance matrix on each iteration; other methods will be compared to this method. To compare other methods to the full EVD method, all the adjusted networks have a straight line fitted to the x,y and z projections and the residues in each projection found. The difference between the

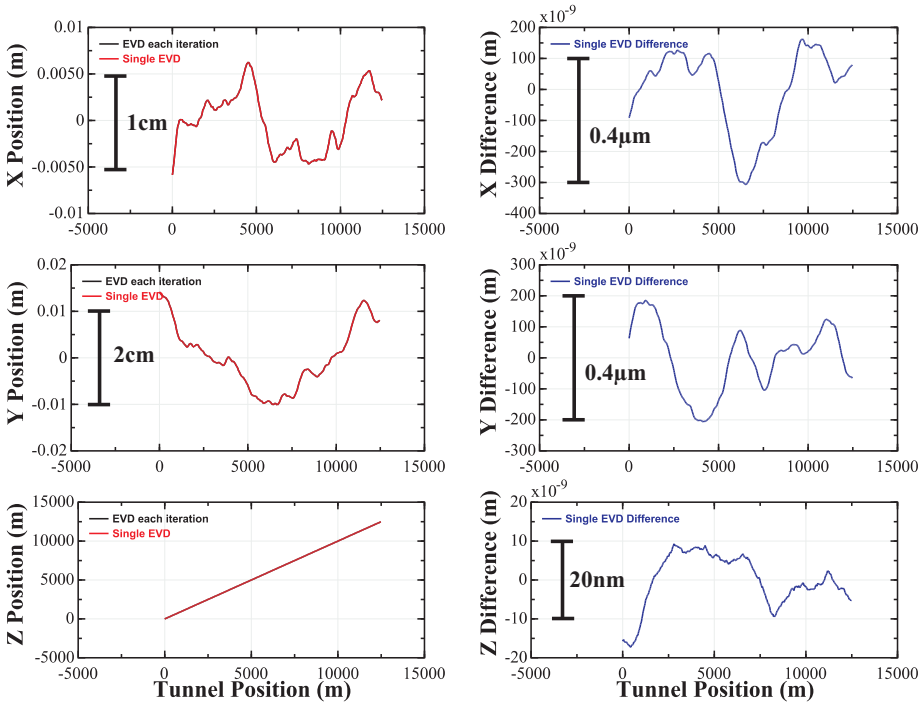

Figure 7.11: Figure comparing a single EVD constraint method to a solution with a full EVD constraint method. In the left figures the two lines are indistinguishable as the difference is at the 0.004% level.

residues from the full EVD method and the comparison method are then computed.

Single EVD at start

A faster way of using an EVD is to only compute one EVD at the start of the solution and use its results to constrain all iterations. Figure 7.11 shows the results of the network adjustment with the single EVD constraint method and the full EVD constraint method along with the differences. Figure 7.12 shows the result if a second EVD is computed for the last iteration. To solve without a final EVD takes approximately one hour. A final EVD takes approximately forty minutes extra.

The analysis was performed with four different random seeds with the range of the differences shown in table 7.4. Table 7.4 shows that both approaches give good approximations to the full EVD solution, however the results with an EVD at the end approximates those with EVD at each iteration more closely but at an irrelevant level of difference. This shows that

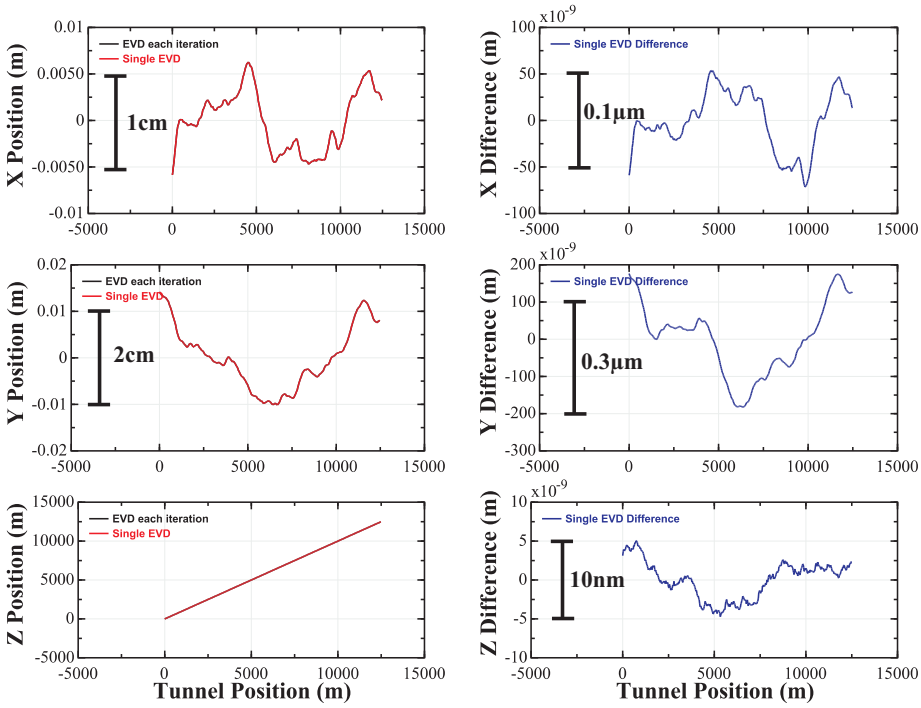

Figure 7.12: Figure comparing a single EVD with a final EVD constraint method to a solution with a full EVD constraint method. In the left figures the two lines are indistinguishable as the difference is at the 0.001% level.

the networks constrained with the single EVD constraint method is a good approximation to the networks constrained with the full EVD constraint method.

If multiple networks are required with the same input parameters, then the initial EVD can be used for all simulations. This will save approximately forty minutes on subsequent networks.

Run Number	With or without end EVD	Difference range (m)		
		X axis	Y axis	Z axis
1	without	4.70×10^{-7}	3.92×10^{-7}	2.66×10^{-8}
1	with	1.25×10^{-7}	3.59×10^{-7}	9.77×10^{-9}
2	without	4.18×10^{-7}	3.85×10^{-7}	2.96×10^{-8}
2	with	2.06×10^{-7}	1.97×10^{-7}	1.46×10^{-8}
3	without	3.56×10^{-7}	6.55×10^{-7}	4.96×10^{-8}
3	with	1.72×10^{-7}	3.50×10^{-7}	2.52×10^{-8}
4	without	5.49×10^{-7}	6.75×10^{-7}	6.75×10^{-8}
4	with	4.12×10^{-7}	4.69×10^{-7}	4.81×10^{-8}

Table 7.4: Results for the Single EVD comparison.

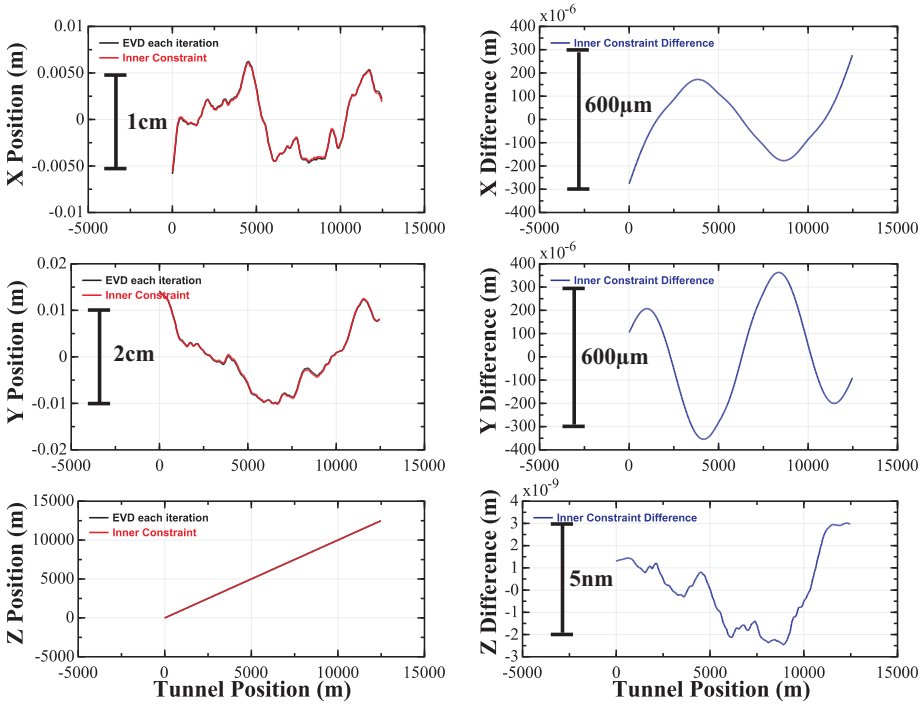

Figure 7.13: Figure comparing an inner constraint method to a solution with a full EVD constraint method

Inner constraint method

The inner constraint method (see section 3.3.2) can be used to constrain the model. Figure 7.13 shows the results of the network adjustment with the inner constraint method and the full EVD constraint method along with the differences. The time to generate the network was approximately 35 minutes. Figure 7.14 shows the results but with the last iteration replaced with an EVD based constraint.

The analysis was performed with four different random seeds with the range of the differences shown in table 7.5. Table 7.5 show that both approaches give solutions which have a similar trend to the full EVD solution but with an oscillatory difference in the X and Y planes. The effect of the final EVD is minimal. This method of generating the constraints is weak because it suffers from the selection problem as described in section 3.3.2. There are many choices of column manipulation of A to make the matrix N_{11} non-singular, and the incorrect choice will not minimise the trace of the output covariance matrix. In fact it can be seen from taking the SVD of A, that the constraint is a combination of the columns of

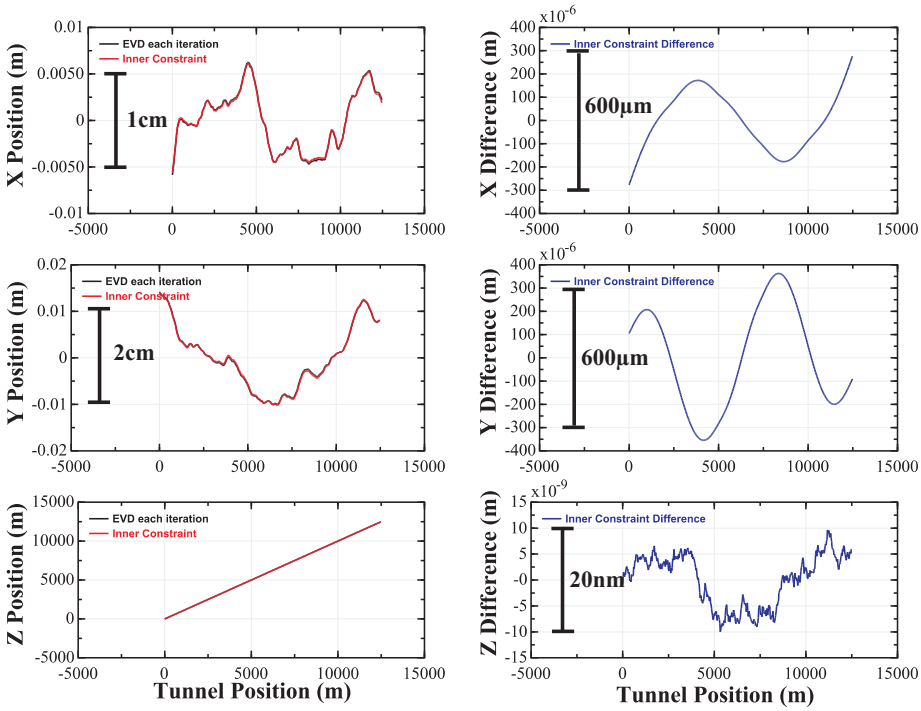

Figure 7.14: Figure comparing an inner constraint method with a final EVD to a solution with a full EVD constraint method

A. This shows that we will not be able to make a choice of column manipulation of A which will minimise the trace of the output covariance matrix.

Run Number	With or without end EVD	Difference range (m)		
		X axis	Y axis	Z axis
1	without	5.53×10^{-4}	7.18×10^{-4}	5.48×10^{-9}
1	with	5.53×10^{-4}	7.18×10^{-4}	1.96×10^{-8}
2	without	7.81×10^{-4}	17.6×10^{-4}	8.75×10^{-9}
2	with	7.81×10^{-4}	17.6×10^{-4}	9.41×10^{-9}
3	without	9.09×10^{-4}	7.91×10^{-4}	6.44×10^{-9}
3	with	9.09×10^{-4}	7.91×10^{-4}	5.88×10^{-9}
4	without	10.1×10^{-4}	5.43×10^{-4}	3.76×10^{-9}
4	with	10.1×10^{-4}	5.43×10^{-4}	3.59×10^{-9}

Table 7.5: Results for the inner constraint method comparison.

Fixed start and first rotation constraint

A constraint can be applied which fixes the first point in the network to be at (x, y, z) = (0,0,0) and the rotation of the first stop to be (θ, ϕ, ω) = (0,0,0). Figure 7.15 shows the results of the network adjustment with fixed start and first rotation constraint method

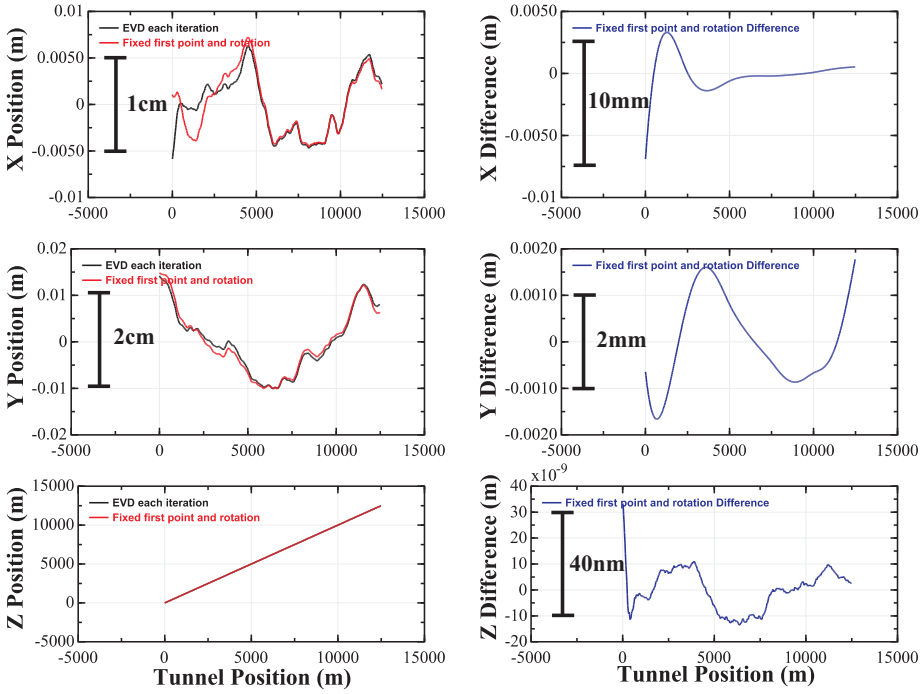

Figure 7.15: Figure comparing a fixed point and rotation constraint method to a solution with a full EVD constraint method

and the full EVD constraint method along with the differences. The time to generate the network was approximately 22 minutes. Figure 7.16 shows the results but with the last iteration replaced by an EVD based constraint.

The analysis was performed with four different random seeds with the range of the differences shown in table 7.6. Table 7.6 show that both approaches give solutions which have significant deviations from the full EVD solution; using an EVD for the final constraint does have some improvement. The deviations are significant and this is not a good method to constrain the model.

Fixed end points constraint

A constraint can be applied which fixes the first point in the network to be at (x, y, z) = (0,0,0), the fourth point from the end to be at (x, y) = (0,0) and the fourth point from the start to be at (x) = (0). This constraint failed to cause the system to converge, its solution was unstable.

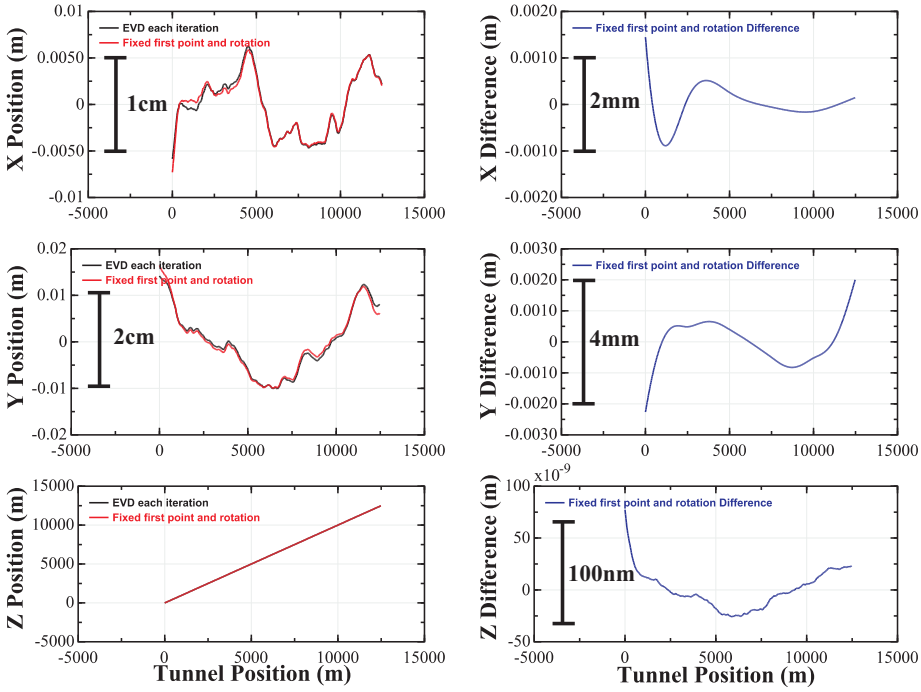

Figure 7.16: Figure comparing a fixed point and rotation constraint method with a final EVD to a solution with a full EVD constraint method

Constraint summary

In the previous sections different ways of constraining the simulated networks have been discussed as the method of using an EVD for each iteration is too slow. The method of using one EVD to constrain all of the iterations, with a different EVD for the last iteration gives a relative difference, to the EVD at every iteration, of 0.001%, the inner constraint with an end EVD gives a relative difference of 6% and the fixed start and rotation constraint with an end EVD gives relative difference of 20%. The closest to the full EVD solution is the single EVD method with a second EVD for the last iteration, this method will be used for all further simulations with simplified network simulation software.

Run Number	With or without end EVD	Difference range (m)		
		X axis	Y axis	Z axis
1	without	0.0102	0.0034	4.67×10^{-8}
1	with	0.00234	0.00427	1.03×10^{-7}
2	without	0.0114	0.0150	1.66×10^{-8}
2	with	0.00342	0.00637	1.64×10^{-7}
3	without	0.0074	0.0076	5.44×10^{-8}
3	with	0.00339	0.00326	1.19×10^{-7}
4	without	0.0072	0.0028	3.88×10^{-8}
4	with	0.00542	0.00214	4.52×10^{-8}

Table 7.6: Results for the fixed start and first rotation comparison.

7.4 Comparison of simplified network simulation software to PANDA

To test the simplified network simulation software it is compared to the PANDA simulations. The input parameters to the software, shown in table 7.7, were adjusted until the error curves output by PANDA and the simplified network simulation software match (section 7.4.1). The parameters were then used to generate a number of networks for use in DMS simulations, the results of the DMS simulations are used as a comparison of the models (section 7.4.2).

7.4.1 Comparison of Error Curves

Using JMinuit [53] the input error parameters of the simplified simulation model were varied until the square of the differences between the error curves produced by the simplified simulation model and the error curves produced by PANDA were minimized. The input parameters found are shown in table 7.7 with the error curves generated by the simplified simulation software and PANDA shown in figure 7.17 and the differences shown in figure 7.18.

Parameter	Value
$\sigma_X Device$	$9.693 \times 10^{-05} m$
$\sigma_Y Device$	$9.691 \times 10^{-05} m$
$\sigma_Z Device$	$3.097 \times 10^{-05} m$
σ_{PRM}	$1.015 \times 10^{-02} m$

Table 7.7: Laser Tracker Network Parameters which best fit the PANDA error curves.

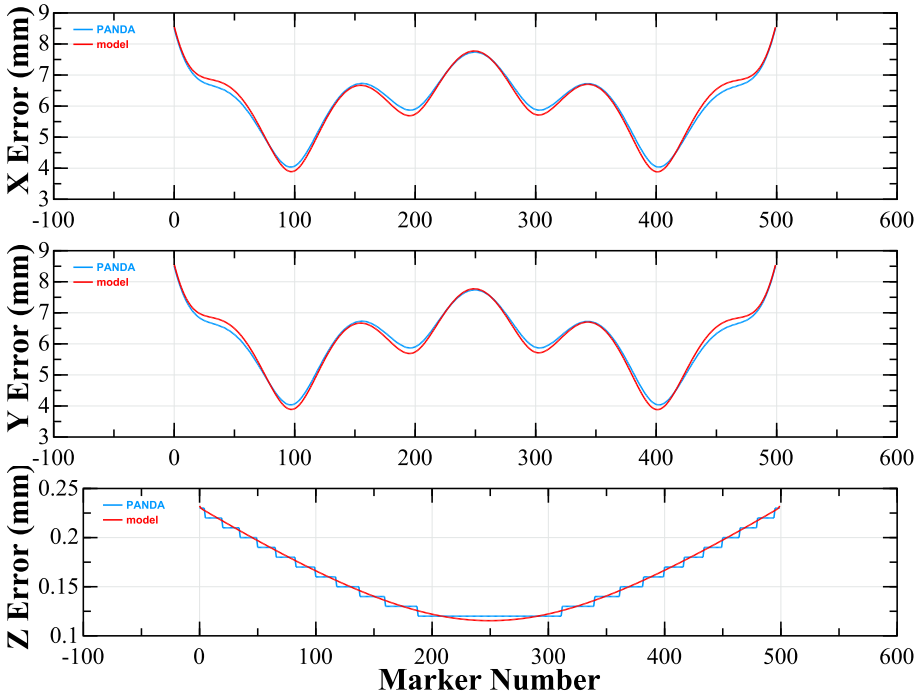

Figure 7.17: The error curves from PANDA and the simplified network simulation model

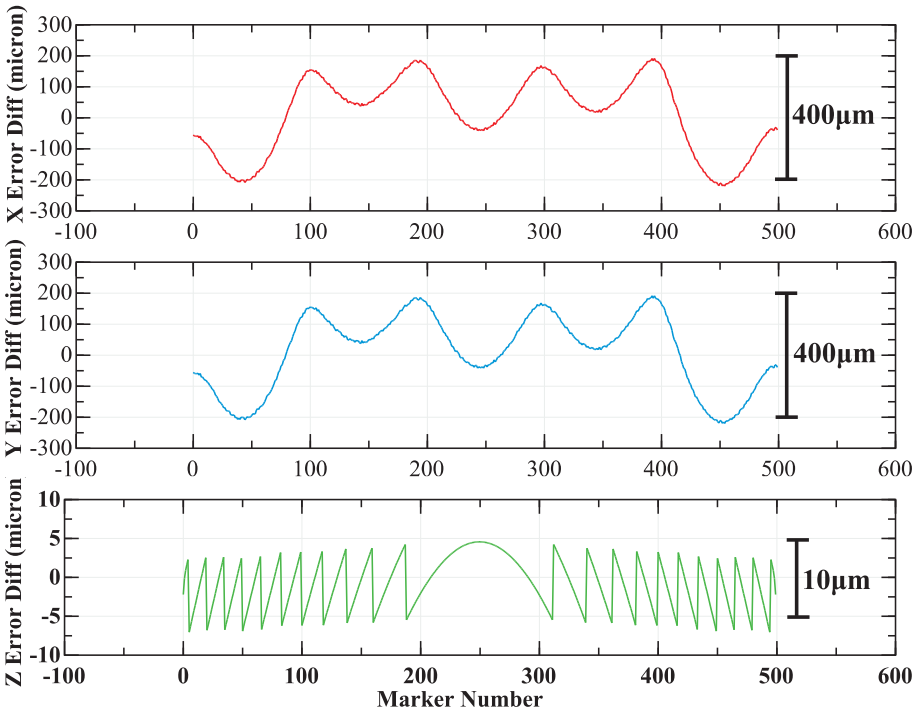

Figure 7.18: The difference between the error curves from PANDA and the simplified network simulation model

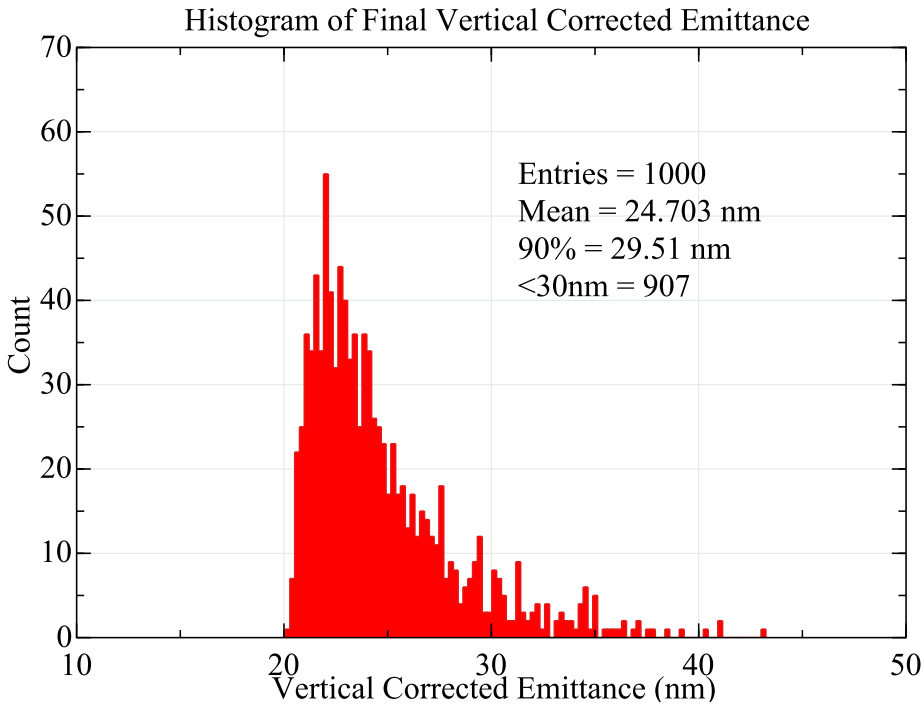

Figure 7.19: A histogram of the final corrected emittance's output by the Merlin DMS simulations with the network generated by the simplified network simulation model

The error curves shown in figure 7.17 and the difference in figure 7.18 agree at the $200\mu m$ level in the horizontal and vertical planes and $10\mu m$ in the longitudinal plane. The error curves generated by PANDA, in the X and Y directions, are smoother than the error curves generated by the simplified network simulation software. This difference is most likely caused by the fact that a ring of four markers is used in the simplified simulation software where as rings of seven markers were used in the PANDA simulations.

7.4.2 Dispersion matched steering comparison

Using the parameters in table 7.7 one hundred networks were simulated using the simplified network simulation software. For each of the generated networks 10 DMS simulations were performed in the same way as described in section 7.2.7. The final corrected vertical emittance's are shown in the histogram in figure 7.19. The process was repeated three times with the summary of the results shown in table 7.8. In each repeat, new networks were generated and DMS simulations performed with different random seeds.

Run Number	Mean (nm)	90% (nm)	% Passed
1	24.70	29.51	90.7
2	24.55	29.14	91.8
3	24.70	29.41	91.3
Average	24.65	29.35	91.3
Standard Deviation	0.086	0.191	0.6

Table 7.8: Results of DMS simulations using the simplified simulation model

The results in table 7.8 show that 91.3% of simulations have a final corrected vertical emittance below the required 30nm. The DMS simulations using reference networks simulated by PANDA show 95.5% of networks passing. The simulations are therefore pessimistic, which is expected as the error curves generated by the simulation model are not as smooth as those generated by PANDA. This shows that the simplified simulation software is good enough for testing the requirments of external alignment on the ILC. If the simplified simulation model could have its memory efficiency improved and could simulate seven network markers per ring, it is expected that the error curves produced by the software would be smoother and the DMS simulations would be a closer match to the PANDA DMS simulations.

7.5 Alignment requirements

The requirement for the external alignment of the ILC was originally formulated in the TESLA TDR [54] as a 1σ deviation of all fiducial markers, from the ideal position of 200μm (500μm) vertically (horizontally) over any 600m segment. The error curves shown in sections 7.2.6 and 7.4.1 extend over the entire network and not over sections of 600m. If we wish to evaluate whether the old method of specification is suitable we need a way to compare the networks generated to this criterion.

To find the errors over 600m for a particular network one hundred random networks are generated. This is relatively quick as generation of the error curves is not necessary. The generated networks are broken up into 600m sections, with each section having a straight line fitted and the residuals found. The residuals for the same section in each of the simulations are averaged and their standard deviations taken as the errors over that section. All of the

sections can then be averaged together to get the error curve of the network over an arbitrary 600m section.

Figure 7.20 shows the average error over a 600m section for networks adjusted with PANDA, with and without PRM's, as well as the errors of the networks adjusted by the simplified network simulation software. From the DMS simulations we know that networks with PRM's adjusted with PANDA give the best performance, followed by the simplified network simulation software and finally the network without PRM's adjusted by PANDA. The error curve over 600m for the PANDA adjusted network with PRM's is indeed the smallest, but it is not below the originally required 200μm over 600m, however the DMS simulations show that the performance is acceptable. The other two error curves over 600m don't show significant differences, except that the troughs are slightly lower in the PANDA adjusted network without PRM's than in the simplified simulation model. The two methods do however show differences over the whole network and only simulations with PRM (PANDA and simplified simulation model) produce acceptable DMS performance. This shows that errors over 600m are not a meaningful measures for the performance of the survey process. Instead the error curves over the entire network needs to be used as a measure of the performance of the survey process.

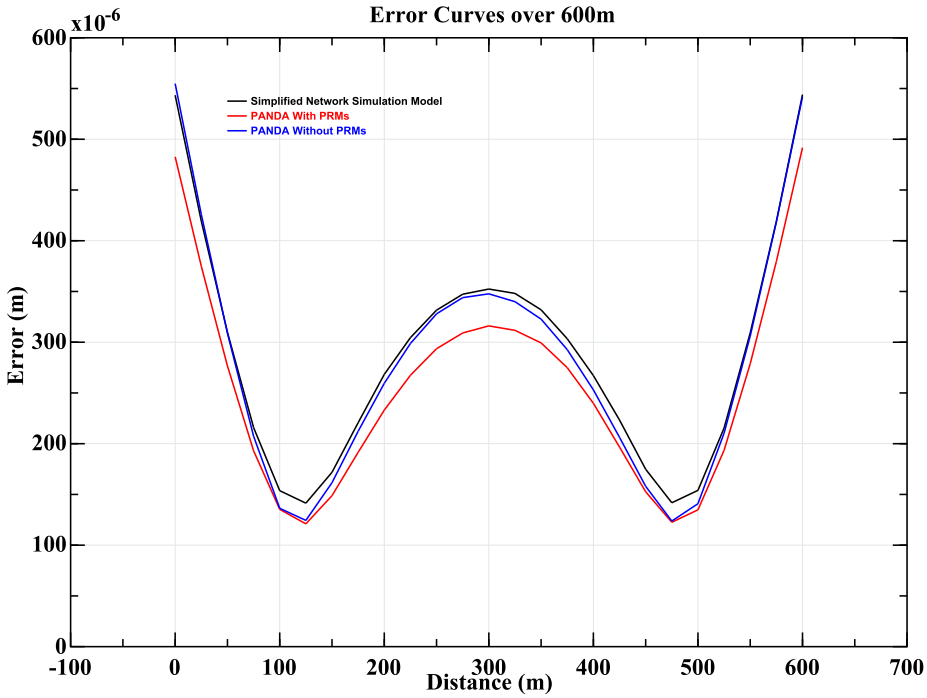

Figure 7.20: Average error over 600m for networks simulated with the simplified simulation model and PANDA with and without PRM's

Chapter 8

Summary and Future Work

8.1 RTRS interferometric measurement system

8.1.1 Summary

The absolute distance measurement system of the LiCAS RTRS has been commissioned and its performance under operational conditions was tested. The system uses Frequency Scanning Interferometry (FSI) and consists of three sub-systems: the reference interferometers (chapter 5), the internal and external FSI measurement interferometers (chapter 6).

The lengths of the reference interferometers, along with their errors, have been measured and are shown in table 5.7. The errors on the reference interferometer lengths are 1.1μm (0.3ppm). Upper limits on the precision of the LiCAS RTRS external and internal measurement interferometers were determined and are shown in tables 6.3 and 6.5 respectively. The systematic error on the distance measured by the measurement interferometers have been calculated as shown in section 6.6. The average statistical and systematic errors for the internal and external FSI lines are shown in table 8.1. The precision is higher on the internal FSI lines than on the external FSI lines, as they use collimators to focus the beams. The external FSI lines have no collimation, they are bare angle polished fibres and therefore, have a lower signal to noise ratio than the internal FSI lines. The external FSI lines do

however, have a much larger acceptance range of ±35.5mm at 0.45m (±79mrad), compared to the acceptance range of the internal FSI lines which varies from ±3mm to ±9mm at 4.5m (±0.7mrad to ±2mrad). The external FSI lines are dominated by statistical measurement errors, and the internal FSI lines are dominated by systematic errors stemming from the reference length uncertainty. The dominance of systematic errors on the internal FSI lines is a concern and needs to be reduced by improving the reference interferometers.

Interferometer Type	Distance Measured	Statistical Error	Systematic Error
External	0.45 m	1.9 μm	0.16 μm
Internal	4.5 m	0.24 μm	1.6 μm

Table 8.1: The average one sigma measurement errors averaged over all external and internal FSI lines

The six internal FSI line measurements from one unit can be combined to reconstruct the relative positions of two of the measurement units with respect to each other. The internal FSI system can determine the relative rotations around the X and Y axis and the distance between the two measurement units. The precision of the reconstruction for each measurement unit is shown in table 6.6, with the average precision shown in table 8.2.

Parameter	Error
Rotation around X axis	1.26×10^{-5} radians
Rotation around Y axis	0.79×10^{-5} radians
Translation along Z axis	2.70×10^{-7} m

Table 8.2: The average one sigma internal FSI reconstruction errors, neglecting errors from calibration constants.

The external FSI measurements can be used to determine the three dimensional position of a retro reflector with respect to a measurement unit. The precision of the reconstruction for each measurement unit is shown in table 6.4, with the average precision shown in table 8.3. The internal reconstruction, external reconstruction and the LiCAS RTRS tilt sensors are compared, and shown to agree within errors (section 6.8).

The two reference interferometers have very good precision when measuring each others lengths; they are capable of precision measurements at the 70 nm level with respect to each other. However, the lengths of the reference interferometers are difficult to predict accurately due to their complex thermal properties. The length changes of the interferometers

Parameter	Error (m)
Translation in X axis	1.07×10^{-6}
Translation in Y axis	3.10×10^{-6}
Translation in Z axis	3.20×10^{-6}

Table 8.3: The average one sigma external FSI reconstruction errors, neglecting errors from calibration constants.

cannot be fully explained from the thermal data alone if only linear thermal expansion terms are used. The reference interferometers have hysteresis during thermal ramping along with thermal stabilisation problems as they can take up 24 hours to stabilise after a two degrees Kelvin temperature change. Data taken when the reference interferometers are not in thermal equilibrium cannot be used as the reference interferometer length cannot be accurately determined. There were also mechanical instabilities seen in the reference interferometers: it is known that the length ratio of the two reference interferometers has changed over a short period by approximately 4×10^{-6} during the operation in DESY, Hamburg. These effects mean that the current evacuated reference interferometers have to be improved before they can be used in a future system.

8.1.2 Future work

Improvements to the interferometric measurement system can be made by creating a more stable reference interferometer. A reference interferometer with smaller errors in its length would reduce the systematic errors on the internal and external FSI measurements. The problems described above could be solved by making a more compact interferometer with fewer mechanical components. One possible solution is not to use an evacuated interferometer, but to use a highly thermally stabilised optical fibre as the reference interferometer. The optical fibre can be coiled to make it more compact to reduce thermal gradient issues and the absence of mechanical parts would avoid mechanical hysteresis effects. Optical fibres do, however, have dispersion and significant coefficients of thermal expansion (CTE), and thus their dispersion curves and CTEs would have to be well calibrated and their temperatures accurately measured.

Currently only statistical precision of the reconstruction of the external and internal FSI systems has been studied. The effects of the systematic measurement errors on the internal and external reconstruction still requires study. A study of the systematic errors will allow a better understanding of the required accuracy for the reference interferometer lengths.

8.2 Reference network simulations

8.2.1 Summary

The alignment of the ILC is important for emittance preservation. Simulations of reference networks measured by laser trackers, neglecting systematic errors from refractive effects, show that only 30% of DMS simulations give a final vertical emittance below the required 30nm. The reason for this poor performance is that overlapping measurements are prone to long range error growth. If the measurements are reinforced with long range primary reference marker measurements, using GPS every 2.5km, the long range error growth will be reduced and reference network simulations show that 95% of DMS simulations give a final vertical emittance of less than the required 30nm. This shows that long range primary reference marker measurements are required at the ILC unless novel methods can achieve a greater measurement accuracy. To study the measurement precision required by a novel device, such as the LiCAS RTRS, a simplified network simulation software has been developed. The simplified network simulation software can produce simulations of realistic reference networks for beam based alignment simulation studies. In the absence of systematics from refraction, the simulation software produces results similar to those found with a commercial software.

The study of errors on reference networks over 600m, shows that there are no significant differences between network measurement schemes that produce acceptable emittance growth and those that do not; however, over the entire length of the reference network there are significant differences between the errors of the different measurement schemes. This shows

that requirements for the alignment of the ILC main linac need to be specified over the entire length of the linac, not just over a short section and that ideally networks should be simulated in their entirety and used as inputs to beam based alignment simulations.

8.2.2 Future work

The reference networks simulated in this thesis do not take account of systematic errors caused by refraction in air. Systematic effects need to be studied in order to understand what level of systematics could be tolerated in the reference network measurements for the ILC. The simplified network simulation software needs to be modified to enable systematics to be included along with improvements on its memory efficiency. These improvements will allow more complex network layouts to be studied. One could then determine the optimal configuration of the ILC reference network. The simplified network simulation model can then be used to determine the required measurement accuracy, with which to measure the reference network.

8.3 Future work on the LiCAS RTRS

The current status of the LiCAS RTRS is that all of the calibration data has been taken for the entire RTRS. The data is currently being analysed in order to determine the calibration constants. The LiCAS RTRS has also performed multiple surveys of the 50m test tunnel in DESY, Hamburg; once the calibration constants have been determined, the surveys can be analysed and compared to a conventional survey performed by the DESY geodesy group. Once the calibration constants and the performance of the RTRS have been determined, the simplified network simulation model can be used to estimate the accuracy with which the entire ILC reference network could be measured by the LiCAS RTRS.

Bibliography

[1] Brian Robert Martin and Graham Shaw. *Particle Physics.* John Wiley and Sons, 2003.

[2] W. E. Burcham and M. Jobes. *Nuclear and Particle Physics.* Pearson Education, 1995.

[3] The TEVNPH Working Group. Combined CDF and D0 upper limits on standard model higgs-boson with up to 4.2^{-}1 fb of data. March 13, 2009.

[4] Phillip James Edwin Peebles. *Principles of physical cosmology.* Princeton University Press, 1993.

[5] Lyndon Evans and Philip Bryant (editors). LHC machine. *Journal of Instrumentation*, 3(08):S08001, 2008.

[6] Edward J. N. Wilson. *An introduction to particle accelerators.* Oxford University Press, 2001.

[7] D. Brandt, editor. *CERN accelerator school proceedings*, number CERN 2009 005, May 2008.

[8] Nicholas Walker James Brau, Yasuhiro Okada. *International Linear Collider Reference Design Report Executive Summary.* http://ilcdoc.linearcollider.org/record/6321/files/ILC_RDR_Volume_1-Executive_Summary.pdf, August 2007.

[9] Nicholas Walker Nan Phinney, Nobukasu Toge. *International Linear Collider Reference Design Report Accelerator.*

http://ilcdoc.linearcollider.org/record/6321/files/ILC_RDR_Volume_3-Accelerator.pdf, August 2007.

[10] G. Grzelak, A. Reichold, J. Dale, M. Dawson, J. Green, Y. Han, M. Jones, G. Moss, B. Ottewell, R. Wastie, D. Kämptner, J. Prenting, M. Schlösser, and C. Uribe-Estrada. The LiCAS-RTRS a rapid and cost efficient survey system for the ILC. In the Proceedings of 9th International Workshop on Accelerator Alignment (IWAA 06), Menlo Park, California, 26-29 Sep 2006.

[11] Dr Patric Brockill. Diagram of the licas rtrs and its measurement procedure. Private Communication.

[12] Yanmei Han, Armin Reichold, Colin Perry, and Richard Bingham. Frequency scanning fibre interferometer for absolute distance measurements over a large target area. In the Proceedings of 9th International Workshop on Accelerator Alignment (IWAA 06), Menlo Park, California, 26-29 Sep 2006.

[13] John Green. *Development of a Prototype Frequency Scanning Interferometric Absolute Distance Measurement System for the Survey & Alignment of the International Linear Collider.* PhD thesis, University Of Oxford, 2007.

[14] Agilent. Agilent 81642a tunable laser module user guide, Febuary 2002.

[15] Greg Moss. *Alignment At the International Linear Collider.* PhD thesis, University Of Oxford, 2010.

[16] Schäfter and Kirchhoff. Schäfter and kirchhoff 57fcm diode laser data sheet.

[17] Schäfter and Kirchhoff. Schäfter and kirchhoff 60fc collimator data sheet.

[18] Sherborne Sensors. Schaevitz lsop/lsoc dc-operated, gravity-referenced inclinometers.

[19] Cecilia Uribe Estrada. Elmb setup for licas. Private Communication, June 2007.

[20] J. R. Cook and G. Thomas. Elmb user guide, Febuary 2005.

[21] Berger Lahr. Icla ifa intelligent compact drive fieldbus servomotor technical documentation.

[22] Dr Patric Brockill. Least squares using linear algebra. Private Communication.

[23] D.E. Wells and E.J. Krakiwsky. *The Method Of Least Squares.* Geodesy and Geomatics Engineering University Of New Brunswick, 1971.

[24] Georges Blaha. A note on adjustment of free networks. *Journal of Geodesy*, 56(4):281–299, December 1982.

[25] Åke Björck. *Numerical methods for least squares problems.* SIAM, 1996.

[26] Jorge Nocedal and Stephen J. Wright. *Numerical optimization.* Springer, 1999.

[27] A. Perelmuter. Adjustment of free networks. *Journal of Geodesy*, 53(4):291–295, December 1979.

[28] Gilbert Strang and Kai Borre. *Linear algebra, geodesy, and GPS.* SIAM, 1997.

[29] Bill Triggs, Philip McLauchlan, Richard Hartley, and Andrew Fitzgibbon. Bundle adjustment a modern synthesis. In *Vision Algorithms: Theory and Practice*, pages 153–177. 2000.

[30] Sun Microsystems. Java.

[31] Bjorn-Ove Heimsund. Matrix toolkits for java.

[32] David M. Doolin Jack Dongarrazy Keith Seymourz. Jlapack - compiling lapack fortran to java, December 1998.

[33] E. Anderson, Z. Bai, J. Dongarra, A. Greenbaum, A. McKenney, J. Du Croz, S. Hammerling, J. Demmel, C. Bischof, and D. Sorensen. LAPACK: a portable linear algebra library for high-performance computers. In *Proceedings of the 1990 ACM/IEEE conference on Supercomputing*, pages 2–11, New York, New York, United States, 1990. IEEE Computer Society Press.

[34] J. Dongarra I. Duff S. Hammarling G. Henry M. Heroux L. Kaufman A. Lumsdaine A. Petitet R. Pozo K. Remington R. C. Whaley L. S. Blackford, J. Demmel. An updated set of basic linear algebra subprograms (BLAS). *ACM Trans. Math. Software.*, 28(2):135–151, 2002.

[35] S. Butterworth. On the theory of filter amplifiers. *Experimental Wireless and the Wireless Engineer*, 7:536–541, 1930.

[36] P. Carré. *Metrologia*, 2:12–23, January 1 (1966).

[37] Paul Andrew Coe. *An Investigation of Frequency Scanning Interferometry for the alignment of the ATLAS semiconductor tracker.* PhD thesis, University Of Oxford, 2001.

[38] N. R. Lomb. Least-squares frequency analysis of unequally spaced data. *Astrophysics and Space Science*, 39(2):447–462, February 1976.

[39] W.H.Press and G.B.Rybicki. Fast algorithm for spectral analysis of unevenly sampled data. *The Astrophysical Journal*, 338:277–280, 1989.

[40] William T. Vetterling and Brian P. Flannery. *Numerical Recipes in C++: The Art of Scientific Computing.* Cambridge University Press, 2 edition, February 2002.

[41] Philip E. Ciddor. Refractive index of air: new equations for the visible and near infrared. *Applied Optics*, 35(9):1566–1573, March 1996.

[42] Bengt Edlen. The refractive index of air. *Metrologia*, 2(2):71–80, 1966.

[43] K. P. Birch and M. J. Downs. An updated edlen equation for the refractive index of air. *Metrologia*, 30(3):155–162, 1993.

[44] K. P. Birch and M. J. Downs. Correction to the updated edlen equation for the refractive index of air. *Metrologia*, 31(4):315–316, 1994.

[45] Geodesy group DESY. Typical laser tracker measurement precision. Private communications.

[46] Louis Lyons. *Statistics for Nuclear and Particle Physicists*. Cambridge University Press, April 1989.

[47] T.O. Raubenheimer and R.D. Ruth. A dispersion-free trajectory correction technique for linear colliders. *Nuclear Instruments and Methods in Physics Research Section A: Accelerators, Spectrometers, Detectors and Associated Equipment*, 302(2):191–208, April 1991.

[48] N. Walker. Emittance preservation in a possible ILC main linac which follows the earths curvature. EUROTeV-Report 2005-17-1, DESY, Hamburg, Germany, 2005.

[49] N. Walker D. Kruecker, F. Poirier. Energy adjustment strategy for dispersion free steering at the ILC using the MERLIN package ILCDFS. EUROTeV-Report 2006-106, DESY, Hamburg, Germany, 2006.

[50] GeoTec GmbH. Panda, January 2005.

[51] N. Walker D. Kruecker, F. Poirier. An ilc main linac simulation package based on merlin. EUROTeV-Report 2006-71, DESY, Hamburg, Germany, 2006.

[52] Nick Walker, Andrzej Wolski, Dirk Krucker, Glen White, Frank Jackson, and Dan Bates. A C++ class library for accelerator simulations.

[53] FreeHep. Jminuit - a java port of minuit.

[54] R. Brinkmann et al. Tesla technical design report. March 2001.

Appendix A

Glossary

ADC Analogue to Digital Converter.

APC Angle Polished Connector.

BBA Beam Based Alignment.

BDS Beam Delivery System.

BPM Beam Position Monitor.

CTE Coefficient of Thermal Expansion.

DESY Deutsches Elektronen-Synchrotron.

DFS Dispersion Free Steering.

DMS Dispersion Matched Steering.

DR Damping Ring.

EDFA Erbium Doped Fibre Amplifier.

ELMB Embedded Local Monitor Board.

EVD Eigenvalue Decomposition.

FEL Free Electron Laser.

FFT Fast Fourier Transform.

FODO Focusing Defocusing.

FSI Frequency Scanning Interferometer.

GUT Grand Unified Theory.

ILC International Linear Collider.

IP Interaction Point.

IRU Interlock Relay Unit.

LHC Large Hadron Collider.

LiCAS Linear Collider Alignment and Survey.

LSM Laser Straightness monitor.

MI Measurement Interferometer.

ML Main Linac.

NA Numerical Aperture.

NC Normal Conducting.

OMD Optical Matching Device.

PRM Primary Reference Marker.

RF Radio Frequency.

RI Reference Interferometer.

RM Reference Marker.

RTE Relative Thermal Expansion.

RTML Ring To Main Linac.

RTRS Rapid Tunnel Reference Surveyor.

SC Superconducting.

SM Standard Model.

SUSY Supersymmetry.

SVD Singular Value Decomposition.

TME Theoretical Minimum Emittance.

XFEL X-ray Free Electron Laser.